STRONTIUM ADDITIONS IN AZ31 MAGNESIUM ALLOY

By
Alireza Sadeghi

A Thesis Submitted to the Faculty of Graduate Studies and Research in Partial Fulfillment of the Requirements for the Degree of Doctor of Philosophy

Department of Mining and Materials Engineering
McGill University
Montreal, Canada

January 2012

ABSTRACT

Magnesium is a low density metal that is an attractive alternative to steel and aluminum for weight reduction in automotive design. Automotive applications of Mg have steadily grown since the early 1990s, beginning initially with internal structural castings such as steering wheels and instrument panels in which casting alloys with good room temperature strength and ductility were used. Limited deformation mechanisms at moderate temperatures and resulting poor formability have been the major limitations to the development of Mg wrought alloys. Specialized alloys with improved deformation behaviour exist for aerospace applications, however these are based on expensive alloy systems containing silver and rare-earth (RE) elements such as yttrium and neodymium. Effective use in high volume applications such as automotive components requires a more cost effective solution.

Conventional low cost extrusion alloys based on the Mg-Al-Zn and Mg-Zn-Zr systems (AZ and ZK series, the most widely used being AZ31 with 3wt%Al and 1wt%Zn) offer a solution however, they suffer from major problems of extrudability and poor formability. Strontium (Sr) has been introduced to replace RE additions in Mg alloys with an alkali-earth element. Sr has been used as an effective alloying element for grain and second phase refinement as it precipitates as intermetallic phases with high thermal stability. A few studies have been conducted on the behaviour of these Sr-containing thermally stable precipitates during high temperature deformation. The primary objectives of this research were to study the microstructure, mechanical properties and texture evolution of AZ31 alloy containing various levels of Sr during hot deformation. Experimental techniques such as optical microscopy, thermal analysis, hot compression, room temperature mechanical testing, Scanning Electron Microscopy (SEM), Energy Dispersive Spectroscopy (EDS), Electron Probe Micro-Analysis (EPMA), Electron Back Scattering Diffraction (EBSD) and X-ray

diffraction were used to thoroughly characterize the microstructure and texture of the alloys.

In the first part of this study, the precipitation and solidification of AZ31-Sr castings was studied by thermal analysis and numerical modeling as a background to understand the formation of secondary phases and microstructural development. This was achieved by casting AZ31 alloys containing various levels of Sr, recording the cooling curves and comparing the findings with computer simulated generated using FactSage (thermodynamic calculation software). The results indicated that small amounts of Sr refined the β-$Mg_{17}Al_{12}$ globular phase and increased its thermal stability during annealing. With higher concentrations of Sr, the amount of β phase decreased and the weight percent of Sr-rich (Al-Mg-Sr) interdendritic precipitates increased. The precipitation temperatures of the different phases as determined by thermal analysis were in close agreement with Scheil cooling results calculated using FactSage. TEM observations and EDS analysis on extracted precipitates revealed Mg and Zn solubility in the Al_4Sr particles. As calculated *in silico* and confirmed experimentally by TEM, increasing the Sr content resulted in a decrease in Al solid solubility with a slight increase in Mn solubility.

In the second part of this study the recrystallization and texture evolution during hot bar extrusion of AZ31-Sr alloys in three sections is characterized. In the first section (3.1) it was shown that Particle-Stimulated Nucleation (PSN) occurred in the deformed regions around the precipitates in certain hot working conditions at 350^{o}C. Increasing the amount of Al-Sr stringers in AZ31 increased the potential sites for PSN. Moreover, PSN through Al-Sr stringers resulted in the recrystallization of new grains with orientations other than the basal fibre texture which results in the reduction of fibre texture strength. In section 3.2 the formation of new phases resulting from the addition of trace levels of Sr in AZ31 and its effects on mechanical properties and texture were investigated. Sr reduced the strength of the basal texture in hot compression and extrusion which was

attributed to the decrease in twinning and the change in the concentration of Al and Sr atoms in Mg solid solution. In the last section (3.3), the texture results of hot extrusion at four temperatures for four alloys and hot compression of ten alloys at four temperatures were combined to plot a micro mechanism map across the extrusion temperature range and Sr levels.

In the following two chapters, the yield asymmetry of AZ31-Sr extruded bars (section 5.1) and the effect of annealing before hot extrusion (section 6.1) were examined. The tensile and compressive strengths of extruded AZ31 alloys containing different levels of Sr depended more on the extrusion temperature than on the Sr concentration and also the yield asymmetry of the AZ31+xSr alloys increased with increasing extrusion temperature. However, the increase was less when Sr was present in the alloy. Section 6 reports results obtained from AZ31+0.8Sr subjected to annealing prior to extrusion at four different times. An increase in the duration of the pre-deformation anneal switched the plane facing the extrusion direction from first order prismatic (100) to second order prismatic planes (110). This occurred as a result of a change in the dominant slip direction via Al depletion in the Mg solid solution and the related decrease in lattice resistance.

In the final of part of this thesis, the microstructures and textures of hot extruded AZ31-Sr tubes were examined. Section 7.1 reports on seamed tubes that were extruded using a porthole die. The complex strain path inside the die could be divided into several simple curvatures which occur during ECAP (Equal Channel Angular Pressing). Extra texture components (δ) appeared in the pole figures as a result of circumferential flow in the extrusion die. It was observed that increasing the Sr in the alloy, reduced the amount of Al in the Mg solid solution and lowered the lattice resistance against dislocation slip. As a result, the grains deformed more easily in circumferential directions and selective work hardening-DRX (Dynamic Recrystallization) cycles resulted in more grains with an unfavourable slip orientation (δ components). In section 7.2 the expansion

behaviour of seamless AZ31-Sr tubes was studied by compressing the tubes with pure-copper cylinder-inserts. The texture of the extruded tube is comprised of two components: hoop direction (HD) and radial direction (RD), which behave differently during expansion. The HD component undergoes extension twinning while the contraction and double twinning occurs in RD grains. It was demonstrated that at room temperature AZ31 had more ductility and less strength than Sr-containing alloys. However, in expansion at 200^{o}C, AZ31 showed a higher flow stress and none of the samples failed within the tested strain range. Results indicated that either by increasing the expansion temperature or level of Sr, the volume fraction of twinning was reduced.

RÉSUMÉ

Le magnésium à 1 / 3 de la densité de l'acier et 2 / 3 de l'aluminium offre une option plus viable pour l'automobile significative la lumière de pondération. Les applications automobiles de Mg ont commencé à croître depuis le début des années 90, d'abord avec moulages internes structurels tels que le volant et le tableau de bord en utilisant des alliages de fonderie avec force à température ambiante une bonne et une ductilité. Mécanismes de déformation limitée à des températures modérées et de la formabilité résultante pauvres ont été les principaux obstacles au développement des alliages de magnésium forgé dans le passé. Alliages spécialisés avec le comportement de déformation améliorées existent pour les applications aérospatiales, mais ceux-ci sont basées sur des systèmes d'alliage contenant de l'argent coûteuses et les terres rares (RE) des éléments tels que l'yttrium, le néodyme. Les applications automobiles nécessitant des performances et optimisation des coûts ne peut pas faire usage de ces alliages pour les applications à volume élevé.

Inférieure conventionnel d'extrusion d'alliages de coûts sur la base des Mg-Al-Zn et Mg-Zn-Zr systèmes (AZ et ZK série, la plus largement utilisée étant AZ31 avec 3WT% Al et Zn% 1wt) existent également, cependant, ils souffrent de deux problèmes majeurs de extrudabilité et formabilité pauvres. Strontium (Sr) a été introduit pour remplacer les ajouts RE en Mg avec un élément alcalino-terreux. Sr a été utilisé comme un élément d'alliage efficaces pour le grain et le raffinement deuxième phase car il précipite sous forme de phases intermétalliques avec une grande stabilité thermique. Quelques études ont été menées sur le comportement de ces Sr contenant thermiquement stable précipités pendant la déformation à haute température. Les principaux objectifs de cette recherche était d'étudier la microstructure, propriétés mécaniques et évolution de la texture d'un alliage contenant AZ31 différents niveaux de Sr lors de la déformation à chaud. Les techniques expérimentales telles que la microscopie optique, analyse thermique, compression à chaud, la température ambiante à la traction,

microscopie électronique à balayage (MEB), la spectrométrie à dispersion d'énergie (EDS), Electron Probe Micro-Analysis (EPMA), diffraction d'électrons rétrodiffusion (EPCA) et X- diffraction des rayons ont été utilisés pour caractériser complètement la microstructure et la texture des alliages.

Dans la première partie de cette étude, les précipitations et la solidification des moulages AZ31-Sr est étudié par analyse thermique et de modélisation numérique comme toile de fond pour comprendre la formation de phases second et le développement des microstructures. Ceci a été réalisé via la synthèse de AZ31 alliages contenant différents niveaux de Sr, coulée dans des moules de sable, l'enregistrement des courbes de refroidissement et en comparant les résultats avec les résultats de simulation de FactSage (logiciel de calcul thermodynamique). Les résultats indiquent que de petites quantités de Sr affiner la phase β-globuleux Mg17Al12 et d'augmenter sa stabilité thermique au cours du recuit. Avec des concentrations plus élevées de Sr, le montant de la phase β diminue et le poids pour cent de Sr-riches (Al-Mg-Sr) interdendritiques précipités augmente. Les températures de précipitation des différentes phases tel que déterminé par analyse thermique sont en bon accord avec les résultats de refroidissement Scheil obtenus en utilisant les calculs thermodynamiques via FactSage. TEM investigation et d'analyse EDS sur les extraits précipités révélé Mg et Zn soluble dans les particules Al4Sr. Il a été calculé par le modèle thermodynamique et confirmé par TEM qui en augmentant la teneur de Sr, Al solubilité solide diminue tandis que le niveau de Mn augmente légèrement.

La deuxième partie de cette étude caractérise l'évolution recristallisation et la texture lors de l'extrusion à chaud de barres AZ31-Sr alliages en trois sections. Dans la première section (3.1), il a été démontré que des particules stimulée par nucléation (PSN) survient dans les régions déformées autour des précipités dans certaines conditions de travail chaudes au 350oC. Augmenter la quantité d'Al-Sr dans les longerons AZ31 augmente les sites potentiels pour le PSN. Par ailleurs, le PSN à travers Al-Sr longerons résultats dans la recristallisation des grains de

nouveaux avec d'autres orientations que la texture fibreuse basale qui se traduit par la réduction de la force de texture fibreuse. Dans la deuxième section (3,2) la formation de nouvelles phases résultant de l'addition de traces de Sr dans AZ31 et ses effets sur les propriétés mécaniques et la texture ont été étudiées. Il a été démontré que Sr réduit la résistance de la texture de base dans la compression à chaud et d'extrusion qui peut être attribué à la diminution de jumelage et le changement de la concentration d'atomes Al et Mg Sr dans la solution solide. Dans la dernière section (3.3), les résultats texture de l'extrusion à chaud à quatre températures pour quatre alliages et compression à chaud de dix alliages à quatre températures ont été combinées pour tracer une carte micro mécanisme à travers la gamme de température d'extrusion et les niveaux de Sr.

Dans les deux prochains chapitres, le rendement de l'asymétrie AZ31-Sr barres extrudées (section 5.1) et l'effet de recuit avant extrusion à chaud (section 6.1) ont été examinés. Il a été démontré que les forces de traction et de compression des extrudés AZ31 alliages contenant différents niveaux de Sr dépendent davantage de la température d'extrusion que sur la concentration en Sr et le rendement d'asymétrie de l'AZ31 + alliages XSR augmente avec la température d'extrusion augmente. Toutefois, le montant de l'augmentation est plus faible lorsque Sr est présent dans l'alliage. Section 6 rapports sur AZ31 0,8 Sr soumise à un recuit avant l'extrusion à quatre moments différents. Une augmentation de la durée de la déformation pré-recuit commutateurs de l'avion face à la direction d'extrusion de premier ordre prismatiques (100) pour les avions de second ordre prismatiques (110) en raison de changements dans la direction de glissement dominante par le biais de l'épuisement des Al Mg solides solution et la diminution de la résistance liée treillis.

Lors de la finale d'une partie de l'étude, les microstructures et les textures de extrudée à chaud AZ31-Sr tubes ont été examinés. La section 7.1 des rapports sur les tubes qui ont été sertis extrudé en utilisant une matrice hublot. Le chemin de déformation complexe intérieur de la filière pourrait être divisé en plusieurs

courbures simples qui se produisent pendant l'ECAP. Composants texture supplémentaire (δ) apparaissent dans les chiffres pole à la suite d'écoulement circonférentiel dans la filière d'extrusion. On a observé que plus le Sr dans l'alliage, la baisse est la quantité d'Al Mg dans la solution solide et plus la résistance en treillis contre le glissement de dislocations. En conséquence, les grains pourraient se déformer plus facilement dans les directions circonférentielle et sélective écrouissage-DRX du cycle laisse plus de grains avec l'orientation de glissement défavorable (composants δ). Dans la section 7.2 le comportement d'expansion sans soudure AZ31-Sr tubes étudiés en comprimant les tubes avec pur-cylindre de cuivre-inserts est décrite. La texture du tube extrudé est compromise de deux éléments, la direction hoop (HD) et la direction radiale (RD), qui se comportent différemment lors de l'expansion. La composante HD subit de jumelage d'extension tandis que le jumelage de contraction et le double se produit dans les grains de RD. Il a été démontré que, à température ambiante AZ31 a plus de ductilité et de moins de force que Sr-alliages contenant. Toutefois, en expansion à 200oC, AZ31 montre un stress plus élevé de flux, et aucun des échantillons échouent dans la gamme souche testée. Les résultats indiquent que ce soit en augmentant la température ou le niveau de l'expansion Sr, la fraction volumique de jumelage est réduite.

ACKNOWLEDGEMENTS

Foremost, I would like to express my deepest gratitude to my research supervisor, Professor Mihriban Pekguleryuz, for her guidance and support, for providing me with every opportunity and believing me in all aspects of my education. Her personal generosity, prompt response, and her love of and dedication to her work and her students are a steady source of encouragement to me. It was a pleasure and honour to work with a woman who has a broad and profound knowledge, not only in the academic field but also in many other aspects.

Special thanks are due to Dr. Majid Hoseini and Dr. Étienne Martin for their valuable advice and suggestions and for sharing their knowledge and expertise. I am grateful to Pierre Vermette for his in-depth industrial experience. I thank the staff at McGill University's department of Mining and Materials Engineering. I am very fortunate to be a part of the team of graduate students in the Materials Engineering department whose friendship and conversation created a very pleasant working atmosphere. Many thanks are due to Mert Celikin, Deniz Temur Sultan, Hemant Borkar, Amir Rezaie Farkoosh, Mohsen Masoumi, and Mandana Bornapour for helpful discussions during our group meetings. My appreciation also goes to my friends in the department, Ahmad Rezaeian, Amir Farzadfar, Mehdi Sanjari, and Maziar Shahmohammadi for many interesting and valuable discussions and for always being willing to lend a hand and give advice. I would like to acknowledge Applied Magnesium (formerly Timminco) for industrial support and for providing the raw materials and master alloy. Also I would like to gratefully acknowledge the financial support of McGill University through the MEDA (McGill Engineering Doctoral Award) program.

Last, but not least, I would like to express my sincere appreciation to my wife, Zahra, for her unconditional love, constant support and encouragement, which always motivated me to strive for something better. Special thanks to our

parents and brothers and sisters; I am always grateful for their enduring support and encouragement in every step in my life, career and study. This work would not have been possible without their endless love and support. I am indebted to Amir Hossein, my dear son, whose ongoing smile has accompanied me throughout the completion of this thesis.

CONTRIBUTIONS OF AUTHORS

This thesis was prepared according to the guidelines for a manuscript-based thesis. These guidelines are published by the Graduate and Postdoctoral Studies office of McGill University. The information related to the authors of the manuscripts is cited as follows:

The following nine manuscripts were used to prepare this thesis. The first two are incorporated in Chapter 3, appearing as sections 3.1, 3.2. The following three are presented in chapter 4, as sections 4.1, 4.2 and 4.3. Chapters 5 and 6 contain one article each. The final two manuscripts are included in Chapter 7, appearing as sections 7.1, 7.2 . All the manuscripts have been published, accepted or submitted for publication as indicated.

1- **Alireza Sadeghi** and Mihriban Pekguleryuz, "Precipitation during the Solidification of Mg-3wt%Al-1wt%Zn-(0.001-1%) Sr Alloys," Published in AFS 2010 conference proceeding, Orlando March 2010.
2- **Alireza Sadeghi** and Mihriban Pekguleryuz, "Microstructural Investigation and Thermodynamic Calculations on the Precipitation of Mg-Al-Zn-Sr Alloys," Journal of Materials Research, Volume 26, Number 7, 14 April 2011, Pages 896-903.
3- **Alireza Sadeghi**, Mihriban Pekguleryuz, "Recrystallization and Texture Evolution of Mg-3%Al-1%Zn-(0.4-0.8)%Sr Alloys during Extrusion," Materials Science and Engineering A, Volume 528, Issue 3, 25 January 2011, Pages 1678-1685
4- **Alireza Sadeghi**, Mihriban Pekguleryuz, "Microstructure, mechanical properties and texture evolution of AZ31 alloy containing trace levels of strontium," Materials Characterization, Volume 62, Issue 8, August 2011, Pages 742-750.
5- **Alireza Sadeghi**, Majid Hoseini, Mihriban Pekguleryuz, "Effect of Sr addition on Texture Evolution of Mg-3Al-1Zn (AZ31) Alloy during

extrusion," Materials Science and Engineering: A, Volume 528, Issues 6.1.8, 25 March 2011, Pages 3096-3104.

6- **Alireza Sadeghi**, Scott Shook, Mihriban Pekguleryuz, "Yield Asymmetry and Fracture Behaviour of Mg-3%Al-1%Zn-(0-1)%Sr Alloys Extruded at Elevated Temperatures," Materials Science and Engineering: A, Volume 528, Issues 25-26, 25 September 2011, Pages 7529-7536.

7- **Alireza Sadeghi**, Mihriban Pekguleryuz, "Effect of Annealing on the Microstructure and Texture Evolution of Mg-3Al-1Zn-0.8Sr Alloy during Hot Extrusion," Submitted to Journal of Materials Science – Available online 10 April 2012, DOI: 10.1007/s10853-012-6416-0

8- **Alireza Sadeghi**, Majid Hoseini, Mihriban Pekguleryuz, "Tube Extrusion of AZ31 Alloy with Sr Additions," Materials Science and Engineering: A, Volume 544, 15 May 2012, Pages 70-79.

9- **Alireza Sadeghi**, Étienne Martin, Mihriban Pekguleryuz, "Expansion of hot extruded AZ31+Sr seamless tubes: Texture evolution and twinning," to be submitted

All the manuscripts were co-authored by Prof. Mihriban Pekguleryuz, who supervised the research projects, provided guidance and edited the manuscripts. All the experiments were planned and conducted by the candidate. All analyses (microstructure, mechanical properties and texture) and interpretation (other than the assistance from co-authors mentioned below) were performed by the candidate. Two of the manuscripts include Dr. Majid Hoseini (post-doctoral researcher, Department of Mining and Materials Engineering, McGill University) for his contribution towards the understanding of the deformation structure and texture analysis. Manuscript 6 includes Mr Scott Shook (Applied Magnesium, industrial partner of the project) for his contribution of preparing the industrial sample. Paper 9 includes Dr. Étienne Martin (post-doctoral researcher, Department of Mining and Materials Engineering, McGill University) for his contribution in understanding texture and twinning.

TABLE OF CONTENTS

LIST OF FIGURES

LIST OF TABLES

Chapter 1

Introduction

Magnesium alloys are important candidate materials in the automotive industry to reduce the total mass of a vehicle and therefore improve fuel economy [Beals 2007]. The low density of magnesium (1/3 and 2/3 that of steel and aluminum respectively) is attractive to the car designer for the purpose of weight reduction. Following the early use of magnesium by Volkswagen in the 1970s, a renewed interest in magnesium emerged in the early 1990s when automotive parts containing magnesium such as steering wheels, valve covers and instrument panels appeared. The development of new Mg components continued with the recent introduction of new alloys (AE44, AS31, AJ62). High temperature strength, corrosion resistance and forming ability were key properties of research into these materials.

Magnesium alloys are commercially produced for both casting and wrought applications. Magnesium wrought alloys have been developed for aerospace use and are not ideal for cost sensitive applications. Furthermore, while strength is more important than formability in aerospace parts, formability is a key factor in the wider application of Mg wrought alloys in the automotive industry. Die cast magnesium has to a large extent fulfilled the cost and performance requirements of automotive components, since this technique allows the manufacture of parts with complex geometry. However, wrought magnesium alloys have superior mechanical properties, and are therefore of great interest for a wide range of structural applications, such as the car body (enclosures, panels, doors, pillars, roof and front end components). In order for wrought magnesium to be effectively used in this sense, three main areas require improvement:

(i) ***Formability and Workability:*** According to von Mises criterion, in order to attain uniform deformation a combination of at least five independent deformation modes are necessary. In the hexagonal close-packed (HCP) structure of Mg, only the basal plane is close-packed and its critical resolved shear stress is much lower

at room temperature than in the other slip systems (prismatic and pyramidal). During the deformation of HCP Mg alloys at moderate temperatures, only two independent slip systems are active which allows a limited ability to accommodate strain uniformly. Twinning provides a third deformation mechanism, which depending on its mode, may eventually lead to compression bands and edge cracking during working and forming operations.

Industrial applications of wrought alloys in their as-extruded or as-rolled state is limited. Such alloys usually need an additional processing step before application. For example, drawing and stretching is necessary for a rolled sheet to be shaped into a part and an extruded rod or tube needs to be bent and formed before it can be used in an automotive assembly. In wrought Mg alloys, the formation of a strong basal texture in the manufacturing process increases the deformation inhomogeneity during processing and prohibits many potential applications [Balla 1994]. Preferred orientation develops in recrystallized Mg alloys when the deformation process takes place at both room and elevated temperatures. Grains which have a low resolved shear stress on their basal planes (basal planes are perpendicular to the compression axis) have limited basal dislocation movement, therefore little work-hardening occurs in these "basal" grains. Consequently, the grains with higher dislocation densities (more work-hardened) become more prone for dynamic recrystallization (DRX), while the "basal" grains (less work-hardened) remain unaltered. This sequence is also repeated for newly recrystallized grains. The grains which remain in the basal orientation are the source of strong basal texture formed during hot deformation of Mg alloys. The stronger the basal texture, the stronger the directional properties and mechanical anisotropy and the lower the formability and workability.

(ii) ***Mechanical properties at elevated temperatures***: For parts subjected to prolonged exposure to elevated temperature and loading over time, a material with good creep resistance is needed. Most magnesium alloys have a low resistance to creep deformation. In some Mg alloys this is due to the low melting point of intermetallic phases (e.g. $Mg_{17}Al_{12}$), which are prone to soften at high

temperatures [Luo 2004] or more concisely, on the discontinuous precipitation of this phase from the supersaturated α-Mg during creep [Pekguleryuz 2010]. Over the past few years, numerous attempts have been made to design new magnesium alloys with adequate high-temperature performance by adding alloying elements such as rare earth (RE) and alkaline earth (Ca, Sr) to be used in critical engine parts [Pekguleryuz 2010, Pekguleryuz 2004].

(iii) ***Oxidation and corrosion***: Most magnesium alloys have poor corrosion resistance in ambient air or aqueous environments due to their electrochemically active state. There are two primary reasons for the poor corrosion resistance of magnesium alloys: 1) Galvanic corrosion between the secondary phases or impurities and the Mg matrix and 2) The oxide or hydroxide film that forms on magnesium is much less stable than the passive films on metals such as aluminum alloys and stainless steel [Salman 2009]. The oxide film formed on magnesium and its alloys cannot protect its matrix since the Pilling-Bedworth ratio of magnesium oxides (0.79) is less than 1 [Liu 2010].

Substantial research has been conducted to improve the corrosion behaviour of Mg alloys by adding alloying elements. For example, it has been reported in a recent study that the total corrosion resistance of a Mg-5Al alloy is increased with increasing Sr content to 1.0 wt% and that it further decreased with increases in Sr concentration. Moreover, Sr addition to Mg–5Al alloys facilitates the formation of an $Al(OH)_3$ passive film on the surface. In addition, the amount of chloride in the passive film decreases with increasing Sr content, indicating a more protective passive film on the Mg–5Al–1Sr alloy surface [Nam 2011].

Other than difficulties in meeting the performance requirements for applications, Mg also has many limitations for production and fabrication. Generally, magnesium is found to extrude more slowly than aluminum alloys. Alloying with aluminum and zinc lowers the maximum extrusion speed even further [Atwell 2007]. Further processing of magnesium extruded sections for certain applications has even more restrictions (e.g. limits to the bending radii of extruded cross sections) [Stalman 2001]. Using magnesium sheets for

manufacturing stamped parts requires precise pressing equipment for controlling the deformation velocity and heated tools are needed, even when the blank sheets are preheated [Doege 2001]. This has a significant impact on the cost of mass production. Combining all these considerations, substantial improvements are required to economically meet the demands of industrial applications.

Much research has been conducted to overcome the limitations of magnesium and its alloys either by changes in the processing parameters or by the addition of certain alloying elements. Rare earth (RE) elements are added to Mg-Al alloys in order to suppress the formation of $Mg_{17}Al_{12}$ precipitates and form thermally stable Mg-RE and Al-RE precipitates to increase the heat resistance of the alloy [Wenlong 2009]. Automotive applications requiring both performance and cost optimization cannot make use of alloys containing expensive RE alloying additions for high volume applications [Rokhlin 2003]. Using the more cost-effective mischmetall (combination of RE elements) has drawbacks as well, since this can lead to microstructural instability due to a complex phase content of the alloy. Alloys containing less expensive alkali-earth elements (e.g. Ca,Sr) have been developed as alternatives to Mg-RE alloys [Baril 2003]. Strontium (Sr) added to Mg alloys achieved properties similar to RE additions at a much lower price [Baril 2003].

The first addition of Sr into Mg alloys was to refine the grains in casting alloys [Koubichek 1959, King 1973, Aliravci 1992, Pekguleryuz 1992, Gruzleski 1992, Liu 2009]. The surface active Sr atoms likely slow down dendrite growth by segregating to the surface of Mg grains [Pan 2006]. It was also shown that Sr could also refine the $Mg_{17}Al_{12}$ precipitates [Koubichek 1959]. In 2002-4, the Mg-Al-Sr (AJ) series of alloys were developed by the addition of higher levels of Sr to Mg-Al alloys [Pekguleryuz 1992, Pekguleryuz 2001, Pekguleryuz 2003]. These Mg-Al-Sr alloys had an excellent combination of creep performance and castability and have been used in BMW engine blocks since 2004. It was proposed that the high creep resistance is related to the absence of the low melting point β-$Mg_{17}Al_{12}$ intermetallic phase and to the minimization of Al supersaturation in the primary magnesium [Baril 2003]. It has also recently been

found that dynamic precipitation of Mn intermetallics play a role in the enhancement of creep resistance [Kunst 2009]. In the AJ series, depending on the Al:Sr ratio, various alloy compositions with different combinations of precipitates have been developed, which result in differing creep resistance, strength and casting properties [Pekguleryuz 2003, Pekguleryuz 2004, Kunst 2009, Baril 2003, Pekguleryuz 2001].

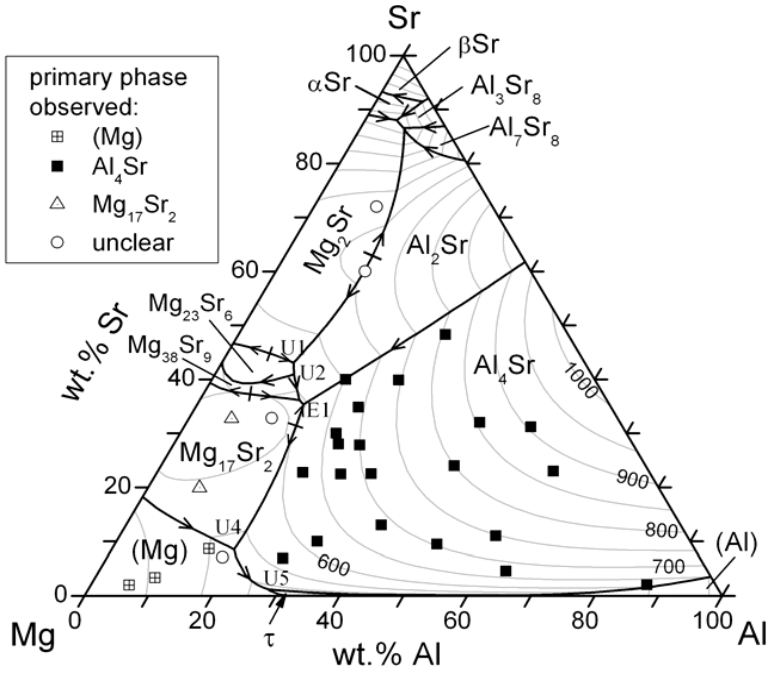

Figure.1.1. Calculated liquidus projection of the Mg-Al-Sr system. The black lines represent monovariant lines and the grey lines isotherms with an interval of 50°C. The data points show compositions of samples with experimentally observed primary phases including data from other researchers [Janz 2007].

To further understand experimental observations, the interactions of Sr with Mg and other alloying elements have been studied *in silico* by thermodynamic modeling. Binary and ternary phase diagrams of Mg-Al-Sr have been developed by a combination of modelling and experimental data (Fig.1.1). Additionally, new equilibrium and non-equilibrium binary and ternary precipitates

have been discovered and their compositions and crystal structures have been extensively studied [Janz 2007, Raghavan 2007, Aljarrah 2007].

The effect of Sr has not been limited to casting alloys, there have been several investigations on the effects of Sr on precipitation in commercial wrought alloys [1 Bai 2006, Zeng 2006, Zhao 2007] and also on the effects on further hot deformation processes and mechanisms [Guan 2007, 2 Bai 2006]. Bai *et al* [1 Bai 2006] reported that Sr increased the creep resistance of Mg extrusions by providing thermally resistant precipitates which pin the grain boundaries.

It has been reported that the mechanical properties of Mg alloys are improved by Sr grain refinement, however high levels of Sr resulted in cleavage cracking in tension [Zeng 2006]. Guan *et al.* [Guan 2007] reported that Sr added to AZ80 had a higher degree of recrystalization in the microstructure after extrusion compared to AZ80. The effect of Sr on grain refinement and modification of precipitates has also been previously reported for wrought alloys [Aliravci 1992]. A higher level of Sr forms thermally stable precipitates which increase the strength and improve the creep behaviour [1 Bai 2006, Zeng 2006, Zhao 2007, Guan 2007, 2 Bai 2006]. The following literature review focuses on the crystallography, microstructure, deformation and mechanical properties of AZ31 alloy and the effects of Sr on these.

Chapter 2

Literature Review

2.1. Mg-Al-Zn (AZ) Alloys

The well-known AZ series of magnesium alloys contains aluminum and zinc as alloying elements. Aluminum is the most favourable alloying element in magnesium because it improves castability by reducing the freezing range and improves strength by solid solution and precipitation of the intermetallic beta phase (β-$Mg_{17}Al_{12}$) [Jing 2006]. Aluminum in conjunction with super heating increases the strength and refines the cast structure of magnesium. Zinc imparts grain refinement and is useful in increasing the tensile properties of Mg-Al alloys with a minimal loss of ductility. Additionally it has a significant effect on the tendency of Mg – Al castings to form micropores with imperfect feeding conditions. Small amounts of Zinc have a relatively small effect on the structure of Mg-Al alloys. The grain boundary eutectic becomes more divorced (Fig.2.1) and if the Zn:Al ratio exceeds about 1:3 a ternary phase ($Mg_{32}(AlZn)_{49}$) appears. Alloy compositions in this review are in weight % unless otherwise specified.

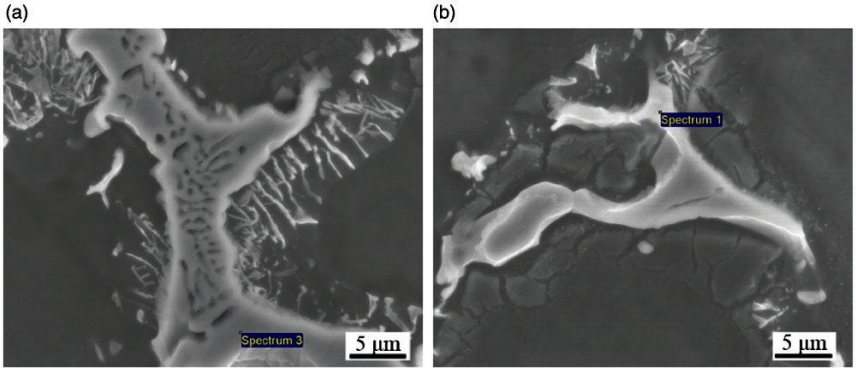

Elements	Mg (at%)	Al (at%)	Zn (at%)
Percentage	54.22	21.78	24.00

Elements	Mg (at%)	Al (at%)	Zn (at%)
Percentage	53.86	21.49	24.66

Figure.2.1. SEM micrographs of eutectic structures and accompanying EDS measurement of elements in as-cast Al-Mg-Zn alloy: (a) A typical eutectic phase. (b) A divorced eutectic phase.

Mg-Al-Zn casting alloys are usually around the composition of M-9Al-1Zn. Because of poor strength and creep resistance at elevated temperatures, applications of AZ alloys are limited parts which do not undergo elevated stresses or temperatures.

Research has shown that the discontinuous grain boundary precipitation of the $Mg_{17}Al_{12}$ phase from the super-saturated solid solution and coarsening of this interdendritic phase at elevated temperatures results in poor high temperature properties. Mg-Al alloys not containing Zn (AM) are used for their enhanced ductility over the AZ alloys. Recently a new series of Mg-Al alloys containing Sr have been developed which show improved high temperature mechanical properties and can meet the materials requirements for powertrain applications based on the nominal composition of Mg-6Al-2Sr. [Baril 2003].

Mg-Al-Zn alloys span a large range of properties from high ductility to high strength and castability. Mg-3Al-1Zn sheet and plate find applications in medium strength service at temperatures bellow 150^{o}C. Diverse uses including aircraft fuselage, concrete tools, cell phone, camera, notebook cases and textile machinery can benefit from the light weight of AZ31. Super-plastic forming of AZ31 at elevated temperatures allows the production of a wide variety of intricate parts for automotive use.

2.1.1. Crystallography of AZ31 Alloy

The crystal structure of magnesium and most of its alloys is hexagonal close packed (HCP) [Avedesian 1999]. The lattice parameters of pure magnesium have been measured to be a=0.32092 and c=0.52105. In an ideal HCP structure of pure Mg with an ABABA stacking of atomic layers, the axial ratio (c/a) would have the ideal value of 1.633 at 25^{o}C (Fig.2.2). Based on the radius and valency of the solute atom, the introduction of an alloying element in solid solution may increase or decrease the lattice parameters and the axial ratio (e.g. Au and Ce decrease while Ti and Zr increase the c/a ratio) [Raynor 1956].

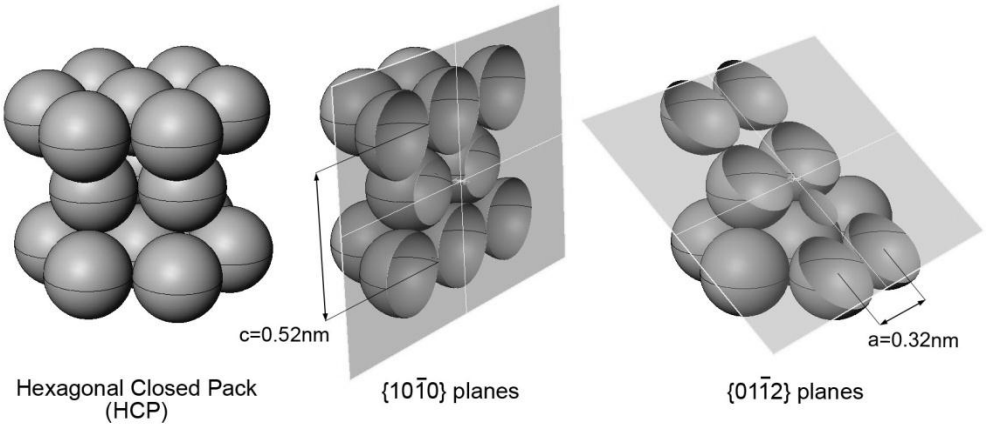

Figure 2.2. Hexagonal close packed (HCP) unit cell of Mg.

It has been reported by Lubarda [Lubarda 2003] that in an Mg-rich Mg-Al solution, the effective lattice spacing decreases with the introduction of Al solutes. Zinc additions in the range 0.2–0.7 at.% Zn contract both *c* and *a* spacing [Becerra 2008].

Two different axial systems could be used in a HCP structure to define the indices of planes and directions [Partridge 1967]. The two systems are named as 1) the 4-axis hexagonal Miller-Bravais system and 2) the 3-axis Miller system. The four axis system is based on the three *a* directions in the basal plane and the *c* direction of the hexagonal plane. In this system the *a* direction would have 4 indices [uvtw] such that

$$d=ua_1+va_2+ta_3+wc$$

here the a_3 is redundant since $a_3=-(a_1+a_2)$. The redundant digit is sometimes omitted to give a 4-axis, 3-digit notation, i.e. u.v.w. In the 3-axis Miller system, any direction would have 3 indices based on two <*a*> directions and the <*c*> direction of the hexagonal plane. It is very important to avoid confusing the two 3-index notations based on 3 and 4 axes, because they produce different notations for a given direction. Directional Miller indices UVW can be converted to Miller-Bravais indicies uvtw by the following equations:

$$U=u-t,\ V=v-t,\ W=w \text{ or}$$

$$u=1/3(2U-V),\ v=1/3(2V-U),\ t=-(u+v),\ w=W$$

Miller and Miller-Bravais indicies of planes are readily interchanged since since a plane with (hkil) or (hk.l) Miller-Bravais indices has Miller indices

(HKL)=(hkl)

It should be noted that *a* direction is not normal to a plane of same indices except for directions of type <0001> and <hki0>. The indices of the normal to a plane (hkil) are $\left[hki\ \frac{3}{2}\left(\frac{a}{c}\right)^2 l\right]$.

2.1.2. Deformation mechanisms

2.1.2.1. Deformation in Mg

Metals can respond to stress via several mechanisms: slip (dislocation motion), twinning, phase transformation and fracture. In HCP crystals, dislocation motion (slip) occurs either on the basal, prismatic or pyramidal planes (Fig.2.3). In Table 1 different slip systems in Mg are summarized. The close packed nature of the basal plane provides the smallest Burgers vector and provides the most favourable slip plane for dislocations with the lowest critical resolved shear stress (CRSS). Compared to the basal plane, prismatic and pyramidal slip planes are less closely packed. Consequently, movement of dislocations in these planes requires higher stresses. The pyramidal system is the only system in which dislocations can move in the *c* direction. Hence, the Von-Mises criterion of uniform deformation by activation of five independent slip systems would not take place until pyramidal slip is activated. According to Table 2.1, the activation of non basal slip systems requires approximately one hundred times higher stress.

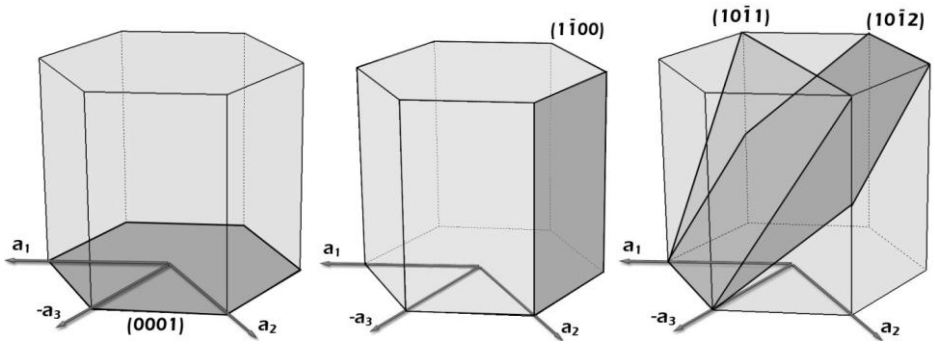

Figure.2.3. Configuration of slip and twinning planes in a hexagonal lattice.

Table 2.1: Slip Systems in Mg HCP crystal

Name	Slip plane	Slip direction	CRSS (MPa)	Reference
Basal **a**	{0001}	<11-20>	0.76	[Bakarian 1943]
Prismatic **a**	{-1100}	<11-20>	39	[Reed-Hill 1957a]
Pyramidal **a**+**c**	{11-22}	<11-22>	80	[Ando 1992]

However, alloying and temperature increases may increase the activity of other slip systems [Horst 2006]. At temperatures above 300^{o}C, non-basal systems start to contribute significantly in deformation. Cross-slip is a mechanism that can occur in crystals when there are two or more slip planes with a common slip direction. For instance, the two basal [0002] and prismatic planes [10-10] in HCP have the closed packed <11-20> slip directions in common. During cross-slip, the dislocations producing the deformation must shift from one slip plane to another. The actual shift can only occur for a dislocation in the screw orientation, since the active slip plane must contain both the Burgers vector and the dislocation line [Abbaschian 2009]. During deformation of Mg, screw dislocations may cross-slip. Koike *et al* [Koike 2003] reported that the plastic compatibility stress associated with grain boundaries imparts substantial cross-slip to non-basal planes. Their detailed analysis indicated that dislocation cross-slip to non-basal planes occurred at a yield anisotropy value of only 1.1 instead of an expected value of 100. Double cross-slip of screw dislocations from the basal plane through the prismatic planes to the basal plane is typical of Mg single crystals deformed at room temperature [Horst 2006].

Cross-slip is considered to be a recovery mechanism, the activity of which increases with increasing temperature [Horst 2006]. The fact that magnesium poly-crystals exhibit extensive non-basal cross-slip ensures a minimum of four independent slip systems [Agnew 2005]. Experimentally, few solutes have been found to lower the stress for cross-slip: Al and Zn lower the stress at low (below room) temperatures [Akhtar 1969], while Li can lower the cross-slip stress in both regimes [Urakami 1971].

In situ experimental measurements of Couret and Caillard [Couret 1985 a and b] showed that cross-slip in magnesium is the result of a double kink nucleation mechanism at temperatures above RT. A basal screw dislocation constricts at kinks of height *c* and spreads on two neighbouring basal planes. At low (below room) temperatures, cross-slip instead occurs by the Friedel-Escaig mechanism which includes constriction and bowing of a screw dislocation [Yasi 2012].

Because of the insufficient number of slip systems in Mg alloys, deformation twinning is an important mechanism for plastic deformation. Twinning provides additional independent slip systems and is a source of work hardening and dynamic recovery [Koike 2003]. Three types of twins are frequently reported in magnesium alloys: extension twins, contraction twins and double twins [Jiang 2006] (Table 2.2). For metals with a *c/a* ratio of less than $\sqrt{3}$ (e.g. magnesium), normally only the {10-12}<10-11> twin is activated [Yang 2008]. {10-12} extension twinning can be activated if the tensile stress is applied parallel to the *c*-axis or if the compressive stress is applied perpendicular to the *c*-axis [Park 2010]. Contraction twinning could also activate during the deformation of Mg alloys including {10-11} twins and {10-13} twins which can accommodate compression along the *c*-axis.

Table.2.2. Different types of twins in Mg and its alloys

Deformation type	Crystal plane	Misorientation angle/axis	Reference
Extension	{10-12}	86.3 <1-210>	[Park 2010]
Contraction	{10-11}	56.2<1-210>	[Knezevic 2010]
	{10-13}	64<1-210>	[Jiang 2006]
Double (contraction)	{10-11}–{10-12}	38<1-210>	[Jiang 2006]
Double (contraction)	{10-13}–{10-12}	22<1-210>	[Jiang 2006]

Contraction twins can activate when there is a compression strain component parallel to the *c*-axis or when macroscopic tension is being applied

perpendicular to the *c*-axis [Jiang 2006]. In addition to primary twinning, secondary twinning can take place within the reoriented primary twins. This is known as double twinning. Generally {10-11} or {10-13} contraction twins form first, after which {10-12} extension twins are propagated within the original contraction twins [Jiang 2006].

2.1.2.2. Deformation in AZ31

Room temperature deformation in AZ31 consists of dislocation slip in the basal planes and twinning to fulfill the von Mises criterion of homogeneous deformation. At elevated temperatures, twinning is reduced and dynamic recrystallization contributes to work softening (strength decreases while elongation increases). The inhomogeneous microstructure of large grains surrounded by small recrystallized ones represents hot deformed AZ31. In AZ31, the Mg matrix is strengthened by the presence of Al and Zn in the solid solution.

AZ31, like other Mg alloys, has a significantly lower tensile yield strength compared to compressive yield strength, which leads to a high mechanical anisotropy. Much research has been carried out to increase tensile strength by either refining the grain size [Yamashita 2001, Takuda 1992] or controlling the deformation process [Mwembela 1997]. It has been reported [del Valle 2005] that by the simultaneous occurrence of grain boundary sliding (GBS) and crystallographic slip (CS) in AZ31 at certain temperatures and strain rates, tensile ductility is significantly improved (up to 320 %).

2.2. Alloying of Mg Alloys with Sr

2.2.1. Solid Solubility

In the alloying system investigated in this study (AZ31+Sr), Al, Zn and Sr all have solid solubility in Mg, however the solubility of Sr is limited. The commercial AZ31 alloy also has Mn added in order to improve the corrosion resistance of the alloy; Mn is also soluble in solid Mg. The level of solubility of substitutional atoms in a matrix can be qualitatively predicted using the following four factors defined by Hume-Rothery:

Crystal structure factor: For the extensive solubility of an element in a metal, the host and the solute elements should have the same type of crystal structure. Of the alloying elements present in the alloy, Zn has a HCP structure, Al, Mn and Sr are all cubic.

Relative size factor: As the atomic radii difference between two elements increases, the solid solubility becomes restricted. All of the divalent elements in Group IIA have unfavorable size factors for forming solid solutions in Mg (r_{Mg}=160pm). Beryllium (r_{Be}=112pm) will rarely dissolve in magnesium both in the liquid and the solid state. Calcium (r_{Ca}=197pm) with a more favourable size-factor dissolves in Mg to a limited extent [Raynor 1956]. The size factors of strontium and barium (r_{Sr}=215pm, r_{Ba}=222pm) with respect to magnesium are less favorable than that of calcium; consequently, negligible solid solubilities are expected.

***Chemical affinity factor*:** Solid solubility is favored when the two metals have lower chemical affinity. Pure Mg forms an intermetallic phase with Sr ($Mg_{17}Sr_2$, T_m=660^oC [Janz 2007]).

Relative valence factor: A metal of lower valence tends to dissolve more of a metal of higher valence than *vice versa,* because the higher valence increases the bond stability. For example, Al has three electrons in its valence layer and Mg has two. In the case of Sr being dissolved in Mg, both elements have the same valence which does not favour a high solid solubility.

All four Hume-Rothery factors suggest a very low solid solubility of Sr in Mg. Different maximum equilibrium concentrations of Sr in pure Mg have been reported. However, Sr completely dissolves in molten Mg [Avedesian 1999]. Hehmann *et al.* reported a Sr solubility of 0.04 at% at room temperature [Hehmann 1989], while a solubility of 0.5 at% was reported by Brown *et.al* in an Mg-Sr phase diagram [Brown 1979]. Zhao *et al*. have also reported a significant

dissolution of Sr in Mg solid solution [Zhao 2007] (Fig.2.4). There have been some attempts to increase the solubility of Sr by rapid solidification. It has been reported that Mg is able to dissolve 3.1 at% Sr as a result of solute trapping [Hehmann 1989].

Although, Sr has limited solubility in α(Mg), in certain conditions it may dissolve in other precipitates. The $Mg_{17}Al_{12}$ phase in Mg-Al alloys is able to dissolve excess Sr [Guan 2007]. Zhao *et al*. [Zhao 2008] have studied the effect of Sr on AM50 alloy. Their EDS results indicate that, in AM50+0.1Sr, there is strontium dissolution in the $Mg_{12}Al_{17}$ precipitates (Fig.2.4). In contrast Aljarrah *et al*. [Aljarrah 2007] reported a negligible solubility of Sr in $Mg_{17}Al_{12}$ by EPMA analysis, and Janz *et al*. determined the soubility to be <1 wt% [Janz 2007].

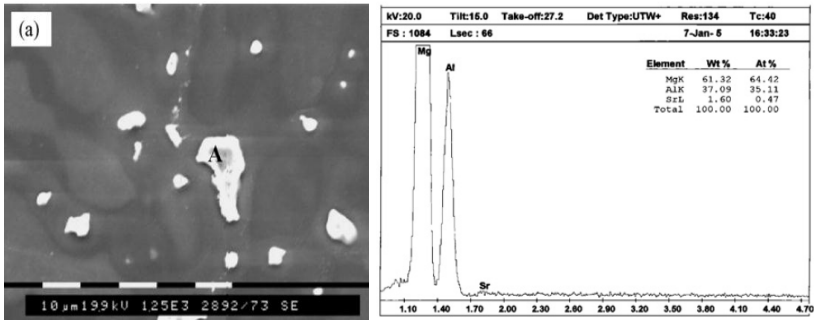

Figure.2.4. SEM micrograph and EDS pattern of as-cast Mg–5Al–0.1Sr alloys: (a) SEM of $Mg_{17}Al_{12}$ particles in as-cast Mg–5Al–0.1Sr alloy; (b) EDS spectrum from the nucleus area 'A' in (a).

Sr is able to effect the solid solution composition by changing the solubility of other elements. In a previous study, the addition of Sr to AE42 was found to reduce the level of Al solute in the α-Mg matrix due to the formation of an additional Mg_8Al_4Sr intermetallic phase [Dargusch 2009]. The same effect was also observed in AJ alloys in which the addition of Sr minimized Al supersaturation in the primary magnesium [Baril 2003].

2.2.2. Precipitation of Sr-rich Phases in Mg-Al Alloys

As described above, one of the reasons for the limited solubility of Sr in Mg is the affinity of Sr to bind with Mg and/or other elements present in the alloy. In Table 2.3, different alloys containing Sr are compared. In some cases, researchers did not observe any new precipitates, and the presence of Sr in solid solution was also not confirmed [Liu 2008, Cheng 2008]. Some authors reported the presence of free Sr at the interdendritic regions and grain boundaries [Lio 2008, Guan 2007]. This is likely due to the surface active behaviour of Sr in Mg. However, most of the studies on Sr-containing Mg alloys have reported the formation of Sr-containing intermetallics. These precipitates are usually thermally stable and increase the elevated-temperature mechanical properties of the alloy. Significantly, there appears to be an optimum level for Sr addition in terms of mechanical performance or microstructural refinement at ambient temperatures, beyond which the properties decrease as a result of precipitate brittleness [Liu 2010].

Table.2.3. Summary of reported interactions of Sr with different Mg alloys.

Alloy	Sr (wt%)	Precipitation	Observed effect	Reference
Mg- 4Al-12Zn-0.3Mn	0.2 - 0.8	$Mg_{51}Zn_{20}$ $Mg_{32}(Al,Zn)_{49}$	Increase of ultimate and yield strengths. Decrease of ductility	[Xiaofeng 2009]
Mg-9Al-1Zn-0.8Ce	0.2	Sr at grain boundaries	Grain size refined by the growth restriction effect on the primary α-Mg phases.	[Lio 2008]
Mg-9Al-1Zn	0.1-0.3	No new phase detected	Hardness increased and Grain size refined by increase of the effective number of potential crystal nucleus, the reduction of growth rate	[Liu 2008]
Mg-3Al-1Zn	0.1	$Mg_{17}Sr_2$	Grain refinement by increasing growth restriction factor (not increasing the nucleation sites because of the large mismatch)	[Yang 2008]
Mg-5Sn	0.4-4.8	rod & bone shape MgSnSr	Grain refinement. Improved yield strength (GR+DH). UTS and ε_t first increased then decreased. UTS improved at elevated temperatures	[Liu 2010]
Mg-8.5Al-0.5Zn	0.02-0.3	$Mg_{17}Al_{12}$ $Mg_{17}Al_{12}$ Sr at GB and β	UTS and ε_t are improved due to GR and distribution of second phases	[Guan 2007]

Mg-5.5Zn-0.5Zr	0.1	No new phase detected	Grain refinement by increasing growth restriction factor (not increasing the nucleation sites because of the large mismatch)	[Cheng 2008]
Mg-4Al-2Sn	1	$Mg_{17}Al_{12}$ SrMgSn	Grain size was reduced slightly The tensile strength was decreased at room temperature. However, the high temperature tensile strength was increased. The creep strength was improved	[Kim 2010]
Mg–4Al	2	Al_4Sr AlMgSr	significant increase of tensile properties	[Bai 2006b]
Mg-3Al-1Zn	2.5-5	Al_4Sr $Mg_{11}Al_5Zn_4$ $Mg_{17}Sr_2$ Mg_2Sr	Grain refinement, formation of a lamella-like eutectic phases, Change of β-$Mg_{17}Al_{12}$ morphology	[Wu 2011]
Mg-4Al	4	(Mg,Al)17Sr2 (Mg,Al)4Sr	$Mg_{17}Al_{12}$ is unlikely to be found in the microstructure of this alloy	[Zhang 2008]
Mg-8Al	1.5	(Mg,Al)4Sr Mg17Al12	The microstructure agrees well with the calculated solidification paths	[Zhang 2008]
Mg-5Al	0.15	Mg17Al12	No Sr-rich precipitate was observed	[Zhang 2008]
Mg-3Al-1Zn-0.26Ca-0.2Ce	0.2	$Mg_{17}(Al, Zn)_{12}$ Al_8Mn_5 Al_2Sr	the type of intermetallic compound of Al–Sr depends on the concentration of Sr in alloys	[Shanga 2010]

Sr binds with Al in Mg alloys and forms high-melting point stoichiometric intermetallics that have high thermal stability (formation temperature >490^{o}C). Because of the higher electronegativity difference between Sr and Al (0.69 compared to 0.30 for Mg and Al), Sr forms Al-Sr intermetallics and likely reduces Al solid solubility in the α-Mg matrix [Dargusch 2009]. In the Al-Sr binary phase diagram, three intermetallics are known: Al_4Sr, Al_2Sr and Al_7Sr_8 (also reported as AlSr and Al_2Sr_3) [Alcock 1989]. Al-Sr, Mg-Sr and Mg-Al-Sr precipitates in Mg alloys are summarized in Table 2.4. All the precipitates in the Mg-Al-Sr system can be classified into two groups: precipitates with Al and precipitates without Al.

Table.2.4. Probable Sr precipitates when Sr is added to Mg-Al alloy

phase	At% Sr	Melting Temperature	Crystal symmetry	Pearson symbol	Ternary solubility wt%	Reference
$Mg_{17}Sr_2$	10	660^{o}C	hexagonal	hP38	16.5 Al	[Janz 2007]
Al_4Sr	20	congruently at	tetragonal	tI10	10.2 Mg	[Alcock1989]

		1040°C				
Al_2Sr	33.3	peritectic at 936°C	orthorhombic	oI12	18 Mg	[Alcock1989]
Al_7Sr_8	53.3	peritectic at 666°C	cubic	cP60	1 Mg	[Alcock1989]
$Al_{38}Mg_{58}Sr_4$	4	peritectic at 477°C	-	-	<1Sr	[Janz 2007]

Sr-containing precipitates without Al, $Mg_{17}Sr_2$ and $SrZn_5$, (if Zn is also present in the system) only form at high concentrations of Sr where the affinity of free Al is decreased when most of it is captured in the Al-Sr intermetallics. Sr precipitates with Al (Al_4Sr and Al_2Sr) are formed when Sr meets a high concentration of Al in the alloy.

2.2.2.1. Precipitates of Sr with Al

Al_4Sr is the most common Al-Sr precipitate which usually precipitates in the presence of Al in Mg alloys. Under normal conditions, the primary Al_4Sr phase is preferentially formed from the melt in <110> directions [Zhang 2002]. The Al_4Sr phase has a body-centered tetragonal structure (Pearson symbol: tI10; Space group: I4/mmm) (Fig. 2.5a) [Jing 2005, Alcock 1989]. In Mg Al-Sr alloys, Al_4Sr is usually revealed along the grain boundaries with a lamellar eutectic morphology [Jing 2005]. Additionally, the Sr-containing phases can also exhibit dendritic morphology (Fig. 2.5b). Very small precipitates containing Sr were also detected at a twin boundary (Fig.2.5c).

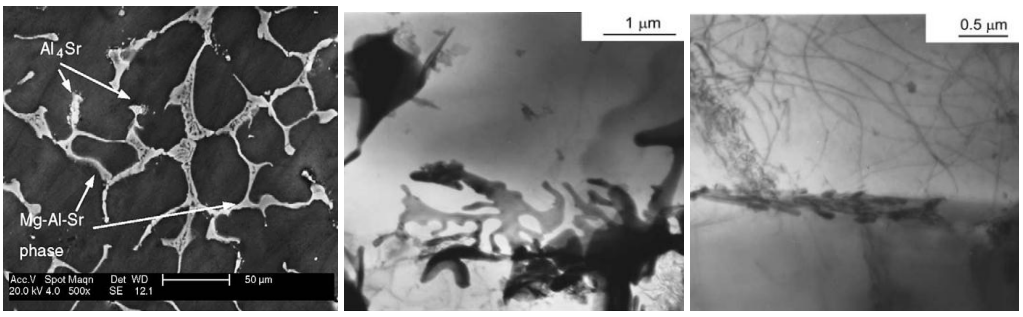

Figure 2.5. (a) SEM micrograph of Mg-4Al-3Sr [Jing 2005], and The TEM morphology of Sr containing phases in semisolid molded structure; (b) Mg–Al–Sr phase with dendritic shapes; (c) continuous type precipitates at a twin boundary [Czerwinski 2005].

Their disc-like shape and arrangement suggests that they could be formed by a continuous mode of precipitation [Czerwinski 2005]. Jing *et al.* [Jing 2005] have reported that by increasing the amount of Sr, a ternary Mg-Al-Sr intermetallic in bulky morphology will form. With increasing Sr, the volume fraction of Al_4Sr decreases, while the Mg-Al-Sr ternary intermetallic increases.

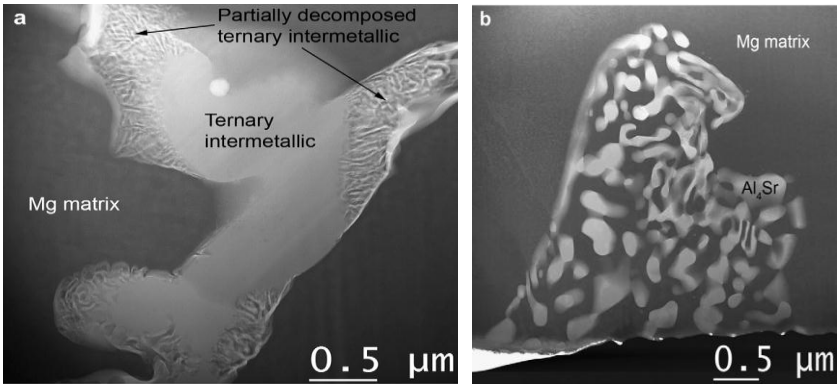

Figure.2.6. (a) TEM micrograph of a partially decomposed particle of the ternary intermetallic after a heat treatment at 175^{o}C for 1500 h. (b) TEM micrograph of a completely decomposed ternary intermetallic particle after heat treatment at 300^{o}C for 24 h [L'Esperance 2010].

The bulky Mg-Al-Sr precipitate has been observed by many researchers and different stochiometries have been suggested [Dargusch 2009, Chartrand 1994, Baril 2003, L'Esperance 2010, Janz 2007]. Table 2.5 summarizes a number of studies which have reported the presence of this so called "bulky" precipitate. Except for one of the suggested stoichiometries ($Al_{38}Mg_{58}Sr_4$ [Janz 2007]), all the ternary precipitates seem to be unstable during annealing at high temperatures. L'Esperance *et al.* [L'Esperance 2010] have shown how the bulky precipitate decomposes to Al_4Sr and Mg when subjected to heating (Fig.2.6).

Table.2.5. Different stoichiometries reported for Mg-Al-Sr precipitates

Phase	Crystal structure	Stability	At% of Sr in the compound	Alloy	Reference
Mg_8Al_4Sr	hexagonal	Unstable	0.07	3.7Al+1.9RE+1Sr	[Dargusch 2009]

$MgAl_6Sr_{10}$	-	Unstable	0.58	27.7Al+6.6Sr	[Chartrand 1994]
$Mg_{13}Al_3Sr$	-	Unstable	0.06	5Al-2Sr	[Baril 2003]
Mg_9Al_3Sr	tetragonal	Unstable	0.07	6Al-2.3Sr	[L'Esperance 2010]
$Al_{38}Mg_{58}Sr_4$	-	Stable	4	31.5Al+10Sr	[Janz 2007]

2.2.2.2. Sr Precipitates with Mg

The distinct Mg-Sr precipitates that form with increasing Mg/Sr ratio, indicated in the Mg-Sr binary phase diagram are $Mg_{17}Sr_2$, $Mg_{38}Sr_9$, $Mg_{23}Sr_6$ and Mg_2Sr intermetallics. $Mg_{17}Sr_2$ is the most probable precipitate in commercial alloys where the Sr concentration is not very high. There has been some research investigating the effect of this Mg-Sr precipitate on the grain refinement of Mg, based on the lattice registry between the precipitate and primary Mg [Zhang 2002, Yang 2008]. The crystal structure of $Mg_{17}Sr_2$ is hexagonal with $a = b = 10.469$ nm and $c = 10.3$ nm [Zhang 2002]. The α-Mg phase has a hexagonal close-packed crystal structure with $a = 0.320$ nm and $c = 0.52$ nm [Yang 2008]. The researchers reported that the 6% lattice disregistry between $Mg_{17}Sr_2$ and α-Mg indicates that $Mg_{17}Sr_2$ could not act as a heterogeneous nucleus for the α-Mg phase. Therefore, the $Mg_{17}Sr_2$ phases could not directly influence grain refinement unless the free Sr was obtained by the dissolution of $Mg_{17}Sr_2$ phases [Zhang 2002]. However, in another experiment, nano sized $Mg_{17}Sr_2$ precipitates were observed in as cast Mg-5Al-2Sr at the sub grain boundaries in the shape of fine discs with strict orientational relationship with the surrounding matrix (Fig.2.7) [Czerwinski 2005].

Guan *et al*. [Guan 2007] reported that $Mg_{17}Sr_2$ precipitates are able to inhibit the growth of dynamically recrystallized grains in AZ80+0.3Sr. Also, $Mg_{17}Sr_2$ has the ability to dissolve other elements in its crystal structure. Aljarrah *et al.* [Aljarrah 2007] reported a maximum solubility of 21.3 at% Al for this precipitate.

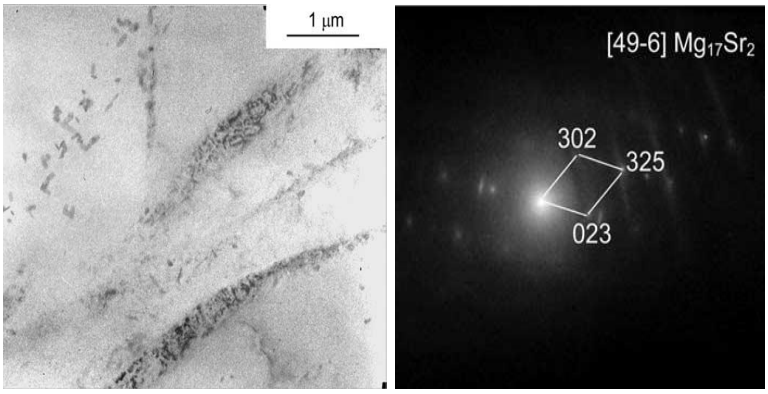

Figure.2.7. TEM micrograph (a) and SAD diffraction pattern (b) of Sr containing precipitates distributed at sub-grain boundaries of α-Mg. The precipitates were identified as $Mg_{17}Sr_2$ [Czerwinski 2005].

2.3. Microstructures of Mg-Al-Sr Alloys

2.3.1. As-Cast Structure

The structure of cast Mg-Al-Sr alloys have been found to be characterized by primary α(Mg) dendrites and one or more second phases at the grain boundaries or in the interdendritic regions [Baril 2003]. The secondary phase morphologies are lamellar, divorced eutectic, or massive. Al and Sr contents of the alloy have been found to have a strong influence on the relative volume fraction of the various phases [Baril 2003] and the castability of the alloy mixture [Cao 2010]. It has also been reported by Cao *et al.* [Cao 2010] that increasing the concentration of Al at a given level of Sr reduces the hot tearing susceptibility (HTS). They reported that with the Mg-xAl-1.5 Sr alloys, the HTS decreased significantly with increasing Al content from 4 to 8 wt%. In Mg-xAl-3Sr alloys, the trend was similar but not as significant. Additionally, at the same Al content, the HTS was significantly lower at 3 wt%Sr than at 1.5 wt%Sr.

2.3.2. Grain and Second-Phase Refinement

To improve the formability and mechanical properties of Mg alloys, attempts are being made to achieve finer grain sizes and higher homogeneity combined with a uniform distribution of intermetallic phases. Many grain refining technologies have been developed for Mg alloy systems such as super heating, agitation,

addition of particles and solute elements [Zeng 2006]. Gruzleski and Aliravci [Gruzleski 1992] have patented the idea of adding 0.005 to 0.03 % Sr to AZ91 to significantly reduce grain size and microporosity. They have proposed that Sr may poison the grain surface or poison the fast growing directions of the grains by preferential adsorption of Sr at these sites. The possibility of changing the liquid surface tension has also been suggested by the same authors [Gruzleski 1992]. Subsequently, many other researchers have attempted to use Sr for grain refinement in Mg alloys (Table 2.6). The effect of Sr on the growth kinetics of α-Mg can be explained through the growth restrictive effect of Sr rejected ahead of the solid/liquid interface. Because its solid solubility in magnesium is relatively low, rapid solute enrichment in the liquid ahead of the growing interface is likely during solidification [Lee 2000]. Pan *et al*. [Pan 2006] have also studied the grain refining effect of Sr in AZ91 and observed Mg-Sr-Al-Fe-Mn nucleating particles at the grain centers and Sr solute atoms segregated along the grain boundaries. They reported that the grain refinement was facilitated by both Mg-Sr-Al-Fe-Mn nucleating particles and Sr solute atoms, and the former played a dominant role in the process. However, Zhou *et al.* [Zhou 2010] reported that the enrichment of RE and/or Sr elements at the solidification front, especially at the tips of α-Mg dendrites, restricted the growth of α-Mg dendrite in AZ91 and changed the preferential growth of α-Mg. This resulted in grain refinement and the blunting of α-Mg dendrites. The same refinement effect has also been reported for AZ31 which has 1/3 the Al content of AZ91 [Wang 2008]. Lee *et al*. [Lee 1998] found that Sr had a better refining effect on AZ91 than Y and Nd. Liu *et al*. [Liu 2008] concluded that Sr combined with Ce had a better grain refining effect on the AZ91 cast structure than Ce alone.

Table.2.6. Grain refinement of Mg via Sr reported by different researchers

Alloy	Added Sr-wt%	As-cast GS-μm	Refined GS-μm	Reduction R%	%(R%) /Sr(wt%)	Reference
ZK60	0.1	90	33	63	630	[Cheng 2008]
Mg-9Al-1Zn-	0.2	40	30	25	125	[Liu 2008]

0.8Ce						
Mg-14Li-1Al	0.3	600	260	56	186	[Li 2011]
Mg-3Al-1Zn	0.1	200	110	45	450	[Yang 2008]
Mg-4Al-2Sn	1.3	85.0	73.8	13	10	[Kim 2010]
Mg-9Al-1Zn	0.1	1140	230	79	790	[Zhou 2010]
Mg-3Al-0.2C	0.5	180	110	39	78	[Du 2009]
Mg-9Al-1Zn	0.6	235.4	52.5	77	128	[Pan 2006]
Mg-9Al-1Zn	0.5	102	62	39	78	[Zhao 2007]

Sr also effects precipitation in Mg alloys [Zhao 2008, Yang 2008, Cheng 2008]. By comparing the microstructures and secondary phase dispersions, Zhao *et al*. [Zhao 2008] concluded that Sr acts as a heterogeneous nucleation site for the $Mg_{17}Al_{12}$ phase in AM50 alloy. It is interesting to note that they did not observe any grain refinement following Sr addition.

Some research has focused on the refinement efficiency of different types of Sr containing master alloys used in Mg, ranging from Al-Sr to Mg-Sr [Li 2008]. The effects of different thermo-mechanical processes on the efficiency of master alloys have also been studied. Li *et al*. [Li 2008] have investigated the refinement efficiency of differently processed Al-10Sr master alloys (commercial, solutionized, rolled and remelted + rapidly cooled). They reported that the refinement efficiency of the Al-10Sr master alloy obtained by remelting and rapid cooling was the highest, followed by rolled, solutionized and commercial Al-10Sr master alloys. The difference in refinement efficiencies for different Al-10Sr master alloys may be related to the dissolution rates of Al_4Sr phases with different morphologies and sizes in the melt of AZ31 magnesium alloy.

2.4. Ambient and Elevated Temperature Mechanical Properties

2.4.1. Tensile and Compressive Strength

Depending on the amount added, Sr could either strengthen or weaken the mechanical properties of the alloy. It has been reported that by adding Sr, hardness and grain refinement improves as a result of homogeneous distribution

of fine dispersoids within the matrix of AZ91 alloy [Lee 1998]. Zeng *et al*. [Zeng 2006] reported the improvement of yield strength of AZ31 alloys by microstructural refinement when Sr was added to the alloy. It has been suggested that the formation of Sr-rich precipitates could also act as reinforcements when the alloy is subjected to stress. Trojanova *et al*. [Trojanova 2008] studied the deformation behaviour of a squeeze cast AJ50 Mg alloy in tension and compression, from ambient to elevated temperatures. They suggested that the main hardening process was the storage of dislocations at Al_4Sr and $Mg_{17}Al_{12}$ incoherent and impenetrable obstacles. It is important to note that the volume fraction of the precipitates also has an important effect on mechanical properties; when the concentration of Sr exceeds an optimum level, the secondary phases can increase brittleness [Liu 2010, Xiaofeng 2009].

Another important effect of Sr is its influence on the mechanical properties of the alloy by controlling the precipitation of other Mg precipitates, or altering the solid solubility of different elements in Mg and/or Sr-containing precipitates. Zhao *et al.* [Zhao 2007] observed four changes that significantly effect the high temperature performance of AM50 with trace amounts of strontium: 1) The beta ($Mg_{12}Al_{17}$) precipitates formed a spherical morphology and their distribution became homogeneous; 2) The discontinuous precipitation of the $Mg_{17}Al_{12}$ phase was effectively stopped; 3) Sr increased the thermal stability of the beta phase by dissolving in the precipitate and changing its valence electron structure, and 4) Sr dissolved in the Mg solid solution. All these contributed to precipitate and solid solution strengthening of the alloys. Errors encountered in measuring stress strain curves are summerized in Appendix I.

2.4.2. Creep

The effect of Sr addition on creep behaviour of Mg alloys has been studied by many researchers [Kunst 2009, Dargusch 2009, Kim 2010, Yan 2008, Bai 2006]. It has been reported that the addition of Sr had a similar effect to RE elements on the creep resistance of AE42 [Dargusch 2009]. The results of different studies focusing on the effect of Sr on the creep behaviour of Mg alloys is summarized in

Table 2.7. The improvement of creep resistance has been associated with several different effects of Sr on the Mg alloy, which are summarized below:

***Thermally stable precipitates**:* Improvements in the creep resistance of Mg-Al-Sr alloys have been mainly attributed to the formation of thermally stable intermetallic phases, Al_4Sr and the Mg–Al–Sr ternary phase, which resulted in a pinning effect at the magnesium grain boundaries [Bai 2006].

Removing weak precipitates: Additions of alkaline earth elements Sr and Ca into Mg–Al alloys were found to suppress the precipitation of $Mg_{17}Al_{12}$ and form thermally-stable compounds at the grain boundaries, leading to effective restriction to grain boundary sliding and migration [Yan 2008]. The same mechanism has also been observed for the Mg-4Al-2Sn alloy [Kim 2010]. The addition of Ca and Sr resulted in the formation of CaMgSn and SrMgSn ternary phases within the grains. Void initiation was observed at the $Mg_{17}Al_{12}$ phase, and cracks propagated along the grain boundaries. However, the ternary phases of SrMgSn and CaMgSn effectively impeded crack propagation.

Depletion of Al solutes from primary Mg: The improved creep resistance of the Sr containing AE42 has been associated with at reduced level of Al solute in the α-Mg matrix [Dargusch 2009].

Distribution of fine precipitates: Excellent creep resistance has been achieved in AJ alloys by matrix strengthening from well-distributed Al-Mn and Mg-Al precipitates [Kunst 2009].

Table.2.7. Effects of Sr on Creep Properties of Mg Alloys

Alloy	Sr (wt%)	Precipitation	Observed effect	Reference
Mg-4Al-2RE	1	Mg_8Al_4Sr	Improved creep resistance by removing Al from solid solution	[Dargusch 2009]

Mg–4Al	2	Al_4Sr AlMgSr	the creep resistances is obviously reduced after extrusion deformation	[Bai 2006b]
Mg- 4Al-12Zn-0.3Mn	0.2 - 0.8	$Mg_{51}Zn_{20}$ $Mg_{32}(Al,Zn)_{49}$	Decrease of creep resistance	[Xiaofeng 2009]
Mg-4Al	1-3	Al_4Sr AlMgSr	Creep properties are significantly improved by formation of thermally stable inter-phases	[Bai 2006a]
Mg-8.5Al-1Ca	0.3Sr	$(Mg,Al)_2(Ca,Sr)$	precipitates in this alloy were stable and provided resistance against lattice diffusion creep	[Sato 2008]
Mg-6Al	2.6-2.8	Al_4Sr Mg_9Al_3Sr	excellent creep resistance by matrix strengthening from well-distributed Al-Mn and Mg-Al precipitates	[Kunst 2009]
Mg-5Al	1-1.6	$Al_{14}Mg_{13}Sr$	The creep resistance increased with increasing Sr content. The Al super saturation of α-Mg matrix surrounding the second phase particles was relatively low.	[Pekguleryuz 2001]
Mg-4Al-2Sn	1.3	$Mg_{17}Al_{12}$ Mg_2Sn SrMgSn	The creep strength was improved by the addition of Sr.	[Kim 2010]

2.5. Hot Deformation and Recrystallization

Recrystallization during deformation (usually at high temperatures) is called dynamic recrystallization (DRX). DRX is important because it lowers the flow stress of the material during hot working and has a significant influence on the texture and grain structure of the deformed material. Trojanova *et al*. [Trojanova 2008] reported the importance of the role of the recovery processes in reducing internal stresses during the hot deformation of an AJ50 Mg alloy. There are many different DRX mechanisms that are active during the hot deformation of Mg. In metals which have low or medium stacking fault energy (SFE), DRX may take place when certain critical deformation conditions are met. New grains start to form on the boundaries; as they grow they are introduced to more deformation and their dislocation density increases (Fig.2.8). Therefore the grain runs out of driving force for further growth and it will stop.

The next groups of mechanisms are somehow different from the previous. In this division recrystallization happens suddenly by the re-arrangement of the grain and sub-grain structure. Geometric DRX (where the serrations of the highly deformed grain become comparable to the grain thickness and new equiaxed grains form by the interpenetration of the grain boundaries [Humphreys 2004]) and progressive lattice rotation are categorized in this division.

There are several studies regarding the effect of extrusion parameters on Mg microstructure. Shahzad *et al*. reported that the extrusion temperature influenced the activation of various modes of plastic deformation and DRX response in Mg AZ80 alloy. It was also reported that at lower temperatures, twinning was more active, new grains nucleated at the twin boundaries and a fine grain size was achieved. While at higher temperatures, the bulging of original grain boundaries was predominant and new grains were initiated at the original grain boundaries and a coarse grain size was achieved [Shahzad 2009].

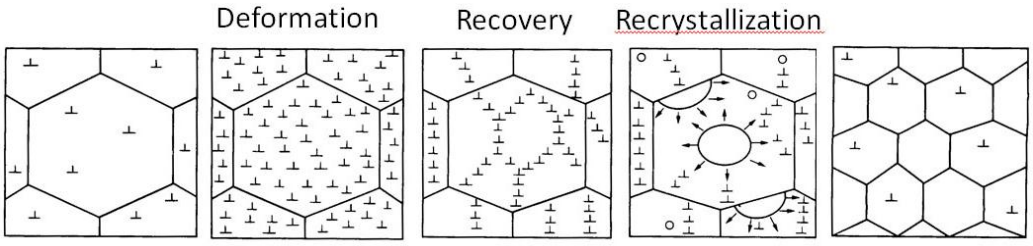

Figure 2.8: Schematic diagram showing the sequence of recrystallization events in a polycrystalline material.

2.5.1. DRX associated with Bulging of Grain boundaries

The general characteristics of bulging of grain boundaries can be summarized as follows: 1) the stress-strain curve during DRX generally consists of a broad peak followed by a plateau (Fig. 2.9); 2) There should be an accumulation of strain (ε_c) which is also called critical strain before recrystallization starts at the peak stress (σ_{max}); 3) The critical strain decreases with decreasing stress or Zener – Holloman parameter:

$$Z = \varepsilon \exp\left(\frac{Q_{HW}}{RT}\right)$$

where Q_{HW} is the activation energy for hot deformation, ε is the strain rate and T is the absolute temperature.); 4) The size of the dynamically recrystallized grains decreases with increasing stress; 5) The flow stress and the size of the DRX grains are nearly independent of the initial grain size since the effect of small grain size on work hardening (strength increase) is counterbalanced by recrystallization (work softening) at the boundaries. The DRX grain size is controlled by the restriction of grain growth due to work hardening inside the newly recrystallized grain. However, the kinetics of DRX are accelerated in specimens with smaller initial grain sizes, and 6) New grains during dynamic recrystallization initiate at the grain boundaries [Humphreys 2004].

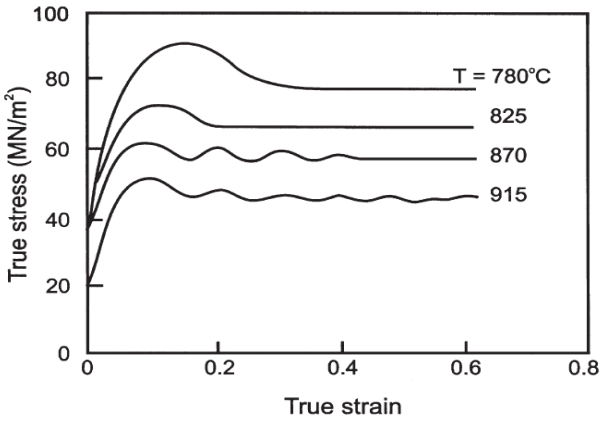

Figure.2.9. The effect of temperature on the stress-strain curves for 0.68%C steel, deformed in axisymmetric compression, ε = 1.3 x 10^{-3} S^{-1} [Humphreys 2004].

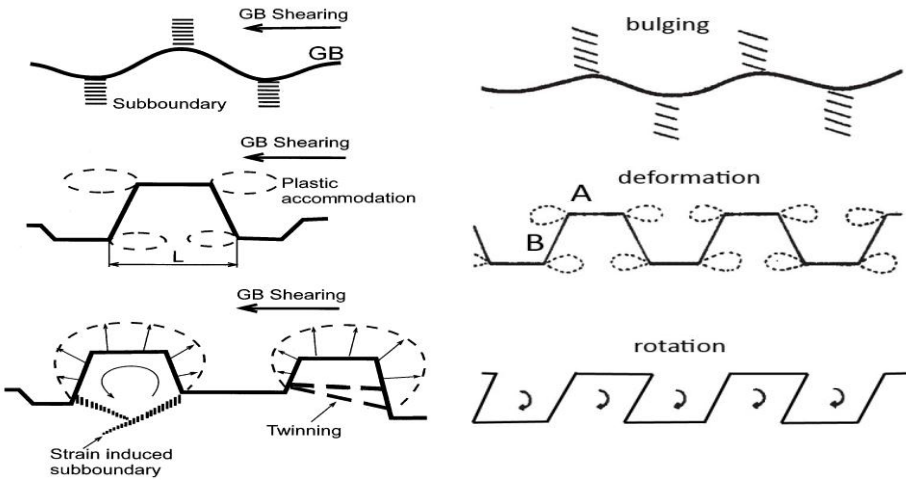

Figure.2.10. Two different proposed models for DRX nucleation, (a) Wusatowska et al. 2002, (b) Drury and Humphreys, 1986.

There are different assumptions related to the nucleation site and mechanisms of DRX [Wusatowska 2002, Drury 1986]. The theories all agree that nucleation starts from a bulge in a high angle grain boundary and it is followed by growth toward the grain with higher dislocation density. Bailey and Hirsch [Bailey 1962] described that the grain boundary "sweeps up" the dislocations creating a strain-free volume in the crystal; if this volume reaches a critical size of 150 Å a stable nucleus forms. There are different theories regarding how the bulge is separated from the original grain. Fig.2.10 demonstrates the two ideas about nucleation in DRX. Wusatowska *et al*. have suggested that the DRX grains nucleate by bulging of grain boundaries and their evolution can be accelerated by two possible ways: 1) during hot deformation during high angle boundary migration twinning could prepare the nucleus, and 2) while at lower temperatures strain induced sub-boundaries of moderate angle separate the bulged portion of the parent grain [Wusatowska 2002].

Microstructural Evolution during DRX

When there is a large difference between the size of the DRX grains and the initial grains a necklace structure of grains may be formed. This procedure is repeated until all the large grains are consumed and all the structure is occupied by the new DRX grains (Fig.2.11).

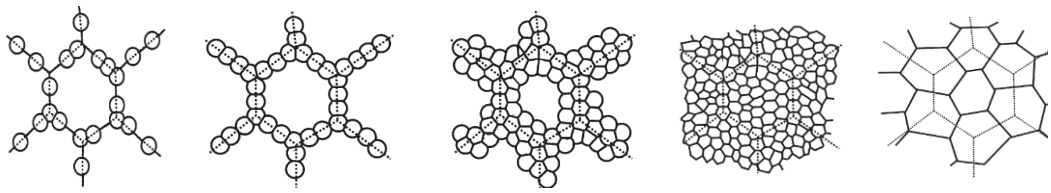

Figure.2.11. Microstructure evoloution during dynamic recrystallization. (a)–(d) Large initial grain size, (e) small initial grain size. The dotted lines show the prior grain boundaries.

The chain of new DRX grains is evident in many materials. Laser *et al.* [Laser 2004] studied the DRX behaviour of AZ31 alloy. They also observed the necklace of DRX grains at grain and twin boundaries. Unlike static recrystallization, the mean grain size does not change when DRX proceeds. The presence of very small grains along with the original coarse grains affects the deformation mode of the whole matrix. In some cases where deformation by glide and climb is restricted in the matrix (dispersion hardened or lack of slip systems), small grains in the boundary region are perfect sites for grain boundary sliding and accomodating the imposed deformation [Drury 1989].

2.5.2. DRX mechanisms without bulging of grain boundaries

There are DRX processes which are different from the mechanism where new grains recrystallize from the parent grains at pre-existing grain boundaries. Haterly has classified two separate mechanisms of continuous DRX: 1)Progressive Lattice Rotation and 2) Geometrical Recrystallization.

2.5.2.1. Progressive Lattice Rotation

In deformation conditions with high Zener – Holloman parameters (low temperature and high strain rate) new grains with high angle boundaries could form by rotation of the subgrain walls and little accompanying boundary migration (Fig.2.12).

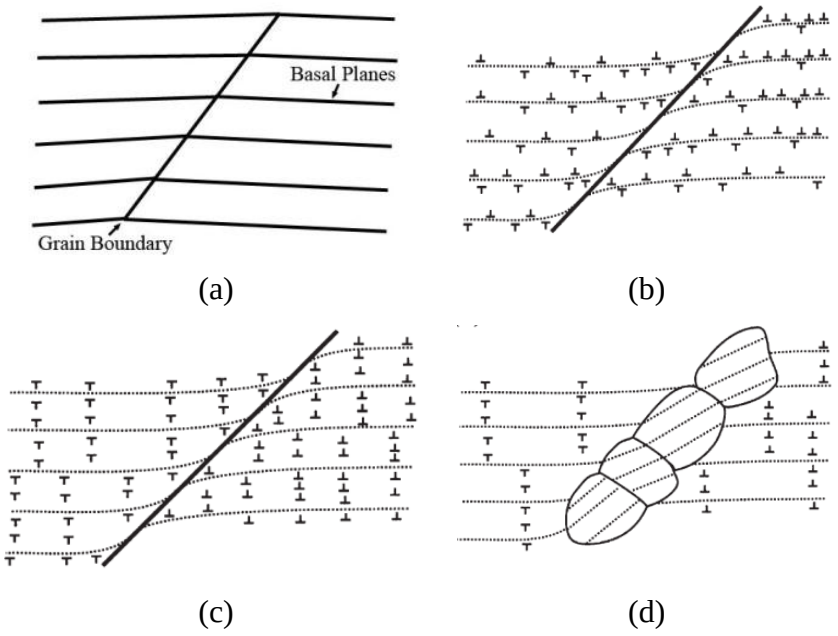

Figure .2.12. Schematic diagram of deformation and dynamic recrystallization in grain boundary regions [Humphreys 2004].

This mechanism is activated by strain and is not yet clearly understood, but it is thought to be active in materials with inhibited dislocation mobility. For instance in Mg alloys because of the lack of active slip systems or Al-Mg alloys where solute drag slows down the dislocation movement, progressive subgrain rotation is frequent.

In Mg alloys a misorientation gradient develops from the boundaries to the center of the grain because of the restricted number of active slip systems under deformation. Simultaniously, as a result of strain, accelerated inhomogenious dynamic recovery occurs near the grain boundaries. When deformation is increased, the closed cells surrounded by low angle boundaries near the initial high angle boundaries start to rotate and form high angle boundaries around them.

2.5.2.2. Geometric Dynamic Recrystallization

Geometric DRX usually occurs in alloys which have undergone very large strains. In this mechanism, high angle grain boundaries become serrated in pancaked grains as a result of dynamic recovery (Fig 2.13).

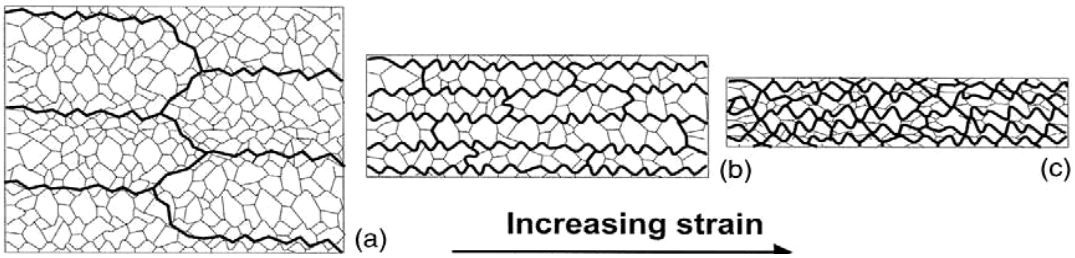

Figure.2.13. Geometric dynamic recrystallization. As deformation progresses, the serrated HAGBs (thick lines) become closer, although the subgrain size remains approximately constant. Eventually the HAGBs impinge, resulting in a microstructure of mainly high angle boundaries.

The wavelength of the serrations is of the order of the size of the subgrains. By subjecting the material to a large reduction in cross section by, for example, hot rolling or extrusion grains start to become pancaked. The subgrain size is independent to the amount of strain, therefore the fraction of high angle boundaries increases with increasing deformation, and finally the size of grain serrations becomes comparable to the grain thickness. By further deformation, the serrated boundaries impinge upon each other and form new equiaxed grains the size of which is comparable to the subgrain size. The sequence of the progress is shown schematically in Fig.2.13.

2.5.3. Effect of Second Phases on Recrystallization

There are three major effects that second phase particles have on recrystallization: 1) They can pile up dislocations, therefore increase the stored energy and driving force for recrystallization; 2) Certain large particles may act as nucleation sites for new recrystallized grains; and 3) Particles could pin the high angle boundary migration during growth if they are closely spaced. While the last effect slows down recrystallization, the first two accelerate recrystallization. With a sufficiently small spacing of thermally stable particles, it is possible to stop recrystallization up to the melting temperature of the matrix. By varying the particle size and spacing, it has been demonstrated that acceleration or retardation of recrystallization is possible in the same alloy as shown in Fig. 2.14 [Doherty 1962]. This effect is known as particle stimulated nucleation (PSN).

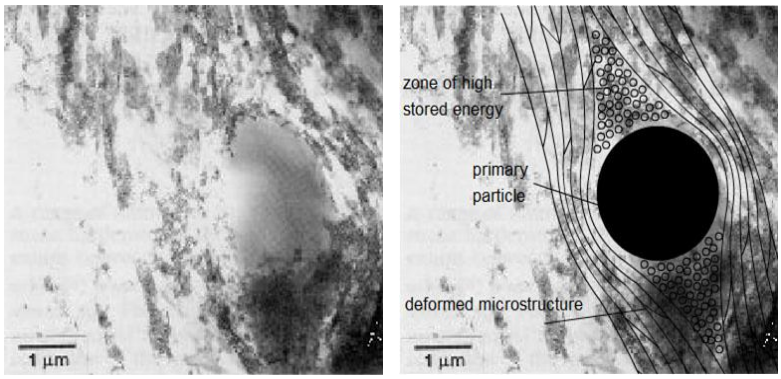

Figure.2.14. (a) TEM micrograph showing a particle in a deformed structure, (b) schematic overlay showing the deformed microstructure and the zone of stored energy

There are three important aspects of PSN of recrystallization: 1) The orientation of the newly recrystallized grains resulting from PSN is different from those produced from bulging of grain boundaries. Therefore, there could be more control on the annealing texture; 2) By controlling the alloy composition and processing the number of potential nuclei and subsequently the final recrystallized grain size may be controlled; and 3) This mechanism has a minor effect on recrystallization when the working temperature is high. High deformation temperature affects the formation of nuclei within deformation zones and the growth of nuclei beyond the particle. This process therefore occurs below an upper limit in temperature and above a critical strain rate [Humphreys 2004]. The size of the distributed particles is also important. Clusters of particles are known to be more effective than single particles [Wang 2011] and a cluster of fine particles (<1 μm) still results in PSN.

Although considerable research has been carried out regarding PSN in Al alloys, there is limited knowledge of PSN in Mg alloys [Jiang 2005]. In Mg alloys, PSN is in competition with new grains formed at other sites (e.g. grain mantle regions). When Mn has been added to pure Mg to form large Mn clusters, new grains from grain boundary sites dominated the microstructure after annealing, rather than PSN [Robson 2009].

Jiang *et al.* [Jiang 2005] studied the possibility of PSN around the $Mg_{17}Al_{12}$ and AlMn precipitates in AZ31. They reported that $Mg_{17}Al_{12}$ could stimulate

nucleation until it dissolves in the matrix at 350^{o}C. However, AlMn precipitates could also be effective until higher temperatures (400^{o}C). The researchers suggested that alloy design leading to a suitable distribution of second-phase particles can improve the properties and formability of wrought Mg alloys [Jiang 2005]. Table 2.8 summarizes studies conducted on PSN in Mg alloys.

Table.2.8. Effect of Particles on PSN during Hot Deformation of Mg Alloys

Alloy	Precipitate	Deformation process	Effect	Reference
Pure Mg +Mn	Mn particles	Hot compression	Following deformation, the matrix surrounding the Mn particles undergoes a rotation, consistent with that observed in other alloy systems where PSN occurs	[Robson 2009]
AZ41+Mn, Ca	$Mg_{17}Al_{12}$ Al_8Mn_5 $A1_2Ca$	Hot compression	Large particles promote recrystallization. The actual geometry, size and distribution of the particles have a distinct effect on DRX	[Wang 2011]
AZ31+ TiCAl	Al-C-O-Fe-Mn	Extrusion & ECAP	Refined microstructure and weakening of the (0002) pole figure	[Torbati 2010]
AZ31	$Mg_{17}Al_{12}$ AlMn	Hot compression	Some evidence of PSN was observed	[Mwembela 1997]
AZ31	$Mg_{17}Al_{12}$ AlMn	Hot compression	PSN took place during hot deformation and was facilitated by the fragmentation of the $Mg_{17}Al_{l2}$	[Jiang 2005]
AZ31	$Mg_{17}Al_{12}$	Hot compression	PSN is rarely observed and is not believed to significantly contribute to the development of DRX	[Beer 2007]
WE54	Mg-Nd Mg-Y Mg-Nd-Y	Extrusion	PSN took place and weakened the basal texture	[Balla 1994]
WE43	Mg-Nd Mg-Y Mg-Nd-Y	Extrusion	Recrystallization at second phase particles were observed	[Mackenzie 2004]

2.6. Texture and Preferred Orientation

In Mg alloys, thermo-mechanical conditions play important roles in the activation of different deformation micro-mechanisms that influence the final texture [Bohlen 2005, Park 2009, Chen 2007, Shahzad 2009, McQueen 1992]. The strong basal texture in Mg is the source of directional mechanical properties and anisotropy which is not desirable. In order to control the basal texture, an understanding of how the preferred orientation is formed is necessary.

2.6.1. The Formation of the Basal Texture

Different planes in the hexagonal structure of Mg have different atomic packing based on the atomic density (and interatomic distance). The basal (0002) plane is close-packed and provides the largest interplanar spacing (***d***) and certain distances on this plane have the smallest Burgers vector (***b***) for dislocation slip. The shear stress, τ, to move a dislocation in a slip system (the Peierls-Nabarro stress) is exponentially related to ***b*** and ***d*** as $\tau \propto e^{\frac{d}{b}}$. Consequently, the basal slip system has the highest resolved shear stress compared to the other slip systems (prismatic and pyramidal). It has been reported that moving a dislocation on the prismatic and pyramidal planes needs approximately 40 and 80 times higher shearing stress respectively compared to the basal plane [Reed-Hill 1957a, Ando 1992]. Consequently dislocations are mainly moved on the basal planes. There are only two independently activated basal slip systems in Mg alloys, which limits the formability of these materials.

Although the basal plane has the lowest critical resolved shear stress in Mg [Sandlöbesa 2011], other planes also contribute in moving dislocations. Koike *et al*. [Koike 2003] have shown the activation of non-basal slip close to grain boundaries attributed to grain-boundary compatibility stress. This suggests that the role of non-basal slip in sub-grain formation may be more important than previously believed. Based on a polycrystalline approach, it has been suggested that the ratio of critical resolved shear stress $\tau_{prism}/\tau_{basal}$ ~ 2-2.5, which is an order of magnitude lower than previous estimations based on single crystal observations [Agnew 2005]. Staroselsky *et al* [Staroselsky 2003] have used a crystal-

mechanics based model to simulate strain stress response and texture formation in AZ31 and reported that the pyramidal $\{101\bar{1}\}\langle 112\bar{0}\rangle$ system is as active as the basal $(0001)\langle 112\bar{0}\rangle$ system. By using slip line trace analysis and EBSD Keshavarz *et al* [Keshavarz 2006] have provided evidence for the operation of significant levels of prismatic slip during tensile straining of AZ31 sheet at room temperature. It has also been shown that the addition of solute atoms such as Li and Y enhances the activity of <c+a> slip mode [Agnew 2001].

However, when the basal plane is not favourably oriented for slip (when the basal plane is perpendicular to the stress axis with shear stress on the plane close to zero) slip is restricted in Mg. In an Mg single crystal or one of non-random orientation this limitation is accentuated.

During straining of a crystalline solid dislocation glide causes a crystallographic rotation, reflective of the symmetry of the deformation modes and the imposed deformation [Agnew 2001]. In Mg alloys, the deformation textures have strong basal components as a direct consequence of easy basal slip [Humphreys 2004]. The basal texture in magnesium alloys forms by different mechanisms. It has been reported that deformation twinning effectively reorients the basal planes [Martin 2011]. Agnew *et al* [Agnew 2001] reported that a basal texture is usually formed because {10-12} twinning reorients the *c* axis parallel to the compression axis. This is expected to occur in the early stages of deformation [Ion 1982]. Extension twinning may also be responsible for textural changes and that its activation is dictated by Schmid factors applicable to different twinning planes [Godet 2006].

Ion *et al.* [Ion 1982] observed microscopic bands after hot compression of a Mg-0.8Al alloy. They suggested that the bands form as a consequence of rotational DRX during hot working. This mechanism involved dynamic polygonization of rotated lattice regions adjacent to grain boundaries. They suggested the material starts to deform by {10-12} twinning which reorients the c axis parallel to the compression direction. This new direction is not favourable for dislocation glide. Simultaneously, new small recrystallized grains form at the distortion region of the grain boundaries. Especially at higher temperatures non

basal slip systems operate, thus giving rise to the rotated region and accommodating the imposed deformation. When the strain increases, sub-grains form at the mantle region by dynamic recovery and finally high grain boundaries form by sub-boundary migration and coalescence. This mechanism has also been described elsewhere [del Valle 2003, Janecek 2010].

Martin *et al.* reported that micro-bands formed by basal slip during straining and their misorientation was increased by straining [Martin 2010]. Their orientation changes involved a rotation axis that lay in the basal plane and as a result of such rotations, the basal planes within the micro-bands became more favorably oriented to glide. They reported that the basal dislocations within the micro-band boundaries were responsible for rotating the micro-band c-axis away from the initial unstable orientations toward the compression axis.

Jin *et al.* discussed that after the basal texture originates from {10-12} twinning, by subsequent deformation, the grains with the c-axis parallel to compression stress direction are insensitive to dynamic recrystallization and this was considered to be the main reason for the progressive strengthening of the basal texture [Jin 2006].

When thermal energy is present in the deforming system, recrystallization takes place where the dislocation density is highest (work hardened grains). As a result grains with basal orientation and are less work hardened stay unaltered during DRX and the work hardened grains transform to new grains with different orientations. Again the newly recrystallized "basal" grains will stay unrecrystallized while the others undergo DRX. This cycle is repeated until all the microstructure is occupied by "basal" grains which form the strong basal texture.

In different industrial fabrication processes, the basal texture could exhibit different forms based on the direction of applied stress and the geometry of the deformation zone. For example, in hot compression or forging a cylindrical bar the basal poles move toward the compression axis. The texture in hot compression is similar to the hot rolling texture. However, during extrusion or

wire drawing, the shape of the basal texture changes according to the symmetry of deformation (Fig.2.15).

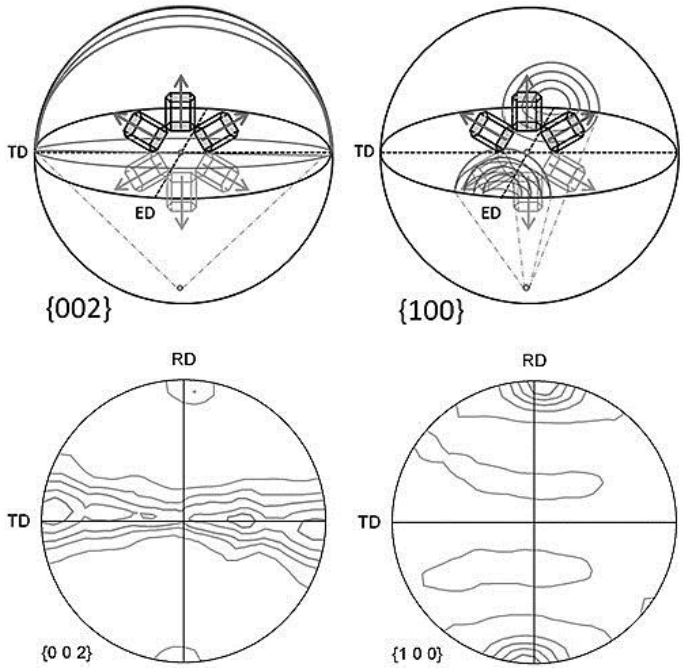

Figure.2.15. Orientations of Mg crystal structure forming the ring basal texture during extrusion.

During the axisymmetric extrusion of the AZ31 (Mg-3Al-1Zn) alloy, the basal planes normally align with the extrusion axis and form a strong ring fiber texture of the basal planes which is responsible for the anisotropic mechanical behaviour of extruded bars [Kleiner 2004].

Several studies have explored dynamic and/or static recrystallization as a means to control the texture and microstructure of Mg extrusion alloys [Bohlen 2005, Mackenzie 2007]. The addition of alloying elements either as a solute in the Mg matrix or to form secondary phase precipitates is among the methods used for controling the deformation modes and the final texture [Stanford 2008, Stanford 2010, Mackenzie 2007, Mackenzie 2008, Laser 2008, Abuleil 2009, 2 Bai 2006, Zeng 2006, Pekguleryuz 2003, Pekguleryuz 2004, Zhao 2007].

It has been shown in a number of works [Stanford 2008, Stanford 2010, Mackenzie 2007, Mackenzie 2008, Laser 2008] that the addition of RE elements

and their dissolution in the Mg matrix can improve ductility. The effect of AE elements such as Ca [2008, Abuleil 2009, Bai 2006b] and Sr [Bai 2006b] on the extrusion behaviour and mechanical properties of Mg alloys have also been previously studied.

2.6.2. The Effect of PSN on the Final Texture

Grains formed via PSN generally have orientations which are different from those produced by the grain boundary bulging mechanism and can produce texture alteration [Humphreys 2004]. This is particularly interesting for Mg as a way to alter the dominant basal texture after deformation. Fig.2.16 shows the recrystallization of a new grain at the particle interface. Balla *et al*. [Balla 1994] reported that wrought Mg alloys can be produced with random textures, and thus observed no asymmetry in the tensile and compressive deformation behaviour, under conditions where PSN dominates. This is because of the random texture of the new grains that form via PSN [Robson 2009]. Torbati-Sarraf *et al*. added different levels of Al-Ti-C master alloy to AZ31 and reported that the Al-C-O-Fe-Mn precipitates caused PSN during extrusion and ECAP resulted in texture weakening [Torbati-Sarraf 2010].

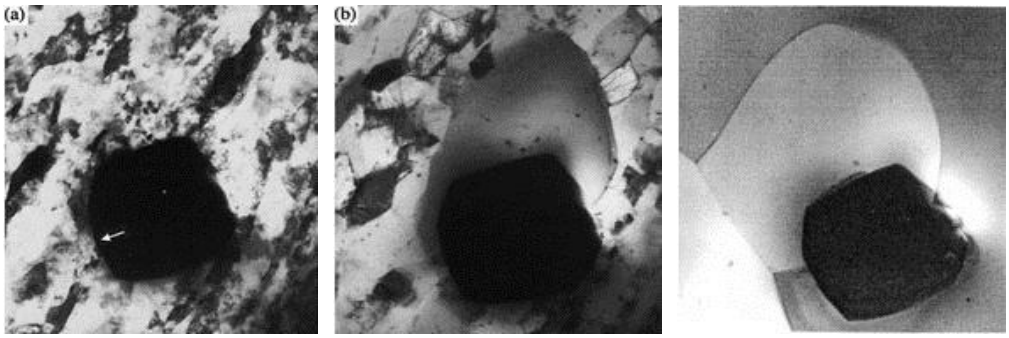

Figure.2.16. TEM micrographs showing the sequence of recrystallization at the interface of a particle in a deforming matrix.

2.7. Hot Extrusion

2.7.1. Extrusion calculations

The force required for extrusion depends on the flow stress of the deforming material, the friction condition, initial temperature, speed of extrusion and extrusion ratio [Hosford 2007]. The extrusion force, *F*, can be estimated by the following equation:

$$F = A_0 k \ln\left(\frac{A_0}{A_f}\right)$$

where *k* is the extrusion constant, and A_0 and A_f are the initial and final billet areas, respectively. *k* depends on factors such as flow stress, friction and redundant work. Neglecting friction and redundant work, *k* can be approximated by:

$$k \cong \bar{Y} = \frac{k\varepsilon^n}{n+1}$$

where $\bar{Y}$ is the average flow stress, and *k* and *n* are material properties obtained from the compression test. In a more precise approach the total extrusion pressure could be derived from adding the pressure for deformation and friction in the deformation zone and the friction in the chamber. By using a slab method analysis, pressure in the die could be calculated as:

$$P_d = \bar{Y}\left(1 - R^B\right)\left(\frac{1+B}{B}\right), B = \mu \cot \alpha$$

where μ is the friction coefficient and α is the half angle of the die. The friction coefficient has been calculated between AZ31 and steel dies using the ring test [Liang 2009, Lapovok 2004]. It has been reported that under dry friction the coefficient is close to 0.35 and by using graphite lubrication m=0.052. In another study the coefficient used was 0.3 based on the magnesium-steel interface [Lapovok 2004]. In hot deformation the strain rate has a significant effect on microstructure evolution. In extrusion the mean strain rate can be calculated by:

$$\varepsilon_m = \frac{6vD_0^2 \ln r_x}{D_0^3 - D_f^3}$$

where υ is the punch velocity, D_0 is the diameter of the initial billet and D_f is the deformed product diameter.

2.7.2. The Extrusion of AZ31

Magnesium alloys are extruded like aluminum alloys and the extrudability is quite similar to aluminum, however the extrusion speed is much lower in magnesium alloys. Indeed the maximum extrusion speed reported for AZ31 is 18% that measured for AA6036 [Atwell 2007]. Mechanical properties and surface finish of the final product are both dependent on the speed and temperature of deformation; these parameters are chosen based on the start of hot cracking and the tendency for grain growth [Lapovok 2004]. During an extrusion process, the temperature rises with increasing speed due to an increased rate of plastic deformation. In the outer region of the billet, the heat of friction combines with the heat of deformation resulting in an inhomogeneity of mechanical properties through the generation of micro cracks at the surface. The effects of extrusion parameters and conditions on the extruded product may be expressed through extrusion limit diagrams. Fig.2.17 is an example extrusion limit diagram for wrought, homogenized and as-cast AZ31 samples [Atwell 2007]. The left (pressure) limit curves were determined using an empirical model extrapolation. The right (cracking) limit curve was fitted using partial cracking data. The results show that the maximum extrusion speed was improved from 18% to 22% after homogenization and to 64% for repeat extrusions.

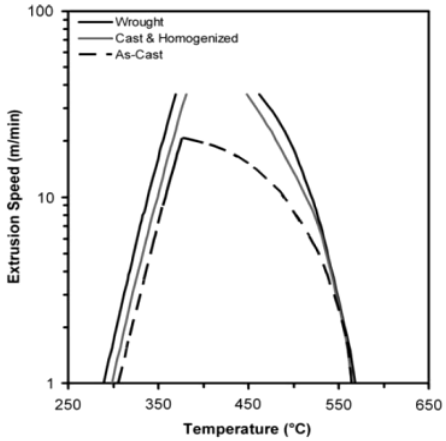

Figure.2.17. Extrusion limit diagram for AZ31 alloy. [Atwell 2007].

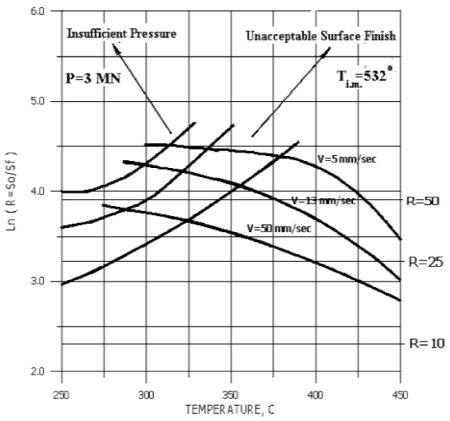

Figure.2.18. Extrusion limit diagram for AZ31 constructed from FE simulation results [Lapovok 2004].

Finite element simulations based on hot compression data have also been used to construct extrusion limit diagrams for AZ31 alloy (Fig.2.18) [Lapovok 2004]. Here it was found that the maximum extrusion ratio dropped from 90 to 40 when the ram speed was increased from 5 to 50 mm s^{-1} Experiments were also undertaken to study the final surface conditions. Round AZ31 billets were extruded at 420^{o}C, with an extrusion ratio of 36 and ram speed varying between 10-22 mm s^{-1}. Surface cracks were observed following high speed extrusion; while the surface of the low speed product was smooth (Fig.2.19) [Lapovok 2004]. Experimental results were supported the calculations whereby the threshold limit for cracking was assumed to be the incipient melting temperature at the billet surface.

Chen *et al*. studied the effect of extrusion ratio on the final microstructure of AZ31 magnesium alloy [Chen 2007]. They found that the ultimate tensile strength (UTS) and yield strength (YS) of AZ31 were enhanced with an increasing extrusion ratio up to 24 and the hardness increased up to an extrusion ratio of 70 (Fig.2.20). They also reported a critical extrusion ratio for grain refinement and improvement of mechanical properties. When extrusion ratio was higher than the critical extrusion ratio, it had little effect on microstructure and mechanical properties.

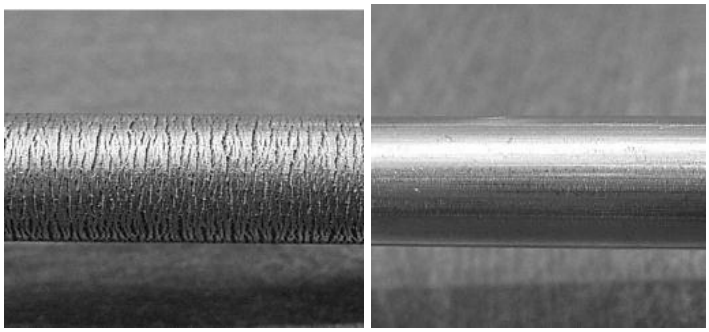

Figure.2.19. Surface conditions of extruded AZ31 billets at 420^{o}C and a ram speed of (a) 10 mm/s, and (b) 22 mm/s.

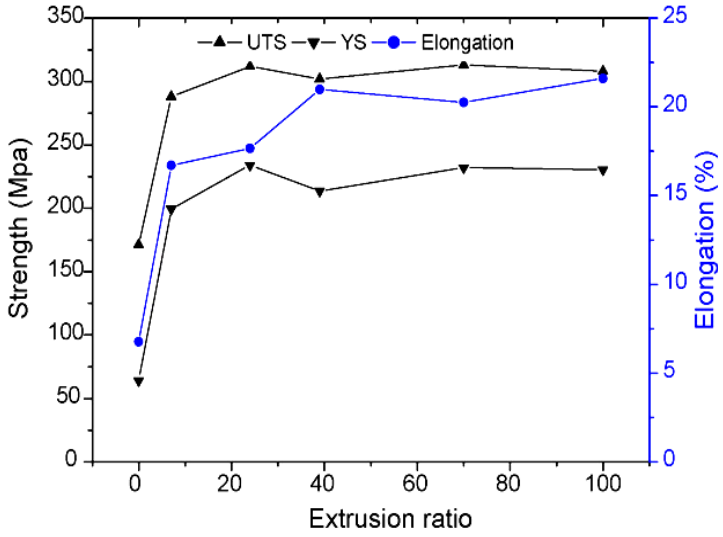

Figure.2.20. Influence of extrusion ratio on tensile properties of AZ31 alloy.

2.7.3. Extrusion of Mg alloys containing Sr

There have been a limited number of studies concerning the effect of Sr additions on the hot deformation behaviour of Mg alloys [Shao-kang 2007, Bai 2006b]. It has been observed that alloys containing Sr (0.02-0.3%) were entirely recrystallized after extrusion while AZ80 with no Sr had a mixed structure of original and DRX grains. Also it was found that the UTS of the extruded alloys was very similar, however elongation was greater with an increased Sr content [Shao-kang 2007]. In a similar study, continuous intermetallic compounds in as-cast samples of an Mg-Al-Sr alloy were found to have converted to a band structure along the extrusion direction after the process. Additionally, the eutectic

Al_4Sr phase was crushed into a large number of smaller blocks, indicating that the Al_4Sr phase was brittle and easily broken during the extrusion process. Since size of the particles is large, they did not have an important effect on dislocation pining and therefore they did not have a significant effect on the tensile properties of extruded alloys [Bai 2006b].

2.8. References

[Abbaschian 2009] Reza Abbaschian, Lara Abbaschian, Robert E. Reed-Hill , Physical Metallurgy Principles 4th Edition. Cengage learning, 2009

[Abuleil 2009] T. Abuleil, N. Hort, W. Dietzel, C. Blawert, Y. Huang, K.U. Kainer, K.P. Rao, " Microstructure and corrosion behaviour of Mg-Sn-Ca alloys after extrusion," Transactions of Nonferrous Metals Society of China, Vol 19, Issue 1 (2009) 40-44.

[Agnew 2001] S.R. Agnew, M.H. Yoo, C.N. Tome, "Application of texture simulation to understanding mechanical behaiviour of Mg and solid solution alloys containing Li or Y" Acta Mater 49, 20 (2001) p4277

[Agnew 2005] Sean. R. Agnew, Ozgur Duygulu, "Plastic anisotropy and the role of non basal slip in alloy AZ31B" International journal of Plasticity, 21, 6 (2005) p1161.

[Akhtar 1969] A Akhtar, E Teghtsoonian, "Solid solution strengthening of magnesium single crystals—ii the effect of solute on the ease of prismatic slip," Acta Metallurgica, Volume 17, Issue 11, November 1969, Pages 1351–1356

[Aliravci 1992] C.A. Aliravci, J.E. Gruzleski, F.C. Dimayuga, "Effect of Strontium on the Shrinkage Microporosity in Magnesium Sand Castings," AFS Trans., 92, (1992).

[Aljarrah 2007] M. Aljarrah, M.A. Parvez, Jian Li, E. Essadiqi, M. Medraj, "Microstructural characterization of Mg–Al–Sr alloys," Science and Technology of Advanced Materials 8 (2007) 237–248

[Ando 1992] S. Ando, K. Nakamura, K. Takashima and H. Tonda, "{11-22}<-1-123> slip in magnesium single crystal," J. Jpn. Inst. Light Metal. 42 (1992), p. 765.

[Atwell 2007] D. L. Atwell, M. R. Barnett, "Extrusion limits of magnesium alloys", Metallurgical and Materials Transactions A, 38A (2007) 3032-3041.

[Bai 2006a] Bai Jing, Sun Yangshan, Xun Shan, Xue Feng, Zhu Tianbai, "Microstructure and tensile creep behaviour of Mg–4Al based magnesium alloys with alkaline-earth elements Sr and Ca additions," Materials Science and Engineering A 419 (2006) 181–188.

[Bai 2006b] Bai Jing, Sun Yangshan, Xue Feng, Xue Shan, Qiang Jing, Tao Weijian, "Effect of extrusion on microstructures, and mechanical and creep properties of Mg–Al–Sr and Mg–Al–Sr–Ca alloys," Scripta Materialia 55 (2006) 1163–1166

[Bailey 1962] J. E. Bailey and P. B. Hirsch, "The Recrystallization Process in Some Polycrystalline Metals," Proc. R. Soc. Lond. A (1962) 267:11-30.

[Bakarian 1943] P.W. Bakarian and C.H. Mathewson, Trans. AIME 152 (1943), p. 226.

[Balla 1994] E.A. Balla, P.B. Prangnella, "Tensile-compressive yield asymmetries in high strength wrought magnesium alloys," Scripta Metallurgica et Materialia, Vol 31, Issue 2, (1994) 111-116.

[Baril 2003] E. Baril, P. Labelle, M.O. Pekguleryuz, "Elevated Temperature Mg-Al-Sr: Creep Resistance, Mechanical Properties & Microstructure," Journal of Metals (JOM-US), TMS, Vol 55, No 11, (2003)

[Beals 2007] Randy S. Beals, Cam Tissington, Xinmin Zhang, Karl Kainer, Joe Petrillo, Mark Verbrugge, and Mihriban Pekguleryuz, "Magnesium Global Development: Outcomes from the TMS 2007 Annual Meeting," TMS 2007 conference review, Journal of Metals (2007) 39-42

[Becerra 2008] A. Becerra, M. Pekguleryuz, "Effects of lithium, indium, and zinc on the lattice parameters of magnesium," J. Mater. Res., Vol. 23, No. 12, Dec 2008

[Beer 2007] A.G. Beer, M.R. Barnett, "Microstructural Development during Hot Working of Mg-3Al-1Zn," Metallurgical and Materials Transactions A, Volume 38, Number 8, 1856-1867.

[Bohlen 2005] J. Bohlen, S.B. Yi, J. Swiostek, D. Letzig, H.G. Brokmeier, K.U. Kainer, "Microstructure and texture development during hydrostatic extrusion of magnesium alloy AZ31,"Scripta Materialia Volume 53, Issue 2, July 2005, Pages 259-264.

[Cao 2010] G. Cao, C. Zhang, H. Cao, Y.A. Chang, and S. Kou, "Hot-Tearing Susceptibility of Ternary Mg-Al-Sr Alloy Castings," Metallurgical and Materials Transactions A, Vol 41A, (2010) 706-716.

[Chen 2007] Y. Chen, Q. Wang, J. Peng, C. Zhai, W. Ding, "Effects of extrusion ratio on the microstructure and mechanical properties of AZ31 Mg alloy", Journal of Materials Processing Technology 182 (2007) 281–285.

[Cheng 2008] CHENG Ren-ju, PAN Fu-sheng, YANG Ming-bo, TANG Ai-tao, "Effects of various Mg-Sr master alloys on microstructural refinement of ZK60 magnesium alloy," Trans. Nonferrous Met. SOC. China 18 (2008) s50-s54

[Couret 1985a] A. Couret, D. Caillard, An in situ study of prismatic glide in magnesium—I. The rate controlling mechanism, Acta Metallurgica, Volume 33, Issue 8, August 1985, Pages 1447-1454.

[Couret 1985b] A. Couret, D. Caillard, An in situ study of prismatic glide in magnesium—II. Microscopic activation parameters, Acta Metallurgica, Volume 33, Issue 8, August 1985.

[Czerwinski 2005] F. Czerwinski, A. Zielinska-Lipiec, "The microstructure evolution during semisolid molding of a creep-resistant Mg–5Al–2Sr alloy," Acta Materialia 53 (2005) 3433–3444

[Dargusch 1998] M. S. Dargusch and G. L. Dunlop, "Magnesium alloys and their applications," Wolfsburg, WerkstoffInformationsgesellschaft mbH. 1998, 277–282

[Dargusch 2009] M.S. Dargusch, S.M. Zhu, J.F. Nieb, G.L. Dunlop, "Microstructural analysis of the improved creep resistance of a die-cast

magnesium–aluminium–rare earth alloy by strontium additions," Scripta Materialia 60 (2009) 116–119.

[del Valle 2003], J.A. del Valle, m.T. Perez-Prado, O.A. Ruano, "Texture evolution during large-strain hot rolling of Mg AZ61 alloy" Materials Science and Engineering A, 355, 1-2 (2003) p68.

[del Valle 2005] J. A. del Valle, M. T. Pérez-Prado and O. A. Ruano, "Deformation mechanisms responsible for the high ductility in a Mg AZ31 alloy analyzed by electron backscattered diffraction," Metallurgical And Materials Transactions A Volume 36, Number 6, 1427-1438

[Doege 2001] E. Doege, K. Droder, "Sheet metal forming of magnesium wrought alloys - formability and process technology", JMPT. 115 (2001) 14–19.

[Drury 1986] M. R. Drury, F. J. Humphreys, "The development of microstructure in Al-5% Mg during high temperature deformation", Acta metall. 34, I I. (1986) 2259-2271.

[Drury 1989] M. R. Drury, F. J. Humphreys, S. H. White, "Effect of dynamic recrystallization on the importance of grain-boundary sliding during creep", Journal of Materials Science 24 (1989) 154-162.

[Du 2009] Jun Du, Jian Yang, Mamoru Kuwabara, Wenfang Li, Jihua Peng, "Effect of strontium on the grain refining efficiency of Mg–3Al alloy refined by carbon inoculation," Journal of Alloys and Compounds 470 (2009) 228–232.

[Godet 2006] S. Godet, L. Jiang, A.A. Luo, J.J. Jonas, "Use of Schmid factors to select extension twin variants in extruded magnesium alloy tubes," Scripta Materialia Volume 55, Issue 11, December 2006, Pages 1055–1058

[Gruzleski 1992] J.E. Gruzleski and A. Aliravci, "Low Porosity, Fine-Grain Sized Strontium Treated Magnesium Alloy Castings," US Patent US005143564A, (1992)

[Guan 2007] GUAN Shao-kang, W, ANG Li-guo, YANG Qing, CAO Wen-bo, "Microstructures and mechanical properties of double hot-extruded

AZ80+xSr wrought alloys," Trans. Nonferrous Met. SOC. China 17(2007) 1143-1151

[Horst 2006] Horst E. Friedrich, Barry L. Mordike, "Magnesium technology: metallurgy, design data, applications," Springer, 2006.

[Hosford 2007] W. F. Hosford, R. M. Caddell, "Metal Forming Mechanics and Metallurgy," third edition, Cambridge University Press, 2007.

[Humphreys 2004] F.J. Humphreys, M. Hatherly, "Recrystallization and related annealing phenomena", 2nd Edition, Elsevier, 2004.

[Ion 1982] S.E. Ion, F.J. Humphreys, S.H. White, "Dynamic recrtstallization and development of microstructure during high temperature deformation of Magnesium" Acta Metallurgica, 30, 10 (1982) p1909.

[Janecek 2010] M. Janecek, S. Yi, R. Kral, J. Vratna, K.U. Kainer "Texture and Microstructure evolution in ultrafine grained AZ31 processed by EX-ECAP", J Mat Sci, 45 (2010) p4665.

[Janz 2007] A. Janz, J. Gro¨bner. D. Mirkovic´, M. Medraj. "Experimental study and thermodynamic calculation of AlMgSr phase equilibria," Intermetallics 15 (2007) 506-519

[Jiang 2005] L. Jiang, G. Jie Huang, S. Godet, J. J. Jonas, Alan A. Luo, "Particle-Stimulated Nucleation of Dynamic Recrystallization in AZ31 Alloy at Elevated Temperatures," Materials Science Forum, (2005) 488-489.

[Jiang 2006] Lan Jiang, John J. Jonas, Alan A. Luo, Anil K. Sachdev, Ste´phane Godet, "Twinning-induced softening in polycrystalline AM30 Mg alloy at moderate temperatures," A Scripta Materialia 54 (2006) 771–775.

[Jin 2006] Qinglin Jin, Song-Yong Shim, Su-Gun Lim, "Correlation of Microstructural evolution and formation of basal texture in a coarse grained Mg-Al alloy during hot deformation" scripta materialia, 55,9 (2006) p 843.

[Keshavarz 2006] Z. Keshavarz, M. Barnett, "EBSD analysis of deformation modes in Mg-3Al-1Zn", scripta materialia 55, 10 (2006) p915.

[Kim 2010] B. H. Kim, K. C. Park, Y. H. Park, I. M. Park, "Microstructure and creep properties of Mg-4Al-2Sn-1(Ca,Sr) alloys," Trans. Nonferrous Met. SOC. China 20 (2010) 1184-1191

[King 1973] H. W. King, "Solid solution and intermetallic phases containing strontium," Int. Conf. Strontium Containing Compounds, NRC, Ottawa, Canada, (1973) 212-243.

[King 1987] A.H. King, M.H. Yoo, On the availability of dislocation reactions at grain boundaries in cubic ordered alloys, Scripta Metallurgica, Volume 21, Issue 8, August 1987, Pages 1115-1119

[Kleiner 2004] S. Kleiner, P.J. Uggowitzer, "Mechanical anisotropy of extruded Mg-6%Al–1% Zn alloy," Materials Science and Engineering: A, Volume 379, Issues 1-2, 15 August 2004, Pages 258-263.

[Knezevic 2010] Marko Knezevic, Amanda Levinson, Ryan Harris, Raja K. Mishra, Roger D. Doherty, Surya R. Kalidindi," Deformation twinning in AZ31: Influence on strain hardening and texture evolution," Acta Materialia 58 (2010) 6230–6242

[Koike 2003] J.Koike, T.Kobayashi, T. Mukai, H.watanabe, M.Suzuki, K.Maruyama, K. Hilgashi, "the activity of non basal slip systems and dynamic recovery at room temperature in fine grained AZ31B Magnesium alloys," Acta Materialla, 51, 2003, 2055-2065.

[Koubichek 1959] L. Koubichek, "Effect of Small Additions of Elements on Grain Size and the Refinement of the Mg4Al3 [Mg17Al12] Phase in ML5 Alloy," Izv. Vyschikh. Outchebnykh Za Vedeny, Metallurgy of Non-Ferrous Metals, No 6, (1959)

[Kuhn 2000] H. Kuhn, D. Medlin, eds. 2000. ASM Handbook: Mechanical Testing and Evaluation. Vol. 8: ASM International.

[Kunst 2009] Martin Kunst, Andreas Fischersworring-Bunka, Gilles L'Esperanceb, Philippe Plamondonb, Uwe Glatzelc, "Microstructure and dislocation analysis after creep deformation of die-cast Mg–Al–Sr (AJ) alloy," Materials Science and Engineering A 510–511 (2009) 387–392

[L'Esperance 2010] Gilles L'Esperance, Philippe Plamondon, Martin Kunst, Andreas Fischersworring-Bunk, "Characterization of intermetallics in Mg–Al–Sr AJ62 alloys," Intermetallics 18 (2010) 1–7

[Lapovok 2004] R.Ye. Lapovok, M.R. Barnett, C.H.J. Davies," Construction of extrusion limit diagram for AZ31 magnesium alloy by FE simulation", Journal of Materials Processing Technology 146 (2004) 408–414.

[Laser 2004] T. Laser, Ch. Hartig, R. Bormann, J. Bohlen, D. Letzig, "Dynamic Recrystallization of Mg-3Al-1Zn", Proceedings of the 6th International Conference Magnesium Alloys and Their Applications, 2004 Weinheim.

[Laser 2008] T. Laser, Ch. Hartig, M.R. Nürnberg, D. Letzig. R. Bormann, "The influence of calcium and cerium mischmetal on the microstructural evolution of Mg–3Al–1Zn during extrusion and resulting mechanical properties," Acta Materialia, Vol 56, Issue 12 (2008) 2791-2798.

[Lee 1998] S. Lee, S. H. Lee, D. H. Kim, "Effect of Y, Sr, and Nd Additions on the Microstructure and Microfracture Mechanism of Squeeze-Cast AZ91-X Magnesium Alloys", Metallurgical and Materials Transactions A, 29A (1998) 1221-1235

[Lee 2000] Y. C. Lee, A. K. Dahle and D. H. StJohn, "The role of solute in grain refinement of magnesium," Metallurgical and Materials Transactions A, Vol 31, No 11 (2000) 2895-2906.

[Li 2011] LI Rui-hong, PAN Fu-sheng, JIANG Bin, YIN Heng-mei, LIU Ting-ting, "Effects of yttrium and strontium additions on as-cast microstructure of Mg-14Li-1Al alloys," Trans. Nonferrous Met. SOC. China 21 (2011) 778-783.

[Liang 2009] S.J. Liang, Z.Y. Liu, E.D.Wang, "Simulation of extrusion process of AZ31 magnesium alloy", Materials Science and Engineering A 499 (2009) 221–224.

[Liu 2008] S.F. Liu, L.Y. Liu, L.G. Kang, "Refinement role of electromagnetic stirring and strontium in AZ91 magnesium alloy," Journal of Alloys and Compounds 450 (2008) 546–550.

[Liu 2009] S.F. Liu, B. Li, X.H. Wang, W. Su, H. Han, "Refinement effect of cerium, calcium and strontium in AZ91 magnesium alloy," journal of materials processing technology 209 (2009) 3999–4004.

[Liu 2010] Hongmei Liu, Yungui Chen, Haofeng Zhao, Shanghai Wei, Wei Gao, "Effects of strontium on microstructure and mechanical properties of as-cast Mg–5wt.%Sn alloy," Journal of Alloys and Compounds 504 (2010) 345–350.

[Liu 2010] Liu Xian-bin, Shan Da-yong, Song Ying-wei, Han En-hou, " Effects of heat treatment on corrosion behaviours of Mg-3Zn magnesium alloy" Trans. Nonferrous Met. SOC. China 20 (2010) 1345-1350.

[Lubarda 2003] V.A. Lubarda, "On the effective lattice parameter of binary alloys," Mechanics of Materials 35 (2003) 53–68.

[Luo 1994] A. Luo, M.O. Pekguleryuz, "Cast Magnesium Alloys for Elevated Temperature Applications," Journal of Materials Science, Vol 29, No 20, (1994)

[Luo 2004] A.A. Luo, "Recent magnesium alloy development for elevated temperature applications," International Materials Review 49 (2004) 13–30.

[Mackenzie 2004] L.W.F. Mackenzie, Gordon W. Lorimer, F. John Humphreys, T. Wilks, "Recrystallization Behaviour of Two Magnesium Alloys," Materials Science Forum, (2004) 467-470.

[Mackenzie 2007] L.W.F. Mackenzie, B. Davis, F.J. Humphreys, G.W. Lorimer, "The deformation, Recrystalization and texture of three magnesium alloy extrusions," Materials Science and Technology. Vol. 23, no. 10, pp. 1173-1180. Oct. 2007.

[Mackenzie 2008] L.W.F. Mackenzie, M.O. Pekguleryuz, "The recrystallization and texture of magnesium-zinc-cerium alloys," Scripta Materialia, Vol 59, No 6 (2008) 665-668.

[Martin 2010] E. Martin, J. Jonas, "Evolution of Microstructure during the hot deformation of Mg-3%Al", Acta Mater, 45, 12 (2010) p4253.

[Martin 2011] E. Martin, R.K. Mishra, J.Jonas, "Effect of twinning on recrystallization textures in deformed magnesium alloy AZ31" Philosophical Magazine, 91,27 (2011) p3613.

[McQueen 1992] H. J. McQueen, M. Pekguleryuz, "Hot Workability of Magnesium Alloys" Magnesium Alloys and their Applications, Apr, 1992 Garmisch Partenkirchen, Germany, (1992) 101-108.

[Mwembela 1997] A Mwembela, E.B Konopleva, H.J McQueen, Microstructural development in Mg alloy AZ31 during hot working, Scripta Materialia, Volume 37, Issue 11, 1 December 1997, Pages 1789-1795

[Mwembela 1997] A. Mwembela, E.B. Konopleva and H.J. McQueen, "Microstructural development in mg alloy AZ31 during hot working," Scripta Materialia Vol 37, Issue 11 (1997) 1789-1795.

[Nam 2011] N.D. Nam, W.C. Kim, J.G. Kim , K.S. Shin, H.C. Jung, "Corrosion resistance of Mg–5Al–xSr alloys," Journal of Alloys and Compounds 509 (2011) 4839–4847

[Pan 2006] PAN Yichuan, LIU Xiangfa, YANG Hu, "Sr Microalloying for Refining Grain Size of AZ91D Magnesium Alloy," Journal of Wuhan University of Technology - Materials Science Edition, Vol 22, No 1, (2006) 74-76.

[Park 2009] S.S. Park, B.S. You, D.J. Yoon, "Effect of the extrusion conditions on the texture and mechanical properties of indirect-extruded Mg–3Al–1Zn alloy," Journal of Materials Processing Technology, Vol 209, Issues 18-19 (2009) 5940-5943.

[Park 2010] Sung Hyuk Park, Seong-Gu Hong, Chong Soo Lee, "Activation mode dependent {10-12} twinning characteristics in a polycrystalline magnesium alloy," Scripta Materialia 62 (2010) 202–205

[Pekguleryuz 2001] M. O. Pekguleryuz, E. Baril, The Minerals, Metals and Materials Society 'Magnesium technology 2001', ed. J. N. Hryn, Warrendale, PA (2001).

[Pekguleryuz 1992] M.O. Pekguleryuz, M.M. Avedesian, "Magnesium Alloying - Some Metallurgical Aspects, "Magnesium Alloys & their Applications, B.L. Mordike, F. Hehman, Eds. DGM, Germany, (1992) 679-686.

[Pekguleryuz 2001] M. Pekguleryuz. E. Baril, "Development of Creep Resistant Mg-Al-Sr Alloys," Magnesium Technology, Edited by J. Hryn, TMS (The Minerals. Metals & Materials Society). 2001

[Pekguleryuz 2003] M. Pekguleryuz, E. Baril, P. Labelle, D. Argo, "Creep Resistant Mg-Al-Sr Alloys", J. Adv. Mat., vol. 35, No. 3, (2003) 32-38.

[Pekguleryuz 2003a] M.O. Pekguleryuz, A.A. Kaya, "Creep Resistant Mg-Based Casting Alloy for Powertrain Applications," Advanced Engineering Materials, DGM, Vol 5, No 12, (2003)

[Pekguleryuz 2003b] M. Pekguleryuz, P. Labelle, E.Baril, D. Argo, ''Magnesium Diecasting Alloy AJ62x with Superior Creep Resistance and Castability," 2003 Magnesium Technology, TMS, San Diego, March 2003, pp. 201-207.

[Pekguleryuz 2004] M.O. Pekguleryuz, A.A. Kaya, "Magnesium Diecasting Alloys for High Temperature Applications," Magnesium Tech., A.Luo, Eds., TMS, (2004) 281-287.

[Pekguleryuz 2010] M. Pekguleryuz, M. Celikin, "Creep Mechanisms in Magnesium Alloys", Int. Mater. Rev., vol. 55 no. 4, 2010, pp. 197-217.

[Pestman 1992] B.J. Pestman, J.Th.M. de Hosson, Interactions between lattice dislocations and grain boundaries in Ni3Al investigated by means of in situ TEM and computer modelling experiments, Acta Metallurgica et Materialia, Volume 40, Issue 10, October 1992, Pages 2511-2521

[Raghavan 2007] V. Raghavan "Phase Diagram Evaluations Al-Mg-Sr (Aluminum-Magnesium-Strontium)", Journal of Phase Equilibria And Diffusion, Volume 28, Number 5, 473-476, 2007

[Reed-Hill 1957a] R.E. Reed-Hill, W.D. Robertson, "Deformation of magnesium single crystals by nonbasal slip," Trans. TMS-AIME 220, 1957, 496–502

[Reed-Hill 1957b] R.E. Reed-Hill, W.D. Robertson, "Additional modes of deformation twinning in magnesium. Acta Metall. 5,1957, 717–727.

[Reed-Hill 1991] R. E. Reed-Hill, R. abbaschian, "physical metallurgy principals," third edition, PWS pub. Boston, 1991.

[Robson 2009] J.D. Robson, D.T. Henry, B. Davis, "Particle effects on recrystallization in magnesium–manganese alloys: Particle-stimulated nucleation," Acta Materialia 57 (2009) 2739–2747.

[Rokhlin 2003] L.L. Rokhlin, "Magnesium Alloys Containing Rare Earth Metals: Structure and Properties," CRC Press, 1 edition (2003).

[Routbort 2003] Jules L. Routbort, Plasticity (Engineering), In: Editor-in-Chief: Robert A. Meyers, Editor(s)-in-Chief, Encyclopedia of Physical Science and Technology (Third Edition), Academic Press, New York, 2003, Pages 425-440

[Salman 2009] S. A. Salman, R. Ichino, M. Okido, "Improvement of corrosion resistance of AZ31 Mg alloy by anodizing with co-precipitation of cerium oxide," Trans. Nonferrous Met. SOC. China 19 (2009) 883-886.

[Sandlöbesa 2011] S. Sandlöbesa, S. Zaefferera, , , I. Schestakowa, S. Yib, R. Gonzalez-MartinezbVolume , "On the role of non-basal deformation mechanisms for the ductility of Mg and Mg–Y alloys," Acta Mater, 59, Issue 2, January 2011, Pages 429–439

[Sato 2008] T. Sato, M.V. Kral, "Microstructural evolution of Mg–Al–Ca–Sr alloy during creep,"Materials Science and Engineering A 498 (2008) 369–376

[Shahzad 2009] M. Shahzad, L.Wagner, "Influence of extrusion parameters on microstructure and texture developments, and their effects on mechanical properties of the magnesium alloy AZ80", Materials Science and Engineering A 506 (2009) 141–147.

[Shanga 2010] L. Shanga, I.H. Junga, S. Yue, R. Verma, E. Essadiqi, "An investigation of formation of second phases in micro alloyed, AZ31 Mg alloys with Ca, Sr and Ce," Journal of Alloys and Compounds 492 (2010) 173–183

[Shao-kang 2007] G. Shao-kang, Z. Shi-jie, W.Li-guo, Y. Qing, C. Wen-bo, "Microstructures and mechanical properties of double hot-extruded AZ80+xSr wrought alloys", Trans. Nonferrous Met. SOC. China 17(2007) 1143-1151.

[Stalman 2001] A. Stalman, W. Sebastian, H. Fredrich, S. Shuman, K. Droder, "Properties and processing of magnesium wrought products for automotive applications", Advanced Engineering Materials, 3, No. 12 (2001), 969-974.

[Stanford 2008] N. Stanford, M.R. Barnett, "The origin of "rare earth" texture development in extruded Mg-based alloys and its effect on tensile ductility," Materials Science and Engineering A, Volume 496, Issues 1-2 (2008) 399-408.

[Stanford 2010] N. Stanford, "Micro-alloying Mg with Y, Ce, Gd and La for texture modification—A comparative study," Materials Science and Engineering A, Vol 527, Issues 10-11 (2010) 2669-2677.

[Staroselsky 2003] A. Staroselsky, L.Anand,"A constitutive model for hcp materials deforming by slip and twinning: application to alloy AZ31B" international Journal of plasticity, 19, 10 (2003) p1843.

[Takuda 1992] Hirohiko Takuda, Shiomi Kikuchi and Natsuo Hatta, "Possibility of grain refinement for superplasticity of a Mg-AI-Zn alloy by pre-deformation,"Journal of Materials Science, Volume 27, Number 4, 937-940

[Th 1993] J.Th.M de Hosson, B.P Pestman, Interactions between lattice dislocations and grain boundaries in L12 ordered compounds investigated by in situ transmission electron microscopy and computer modelling experiments, Materials Science and Engineering: A, Volume 164, Issues 1–2, 30 May 1993, Pages 415-420

[Torbati-Sarraf 2010] S.A. Torbati-Sarraf, R. Mahmudi, "Microstructure and mechanical properties of extruded and ECAPed AZ31 Mg alloy grain refined with Al-Ti-C master alloy," Materials Science and Engineering A 527 (2010) 3515–3520.

[Trojanova 2008] Z.Trojanova, Z. Drozd, P. lukac, A. Chatey, " Mechanical Properties of a Squeeze cast Mg-Al-Sr alloy," Archives of Materials Science and Engineering, Vol 29, Issue 2 (2008) 97-104.

[Urakami 1971] A Urakami, M.E Fine, "Yield drop effects for basal and prismatic slip in Mg-Li alloy single crystals," Acta Metallurgica, Volume 19, Issue 9, September 1971, Pages 887–894

[Wang 2011] Shouren Wang, Ru Ma, Liying Yang,Yong Wang, Yanjun Wang, "Precipitates effect on microstructure of as-deformed and as-annealed AZ41 magnesium alloys by adding Mn and Ca," Journal of Materials Science 46 (2011) 3060–3065.

[Wenlong 2009] Wenlong Xiao, Shusheng Jia, Lidong Wang, Yaoming Wu, Limin Wang, "The microstructures and mechanical properties of cast Mg–Zn–Al–RE alloys," Journal of Alloys and Compounds 480 (2009) L33–L36

[Wright 2007] Stuart I. Wright, Matthew M. Nowell, and John F. Bingert, "A Comparison of Textures Measured Using X-Ray and Electron Backscatter Diffraction," Metallurgical And Materials Transactions A, Volume 38a, August 2007—1845.

[Wu 2011] WU Lu, PAN Fu-sheng, YANG Ming-bo, WU Ju-ying, LIU Ting-ting,"As-cast microstructure and Sr-containing phases of AZ31 magnesium alloys with high Sr contents," Transactions of Nonferrous Metals Society of China, Vol 21, (2011) 784-789.

[Wusatowska 2002] A.M. Wusatowska-Sarnek, H. Miura, T. Sakai, "Nucleation and microtexture development under dynamic recrystallization of copper", Materials Science and Engineering A323 (2002) 177–186.

[Yamashita 2001] Akihiro Yamashita, Zenji Horita, Terence G Langdon, Improving the mechanical properties of magnesium and a magnesium alloy through severe plastic deformation, Materials Science and Engineering: A, Volume 300, Issues 1-2, 28 February 2001, Pages 142-147,

[Yan 2008] Jingli Yan, Yangshan Sun, Feng Xue, Jing Bai, Shan Xue, Weijian Tao, "Creep deformation mechanism of magnesium-based alloys," J Mater Sci (2008) 43:6952–6959.

[Yang 2008] Huajie Yang, Shuming Yin, Chongxiang Huang, Zhefeng Zhang, Shiding Wu, Shuxin Li, and Yandong Li, "EBSD Study on Deformation Twinning in AZ31 Magnesium Alloy During Quasi-in-Situ Compression," Advanced Engineering Materials, 10, No. 10 (2008) 955-960

[Yang 2008] Mingbo Yang, Fusheng Pan, Renju Cheng, Aitao Tang, "Effect of Mg–10Sr master alloy on grain refinement of AZ31 magnesium alloy," Materials Science and Engineering A 491 (2008) 440–445

[Yasi 2012] Joseph A. Yasi, Louis G. Hector Jr., Dallas R. Trinkle, "Prediction of thermal cross-slip stress in magnesium alloys from a geometric interaction model," Acta Materialia, Volume 60, Issue 5, March 2012, Pages 2350-2358

[Zeng 2006] Zeng X., Wang Y., Ding W., Luo A A., Sachdev A.K., "Effect of strontium on the microstructure, mechanical properties, and fracture behaviour of AZ31 magnesium alloy," Metallurgical and Materials Transactions A, Vol 37, No 4, (2006) 1333-1341

[Zhang 2008] C. Zhang, H.B. Cao, G.P. Cao, S. Kou, Y.A. Chan, "The Solidification of Magnesium-Rich Alloys Containing Al, Ca, and Sr," JOM, , vol. 60, 12, (2008) 48–51.

[Zhao 2007] H.L. Zhao, S.K. Guan, F.Y. Zheng Effects of Sr and B addition on microstructure and mechanical properties of AZ91 magnesium alloy J. Mater. Res., Vol. 22, No. 9 (2007) 2423-2428

[Zhou 2010] Zhou Ji-xue, Wang Jie, Wang Jing, Yang Yuan-sheng, "Effects of RE and Sr additions on dendrite growth and phase precipitation in AZ91D magnesium alloy," Trans. Nonferrous Met. SOC. China 20 (2010) s331-s335.

Chapter 3

Precipitation and Solidification

In this Chapter, studies on the precipitation and solidification of AZ31 containing different levels of Sr are presented. The chapter is comprised of two sections; the first section (3.1 *Precipitation during the Solidification of Mg-3wt%Al-1wt%Zn-(0.001-1%) Sr Alloys*) details experiments determining the relationship between cooling rate and the microstructure of AZ31+Sr alloys. Microstructural investigations and thermal (cooling-curve) analyses were carried out to study the precipitation occurring in AZ31 magnesium alloy containing up to 1wt% strontium. Results indicated that small amounts of Sr refine the β-$Mg_{17}Al_{12}$ globular phase and increase its thermal stability during annealing. With higher concentrations of Sr, the amount of β phase decreases and the weight percent of Sr-rich (Al-Mg-Sr) interdendritic precipitates increases. The precipitation temperatures of the different phases as determined by thermal analysis are in close agreement with Scheil cooling results calculated *in silico* using FactSage.

In section 3.2 (*Microstructural Investigation and Thermodynamic Calculations on the Precipitation of Mg-Al-Zn-Sr Alloys*), microstructural characterisation and thermodynamic simulations of AZ31 Mg alloy containing up to 1 wt% Sr suring solidification are presented. Increasing the Sr content from 0.01 to 1wt% led to the formation of an Al-Sr line compound (Al_4Sr) and to the suppression of Al-Mg precipitate (β-$Mg_{17}Al_{12}$). TEM investigation and EDS analysis on extracted precipitates revealed Mg and Zn solubility in the Al_4Sr particles. It is shown that the Sr content also effects the precipitation of Al-Mn precipitates. Thermodynamic calculations predicted that the increase in Sr limits the Al-Mn reaction and the precipitation of Al-Mn precipitates with low Al/Mn ratio. Microstructural investigations determined the presence of two Al-Mn precipitates (Al_8Mn_5 and AlMn) which were formed either in the form of large dendritic plates or small nano-scale particles in the Mg matrix. It was calculated

by the thermodynamic model and confirmed by TEM that by increasing the Sr content, Al solid solubility decreases while the level of Mn slightly increases.

3.1. Precipitation during the Solidification of Mg-3wt%Al-1wt%Zn-(0.001-1%) Sr Alloys

A. Sadeghi, M.O. Pekguleryuz

Published in AFS 2010 Conference Proceeding, Orlando March 2010.

3.1.1. Introduction

Magnesium alloys with their low density, (~1/3 of the density of steel and 2/3 of the density of aluminum) provide an attractive alternative for significant weight reduction in automobiles. Automotive applications of Mg alloys started growing substantially in the early 1990s with the widespread introduction of diecast steering wheel and instrument panel components. Over the past few years, numerous attempts have been made to design new magnesium alloys with adequate high-temperature performance by adding alloying elements such as rare earth (RE) and alkaline earth (Ca, Sr) to be used in critical engine parts [1]. However for these types of applications requiring high performance and low cost, Mg alloys are not currently economical for high volume production.

The Mg-Al-Sr system was developed in an attempt to replace RE additions to Mg with an alkali-earth element [2]. Sr has been used as an effective alloying element for grain refinement as it precipitates in the form of intermetallic phases with high thermal stability [3]. It has also been proven that Sr refines the grain [4,5] and beta precipitates [6] which is also important for foundry alloys. It is known that Sr is surface active and is likely to slow down dendrite growth by segregating to the surface of Mg grains. By developing a finer structure, Sr improves the yield strength of AZ31 [7]. Additionally, Sr binds with the Al in Mg alloys and forms high-melting point stoichiometric intermetallics that have high thermal stability (formation temperature >490^{o}C (914^{o}F)). Because of its higher electronegativity difference with Al (0.69 compared to 0.30 for Mg and Al), Sr forms Al-Sr intermetallics and likely reduces Al solid solubility in the α-Mg matrix [8].

The objective of this work was to study the formation conditions of different intermetallics and their dependence on the concentration of Sr as an

alloying element in AZ31. To that end, experimental data were compared with thermodynamic calculations of the Mg-Al-Zn-Sr quaternary system using FactSage thermodynamic computation software. The temperature-composition relationships of the AZ31-Sr system in wide temperature and composition ranges were estimated and the modeling predictions are presented. Finally, calculations were compared with experimental results.

3.1.2. Experimental Procedure

AZ31 alloys with different levels of Sr concentration were prepared using AZ31B extruded bars and Sr-10wt%Al master alloy were melted in a graphite crucible using a high-frequency induction furnace. The melt was kept at 700^{o}C (1292^{o}F) for 15 minutes to allow dissolving and homogenizing and then cast at 720^{o}C (1328^{o}F) under an SF_6-CO_2 gas mixture into sand cups fitted with K-type exposed junction thermocouples in the cup center, connected to a data logger (Fig.3.1.1). The response time of the thermocouples was less than 0.5 second and the melt cooling rate was 0.3^{o}C/Sec (0.54^{o}F/Sec). In addition, the cast samples were annealed at different temperatures in a Blue-M convection heat-treatment oven. The chemical compositions of the alloys used in this study (Table.3.1.1) have been determined by inductively coupled plasma (ICP).

Figure.3.1.1. (a) a sand cup with a fixed exposed junction thermocouple, (b) an installed sand cup ready for casting, and (c) the cast sample after solidification.

Table 3.1.1. Chemical Compositions of the Alloys

		1	2	3	4	5	6	7	8	9	10	11
	element	AZ31	AZ31+0.01Sr	AZ31+0.035Sr	AZ31+0.05Sr	AZ31+0.075Sr	AZ31+0. 1Sr	AZ31+0.35Sr	AZ31+0.5Sr	AZ31+1.75Sr	AZ31+1 Sr	AZ31+1.5 Sr*
Chemical comp. (*wt%*)	Al	2.57	2.64	2.58	2.47	2.66	2.62	2.60	2.62	2.69	2.64	3
	Zn	0.66	0.61	0.60	0.63	0.67	0.65	0.69	0.61	0.64	0.68	1
	Mn	0.35	0.34	0.28	0.41	0.33	0.29	0.36	0.29	0.36	0.3	0.3
	Sr	0	0.009	0.029	0.037	0.064	0.08	0.31	0.43	0.71	0.91	1.5

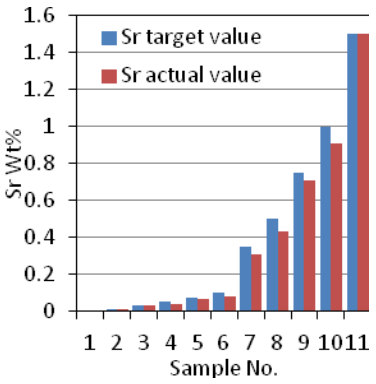

* target composition

The specimens for microstructural investigation via optical microscopy (OM) and field-emission gun / scanning-electron microscopy (FEG/SEM) were etched in a picric-acetic solution. Energy dispersive spectroscopy (EDS) was used to identify the phase compositions. Microstructural observations were made to experimentally verify the quaternary (Mg-Al-Zn-Sr) phase diagram calculated using thermodynamic modelling software (FactStage).

3.1.3. Results and Discussion

3.1.3.1. Microstructural Investigation

As-cast microstructures of AZ31, and AZ31+Sr alloys are shown in Fig. 3.1.2. The structure of the Sr containing AZ31 alloys was mainly comprised of primary α-Mg dendrites or cells and two or more secondary phases, either in the grain boundaries or interdendritic regions, which were qualitatively identified using SEM and EDS. Further quantitative phase identification will be conducted using EPMA and TEM. The β-$Mg_{17}Al_{12}$ precipitate can be distinguished by its globular morphology, see Fig.3.1.2 a-d. Note that small amounts of Sr (0.01-0.5%) seemed to refine the grain size (from 174μm for AZ31 to 115μm for AZ31+0.5%Sr) and the β- $Mg_{17}Al_{12}$ particles. The needle-shaped dark precipitates

are AlMn and Al_8Mn_5 phases. In alloys with higher amounts of Sr, an interdendritic/grain-boundary phase of a different morphology was observed (Fig.3.1.2e-f). The phase likely to precipitate in these higher-Sr alloys is the Al_4Sr intermetallic which is known to be a stable precipitate in Mg-Al-Sr alloys due to its stoichiometry (line compound) in the binary Al-Sr system. However, it is also known to dissolve other elements in higher order (quaternary or higher) systems and assume more a complex stoichiometry [6.1.12], perhaps losing its thermal stability. A recent study reported that in a Mg-Al-Sr alloy the chemical composition of the complex phase (Mg_9Al_3Sr) changed by moving toward an equilibrium condition. During annealing, the Al/Sr ratio increased in the Mg-Al-Sr ternary phase while the Mg content in solid solution decreased. Consequently, the ternary intermetallic decomposed to α-Mg and Al_4Sr [12]. SEM/EDS analyses of the AZ31 containing 0.05% Sr are shown in Fig.3.1.3.

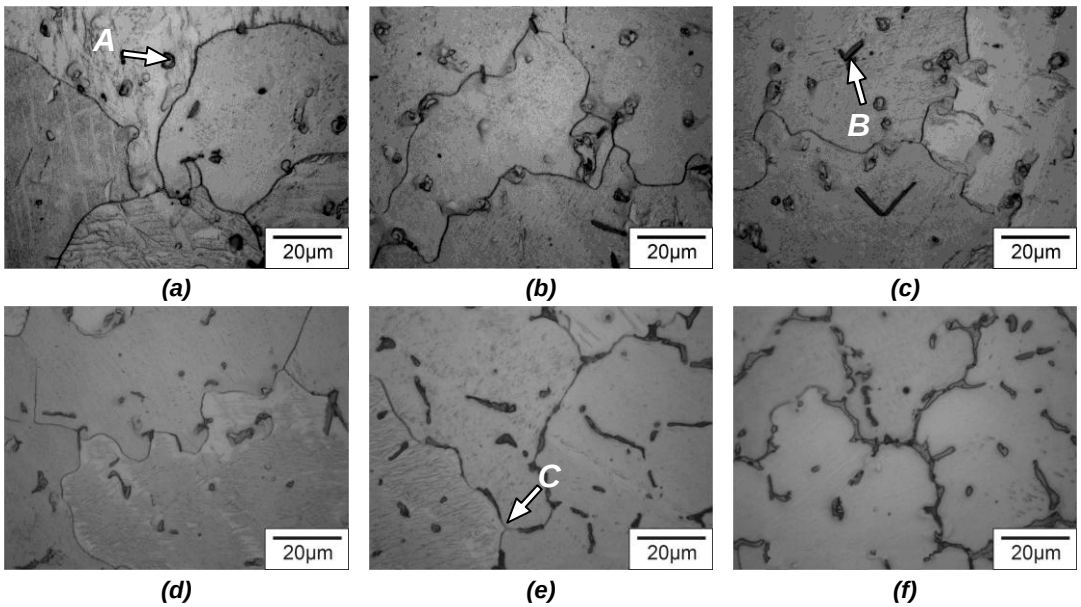

Figure.3.1.2. Typical as-cast microstructures of (a) AZ31, (b) AZ31+0.01%Sr, (c) AZ31+0.1%Sr, (d) AZ31+0.5%Sr, (e) AZ31+1%Sr, (f) AZ31+1.5%Sr, white arrows point (A) $Mg_{17}Al_{12}$, (B) Al-Mn and (C) Al-Mg-Sr precipitates.

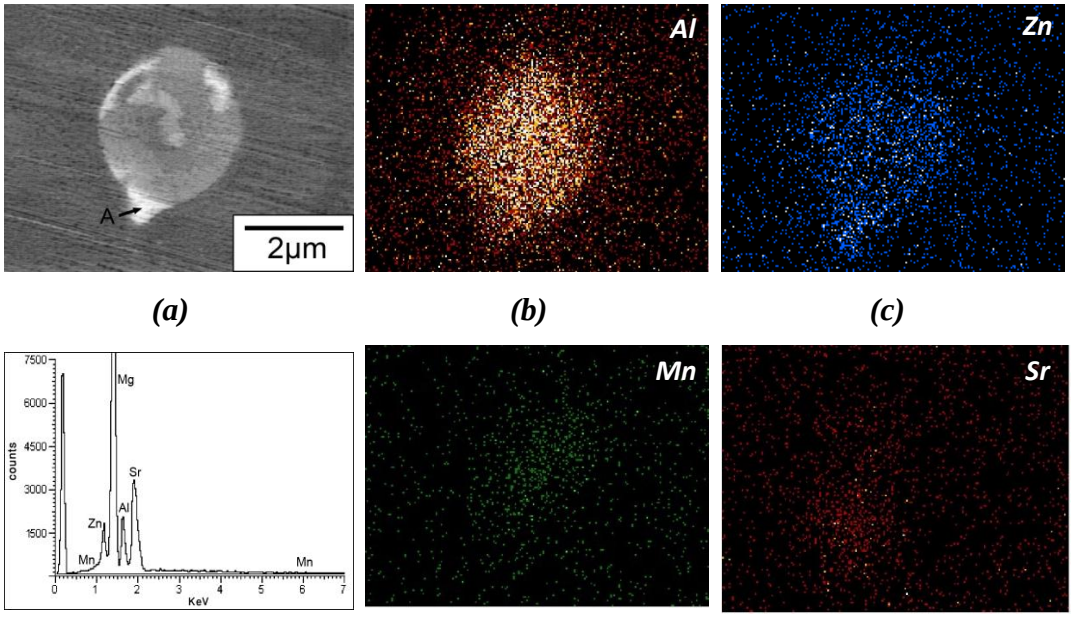

Figure.3.1.3. SEM/EDS analysis of the β-phase in AZ31+0.05%Sr. (a) SEM micrograph and the related X-ray dot maps of (b) Al, (c) Zn, (d)EDS for point A (e) X-Ray dot map of Mn and (f) Sr.

The EDS spectrum and elemental mapping revealed the presence of Sr inside the globular precipitates, previously introduced as the β-phase. Additionally, the results also indicated that the needle-shape Al-Mn precipitates also dissolve small amounts of Sr. It is worth mentioning that the dissolution of Sr inside β particles has also been reported by other researchers [10].

3.1.3.2. Cooling Curves

Temperature-Time (cooling) curves were plotted in order to detect thermal peaks corresponding to precipitate formation during casting in a non-equilibrium condition (Fig 3.1.4). A typical full cooling cure is shown in Fig.3.1.4a and a part of the derivative curves showing the thermal arrest peaks is shown in Fig.3.1.4b. The temperature of formation of each phase is evident in the curves by a peak or a sudden change in the slope.

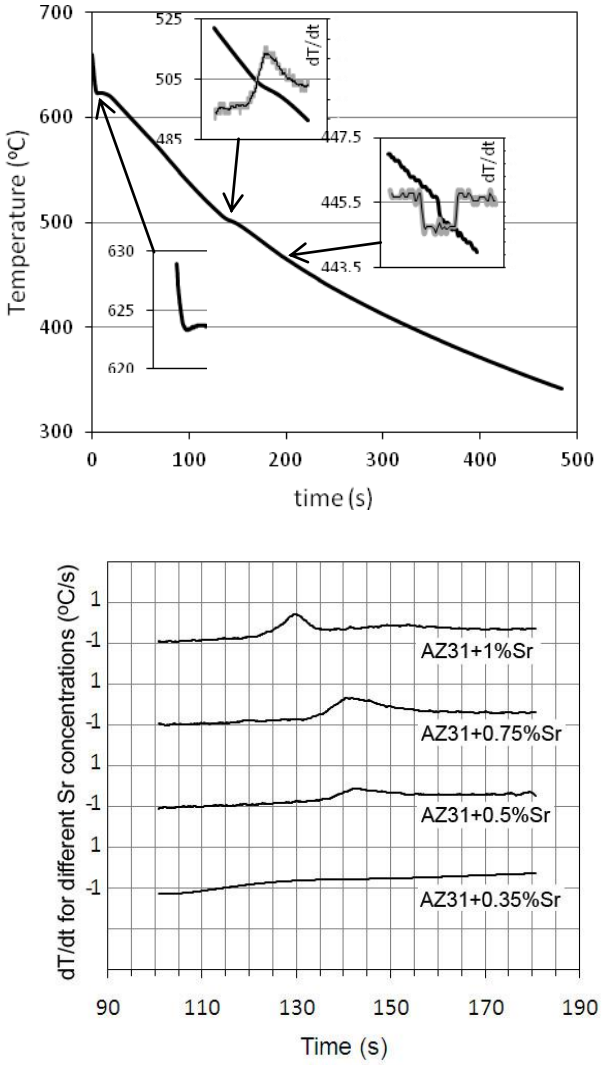

Figure.3.1.4. (a) A typical cooling curve presenting the Temperature-Time curve of solidification. (b) The first derivative of the cooling curves showing the evolution of the thermal arrests (precipitate) by increasing the Sr content in AZ31 alloy.

3.1.3.3. Comparison of Experimental Data with Thermodynamic Calculations

Thermodynamic calculations were conducted using the FTlite database of the computation software. An alloy consisting of Mg, Al, Zn, Sr and their possible intermetallic compounds were introduced into the system

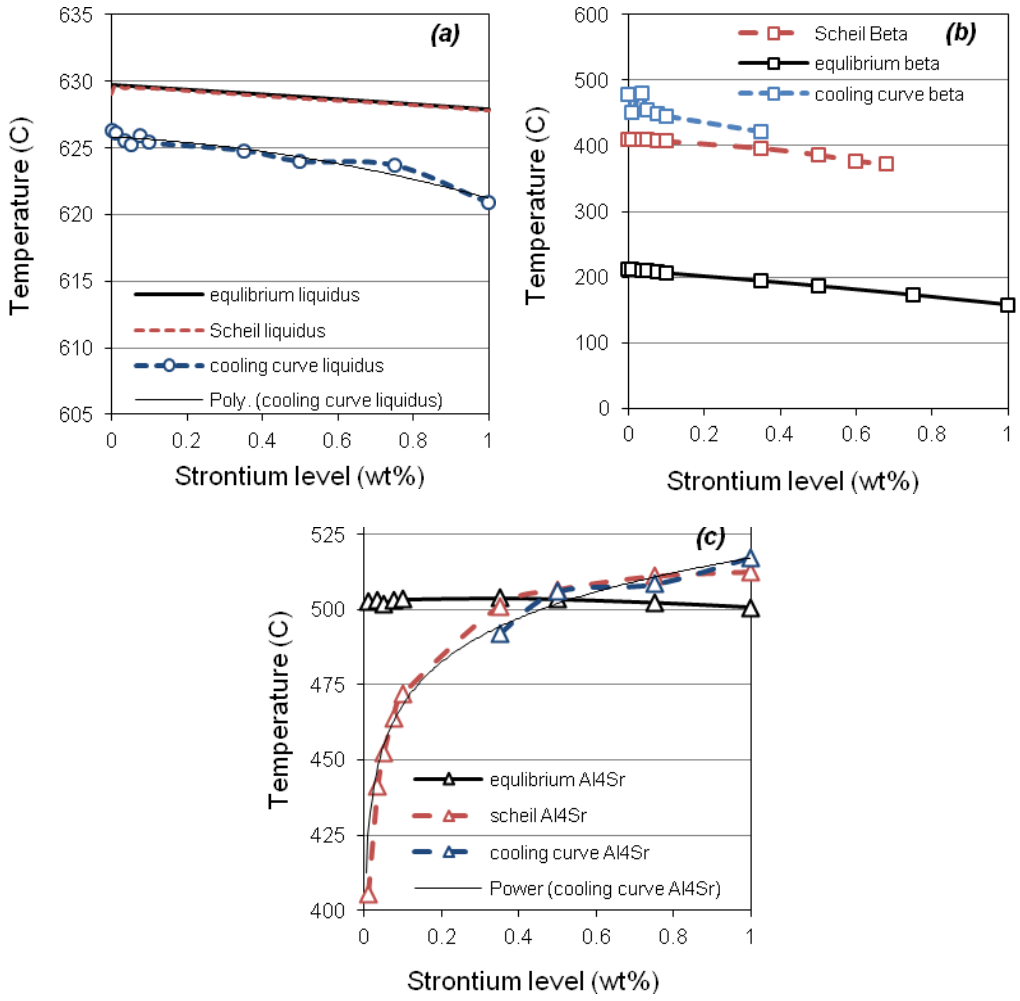

Figure.3.1.5. Comparing the measured results (blue lines) with calculated Scheil (red lines and equilibrium (black lines) for (a) liquidus temperatures, (b) $Mg_{17}Al_{12}$ beta formation, and (c) Al_4Sr formation.

Equilibrium and Scheil cooling conditions (limited back diffusion in the solid) were applied to the system and precipitation temperatures were calculated for different levels of Sr. The calculated results were compared with the measured temperatures obtained from the cooling curves (Fig.3.1.5a-c). Fig.3.1.5a compares the calculated and measured liquidus temperatures for different alloys. The trend of the calculated results is in good agreement with the experimental data however a slight overestimation of ~5^{o}C (9^{o}F) from the measured results was made. The thermocouple errors are only ±1^{o}C (1.8^{o}F), it is believed the remaining difference is due to the Mn and other solutes that are present in the alloys which

results in more complex systems than which was modelled in the computer simulations. All curves showed a decrease in melting point with increasing weight percent of Sr. For β precipitation, the Scheil cooling condition gave a better agreement with experimental measurements (Fig.3.1.5b).

By increasing Sr to 0.35wt%, to a level higher than trace amounts, a new alloy with new phases is formed, and therefore the alloy can no longer be considered AZ31+Sr. The Mg-Al-Sr-Zn alloys with Sr levels higher than 0.5wt% contain Al-Sr (Al_4Sr) and Al-Mg-Sr intermetallics in addition to the β-phase. The affinity of Sr to Al is so strong that it can suppress the formation of the β phase at a specific concentration of Sr. In the cast specimens with more than 0.35%Sr, β was not observed. However, the Scheil-solidification calculation predicts 0.68%Sr as the maximum level that still allows β-$Mg_{17}Al_{12}$ to precipitate. The plot in Fig.3.1.5c shows close agreement between the precipitation temperatures observed in the cooling curves and the calculated Scheil cooling results for Al_4Sr, while the calculations with the equilibrium-solidification conditions deviate from the experimental values.

The amount (wt%) of different phases was also calculated as a function of Sr content using the same thermodynamic model (Fig.3.1.6). It can be seen that the amount of β phase decreases and Al_4Sr increases with increasing Sr. In other words, the formation energy of the Al-Sr phase becomes more negative than β-$Mg_{17}Al_{12}$ and it becomes more stable. Calculations of equilibrium conditions show that the amount of Al_4Sr becomes greater than the amount of β-phase above 1.4% Sr. For high levels of Sr, for example above 2.5%Sr, an intermetallic richer in Sr (Al_2Sr) and an intermetallic compound with zinc ($SrZn_5$) are predicted to form. However, thermodynamic equilibria cannot fully estimate the metastable phases that may form under casting conditions. Furthermore, the computation software's database does not contain all the possible equilibrium phases due to limitations in the amount of experimental data in the literature.

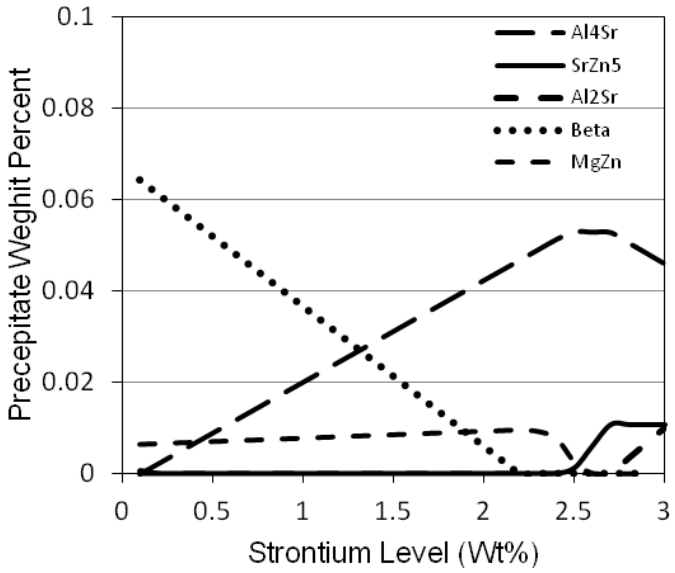

Figure.3.1.6. Calculated amount (weight percent) of different phases precipitating in the Mg-AZ31 system versus Sr concentration.

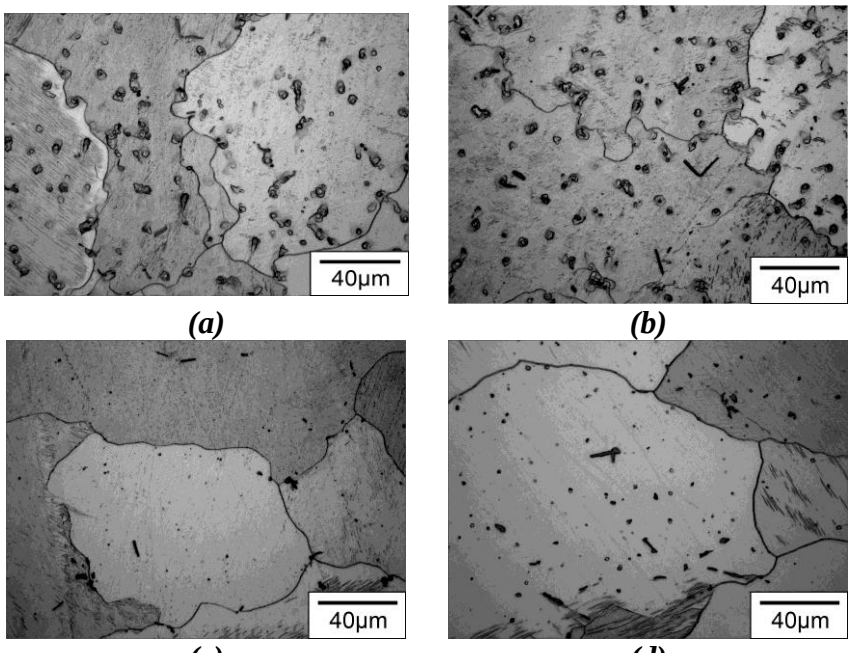

(a) ***(b)*** ***(c)*** ***(d)***

Figure.3.1.7. Microstructures of (a) as-cast AZ31, (b) annealed AZ31 at 400^{o}C-2h, (c) as-cast AZ31+0.1%Sr, (d) annealed AZ31+0.1%Sr at 400^{o}C-2h.

In order to eliminate microsegregation and possible non-equilibrium phases, the samples were homogenized at 400^{o}C and 450^{o}C for two hours and the microstructures were observed by OM. It was observed that at 400^{o}C the globular β-$Mg_{17}Al_{12}$ completely dissolved in the AZ31 matrix. In contrast, adding 0.1% Sr prevented the β phase to completely dissolve under the same annealing conditions (Fig.3.1.7). These precipitates can be available to interact with dislocations even during high temperature deformation. The temperature range between solutionizing of the Al-Sr precipitates (solvus) and the solidus (partial melting) of the alloy is so small (0-25^{o}C for AZ31 to AZ31+1%Sr respectively) that it is almost impossible to prepare a fully homogenized microstructure by soaking. The Sr intermetallics did not dissolve through annealing at 450^{o}C. In specimens with high Sr content (<1wt%), the (Al-Sr-Mg) grainboundary precipitates remained unaltered after annealing, therefore demonstrating a high thermal stability.

3.1.4. Conclusion

Thermodynamic calculations were carried out in order to assess the effect of Sr addition on phase formation in AZ31+Sr alloys. Results were verified by cooling curve analysis using sand cup tests. Small amounts of Sr (0.01-0.035%Sr) led to grain refinement as well as secondary phase refinement while higher amounts of Sr (0.05-1%Sr) formed Al-Sr (Mg) precipitates. Calculations predicted that no β-phase would remain in the structure at 0.68wt%Sr. Non-equilibrium solidification seemed to lower this limit to 0.35wt%Sr.

3.1.5. References

1. Luo A., Pekguleryuz M.O., “Cast Magnesium Alloys for Elevated Temperature Applications,” *Journal of Materials Science*, Vol 29, No 20, (1994)
2. Baril E., Labelle P., Pekguleryuz M.O., “Elevated Temperature Mg-Al-Sr: Creep Resistance, Mechanical Properties & Microstructure,” *Journal of Metals (JOM-US)*, TMS, Vol 55, No 11, (2003)

3. Pekguleryuz M.O., Kaya A.A., "Creep Resistant Mg-Based Casting Alloy for Powertrain Applications," *Advanced Engineering Materials*, DGM, Vol 5, No 12, (2003)
4. J.E. Gruzleski and A. Aliravci, "Low Porosity, Fine-Grain Sized Strontium Treated Magnesium Alloy Castings," US Patent US005143564A, (1992)
5. Liu S.F., Li B., Wang X.H., Su W., Han H., "Refinement Effect of Cerium, Calcium and Strontium in AZ91 Magnesium Alloy," *Journal of Materials Processing Technology,* Vol 209, Issue 8, (2009)
6. L. Koubichek, "Effect of Small Additions of Elements on Grain Size and the Refinement of the Mg4Al3 [Mg17Al12] Phase in ML5 Alloy," Izv. Vyschikh. Outchebnykh Za Vedeny, Metallurgy of Non-Ferrous Metals, No 6, (1959)
7. Zeng X., Wang Y., Ding W., Luo A A., Sachdev A.K., "Effect of strontium on the microstructure, mechanical properties, and fracture behaviour of AZ31 magnesium alloy," *Metallurgical and Materials Transactions A*, Vol 37, No 4, (2006)
8. Darguscha M.S., Zhub S.M., Nieb J.F., Dunlop G.L., "Microstructural analysis of the improved creep resistance of a die-cast magnesium–aluminium–rare earth alloy by strontium additions," *Scripta Materialia*, Vol 60, Issue 2, (2009)
9. M.O. Pekguleryuz, J.E. Gruzleski, "The Dissolution of Non-Reactive Strontium Containing Master Alloys in Liquid Al and A356 Melts," *Canadian Metallurgical Quaternary*, Vol 27, (1989)
10. Zhao P., Wang Q., Zhai C., Zhu Y., "Effects of strontium and titanium on the microstructure, tensile properties and creep behaviour of AM50 alloys," *Materials Science and Engineering A*, Vol 444, Issues 1-2, (2007)
11. Jing B., Yangshan S., Shan X., Feng X., Tianbai Z., "Microstructure and Tensile Creep Behaviour of Mg–4Al Based Magnesium Alloys with Alkaline-Earth Elements Sr and Ca Additions," *Materials Science and Engineering A*, Vol 419, Issues 1-2, (2006)

12. L'Espérance G., Plamondon P., Kunst M., Fischersworring-Bunk A., "Characterization of intermetallics in Mg–Al–Sr AJ62 alloys," *Intermetallics*, Vol 18, Issue 1, (2010).

3.2. Microstructural Investigation and Thermodynamic Calculations on the Precipitation of Mg-Al-Zn-Sr Alloys

Alireza Sadeghi and Mihriban Pekguleryuz

Journal of Materials Research, Volume 26, Number 7, 14 April 2011, Pages 896-903

3.2.1. Introduction

The addition of Sr to Mg-Al alloys was first used to refine the grains and to modify β-$Mg_{17}Al_{12}$ precipitates in casting alloys [1-4]. In 2002-4, the Mg-Al-Sr (AJ) series of alloys were developed by the addition of higher levels of Sr to Mg-Al alloys; these Mg-Al-Sr alloys had an excellent combination of creep performance and castability [4-9] and have been used in BMW engine blocks since 2004. It has been proposed that the observed high creep resistance is related to the absence of the low melting point β-$Mg_{17}Al_{12}$ and to the minimization of Al supersaturation in primary magnesium [8]. These changes are a result of the high affinity of Sr to Al and to the precipitation of thermally stable Al-Sr phases. In the AJ series, depending on the Al/Sr ratio, various alloy compositions with different combinations of precipitates have been developed, which resulted in differing creep resistance, strength and casting properties [5-9].

The effect of Sr has not been limited to casting alloys and there have been investigations on the effects of Sr on the precipitation in commercial wrought alloys [10-13] and on the related effects on hot deformation processes [14, 15]. It has been reported that low levels of Sr reduce the grain size and refine the precipitates [3]. A higher level of Sr forms thermally stable precipitates which increase the strength and improve the creep behaviour [11-15]. In most of the Mg-Al commercial alloys, Mn is also added to increase corrosion resistance [13]. Although, Al reduces the solid solubility of Mn (down to 0.3wt%), it is still present in the solid solution and excess Mn forms Al-Mn precipitates within the microstructure. Increasing the level of Sr may also affect the formation of Mn precipitates.

In the present work, the effect of Sr on precipitation during the solidification of the AZ31 alloy (Mg-3Al-1Zn-0.4Mn), containing 0.01-1% Sr was investigated. Microstructural examinations and thermodynamic modeling (FactSage software) were used for this study to predict and verify the phase selection.

3.2.2. Experimental Procedure

AZ31 extruded bars provided by Applied Magnesium (Denver, CO) were cut into small pieces and melted using a high frequency induction furnace (NORAX). The addition of Sr to AZ31 was carried out using a Sr-10wt%Al master alloy (supplied by Timminco, Haley, ON). The alloy and the additive were melted in a graphite crucible and held at 700^{o}C for 15 minutes to allow complete dissolution. SF_6-CO_2 gas mixture was used to prevent oxidation. The molten alloy was cast into cylindrical preheated steel dies at 720^{o}C (Fig.3.2.1). The chemical compositions of the cast samples were determined by inductively coupled plasma (ICP) from the middle part of the cylinders and are summarized in Table 3.1.1. Alloy compositions are given in wt% unless otherwise indicated.

To investigate the effect of temperature on precipitates, some of the samples were heated from 100^{o}C to 400^{o}C for 2h in a Blue M Lindberg inert-gas mechanical convection-oven and subsequently air cooled. Samples for microstructural observations and analysis were sectioned from cast cylinders and after grinding, polishing was performed using 1 μm diamond paste. Picric-acetic solution was used to etch and reveal the microstructure of the specimens. Field-emission gun / scanning electron microscopy (FEG-SEM, Hitachi S-4700) was used to observe the precipitates and energy dispersive spectroscopy (EDS) was used to measure the elemental composition of the phases. Nano-size precipitates in the microstructures were observed using transmission electron microscopy (TEM, Philips CM200) operating at 200kv. Thin foil specimens were prepared from as-cast samples by grinding and further thinned by jet polishing using a solution of 5% perchloric acid, 35% butanol and 60% ethanol.

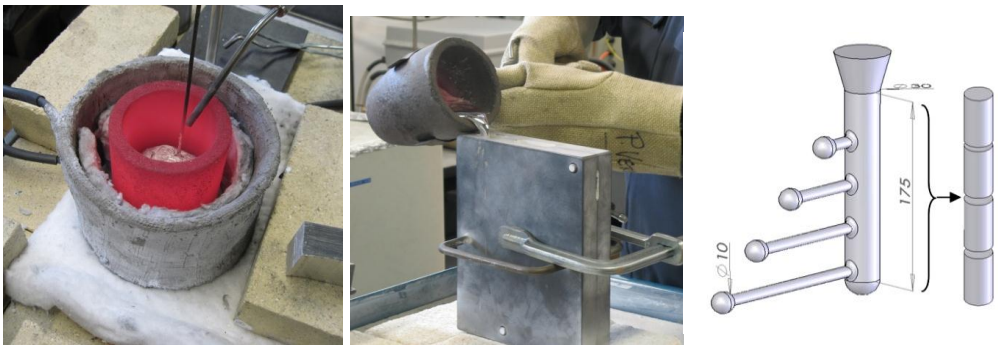

Figure.3.2.1. (a) AZ31-Sr alloy melting in a graphite crucible, (b) casting in a preheated steel die (c) schematic view of the casting part and the machined billets (dimensions are in millimeters).

For more precise analysis of the Al-Sr and Al-Mn precipitate morphology and composition and to eliminate the effect of the Mg matrix on EDS results, intermetallics were extracted by dissolving the surrounding Mg matrix using a solution of 15ml acetic acid and 150ml water. The remaining precipitates were flushed with water and ethanol several times and finally collected using a vacuum filtering device. The extracted particles were analyzed using x-ray diffraction (XRD), SEM and EDS.

3.2.3. Thermodynamic Calculations

A pseudo-binary section for the AZ31 alloy with up to 3% Sr (Fig.3.2.2) was calculated using FactSage software and the FTLite database. The alloy compositions used for this calculation were the same as those given in Fig.3.2.2, (except the level of Mn which changes in different calculations). The ratios of Mg:Al:Zn:Mn were kept constant while the Sr-content was varied. According to the binary Al-Sr phase diagram, depending on the amount of Sr, two different stable Al-Sr intermetallics (Al_2Sr & Al_4Sr) are likely to form during solidification. In an Mg-Al-Sr system the affinity of Sr to Al is so strong that it can suppress the formation of the β ($Mg_{17}Al_{12}$) phase at a specific concentration of Sr [13]. Both the Mg-Al and Al-Sr precipitates have large solidification ranges which make it possible to dissolve other elements and form different complex stochiometries [16-17].

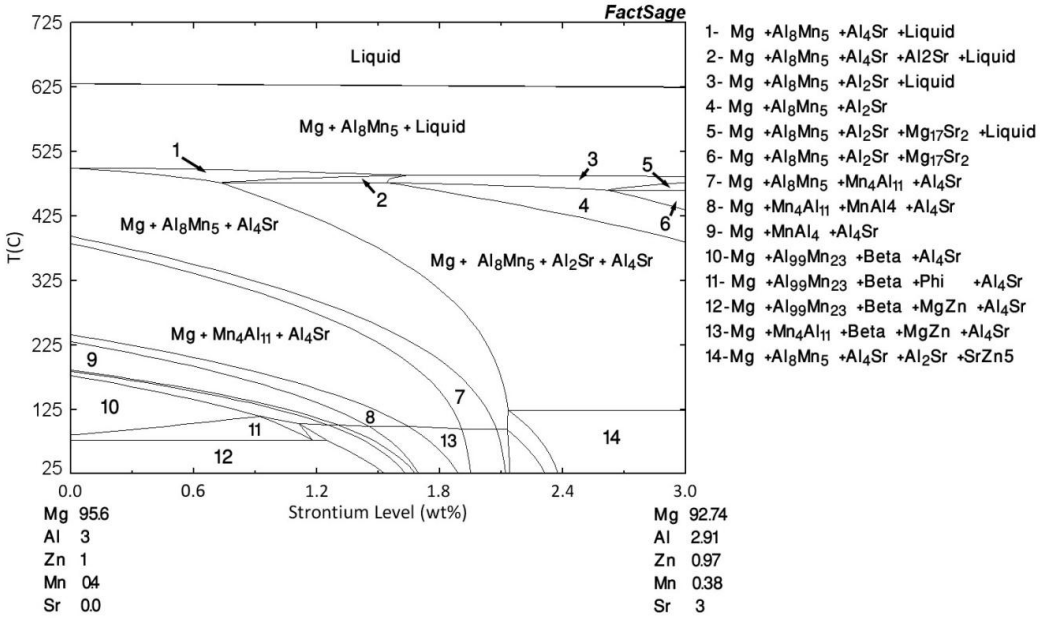

Figure. 3.2.2. Mg-Al-Zn-Mn-Sr phase diagram.

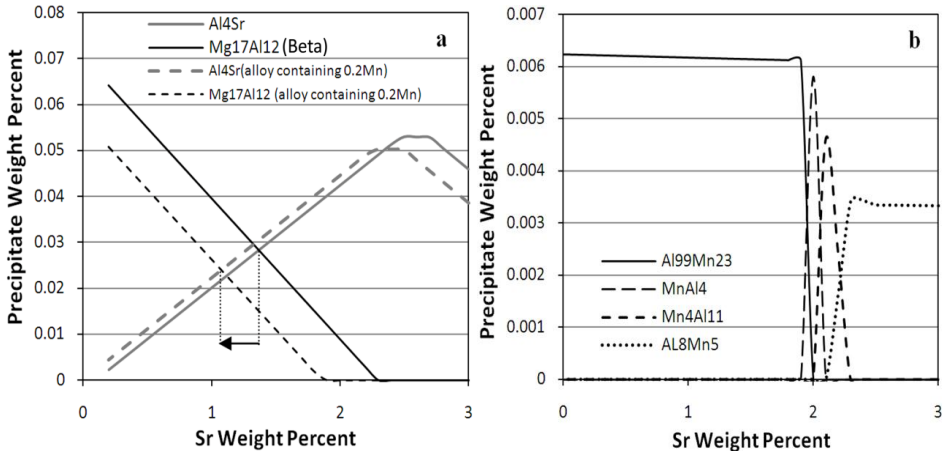

Figure. 3.2.3. Effect of increasing the level of Sr on the phase amounts (in wt%) of (a) Al_4Sr and $Mg_{17}Al_{12}$ and (b)Al-Mn precipitates calculated at 25^{o}C and equilibrium conditions.

As can be seen in the phase diagram (Fig. 6.2.2), thermodynamic modeling shows that the precipitation of Al-Mn particles is also correlated to the level of Sr.

Calculations predicted the decrease in β-$Mg_{17}Al_{12}$ and the increase in Al_4Sr with increasing Sr, which is also effected by the Mn content of the alloy (Fig.3.2.3a).

Since Mn forms intermetallics with Al, the increase in Mn leads to the suppression of the β phase at lower concentrations of Sr (the intercept shifts to the left). With increasing Sr, more Al is bound into Al-Sr precipitates and the formation Al-Mn precipitates with high Al/Mn ratio ($Al_{99}Mn_{23}$, $MnAl_4$ and Mn_4Al_{11}) is suppressed in sequence.

Fig.3.2.3b shows the precipitation sequence of Al-Mn phases with increasing Sr, predicted by thermodynamic calculations. Nonetheless, the Al_8Mn_5 precipitate with the lowest Mn/Al ratio stays in equilibrium with the Al-Sr phases even at high levels of Sr. On the other hand, it is known that thermodynamic equilibrium conditions do not hold during casting [10], therefore, a kinetic model of fast solidification under Scheil cooling condition has been used to calculate the amount of precipitation in a non-equilibrium condition. Scheil cooling assumes a local equilibrium of the advancing solidification front at the solid-liquid interface. In this approach, there is limited solute back-diffusion into the solid and the solute is rejected into the liquid. Complete mixing of solute in the liquid as a result of convection and/or stirring is also assumed.

The relative amounts of the phases calculated under fast solidification conditions in the Scheil mode are presented in Fig.3.2.4. As shown by thermodynamic calculations, out of the four equilibrium Al-Mn precipitates, only the Al_8Mn_5 phase is expected to precipitate at all levels of Sr. The addition of 0.05wt% Sr (Fig.3.2.4a) led to the formation of Al_4Sr, but the precipitation of the β ($Mg_{17}Al_{12}$) and φ ($Mg_6(AlZn)_5$) was not suppressed. At 0.4wt% Sr (Fig.3.2.4b), the β precipitate ceased to form and instead of φ, the MgZn phase precipitated. Finally, at 0.8%Sr, no Mg-containing precipitates existed (Fig.3.2.4c). Although thermodynamic simulation predicted the precipitation of two different Al-Sr precipitates (Al_4Sr and Al_2Sr), the microstructures and cooling curve analysis of the alloys showed only one precipitate during solidification [13].

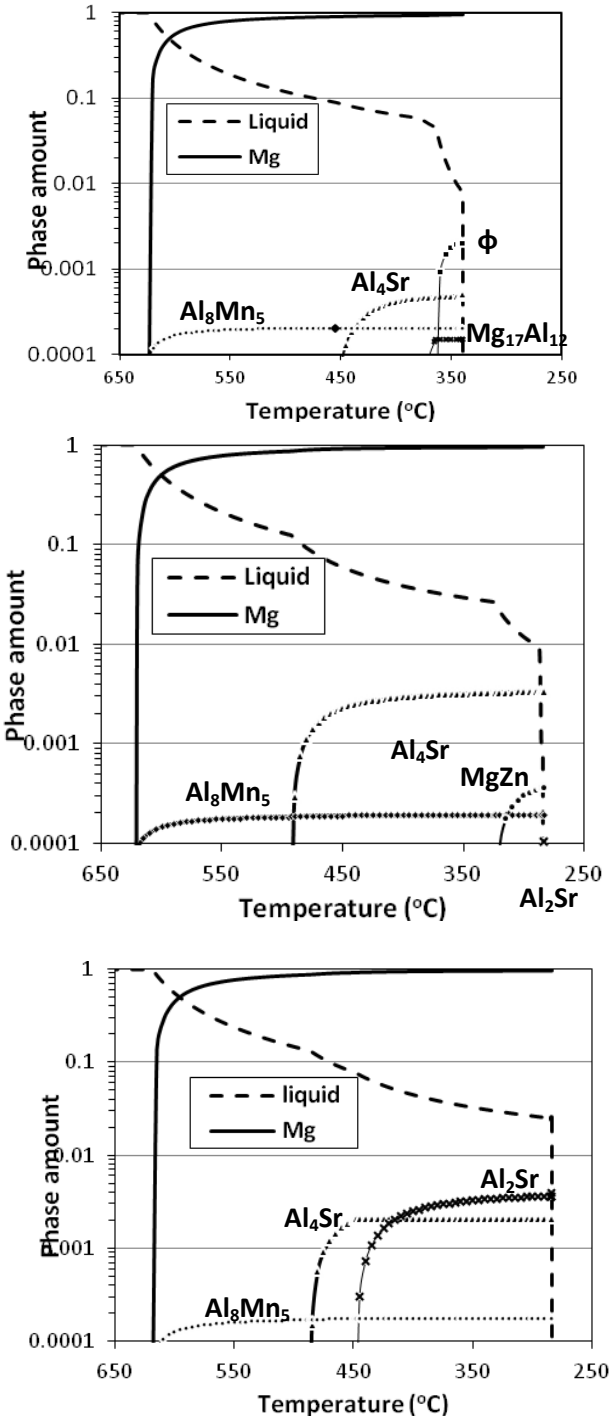

Figure.3.2.4. Phase amounts (atomic fractions) of each phase under Scheil solidification condition vs. temperature: (a) AZ31+0.05%Sr (Mg-2.99Al-0.99Zn-0.39Mn-0.05Sr), (b) AZ31+ 0.4%Sr (Mg-2.98Al-0.99Zn-0.39Mn-0.40Sr), (c) AZ31+0.8%Sr (Mg-2.97Al-0.99Zn-0.36Mn-0.80Sr).

This is attributed to the capture of Sr atoms during solidification in the primary α-Mg dendrite interfaces and the possibility of its back diffusion into the solid which are not considered in equilibrium or even Scheil conditions. Therefore, the concentration of Sr in the liquid phase during solidification is less in reality compared to calculations. As a result, the precipitate with the higher Sr/Al ratio (Al_2Sr) is not likely to form during solidification, or if does its amount and size are not sufficient for microstructural observation.

3.2.4. Results and Discussion

The β-$Mg_{17}Al_{12}$ (determined via SEM/EDS) precipitate can be distinguished by its globular morphology in Fig.3.1.2 a-d (A in Fig.3.1.2a). Note that small amounts of Sr (0.01-0.5%) seemed to refine the β-$Mg_{17}Al_{12}$ particles and the grain size (from 174μm for AZ31 to 115μm for AZ31+0.5%Sr). Previously we have used EDS mapping to reveal the presence of dissolved Sr inside the β phase [13]. The effect of Sr on the refinement of β precipitates [1] and the grain size of Mg-Al-Zn alloys has been previously reported by other researchers [12, 14, 15, 19] and also in our previous work [13].

In alloys with higher amounts of Sr (Fig. 3.1.2e-f), an interdendritic/grain-boundary phase of a different morphology was observed (C in Fig. 3.1.2e). Al-Sr eutectic precipitates were seen in the grain boundaries but no globular β phase was found inside the grains. A higher amount of Al-Sr precipitates along the grain boundaries and inside the grains was found in samples with the highest level of Sr (AZ31+1.5%Sr). In addition to the Al-Sr particles, Al-Mn phases were also present inside the microstructure. Al_8Mn_5 (with dissolved Si) and AlMn (a metastable precipitate with the lowest Al/Mn ratio) are among the particles which could be distinguished with OM and SEM inside the grains by their needle shape morphology (marked as B in Fig. 3.1.2c).

Fig.3.2.5.a and b show the three-dimensional (3D) morphologies of extracted Al-Mn and Al-Sr precipitates after matrix-dissolution. EDS analysis on

the extracted precipitates and TEM-EDS on thin foils indicated the composition of these precipitates to be more complex than simple Al_4Sr stochiometry, containing Zn and Mg. XRD analysis on the extracted precipitates revealed the characteristic peaks of Al_4Sr, but with small deviation (Fig.3.2.6) which suggests that the Al-Sr-Zn-Mg phase is actually Al_4Sr with small amounts of dissolved Mg and Zn which has slightly distorted the lattice parameters. However, it is also known that the Al_4Sr precipitate dissolves other elements in higher order systems (quaternary or higher) and assumes a more complex stochiometry [8-13,16-17, 20], potentially losing its thermal stability.

A recent study reported that in an Mg-Al-Sr alloy the chemical composition of the complex phase (Mg_9Al_3Sr) changed by moving toward an equilibrium condition. During annealing, the Al/Sr ratio increased in the Mg-Al-Sr ternary phase while its Mg content decreased. Consequently, the ternary intermetallic decomposed to α-Mg and Al_4Sr [20]. It has also been observed by Liu *et al.* [21] that the Al/Sr ratio increased during annealing and the complex stochiometry moved toward equilibrium Al_4Sr.

As explained previously, annealing has an effect on phase composition: the Al-Sr precipitate increases its Al content as it moves towards the equilibrium Al_4Sr. The AlMn precipitate is also a non-equilibrium precipitate and is not stable when it is subjected to heat. Experiments have shown that as the annealing temperature increases, the Mn/Al ratio of the AlMn precipitate drops while the ratio is almost constant for the equilibrium Al_8Mn_5 precipitate (Fig.3.2.7).

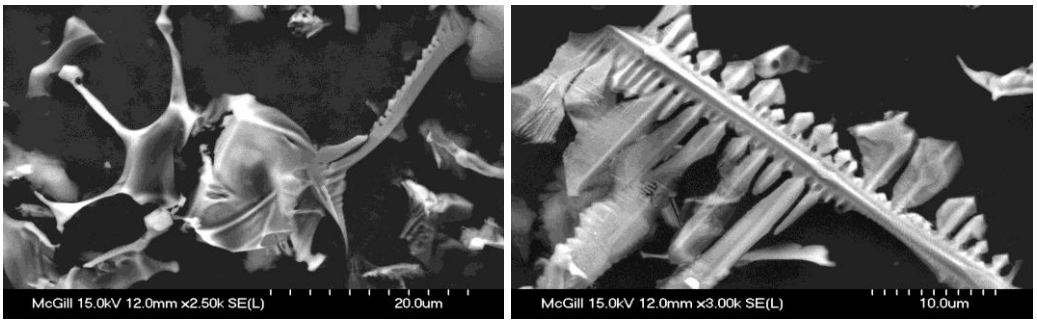

(a) (b)

Figure.3.2.5. SEM image of extracted (a) Al-Sr and (b) Al-Mn Precipitates from as cast AZ31+0.75%Sr.

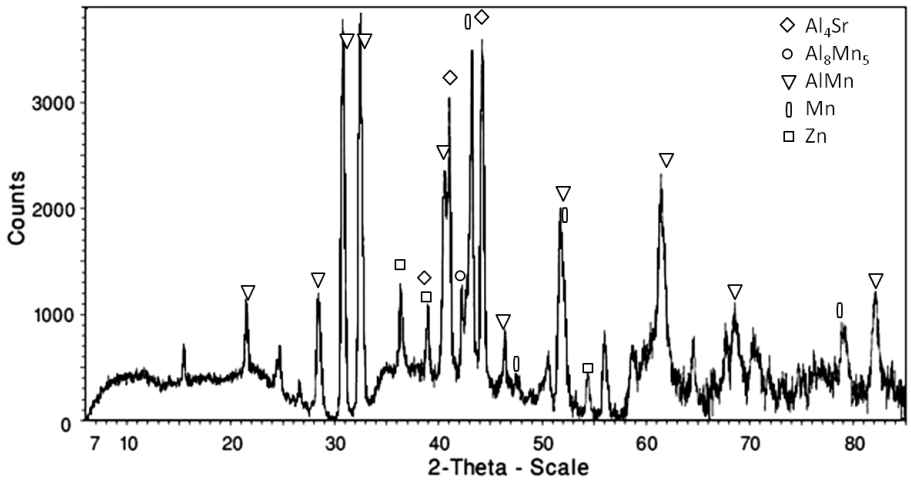

Figure.3.2.6. XRD spectrum of extracted precipitates from as cast AZ31+0.75%Sr.

Excess Mn dissolves into the primary Mg grains. If the concentration of Mn exceeds the solid solubility, it likely binds with the dissolved Al in the primary α-Mg grains and forms Al-Mn phases (probably Al_8Mn_5) nano-size precipitates (Fig.3.2.8a). The precipitation of Al-Mn phase in Mg alloys at elevated temperatures has been reported by other researchers [7].

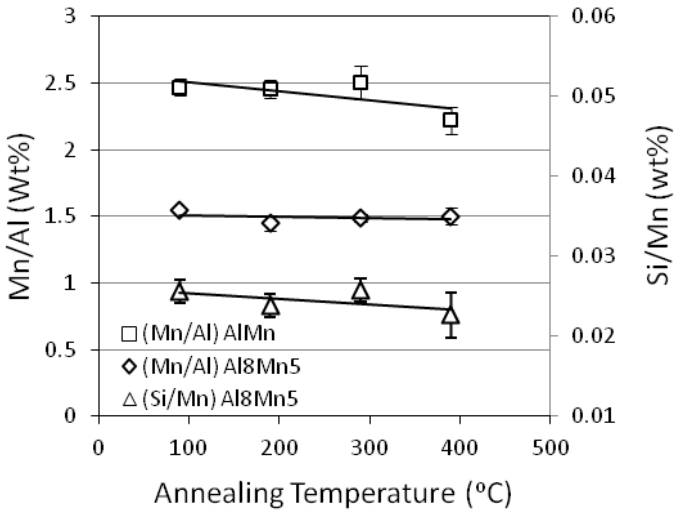

Figure.3.2.7. Change of Al/Mn and Si/Mn ratio of Al_8Mn_5 and AlMn precipitates of AZ31+0.35%Sr by annealing at different temperatures.

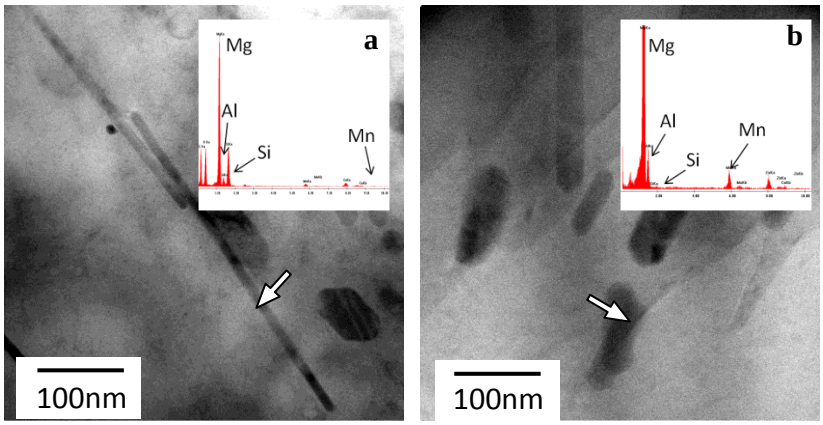

Figure.3.2.8. Nano sized (a) Al-Mn precipitate containing Si (most likely Al_8Mn_5) and (b) Al-Mn precipitate without Si (most likely AlMn) of AZ31+0.75%Sr at 350°C.

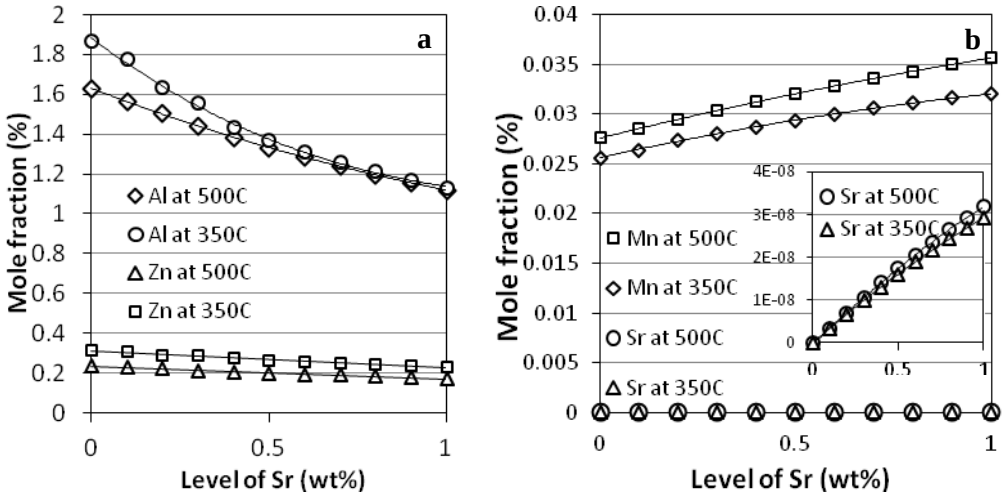

Figure.3.2.9. Calculated change in interitial concentration by increase in Sr level using thermodynamic computation.

Following exposure to heat, the large Al_8Mn_5 precipitates rejected dissolved Si and the Si/Mn ratio dropped (Si/Mn ratio in Fig. 3.2.7). TEM revealed the presence of Al-Mn precipitates inside the grains of the as-cast and annealed samples (Fig.3.2.8b). The addition of Sr also effected the solid solubility of other elements in α-Mg (Fig.3.2.9). The values were computed to be 500°C and 350°C by the thermodynamic model considering the Scheil cooling conditions: 1 wt% increase in Sr resulted in a 36% reduction in Al solid solubility and a 27% reduction in Zn solubility.

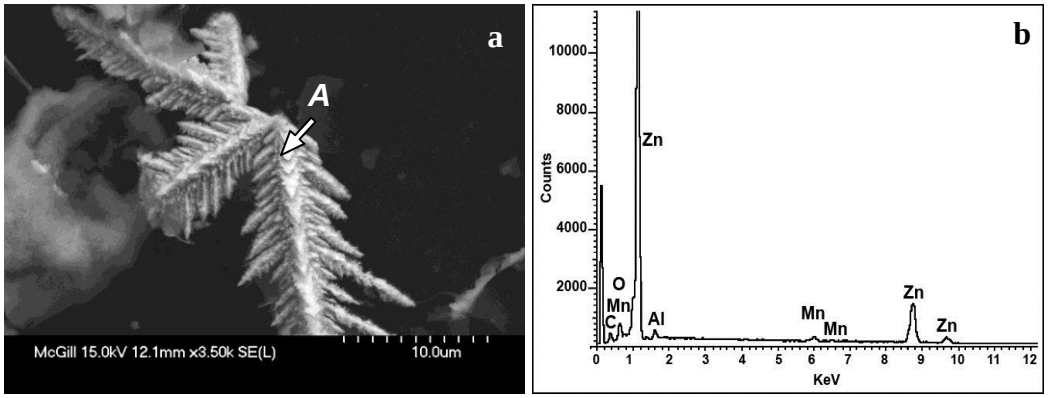

Figure.3.2.10. (a) Pure Zn dendrites after precipitate extraction, (b) EDS analysis of point A.

The trend in Al was confirmed by TEM-EDS analysis of the matrix between the precipitates, which showed ~10% decrease in Al content from 2.8 at% in AZ31. However, a change in Zn concentration was not detected. It has been previously observed that Zn is surface active in Mg and segregates to grain boundaries [22], which could explain the EDS results. Evidence of formation of pure Zn dendrites was also found in this work by precipitate extraction (Fig 3.2.10). Depletion of Al inside the grains as a result of Sr in AJ series has been previously reported [8]. It is known that Al reduces the solid solubility of Mn [18], hence, by increasing the level of Sr and therefore decreasing the Al concentration, the solid solubility of Mn should increase, although the Mn content in solid solution is very low. The calculation predicts ~23% increase in mole fraction (from 0.025 to 0.032 at 350^{o}C) when 1wt% Sr is added to AZ31 (TEM verified the increase from 0.01 to 0.03 atomic percent). The level of dissolved Sr in Mg was increased as well but even at maximum the concentration was very low.

AZ31 alloys containing 0.01-1.5wt% Sr can be divided in to three groups based on their microstructure. The first group contains trace levels of Sr (<0.1 wt%) and the main precipitate is β-$Mg_{17}Al_{12}$ similar to AZ31, but the grains and precipitates are refined. In these alloys a large portion of the precipitates can be dissolved at high temperatures and provide good workability at elevated temperatures, while at lower temperatures precipitates would provide strength.

The second group of alloys have high Sr levels (>1 wt%) and contain a web of thermally stable precipitates at the grain boundaries and interdendritic regions. Although higher creep performance is expected (same as AJ series), severe deformation at high temperatures may result in brittleness and surface cracking. The last group of alloys fit in between the two groups and possess a combination of their characteristics. The amount of thermally stable precipitates is not high enough to cause significant brittleness but they would enhance mechanical properties both at high and low temperatures. Also, since the precipitates do not dissolve at elevated temperatures, they could potentially act as nucleation sites for dynamic recrystallization (DRX) and cause particle stimulated nucleation (PSN) during hot deformation contributing to texture weakening.

3.2.5. Conclusion

Thermodynamic calculations were used to predict the precipitation of various Al-Mg, Al-Sr and Al-Mn phases as a function of Sr in AZ31 and the results were verified by microstructural examinations.

1. Thermodynamic calculations predict the substitution of β-$Mg_{17}Al_{12}$ with Al_4Sr with increasing Sr. The onset of this substitution occurs at lower concentrations of Sr in the presence of Mn, which was confirmed by microstructural examinations.
2. Although equilibrium calculations predicted the formation of four different Al-Mn precipitates, applying the Scheil cooling conditions only predicted the existence of Al_8Mn_5. EDS analysis confirmed the formation of the Al_8Mn_5 phase and revealed the presence of an AlMn non-equilibrium precipitate.
3. Annealing experiments show a decrease in Mn/Al and Si/Mn ratio in the non-equilibrium Al-Mn precipitates. TEM images confirm the formation of nano-scale Mg-Si and Al-Mn precipitates inside the grains.
4. EDS analysis and thermodynamic calculations both show the depletion of Al and slight increase of Mn inside the grains with increasing Sr.

5. Based on the microstructures and phase selection, Sr additions higher than 0.1 wt% but lower than 1.0 wt% can be beneficial for wrought alloy development.

3.2.6. References

1- L. Koubichek, “Effect of Small Additions of Elements on Grain Size and the Refinement of the Mg4Al3 [$Mg_{17}Al_{12}$] Phase in ML5 Alloy,” Izv. Vyschikh. Outchebnykh Za Vedeny, Metallurgy of Non-Ferrous Metals, No 6, (1959).

2- H. W. King, “Solid solution and intermetallic phases containing strontium,” Int. Conf. Strontium Containing Compounds, NRC, Ottawa, Canada, (1973) 212-243.

3- C.A. Aliravci, J.E. Gruzleski, F.C. Dimayuga, “Effect of Strontium on the Shrinkage Microporosity in Magnesium Sand Castings,” AFS Trans., 92, (1992).

4- M.O. Pekguleryuz, M.M. Avedesian, "Magnesium Alloying - Some Metallurgical Aspects, "Magnesium Alloys & their Applications, B.L. Mordike, F. Hehman, Eds. DGM, Germany, (1992) 679-686.

5- M. Pekguleryuz, E. Baril, P. Labelle, D. Argo, ”Creep Resistant Mg-Al-Sr Alloys”, J. Adv. Mat., vol. 35, No. 3, (2003) 32-38.

6- M.O. Pekguleryuz, A.A. Kaya, “Magnesium Diecasting Alloys for High Temperature Applications," Magnesium Tech., A.Luo, Eds., TMS, (2004) 281-287.

7- M. Kunst, A. Fischersworring-Bunka, G. L’Esperanceb, P. Plamondonb, U. Glatzelc, “Microstructure and dislocation analysis after creep deformation of die-cast Mg–Al–Sr (AJ) alloy,” Materials Science and Engineering A, (2009) 510–511.

8- E. Baril, P. Labelle, M.O. Pekguleryuz, “Elevated Temperature Mg-Al-Sr: Creep Resistance, Mechanical Properties & Microstructure,” Journal of Metals (JOM-US), TMS, Vol 55, No 11, (2003) 34-39.

9- M. O. Pekguleryuz, E. Baril, The Minerals, Metals and Materials Society 'Magnesium technology 2001', ed. J. N. Hryn, Warrendale, PA (2001).

10- B. Jing, S. Yangshan, X. Shan, X. Feng, Z. Tianbai, "Microstructure and tensile creep behaviour of Mg–4Al based magnesium alloys with alkaline-earth elements Sr and Ca additions," Materials Science and Engineering A 419 (2006) 181-188.

11- X. Zeng, Y. Wang, W. Ding, A. A. Luo, A. K. Sachdev, "Effect of Strontium on the Microstructure, Mechanical Properties, and Fracture Behaviour of AZ31 Magnesium Alloy," Metallurgical and Materials Transactions A, Vol 37, No 4, (2006) 1073-5623.

12- P. Zhao, Q. Wang, C. Zhai, Y. Zhu, "Effects of strontium and titanium on the microstructure, tensile properties and creep behaviour of AM50 alloys," Materials Science and Engineering A, 444, (2007) 318-326.

13- A. Sadeghi, M. Pekguleryuz, "Precipitation during the Solidification of Mg-3wt%Al-1wt%Zn-(0.001-1%) Sr Alloys," American Foundry Society Annual Congress, Orlando, USA, 10-114 (2010).

14- S. Guan, S. Zhu, L. Wang, Q. Yang, W. Cao, "Microstructures and mechanical properties of double hot-extruded AZ80+xSr wrought alloys," Transactions of Nonferrous Metals Society of China, Vol17, Issue 6, (2007) 1143-1151.

15- B. Jing, S. Yangshan, X. Feng, X. Shan, Q. Jinga, T. Weijianb, "Effect of extrusion on microstructures, and mechanical and creep properties of Mg–Al–Sr and Mg–Al–Sr–Ca alloys", Scripta Materialia 55 (2006) 1163-1166.

16- A. Janz, J. Gröbner, D. Mirković, M. Medraj, Jun Zhu, Y. A. Chang, R. Schmid-Fetzer: "Experimental study and thermodynamic calculation of Al-Mg-Sr phase equilibria," Intermetallics, 15, (2007) 506-519.

17- A. Janz, J. Gröbner and R. Schmid-Fetzer: Thermodynamics and constitution of Mg-Al-Ca-Sr-Mn alloys - Part II - Procedure for multicomponent key sample selection and application to the Mg-Al-Ca-Sr and Mg-Al-Ca-Sr-Mn systems. J. Phase Equilibria & Diffusion, 30, 156.1.175 (2009)

18- M. M. Avedesian, H. Baker, "Magnesium and Magnesium Alloys 1999," ASM International, Materials Park, OH 44073-0002, USA.

19- J.E. Gruzleski and A. Aliravci, "Low Porosity, Fine-Grain Sized Strontium Treated Magnesium Alloy Castings," US Patent US005143564A, (1992).

20- G. L'Esperance, P. Plamondon, M. Kunst, A. Fischersworring-Bunk, "Characterization of intermetallics in Mg–Al–Sr AJ62 alloys," Intermetallics 18 (2010) 1-7.

21- S.F. Liu, B. Li, X.H. Wang, W. Su, H. Han, "Refinement Effect of Cerium, Calcium and Strontium in AZ91 Magnesium Alloy," Journal of Materials Processing Technology, Vol 209, Issue 8, (2009) 3999-4004.

22- A. Becerra, M. Pekguleryuz, "Effects of Lithium, Indium and Zinc on the Grain Size of Magnesium," Journal of Materials Research, vol. 24, No. 5, (2009) 1722-1729.

Chapter 4

Recrystalization and Texture Evolution during Hot Bar Extrusion

This chapter which is comprised of three journal papers discusses the effects of various levels of Sr addition on hot extrusion of Mg-3Al-1Zn bars. In the study presented in Section 4.1 (*Recrystallization and Texture Evolution of Mg-3%Al-1%Zn-(0.4-0.8)%Sr Alloys during Extrusion*) microstructure and texture evolution during the extrusion of AZ31 magnesium alloy containing 0.4 and 0.8 weight present Sr was investigated. Following extrusion at 250^{o}C, the microstructure consisted of fine recrystallized and large elongated grains along with Al_4Sr stringer precipitates. Extrusion at 350^{o}C resulted in larger and more uniform grain size. Grain refinement and nucleation of new grains were associated with sub-grain formation in the elongated grains, grain boundary bulging, and nucleation at the particle interfaces. Texture measurements in the extrusion deformation zone showed an increase in the basal ring fiber-texture from the undeformed zone toward the die opening. Compared to AZ31 without Sr, the texture intensity increased with increasing Sr at 250^{o}C, whereas the strength of extrusion fibre texture decreased at 350^{o}C. The Al solubility in the α-Mg matrix decreased with increasing Sr and the Al solute atmosphere around the dislocations weakened. Due to the reduction of the solute drag effect, dislocation movement was facilitated and dynamic recrystallization became more intensive resulting in strengthening of the texture during extrusion at 250^{o}C. The decrease in texture intensity at 350^{o}C extrusion is attributed to the activation of particle-stimulated nucleation (PSN) that led to the nucleation of new grains with high orientation mismatch to the parent grains.

Section 4.2 (*Microstructure, mechanical properties and texture evolution of AZ31 alloy containing trace levels of strontium*) presents investigations that were carried out to determine the effect of trace levels of Sr on AZ31. The effect

of low levels of Sr (0.01, 0.03, 0.05wt %) on the microstructure, mechanical properties and texture of AZ31 magnesium alloy are reported. Thermodynamic modeling was used to study the effect of Sr on phase precipitation at different temperatures. Cooling curve analysis revealed a decrease in solidification undercooling with the addition of 0.03wt% Sr to AZ31. The as-cast microstructures of the alloys were studied using optical microscopy (OM) and electron probe micro analysis (EPMA). Results showed the refining effect of Sr on the grain size and on the β-$Mg_{17}Al_{12}$ precipitates through growth poisoning and inoculation, respectively. To investigate the mechanical properties of the alloys, as-cast samples were compression tested at elevated temperatures. Hot compression peak stress (σ_{max}) and critical strain before recrystallization (ε_c) increased after an initial drop. The σ_{max} first decreased due to decrease in Al solid solubility and then increased when the amount of the Al-Sr precipitates became significant. The ε_c dropped due an acceleration of the dynamic recrystallization kinetics as a result of grain refinement. It increased with increasing Sr due to dislocation pinning and the retardation of recrystallization stemming from an increased amount of Sr in solid solution. X-ray texture measurements on the hot compressed and extruded samples showed a decrease in maximum intensity of the basal pole figures with increasing Sr as a result of reduced twinning and the changes in the Al and Sr concentrations in Mg solid solution.

In section 4.3 (*Effect of Sr addition on Texture Evolution of Mg-3Al-1Zn (AZ31) Alloy during extrusion*) an experimental investigation regarding texture evolution during the elevated temperature extrusion of AZ31 alloys containing additions of Sr is reported. The crystallographic texture of hot extruded alloys containing different levels of Sr was examined. Hot compression tests were carried out in order to investigate the hot deformation behaviour of the as-cast alloys. It was observed that at different extrusion temperatures and levels of Sr different DRX mechanisms became dominant which effected the final texture. At lower temperatures and at low levels of Sr, bulging of grain boundaries was activated, resulting in a necklaced grain structure. Furthermore, a strong

deformation texture of <10.0> parallel to the extrusion direction developed as a result of bulging at the grain boundaries. Twinning which was activated in the early stages of deformation acted as nucleation sites for DRX. In contrast, at high temperatures and high levels of Sr, PSN became significant, resulting in the weakening of the overall texture following the recrystallization of new grains of random orientation. In order to prevent surface cracking in the extruded sample, a limit for Sr concentration and deformation temperature was determined. A shoulder region was found in between the bulging and PSN-dominant areas where both mechanisms are active.

4.1. Recrystallization and Texture Evolution of Mg-3%Al-1%Zn-(0.4-0.8)%Sr Alloys during Extrusion

Alireza Sadeghi, Mihriban Pekguleryuz

Materials Science and Engineering A, Volume 528, Issue 3, 25 January 2011, Pages 1678-1685

4.1.1. Introduction

In magnesium alloys, dislocation slip at low temperatures (<250^{o}C) occurs predominantly on the basal planes, leading to the development of preferred orientation with alignment of the hexagonal c-axis perpendicular to the metal flow direction during deformation [1]. During axisymmetric extrusion of AZ31 (Mg-3Al-1Zn) alloy, basal planes normally become parallel to the extrusion axis and the basal normals align in the radial directions, this forms a basal pole figure like a ring, which is called the ring fibre texture of the basal planes. This strong texture is responsible for the anisotropic mechanical behaviour of extruded bars [2]. The intensive basal fibre texture significantly reduces subsequent workability and formability of extruded bars and tubes, consequently limiting their applications.

Several studies have explored dynamic and/or static recrystallization as a means to control the texture and microstructure of magnesium extrusion alloys [3-4]. Secondary phases, depending on their size and distribution, can either promote or suppress recrystallization [5]. The particle size, spacing, amount and composition of secondary phases have been observed to yield different recrystallization behaviour in Mg alloys [4-8]. Grains formed via particle-stimulated nucleation (PSN) generally have orientations which are different from those produced by other recrystallization mechanisms and can produce texture alteration [5, 8]. This is particularly interesting for magnesium as a way to alter the dominant basal texture after deformation.

Strontium has been used as an alloying element in Mg to form thermally stable precipitates to improve mechanical properties at elevated temperatures [10-11]. The addition of Sr to AZ31 produces various Mg-Al-(Sr) and Al-Sr precipitates during solidification, depending on the overall Sr content of the alloy.

It has been observed that increasing the weight percent of Sr in the alloy decreases the amount of the β precipitate ($Mg_{17}Al_{12}$), while the amount of Al_4Sr increases [12, 13]; the β phase is suppressed above 0.35 wt%Sr [12]. The thermally stable Al-Sr precipitates remain in the microstructure up to 480°C-500°C (depending on the level of Sr). Hence, these precipitates are present during hot extrusion and could affect the recrystallization, microstructure and the final texture. In the present paper, the effect of Al-Sr precipitates on the recrystallization and texture of Mg-3%Al-1-%Zn-(0.4-0.8)%Sr alloys during hot extrusion was investigated.

4.1.2. Experimental Procedure

AZ31 alloy provided by Applied Magnesium (Denver, CO) was melted in a graphite crucible using a high-frequency induction furnace (NORAX). Sr was added using Sr-10wt%Al master alloy (from Timminco, Haley, ON) to the melt at 700°C and held for 15 minutes to dissolve. The melt was cast from 720°C into cylindrical preheated steel dies under SF_6-CO_2 gas mixture. The chemical compositions of the alloys used in this study (Table.4.1.1) were determined by inductively coupled plasma (ICP).

Table.4.1.1. Chemical Compositions of the Alloys

No.		1	2	3	4
	element	AZ31	AZ31+0.05Sr	AZ31+0.4Sr	AZ31+0.8Sr
Chemical comp. (wt%)	Al	3.15	3.19	2.76	2.83
	Zn	0.89	0.82	0.79	0.79
	Mn	0.52	0.51	0.35	0.35
	Sr	0	0.05	0.34	0.81

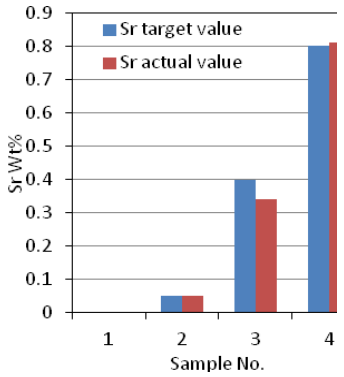

Figure.4.1.1. (a) the 100T extrusion press, and (b) the ceramic insulated band heater and (c) the extrusion matrix, channel and punch in the press frame, (d) the extrusion channel, punch and die piece, (e) the exposed view, and (f) the Mg sample before and after extrusion.

Cylindrical bars (d_0=30mm) machined from the castings were extruded using a 100T hydraulic press and a steel die to 1/9 cross section (D_f=10mm) (Fig.4.1.1). The extrusion rate was 240 mm min^{-1} for all the trials and the extruded bars were cooled in air. A high temperature anti-seize paste containing graphite, calcium hydroxide and zirconium oxide (Molycote P-37) was used for die lubrication at high temperatures.

The deformation temperatures (250^{o}C and 350^{o}C) were maintained constant using a ceramic insulated band heater. Samples from three different zones (billet end, the deformation zone, and the extruded zone) along the center of the longitudinal cross-sections were prepared for microstructural and textural analysis). Hot compression test was conducted on machined cylinders, 9 mm high and 6 mm diameter, using a 510 MTS servohydraulic mechanical testing machine. The specimens were heated to the deformation temperature and then held for 15 min prior to compression. Straining was carried out to true strains of 0.2 and 0.8

at a strain rate of 0.01 s^{-1}. The anvils and specimen were protected under an argon gas atmosphere to avoid oxidation. Boron nitride powder and mica plates were used to minimize the friction at high temperatures during the test.

The as-cast and deformed samples were polished with 1 μm diamond paste after grinding and then etched in picric-acetic solution for microstructural investigation using optical microscopy (OM). Second phase precipitates were studied using field-emission gun / scanning-electron microscopy (FEG-SEM, Hitachi S-4700) with secondary and backscattered electron detectors, and energy dispersive spectroscopy (EDS) was used to identify phase compositions. To observe the 3D morphology of the precipitates and eliminate the effect of the matrix, a precipitate extraction procedure was used as previously described [13]. Nano-sized precipitates and fine microstructures were observed using bright field transmission electron microscopy (TEM, Philips CM200 operating at 200 kV). The thin foil specimens for TEM were prepared from cross sections of extruded samples containing the extrusion direction (ED-r) by grinding and further thinned by ion milling using a Gatan precision ion polishing system (PIPS).

Electron backscattered diffraction (EBSD) was used for micro-texture measurements and grain orientation maps. Backscattered diffraction patterns were collected using a charged coupled device (CCD) camera and TSL data acquisition software was used for interpretation. EBSD data was acquired using a Philips XL-30 FEG-SEM operating at 20 kV with 15 mm working distance and 70^{o} tilted specimen. Two techniques were used for sample preparation: electro-polishing using a 10% Nital solution cooled to 5^{o}C at 20V for 10-15s and polished using PIPS. Errors encountered with EBSD measurement are summerized in Appendix II.

The overall crystallographic texture was evaluated via X-ray diffraction (XRD) using a Bruker D8 X-ray diffractometer using Co Kα radiation. Incomplete pole figures of {0001}, $\{10\bar{1}0\}$ and $\{10\bar{1}1\}$ were recorded, and the orientation distribution function (ODF) was constructed using texture analysis software (TexTools). Recalculated pole figures were derived from the ODFs.

4.1.3. Results and Discussion

4.1.3.1. As-Cast and Extruded Microstructures

We previously studied the as-cast microstructures of the alloys [12, 13]. At low levels of Sr concentration (< 0.3 wt%) the microstructure consists of α-Mg grains containing β-$Mg_{17}Al_{12}$ precipitates either in the grain or interdendritic regions. EDS mapping indicated the presence of dissolved Sr inside the β phase [12]. The effect of Sr on the refinement of β precipitates [14] and the grain size of Mg-Al-Zn alloys have been previously reported by other researchers [14-16] and also in our previous work [12, 13]. Al_8Mn_5 (with dissolved Si) and AlMn (a metastable precipitate with the lowest Al/Mn ratio) particles were distinguishable inside the grains by their needle shape morphology.

As-cast AZ31+0.4%Sr exhibits eutectic Al-Sr precipitates at the grain boundaries but no globular β phase inside the grains. The sample with the highest level of Sr (AZ31+0.8%Sr) revealed a higher amount of Al-Sr precipitates along the grain boundaries and inside the grains [12, 13]. It has been previously reported that the Al-Sr precipitates depart from stochiometry and contain Zn and Mg [13]. At high temperatures, the Al-Sr intermetallic in the as-cast alloy has been observed to reject the dissolved Mg atoms and moves toward an equilibrium Al_4Sr stoichiometry [17, 18]. During annealing a similar change has been noted in Al-Mn precipitates; AlMn starts to reject Mn and it decreases its Mn/Al ratio and the Al_8Mn_5 particles diffuse out their solute Si [13]. Moreover, cooling down, from elevated temperatures after casting decreased the solid solubility of Mn and Si in primary Mg. Consequently, nano-size Mg-Si and Al-Mn dispersed precipitates formed, which were visible using TEM in the hot deformed microstructures (Fig. 4.1.2).

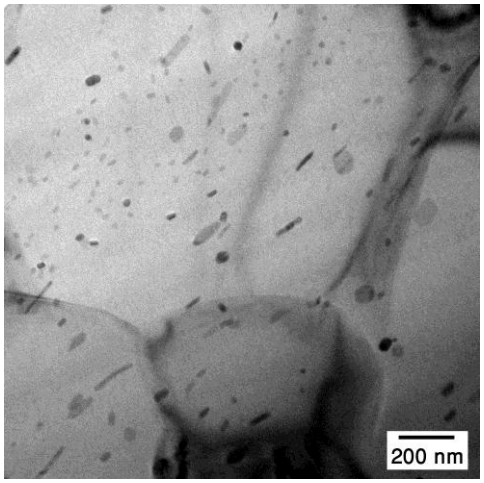

Figure.4.1.2. Bright field TEM image of nano sized Al-Mn and Mg-Si precipitates after hot extrusion of AZ31+0.8%Sr at 350^{o}C. Image is taken from a mid cross section containing the extrusion direction.

Fig. 4.1.3 shows the microstructure of the AZ31+0.8%Sr alloy before (Fig. 4.1.3a), during (Fig. 4.1.3b) and after (Fig. 4.1.3c) entering the extrusion deformation zone at 350^{o}C. Before deformation (Fig. 4.1.3a), the eutectic Al-Sr and peritectic Al-Mn precipitates can be observed, which are distinguished by their morphology and contrast. The large dark precipitates (marked as A) along the grain boundaries and inside the grains are Al-Sr and the smaller needle shape particles (labelled B) are Al-Mn. Fig. 4.1.3b is the transition state between undeformed precipitates and highly deformed stringers (Fig.4.1.3c).

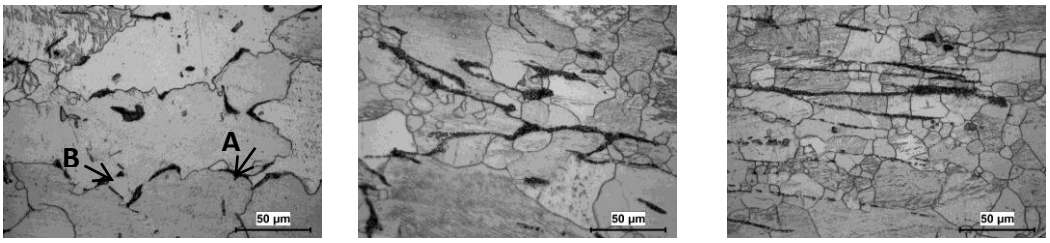

(a) ***(b)*** ***(c)***

Figure.4.1. 3. Microstructure of the AZ31+0.8%Sr alloy, (a) before (precipitates are labelled as A for Al-Sr and B for Al-Mn), (b) during and (c) after entering the deformation zone during extrusion at 350^{o}C.

The eutectic Al-Sr precipitates deformed into stringers in the material flow direction. Backscattered electron (BSE) images of the eutectic Al-Sr precipitates

before and after extrusion are shown in Figs. 4.1.4 a and b. The eutectic morphology of the Al-Sr (labelled A in Fig. 4.1.4c) and Al-Mn precipitates (labelled B in Fig. 4.1.4c) in the as-cast condition are revealed by precipitate extraction.

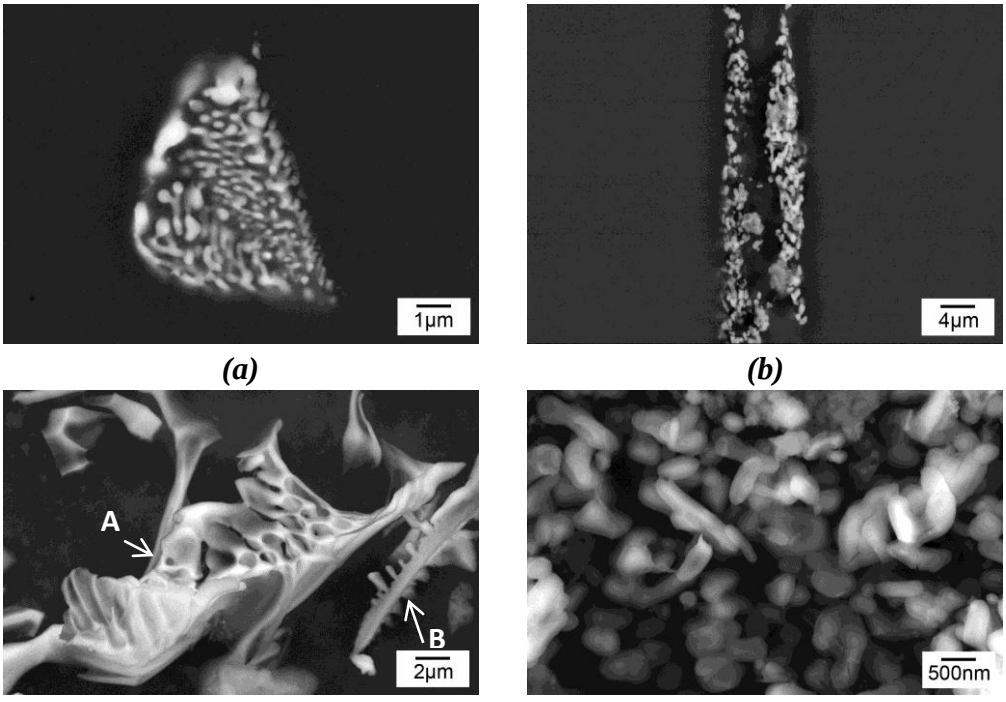

(a) *(b)*

(c) *(d)*

Figure.4.1.4. Backscattered electron images of Al-Sr precipitates in AZ31+0.8%Sr, (a) before and (b) after extrusion at 350^{o}C, and secondary electron images of extracted Al-Sr precipitates (c) before and (d) after the same extrusion process.

These large Al-Sr interdendritic precipitates (Fig.4.1.4.c) were broken to tiny round edged precipitates during extrusion (Fig.4.1.4d). The sizes of the precipitates inside the stringers were measured to be between 0.5-1.5 µm. It has previously been reported [19] that during the extrusion of AZ31 alloy β-$Mg_{17}Al_{12}$ stringers also formed, but the nature of formation was quite different from Al-Sr stringers; here the β precipitates fragmented into smaller dispersed particles which were by passed by dislocations. Consequently, the β particles were not able to accumulate at dislocations behind them to form potential PSN sites.

4.1.3.2. Texture Measurement and Analysis

Deformation zones of the extruded samples were sectioned parallel to the extrusion direction and seven measurements, 5 mm apart, were taken along the cylinder axis. Formation of the basal fiber in the extruded samples was measured in an indirect way: instead of determining the volume fraction of basal planes in the radial direction (direction of pressure in extrusion), the volume fraction of the prism planes perpendicular to the extrusion axis was measured from the constructed ODFs. In Fig 4.1.5.a, the relationship between the two approaches is illustrated schematically.

By plotting the volume fraction of prismatic planes vs. the deviation angle of prismatic normals from the extrusion direction, the distribution of prism planes was derived.

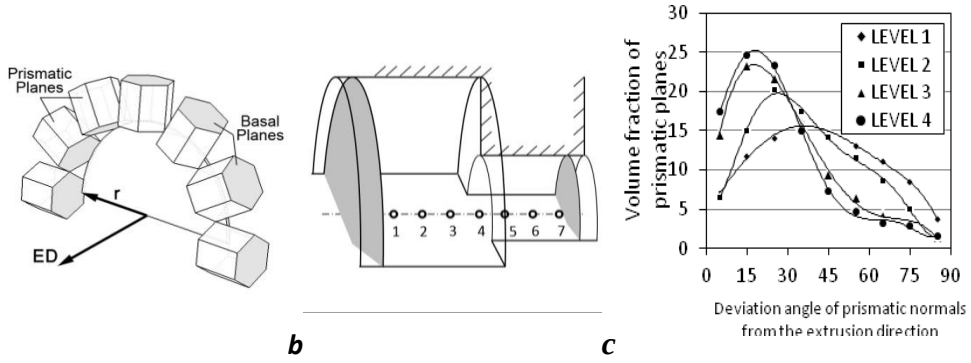

Figure.4.1.5. (a) The relationship between basal and prismatic planes in Mg basal fiber texture after extrusion according to extrusion direction (ED) and radial direction (r). (b) Location of each texture measurement in a sectioned specimen, (c) The distribution of prism planes along the extrusion direction for AZ31+0.8%Sr extruded at 250^{o}C.

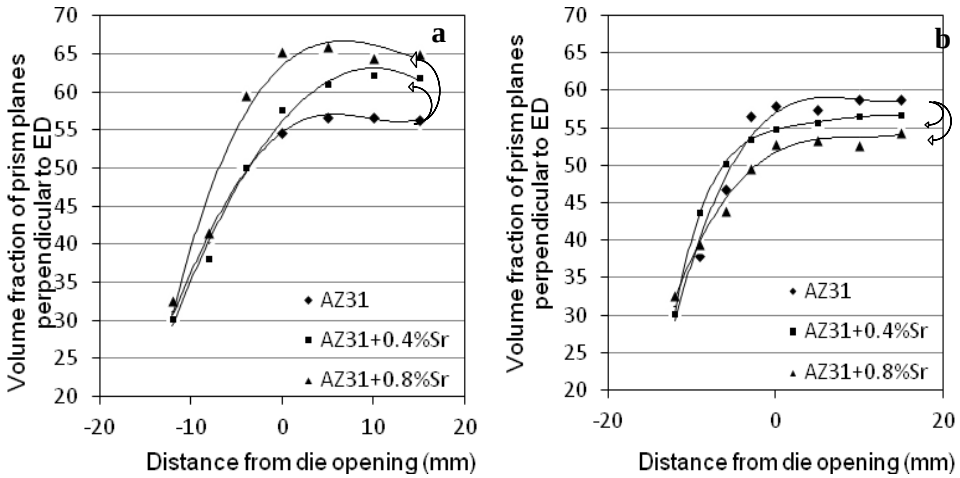

Figure4.1.6. Volume fraction of prism planes with normals less than 15 degree of deviation from the extrusion direction vs. distance from extrusion die opening at (a) 250^{o}C and (b) 350^{o}C (arrows show the increase or decrease of final texture strength with increasing Sr.

At each level indicated in Fig 4.1.5.b, texture was measured using X-Ray diffraction and the distribution curves were derived. Fig. 4.1.5.c shows a sample distribution plot of AZ31+0.8%Sr extruded at 250^{o}C at the different levels indicated in Fig4.b.

Texture results indicated that the peak height increased and shifted to the left as die opening was approached (from point 1 to 5 in Fig. 4.1.5.a), which indicates that the fibre texture became stronger and a larger number of prism planes rotated closer to the extrusion direction. However, the distribution curve did not change from point 5 to 7 because there was no additional deformation that could result in further textural change. The same texture trend (in different degrees) was seen in all four compositions at two different temperatures (250^{o}C and 350^{o}C) (Figure 4.1.6).

The volume fraction of prismatic planes with less than 30^o deviation from the extrusion direction is compared in Fig 4.1.6. It is interesting to note that as the Sr level increased, the strength of the final fiber texture increased during extrusion at 250^{o}C (Fig. 4.1.6a); while, at 350^{o}C the opposite occurred and the final volume fraction of prismatic planes decreased with increasing Sr content (Fig. 4.1.6b). The results indicate that at 350^{o}C, an increase in the amount of particles (Al-Sr stringers) led to a reduction in the strength of the basal fiber texture. Further investigation was conducted in order to elucidate the different mechanisms at these two extrusion temperatures.

4.1.3.3. Recrystalization at the stringer boundaries at 350^{o}C

The extrusion temperature has an important effect on the extrusion structures. Samples with the same composition and the amount of precipitate but extruded at 250^{o}C and 350^{o}C produce very different grain structures. Fig. 4.1.7 shows the true stress – true strain diagrams of AZ31 and AZ31+0.8%Sr at different

temperatures. It can be seen that for both of the alloys the peak stress dropped as the temperature increased from 325°C to 400°C. Note that when the Al-Sr precipitates were present (AZ31+0.8%Sr) in the alloy, the critical strain (ε_c) shifted to the left with increasing temperature (Fig. 4.1.7a). This significant decrease in ε_c can be attributed to the presence of precipitates which are effective in increasing the stored energy and potential nucleation sites and consequently DRX is activating sooner at a lower strain. While in AZ31 with no Al-Sr precipitates, the shift was much smaller, and this is attributed to an increase in DRX kinetics (Fig. 4.1.7b). Evidence for these mechanisms can be found in the microstructures of extruded samples (Fig. 4.1.8). In the microstructure of the samples extruded at 350°C recrystallized grains were linked to stringers. However, at 250°C, ultra fine grains were not necessarily associated with precipitates (Fig. 4.1.8a). All of the alloys extruded at 250°C exhibited a bimodal grain size distribution which consisted of ultra fine equiaxed grains (1.9 μm) surrounding the large elongated grains in the extrusion direction (Fig. 4.1.8a).

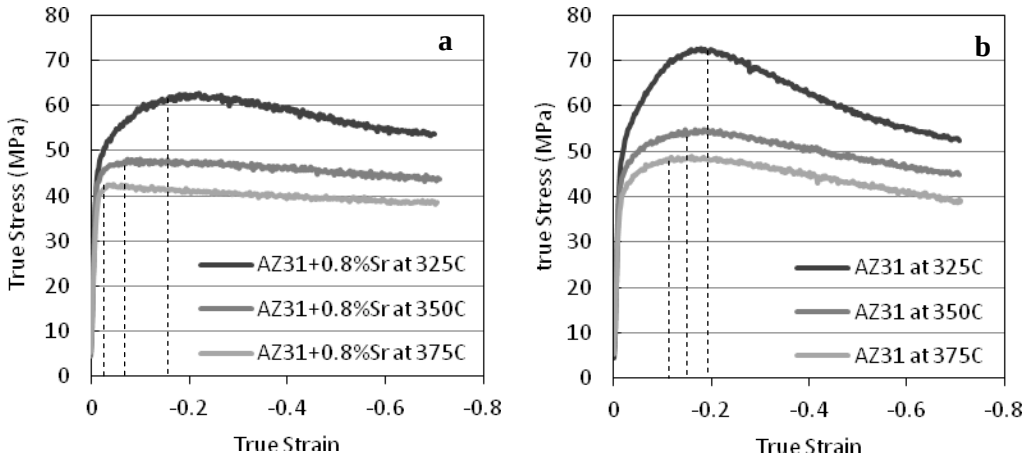

Figure.4.1.7. True stress –true strain diagrams at different temperatures for (a) AZ31 and (b) AZ31+0.8%Sr.

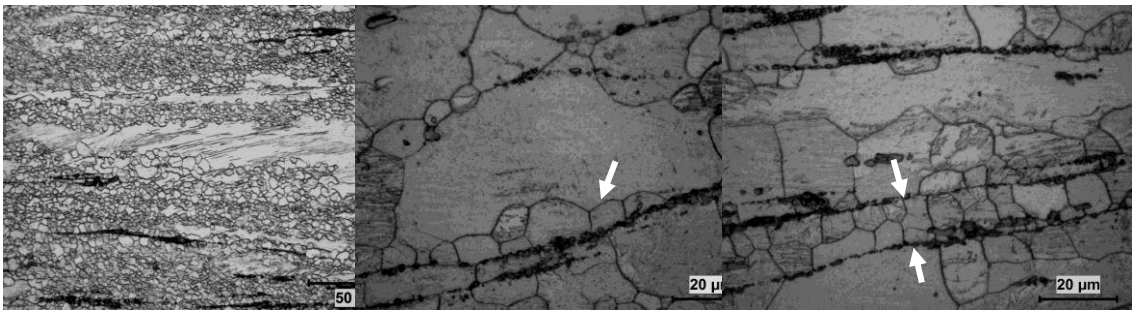

(a) (b) (c)

Figure.4.1.8. Microstructures of the extruded AZ31+0.8%Sr at (a) 250^{o}C, (b,c) 350^{o}C recrystallized grains and stringer association in the same alloy at 350^{o}C.

The large elongated grains remained unrecrystallized and possessed low angle boundary sub-structure. The grain structure in 350^{o}C was coarser (3.6 μm) and more uniform. Figs. 4.1.8 b & c demonstrate the association of recrystallized grains with stringers in AZ31+0.8% Sr following extrusion at 350^{o}C. It can be observed that new grains are starting to grow from the stringer at the grain boundary of the parent grain (Fig. 4.1.8b) and grow inside until they reach another stringer or similar grain boundary (Fig. 4.1.8c). The particle size in the samples investigated ranged from 0.5 to 1.5 μm; these particle sizes have previously been implicated to be sufficient for PSN in aluminium [20, 21] and magnesium alloys [4]. Some of the small particles were clustered to form a joint deformation zone, creating an effective diameter of ~ 4μm.

Fig. 4.1.9a shows the EBSD image quality (IQ) of AZ31+0.8%Sr after extrusion (70-80% indexation). The quality index was computed from the maximum intensity of the Hough peaks. The Hough transformation is an image analysis technique which converts the kikuchi patterns to recognized peaks to reveal the crystal orientation in each material point. Quality index represents the average intensity of the Hough peaks. High quality diffraction patterns have intense Hough peaks; therefore the average intensity will be greater than for low quality patterns. Image quality differences from grain orientations are typically much smaller than those due to phase, grain boundaries and strain. Therefore, IQ maps provide useful visualizations of microstructure. The contrast in these maps arises from a variety of sources, including phase, strain, topography, and grain

boundaries [22]. However, there are some sources of error associated with EBSD measurements (See Appendix II).

As shown in Fig. 4.1.9a, small recrystallized grains associated with stringers could be distinguished everywhere around the microstructure (A). The growth of recrystallized grains appeared to stop when they impinged on another new recrystallized grain or reached the next stringer. The interiors of the elongated unrecrystallized parent grains were characterised by low angle boundaries and local deformation (B in Fig. 4.1.9b).

Humphreys *et al*. [23] generated an equation for the misorientation profile as a function of distance from a particle, which has been verified in Al-Si [23] and Mg-Mn [7] alloys. Since the particles in our extruded alloys were at elongated grain boundaries, the misorientation profiles in two directions (parallel and perpendicular to the elongation direction) were measured and plotted together with the predicted misorientation profile of Humphreys [23], as shown in Fig. 4.1.9.c.

We observed that the misorientation increased toward the grain boundaries which contained the Al-Sr stringer indicating that local deformation and lattice bending was prominent behind the stringer, with the effective diameter of the stringer taken as 4μm.

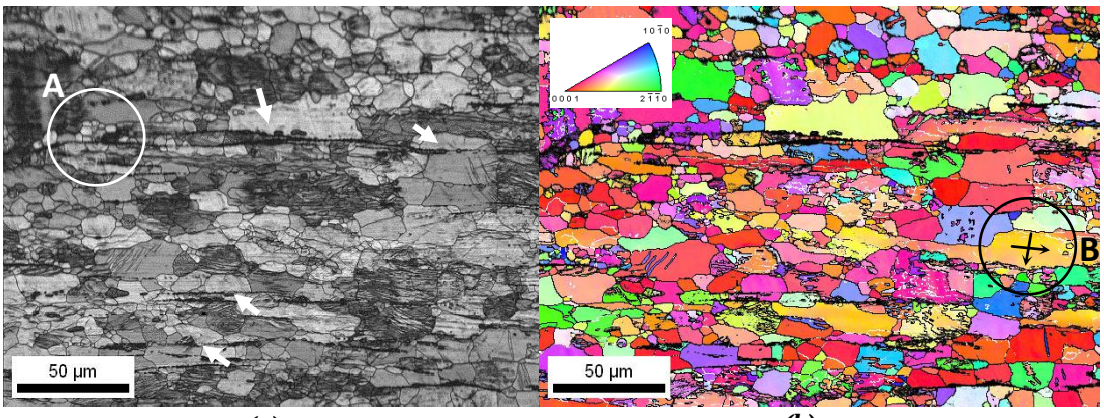

(a) ***(b)***

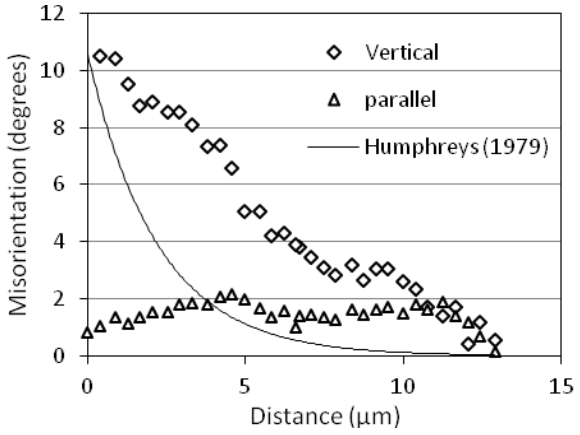

(c)

Figure.4.1.9. Electron Back Scattered Diffraction (EBSD) microstructure of extruded AZ31+0.8% Sr at 350^{o}C, (a) image quality, (b) inverse pole figure, (c) misorientation map of the two arrows marked as B in part b, parallel and perpendicular to the extrusion direction (horizontal direction).

Our results are relatively higher than those of Humphreys *et al.* whose analysis was based on localized deformation around a particle that was located at the center of the grain. In the present work, the particles were located at the grain boundaries where an additive effect of the misorientation of the mantle of the grain was observed. This makes the stringer a perfect location for nucleation of new grains. It should be noted that to completely determine strain at a material point, all six strain components in the normal directions (ε_{xx}, ε_{yy} and ε_{zz}) and the shearing planes (ε_{xy}, ε_{yz} and ε_{zx}) should be measured [24]. It is also important to note the limitation of EBSD in simultaneous measuring of crystallographic orientations in more than one sample direction because of the restrictions in sample positioning and the low permeability of the electron beam.

Another EBSD measurement was carried out in order to compare the orientation dependence of the recrystallized grains associated by stringers with those of the parent grains (60-70% indexation). In Fig.4.1.10a, signs of local deformation (indicated by gradual color change) were observed inside the elongated grain, which are signs of low angle boundaries (LAB). These are an intermediate step to continuous dynamic recrystallization (CDRX): further

deformation increases the mismatch of the LAB and finally a high angle grain boundary (HAGB) grains form.

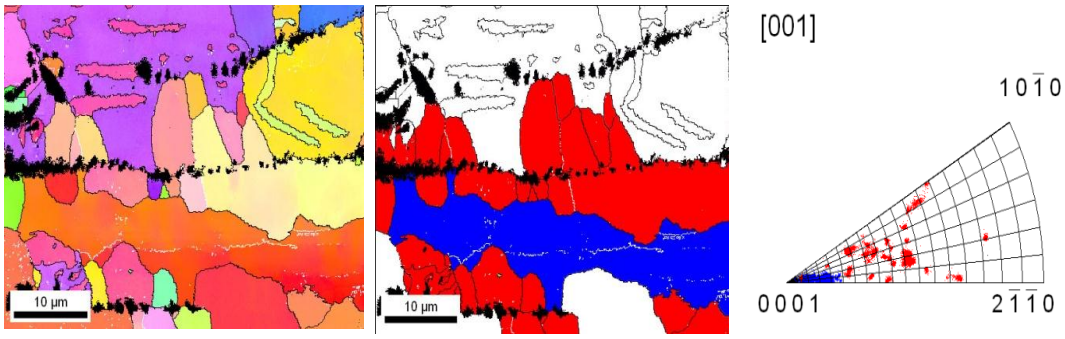

(a) ***(b)*** ***(c)***

Figure.4.1.10. EBSD image showing the microstructure of AZ31+0.8%Sr extruded at 350^{o}C, (a) Inverse pole figure map, (b) same microstructure as previous, parent grain highlighted with blue and recrystallized grains originated from the parent grain and linked to stringers are highlighted with red, (c) inverse pole figure of the highlighted regions. (extrusion direction is horizontal)

The small recrystallized grains linked to the stringers (Fig. 4.1.10b) around the elongated grain (newly recrystallized grains at the boundaries containing Al-Sr precipitates) are highlighted with blue and the elongated grain is highlighted with red as the parent grain (other grains which are not linked to the large elongated grain with precipitates are not selected). In Fig.4.1.10c, the inverse pole figure of the highlighted grains is shown; note that the recrystallized grains have orientations completely different from the parent grain. This also supports the notion that grains nucleated as a result of PSN have different orientations from the original texture and change the overall texture [5].

Following extrusion at 350^{o}C, higher levels of Sr additions produced increased amounts of Al-Sr particles which increased potential nucleation for PSN. Therefore, the ratio of grains which recrystallize via PSN (which do not have the ring basal texture) over those that recrystallize via grain boundary migration or CDRX with the same basal fibre texture increased, and eventually the intensity of the overall fibre texture was decreased (Fig. 4.1.10c).

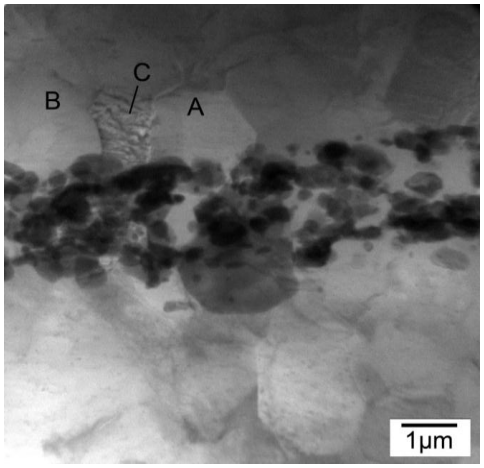

Figure.4.1.11. Bright field TEM image of AZ31+0.8% Sr extruded at 350^{o}C, showing recrystallization of grains A and B originating at the Al-Sr stringer and consuming the C deformation zone. The extrusion direction is horizontal.

TEM verified findings made by OM and EBSD. Fig.4.1.11 shows a stringer consisting of Al-Sr precipitates and the recrystallized grains (A and B in Fig.4.1.11). The two grains grew starting from the stringer and their convex grain boundaries show the direction of growth toward the high dislocation density matrix (C in Fig. 4.1.11).

Thermodynamic calculations and microscopic observations (Figs. 3.1.2 & 3.2.2) confirmed that adding Sr to AZ31 led to the presence of Al-Mn inside the α-Mg grains in addition to the interdendritic Al-Sr precipitates. It has been reported than Mn precipitates can provide PSN sites in Mg alloys [7]. In the group of alloys studied in this work, the level of Mn was constant, hence, it is not likely that these precipitates took part in PSN and texture development, though they may have pinned grain boundaries and effected grain growth kinetics.

4.1.3.4. Deformation mechanisms at 250^{o}C

To explain the different behaviour at 250^{o}C, two questions need to be answered: (i) why did the stringer not participate in PSN leading to texture weakening? and (ii) why, in contrast to 350^{o}C did increasing Sr increase texture?

(i) During extrusion at 350^{o}C all the hexagonal slip systems were activated, therefore, more dislocation movement and accumulation behind the obstacles (grain boundaries and precipitate interfaces) is expected. Furthermore, since the temperature was higher (compared to 250^{o}C) higher, thermally activated processes (vacancy generation and dislocation climb) needed for recovery and recrystallization at the precipitate interface were available and the accumulated dislocations could be easily converted to stable nuclei and grow. Grains forming at the stringers have different texture from the parent grain and resulted in weakening of the overall texture. However, at 250^{o}C the dislocation density and thermal energy are not sufficient for nucleation and growth at the precipitate boundaries. Also, at lower temperatures there is more accumulation of dislocations behind the grain boundaries since dislocations cannot cross slip to the adjacent grains. This leads to grain boundaries contributing more significantly towards the nucleation of DRX. As shown in Fig 4.1.6.a, by increasing the temperature at the same level of Sr, the peak stress drops and ε_c shifts to the left. A decrease in maximum stress was also observed in the absence of Al-Sr precipitates (Fig. 4.1.7b), but the decrease in ε_c occurred when the Al-Sr precipitates started to participate significantly to DRX.

(ii) Extruding at 250^{o}C led to texture strengthening, rather than weakening observed at 350 ^{o}C, leading to the notion that a high potential for PSN is counteracted with another mechanism at lower temperatures. Because of the restrictions in slip systems at 250^{o}C, the effects of other series of micro mechanisms may become dominant and influence the deformation mode to finally lead to texture strengthening. One such mechanism is solute drag. Dislocation atmospheres weaken at high temperatures and therefore, while solute drag would not likely be an important mechanism at 350^{o}C, it would play an important role at 250^{o}C. By pinning dislocations, or affecting the concentration and mobility of vacancies, solute atoms can influence stacking fault energy (SFE) [6]. It is known that solute drag slows down dislocation motion and limits recrystallization [5] and those thermally stable solutes effectively pin grain and sub-grain boundaries [25].

The degree of solute drag would be a function of solute content and the diffusivity (also related to the melting point) of the solute in the alloy.

It is known that an increase in the Sr content of the alloy causes a drop in Al solid solubility in primary α-Mg and there is accompanying increase in Mn solubility [10,13]. Thermodynamic calculation predicts ~23% increase in mole fraction (from 0.025 to 0.032 at 350^{o}C) when 1wt% Sr is added to AZ31 (TEM verified the increase from 0.01 to 0.03 at%) [14]. Mn has a very low diffusion coefficient and would form a very stable dislocation atmosphere at 250^{o}C.

Figure 4.1.12 shows the hot compression results at 250^{o}C and 350^{o}C for specimens with different levels of Sr. Results indicated a drop in strength with increasing levels of Sr at 250^{o}C (Fig. 4.1.12a) which confirms the concept of lower solute drag and easier slip. In contrast, the trend is different at 350^{o}C (Fig. 4.1.12b) where adding more Sr increased the strength. Fig. 4.1.13 shows the same region of two samples with different levels of Sr before entering the deformation zone during extrusion at 250^{o}C. By comparing the microstructure in Fig. 4.1.13a (AZ31) and Fig 4.1.12b (AZ31+0.8%Sr) a difference in the deformation mechanism can be observed. In AZ31 (Fig. 4.1.13a), twins have formed inside the grains and as a result of DRX, smaller grains have formed inside them. The formation of twins is attributed to the high concentration of Al inside the grains and the solute drag effect which limits dislocation movement. Moreover, the high concentration of Al solute would pin the growing boundaries of the new recrystallized nucleates and restrict recrystallization. In contrast, in samples with higher Sr concentration, the lower levels of Al & Mn would exert reduced pinning effect. As a result, dislocation motion would be easier and twinning more limited. Dislocations reach the grain boundaries where they accumulate leading to recrystallization via grain boundary migration. As a result, new grains with the deformation texture nucleate and grow within the necklace microstructure.

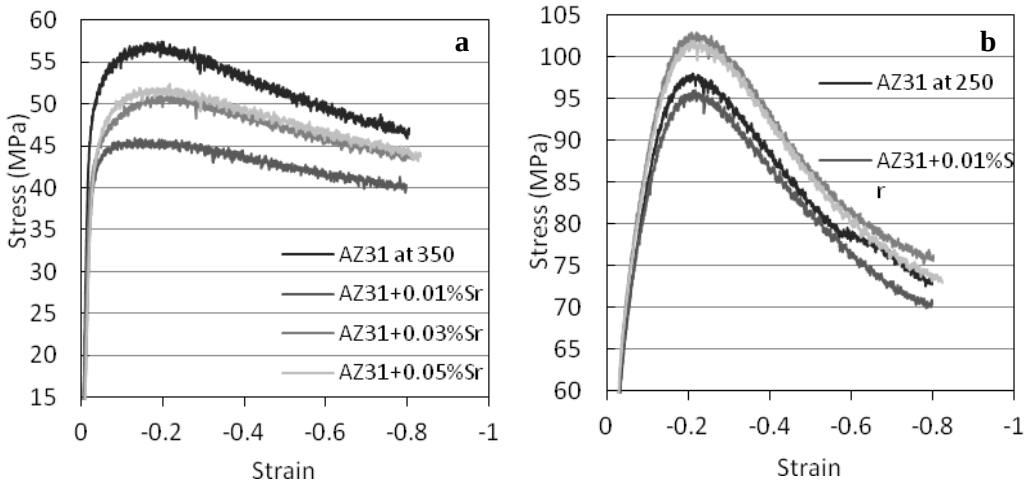

Figure.4.1. 12. True stress – True strain diagram of alloys containing different levels of Sr at (a) 250^{o}C and (b) 400^{o}C.

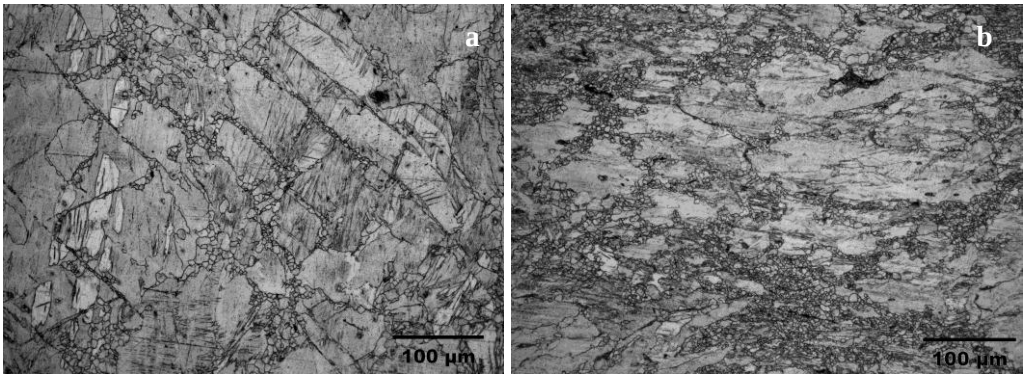

Figure.4.1.13. Microstructure of (a) AZ31 and (b) AZ31+0.8%Sr before entering the die opening during extrusion.

Gall and Jonas [26] have previously reported that above a transition temperature, the drag effect of solute atoms on the growing recrystallized grain boundaries becomes negligible. A similar behaviour was also observed in our samples, i.e. variations in solid solution concentration did affect the deformation mode during extrusion at 350^{o}C. Although there are some new grains that have clearly nucleated at the stringer interface during extrusion at 250^{o}C, their volume is only a small fraction of all the DRX grains. Hence, their contribution to overall texture weakening is insignificant.

4.1.4. Conclusions

The influence of Al-Sr stringers on the recrystallization behaviour of magnesium AZ31 alloy during extrusion at elevated temperatures has been investigated.

1) Al-Sr eutectic precipitates were found to elongate and distribute uniformly during extrusion and pin the grain boundaries, consequently preventing grain growth during recrystallization.
2) The Mg matrix adjacent to the stringers underwent local lattice rotation which led to a misorientation gradient (strain accumulation) close to the particles.
3) Particle stimulated nucleation (PSN) occurred in the deformed regions around the precipitates in certain hot working conditions at 350^{o}C. An increasing amount of Al-Sr stringers in AZ31 increased the high potential sites for PSN.
4) PSN through Al-Sr stringers resulted in the recrystallization of new grains with orientations other than the basal fiber texture results in reduction of fiber texture strength.
5) The effect was not seen at the extrusion temperature of 250^{o}C. Further investigations revealed that thermo-mechanical conditions during extrusion at 350^{o}C provided the appropriate situation for PSN, while 250^{o}C was not sufficiently hot to provide efficient recrystallization. Here, increasing Sr additions led to increased solute drag causing texture strengthening.

4.1.5. References

1. E.A. Ball, P.B. Prangnell, “Tensile-compressive yield asymmetries in high strength wrought magnesium alloys,” Scripta Metallurgica et Materialia, Volume 31, Issue 2 (1994) 111-116.
2. S. Kleiner, P.J. Uggowitzer, “Mechanical anisotropy of extruded Mg–6% Al–1% Zn alloy,” Materials Science and Engineering: A, Vol 379, Issues 1-2 (2004) 258-263.
3. HJ. McQueen, M. Pekguleryuz, “Hot workability of magnesium alloys,” Conf on magnesium alloys and their applications, Garmisch Partenkirchen, Germany, (1992)

4. J. Bohlen, S.B. Yi, J. Swiostek, D. Letzig, H.G. Brokmeier, K.U. Kainer, "Microstructure and texture development during hydrostatic extrusion of magnesium alloy AZ31,"Scripta Materialia Vol 53, Issue 2 (2005) 259-264.
5. L.W.F. Mackenzie, B. Davis, F.J. Humphreys, G.W. Lorimer, "The deformation, Recrystalization and texture of three magnesium alloy extrusions," Materials Science and Technology. Vol. 23, No. 10, (2007) 1173-1180.
6. F.J. Humphreys, M. Hatherly, "Recrystallization and related annealing phenomena," Pergamon Press, Oxford (1996)
7. J. Bohlen, M. R. Nurnberg, J. W. Senn, D. Letzig, S. R. Agnew, "The texture and anisotropy of magnesium–zinc–rare earth alloy sheets," Acta Materialia, 55 (2007) 2101-2112.
8. J.D. Robson, D.T. Henry, B. Davis, "Particle effects on recrystallization in magnesium–manganese alloys: Particle-stimulated nucleation," Acta Materialia, 57, (2009) 2739-2747.
9. Luo A., Pekguleryuz M.O., "Cast Magnesium Alloys for Elevated Temperature Applications," Journal of Materials Science, Vol 29, No 20, (1994) 5259-5271.
10. M. Pekguleryuz, E. Baril, P. Labelle, D. Argo, "Creep resistant Mg-Al-Sr alloys," Journal of Advanced Materials Vol 35, Issue: 3, (2003) .
11. M. Pekguleryuz, A.A. Kaya, "Magnesium diecasting alloys for high temperature applications," TMS Annual Meeting, Symposium on Magnesium Technology Charlotte, NC, (2004).
12. M. Pekguleryuz , M. Avedesian, "Magnesium Alloying - some Metallurgical Aspects," Conf on Magnesium Alloys and their Applications, Garmisch Partenkirchen, Germany, (1992).
13. A. Sadeghi, M. Pekguleryuz, "Precipitation during the Solidification of Mg-3wt%Al-1wt%Zn-(0.001-1%) Sr Alloys," American Foundry Society annual congress, Orlando, USA, (2010).

14. A. Sadeghi, M. Pekguleryuz, "Precipitation of Mg-3%Al-1%Zn-(0.01-1)wt%Sr Alloys during solidification," Journal of Materials Research (in submission).
15. L. Koubichek, "Effect of Small Additions of Elements on Grain Size and the Refinement of the Mg_4Al_3 [$Mg_{17}Al_{12}$] Phase in ML5 Alloy," Izv. Vyschikh. Outchebnykh Za Vedeny, Metallurgy of Non-Ferrous Metals, No 6, (1959).
16. J.E. Gruzleski and A. Aliravci, "Low Porosity, Fine-Grain Sized Strontium Treated Magnesium Alloy Castings," US Patent US005143564A (1992).
17. S.F. Liu, B. Li, X.H. Wang, W. Su, H. Han, "Refinement Effect of Cerium, Calcium and Strontium in AZ91 Magnesium Alloy," Journal of Materials Processing Technology, Vol 209, Issue 8, (2009) 3999-4004.
18. L'Espérance G., Plamondon P., Kunst M., Fischersworring-Bunk A., "Characterization of intermetallics in Mg–Al–Sr AJ62 alloys," Intermetallics, Vol 18, Issue 1, (2010) 1-7.
19. M. Kunst, A. Fischersworring-Bunka, G. L'Esperanceb, "Microstructure and dislocation analysis after creep deformation of die-cast Mg–Al–Sr (AJ) alloy" Materials Science and Engineering A, 510–511 (2009) 386.1.392.
20. Z. Li, J. Dong, X. Q. Zeng, C. Lu, W. J. Ding, "Influence of Mg17Al12 intermetallic compounds on the hot extruded microstructures and mechanical properties of Mg–9Al–1Zn alloy," Materials Science and Engineering A, Vol 466, Issues 1-2, 25 (2007) 134-139.
21. I. J. Polmear, "Light Alloys: Metallurgy of the Light Metals," Arnold Publications (1995).
22. S.I. Wright, M, M. Nowell "EBSD Image Quality Mapping," Microscopy and Microanalysis, 12 (2006) 72-84.
23. F. J. Humphreys, "The nucleation of recrystallization at second phase particles in deformed aluminium," Acta Metallurgica, Vol 25, 11, (1977) 1323-1344.
24. H.S. Zhang, K. Komvopoulos, "In situ synchrotron X-ray microdiffraction analysis of thermomechanically induced phase transformations in Cu-Al-Ni shape-memory alloy," Philosophical Magazine, 90: 16 (2010) 2235 - 2248

25. F. J. Humphreys, "Local lattice rotations at second phase particles in deformed metals," Acta Metallurgica, Vol 27, 12, (1979) 1801-1814.
26. R. Le Gall, J. J. Jonas, "Solute drag effects during the dynamic recrystallization of nickel," Acta Materialia, Vol 47, Issue 17, 26, (1999) 4365-4374.

4.2. Microstructure, Mechanical Properties and Texture Evolution of AZ31 Alloy Containing Trace Levels of Strontium

A. Sadeghi, M.O. Pekguleryuz

Materials Characterization, Volume 62, Issue 8, August 2011, Pages 742-750

4.2.1. Introduction

Strontium is known to be an effective grain refining element in Mg alloys containing high levels of Al [1,2]. Having a low equilibrium solid solubility, Sr has been shown to segregate to the surface of Mg grains and slow down grain growth [3]. It has also been shown that Sr refines the beta ($Mg_{17}Al_{12}$) precipitates in AZ31 [4]. The effects of Sr in AZ31 are dependent on the concentration of Sr in the alloy and the type of second phase which is precipitated. When added to AZ31, Sr forms Al-Sr, Mg-Al-Sr, Mg-Sr and Sr-Zn precipitates. In the Mg-Al-Zn system Sr prefers to bind with Al rather than other elements. Because of this high affinity of Sr to Al, all the precipitates in the AZ+Sr system can be classified into two groups: precipitates with Al and precipitates without Al. Sr-containing precipitates without Al ($Mg_{17}Sr_2$ and $SrZn_5$) only form at high concentrations of Sr where the affinity of free Al is decreased when most of it is captured in Al-Sr intermetallics. Sr precipitates with Al (Al_4Sr and Al_2Sr) are formed when Sr meets a high concentration of Al in the alloy. When the concentration of Al is low or the solidification condition slows down the diffusion of Al, Al-Mg-Sr precipitates form. In different alloying systems, many different stoichiometries for Al-Mg-Sr precipitates have been suggested [5-9]. Recently Janz *et al.* [10] have shown that τ-$Al_{38}Mg_{58}Sr_4$ is the only equilibrium ternary precipitate in the Mg-Al-Sr system and all other reported stoichiometries are non-equlibrium precipitates which depend on the alloy composition and solidification conditions. L'Esperance *et al.* [9] have shown the decomposition of the non-equilibrium Al-Mg-Sr ternary precipitate into Al_4Sr and Mg, by rejecting excess Mg and absorbing Al from the matrix.

The addition of low levels of Sr into Mg-3Al-1Zn will result in a high Al/Sr ratio, and therefore a precipitate with high Al/Sr ratio (e.g. Al_4Sr) will form. Even if the amount of precipitate is very small, it may have significant effects on microstructure, mechanical properties and deformation texture [11-14]. However, research concerning the effect of trace levels of Sr on the most commonly used

wrought AZ31 has not been extensively studied. In this work, the formation of new phases resulting from the addition of trace levels of Sr in AZ31 and its effects on mechanical properties and texture were investigated in as-cast and extruded samples by cooling curve analysis, thermodynamic predictions, electron probe micro-analysis (EPMA), hot compression and texture measurements.

4.2.2. Experimental Procedure

AZ31 alloys containing 0.01, 0.03 and 0.05wt% Sr were prepared using AZ31 extruded bars supplied by Applied Magnesium (Denver, CO) and Sr-10wt%Al master alloy (from Timminco, Haley, ON). AZ31 was melted in a graphite crucible using a high frequency induction furnace (NORAX). The melt was kept at 700^{o}C for 15 minutes under a gas mixture of CO_2-SF_6 to allow for sufficient dissolution and mixing of the alloying additions. The melt was cast at 720^{o}C into preheated (400^{o}C) cylindrical steel dies. The chemical compositions of the alloys were determined by inductively coupled plasma (ICP) and are summarized in Table 4.2.1. Cooling curve analysis was performed using sand cups and exposed junction thermocouples. The details of this analysis have been reported elsewhere [11].

Optical microscopy (OM) specimens were etched in a picric-acetic solution. Grain size was measured using the line intercept method. Electron probe microanalysis (EPMA) was performed on polished samples to identify phase compositions and to investigate the elemental distribution across the microstructure.

Pseudo-ternary phase diagrams of the Mn were calculated and plotted using the thermodyna FactSage software.

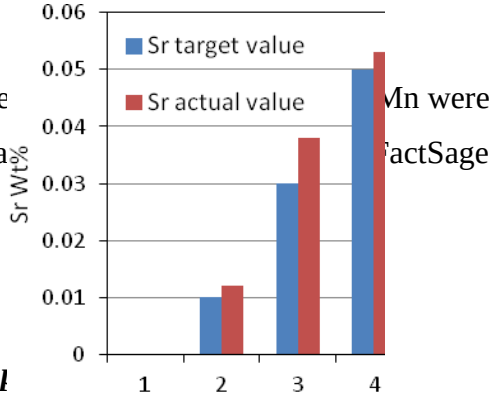

Table.4.2.1. Chemical comp

No.		1	2	3	4

	element	AZ31	AZ31+0.01Sr	AZ31+0.03Sr	AZ31+0.05Sr	
Chemical comp. *(wt%)*	Al	3.15	2.94	2.96	3.19	
	Zn	0.89	0.87	0.86	0.82	
	Mn	0.52	0.49	0.52	0.51	
	Sr	0	.012	.038	.053	

Hot compression samples were machined out of cast bars and compressed using an MTS universal machine equipped with a radiation furnace and a quartz tube conducting Ar gas around the heated sample to avoid oxidation at elevated temperatures. The effect of friction on the contact surfaces between the samples and the anvils was reduced by using boron nitride powder and mica plates. Samples containing different levels of Sr were compressed to a strain of 0.8 at a strain rate of $0.01s^{-1}$ at 250^{o}C and 350^{o}C. In order to retain the as-deformed microstructure, samples were quenched in water immediately after deformation. The hot extrusion of cast cylinders was conducted using a 100T hydraulic press and a forward extrusion die set. Samples were extruded at 250^{o}C and 350^{o}C with a 3:1 extrusion ratio to 10 mm bars with a ram speed of 4 mm s^{-1}. The details of extrusion experiments are explained elsewhere [12].

Texture measurements on the hot compressed and extruded samples were performed using a Bruker D8 X-ray diffractometer to scan a 1 mm square from the surface. Hot compressed samples were sectioned parallel to the cylinder base (section was perpendicular to the compression direction). The deformation zone of extruded samples was sectioned perpendicular to the circular cross section (section contains the extrusion direction). TextTools texture analysis software was used to calculate the orientation distribution function (ODF), to generate the pole figures, and to measure the volume fraction of prismatic planes in various directions.

4.2.3. Results and Discussion

4.2.3.1. Microstructure

One of the important purposes of this research was to determine how trace levels of Sr added to AZ31 would be incorporated into the microstructure during solidification. There are four possible scenarios for Sr atoms to be located in different regions and phases. They could (i) dissolve in α-Mg as a solid solution element, (ii) dissolve in the β-$Mg_{17}Al_{12}$ precipitates, (iii) segregate at the grain boundaries, or

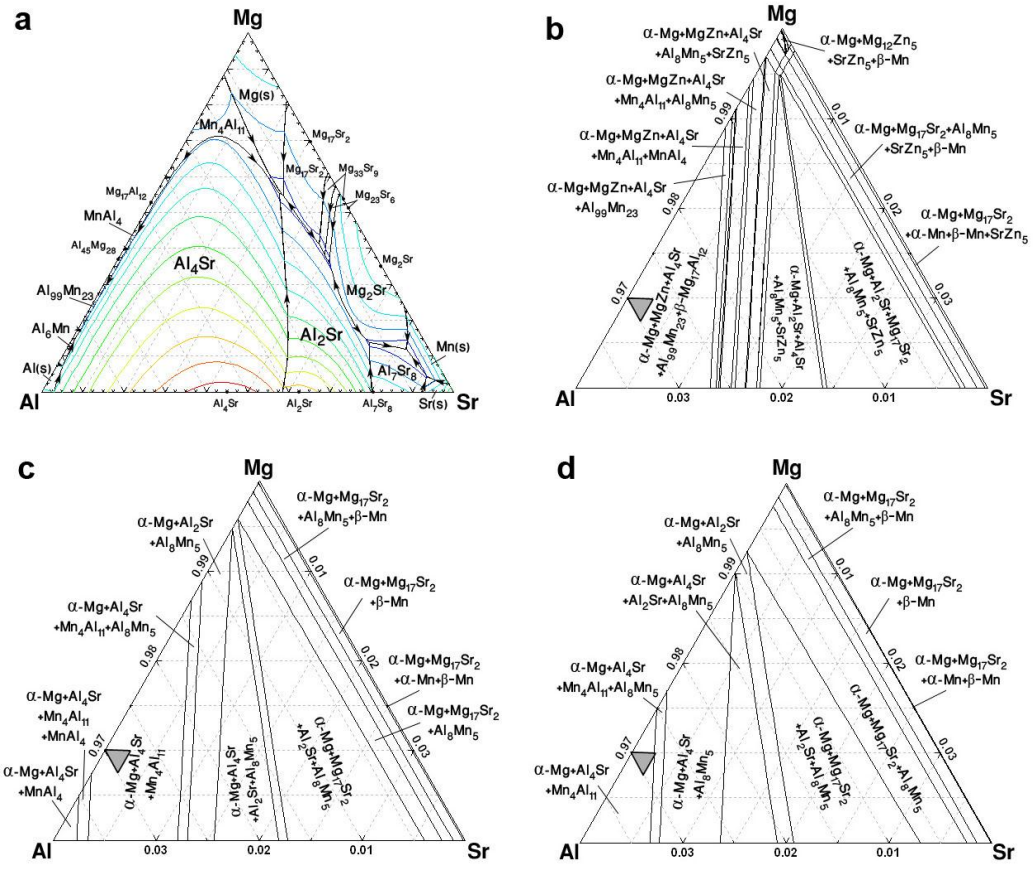

Figure.4.2.1. Pseudo-ternary phase diagrams of the Mg-Al-Sr-1wt%Zn-0.4wt%Mn. (a) Liquidus projection, (b) isothermal cross section at 350°C, (b) at 250°C, and (d) at 25°C. (The area of interest is labelled with the gray triangles.)

(iv) precipitate either as Al-Sr or Al-Mg-Sr secondary phases. Large atomic radius differences (r_{Sr}/r_{Mg}=34) [15] between Sr and Mg results in low maximum equilibrium solid solubility (0.04 at% [16]).

Solute trapping and extension of solid solution has also been reported for Sr atoms in Mg [16]. However, these happen at very high cooling rates (10^5-10^7 Ks^{-1}) which is quite different from the cooling rates observed in conventional casting. Janz *et al* [10] have reported that there is negligible Sr-solubility in Mg and in $Mg_{17}Al_{12}$. They have shown that in samples containing high levels of Sr (>2at%), Sr forms a distinct ternary phase τ-$Al_{38}Mg_{58}Sr_4$ instead of dissolving in β-$Mg_{17}Al_{12}$.

According to the thermodynamic calculations and phase diagrams shown in Fig.4.2.1, Al_4Sr is the only Al-Sr phase in the AZ31+(0.01-0.05)wt%Sr composition range which precipitates after Al_8Mn_5 and α-Mg.

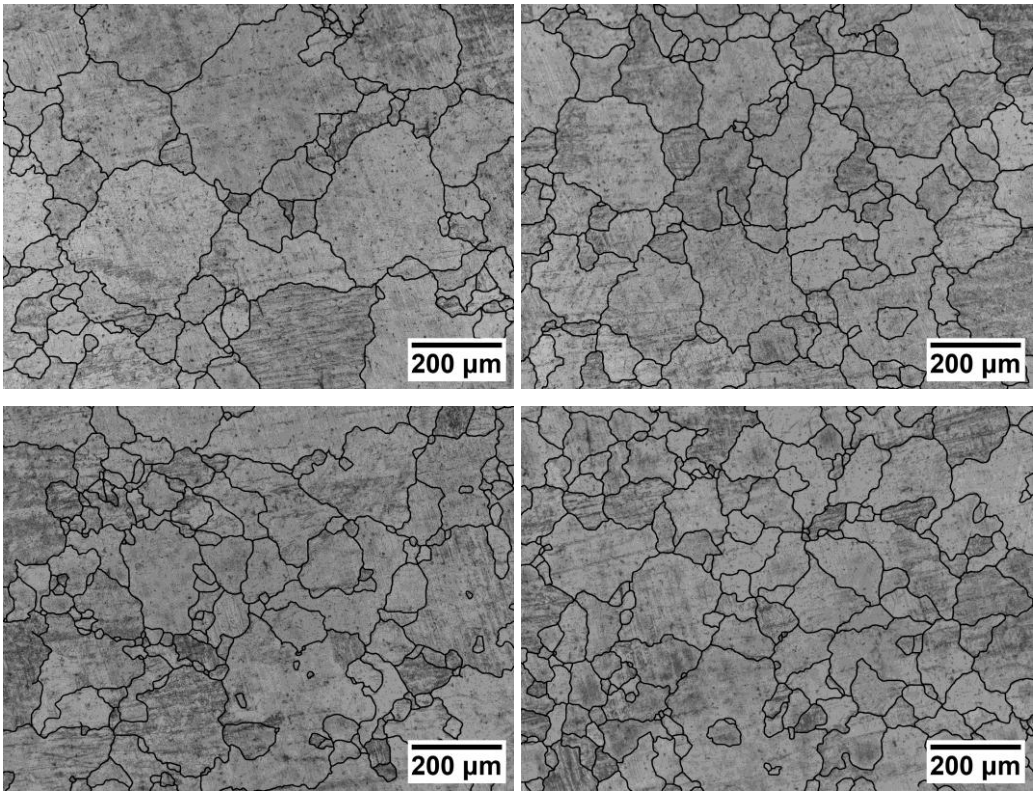

Figure.4.2.2. Optical micrographs of as-cast (a) AZ31, (b) AZ31+0.01%Sr (b) AZ31+0.03%Sr (b) AZ31+0.05%Sr.

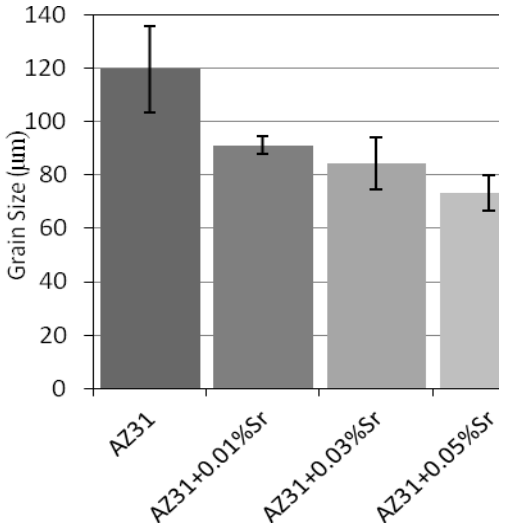

Figure.4.2.3. The grain size of as-cast samples containing different levels of Sr.

Isothermal sections of the pseudo-ternary phase diagram (Fig.4.2.1b-d) showed that from 350^{o}C to 250^{o}C and then down to 25^{o}C, the Al-Sr precipitates were stable while Al-Mn precipitates switched their stoichiometry toward a lower Al/Mn ratio [17]. In Fig. 4.2.3, the grain size of as-cast samples is plotted versus Sr level.

It can be seen in Figures 4.2.2 & 4.2.3 that the grain size was refined with increasing Sr. The fact that Sr precipitates after α-Mg refutes the idea that the grain refining effect of Sr in AZ31 is a result of increased nucleation sites for primary magnesium.

Sr is a surface active element for Mg. It adsorbs to the surface of a growing nucleus or grain and reduces the surface energy (ΔG_s) [19-21]. A reduction in surface energy raises the nucleation onset temperature; in other words, T_{min} in Fig.4.2.4a would increase. Furthermore, when ΔG_s is decreased, a stable nucleus would need smaller volume energy (ΔG_v) to overcome ΔG_s and as a result the critical size of a stable nucleus (r*) will decrease as well. Smaller nuclei would liberate less thermal energy as they become stable and continue to grow. Therefore, T_{max} will decrease as well. Altogether, when T_{min} is increased and T_{max} is decreased, ΔT will decrease. The cooling curve recorded from early stages of solidification (Fig. 4.2.4a,b) also showed a decrease in undercooling

when the level of Sr was increased to 0.03wt%. Undercooling determines the quantity of nuclei forming during solidification; when a large number of stable nuclei form and grow, the recalesence from these grains decreases the undercooling observed in the cooling curve, and at the same time depresses the fastest growing grains.

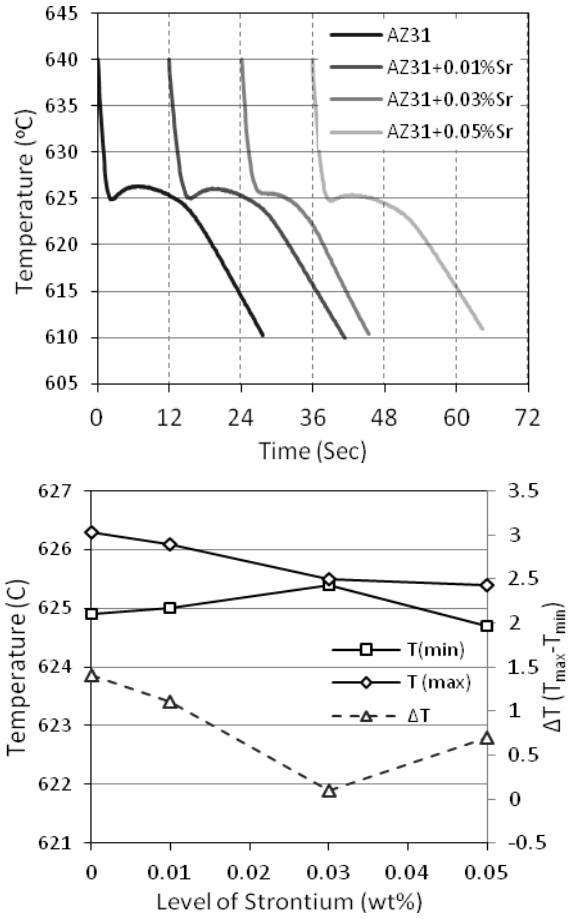

Figure.4.2.4. The cooling curves of AZ31 containing different levels of Sr.

Hence, all these factors indicate that Sr refines the grain size by stimulating inoculation of nuclei and slowing down their growth during solidification. It is interesting to mention that the presence of low levels of Sr in AZ31 also refines the β-$Mg_{17}Al_{12}$ precipitates. The fact that Al-Sr particles are precipitated before β-$Mg_{17}Al_{12}$ may raise the question as to whether those particles act as nucleation sites for β-$Mg_{17}Al_{12}$ precipitates.

Fig. 4.2.5 shows an EPMA of a β-$Mg_{17}Al_{12}$ precipitate next to an Al_4Sr particle in an as-cast AZ31+0.05wt%Sr alloy. The area with a brighter contrast in the backscattered image is the Al_4Sr precipitate. The solution of Zn inside the β-$Mg_{17}Al_{12}$ precipitate can be easily distinguished in the elemental map. No sign of Sr inside the beta phase could be detected which supports the idea that no Sr could be dissolved in beta, but it could prepare a nucleation site for it. Fig. 4.2.6 is another EPMA of the same sample at lower magnification. The overlap of Al and Zn and the association of Sr-containing particles with the beta precipitates in the interdendritic regions can be easily discerned in the elemental maps.

It has been previously reported that although there is substantial solid solubility of Mg in Al-Sr compounds [10], in alloys with high Sr/Al ratio (>0.3), the ternary τ-$Al_{38}Mg_{58}Sr_4$ phase precipitates through a quasi-peritectic (or quasi-eutectic) $L+Al_4Sr \rightarrow \tau+\alpha(Mg)$ or eutectic $L \rightarrow \tau+\alpha(Mg)$ reaction. In the present research, although the level of Sr and Sr/Al ratio were very low, the presence of Al-Sr precipitates in the interdendritic regions connected to the beta particles represents that Sr was supersaturated in the liquid and eutectic reactions. However, EPMA results showed low levels of Mg in Al-Sr precipitates and the formation of Al_4Sr is more likely in the eutectic reaction ($L \rightarrow Al_4Sr+\alpha$-Mg). The introduction of low levels of Sr refined the microstructure of AZ31 and this has important implications for mechanical properties and texture development.

4.2.3.2. Mechanical Properties

Hot compression stress-strain curves of the as-cast AZ31 and AZ31 alloys containing 0.01, 0.03 and 0.05wt% Sr at 250°C and 350°C are shown in Figs. 4.2.7a and b. The results indicate a change in mechanical properties of AZ31 with the addition of low levels of Sr. The main precipitate in the system is β-$Mg_{17}Al_{12}$, however, Al-Sr particles are also formed in the alloys containing Sr. We have previously reported that addition of Sr hampers the formation of beta particles and lowers the solid solubility of Al in α(Mg) [11-14,17]. Although the amount of Sr is very small in the present experiments, it reacts with Al and reduces its activity

in the system. By removing Al from solid solution, Sr would indirectly affect the hot compression behaviour of AZ31.

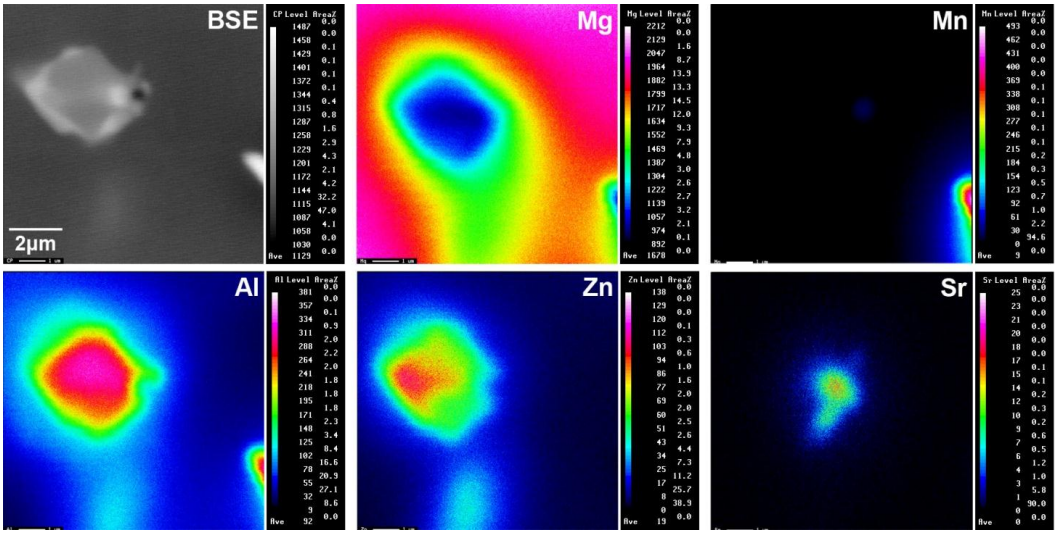

Figure.4.2.5 . Electron probe micro analysis (EPMA), elemental mapping of a β-$Mg_{17}Al_{12}$ precipitate in AZ31+0.05%Sr. The results indicate that Sr is not dissolved in β-$Mg_{17}Al_{12}$, however, it is present as a Sr rich phase next to the β-$Mg_{17}Al_{12}$ precipitate .

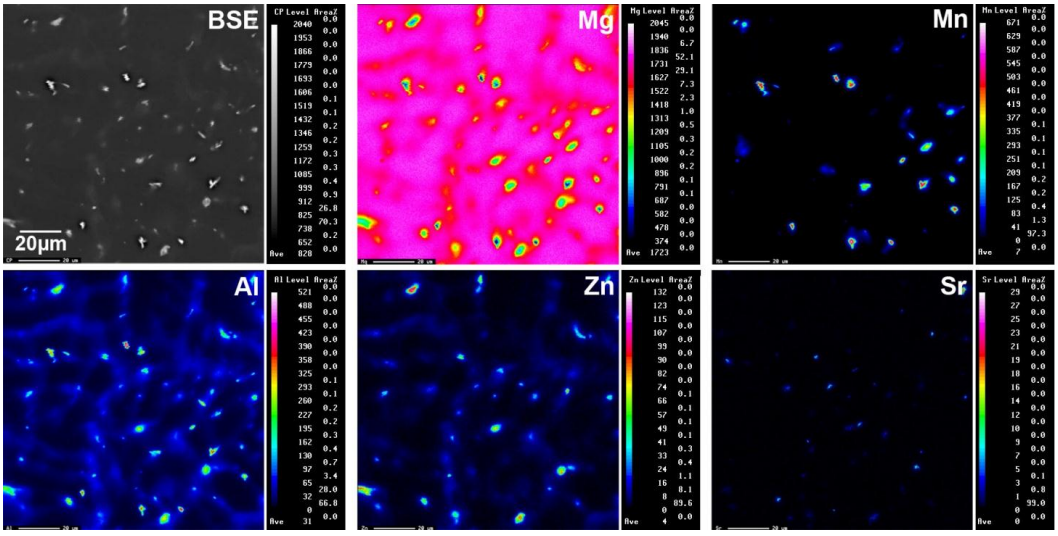

Figure.4.2.6. Electron probe micro analysis (EPMA), elemental mapping of AZ31+0.05%Sr microstructure showing the location of Sr-rich precipitates, the presence of Zn and the absence of Sr in the β-$Mg_{17}Al_{12}$ phase.

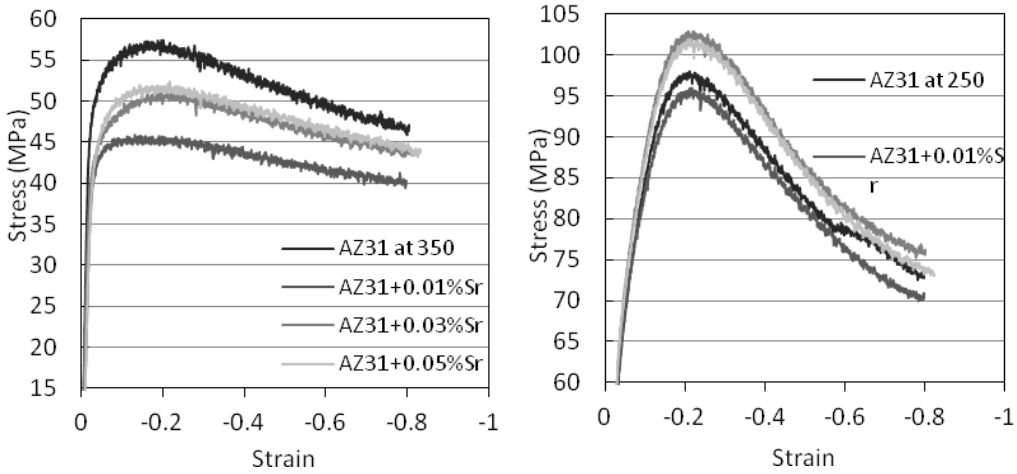

Figure4.2.7. Stress-strain curves for hot compression of AZ31 alloys containing different levels of Sr at (a) 350^{o}C and (b) 250^{o}C.

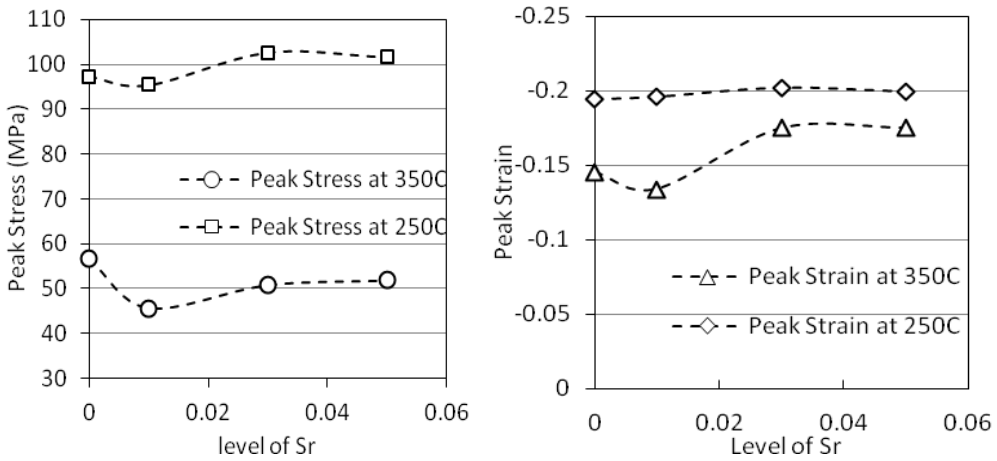

Figure.4.2.8. (a) Peak stress and (b) peak strain (ε_c) of the hot compression stress-strain curves at 250^{o}C and 350^{o}C.

Sr reduces the pinning effect of Al atoms on moving dislocations in primary Mg by depleting Al in solid solution [12,17]. The other effect of Sr on the mechanical properties is through the grain and particle-size refining effect which was described in the previous section.

The characteristics of the hot compression peaks of Fig. 4.2.7 (σ_{max} and ε_c) have been summarized in Figs. 4.2.8a and b. It can be seen that the peak stress of the stress-strain curves first drops (+0.01%Sr) then increases (+0.03% and 0.05%Sr) at both 250^{o}C and 350^{o}C (Fig.4.2. 8a) with increasing Sr. This could be explained

by the fact that at 0.01%Sr, the amount of thermally stable Al-Sr precipitates is not significant enough to increase the strength; here Sr would exert its effect via lowering the Al solid solubility which would make the alloy softer. By increasing the weight percent of Sr to 0.03 and 0.05, the amount of Al-Sr particles becomes effective and not only compensates for the softening effect of the lower Al solubility, but it also increases the strength via secondary phase hardening. It is important to mention that the flow stress during hot compression is almost independent of grain size [18].

In Fig. 4.2.8b, the critical strain before recrystallization (ε_c, strain at the maximum stress) has been plotted against Sr content. It is known that in samples with smaller grain size, the kinetics of DRX is accelerated and a smaller ε_c is expected [18]. Moreover, since Sr decreases the solid solubility of Al, there would be easier dislocation motion which accelerates the kinetics of recrystallization. However, the results of the present study indicate that at 250^{o}C ε_c does not decrease significantly with increasing Sr. A finer grain size is expected to speed up the recrystallization process by providing more nucleation sites at the boundaries; however it also reduces the possibility of twinning. Hence the Sr addition removes high energy twin boundaries which are potential sites for nucleation of recrystallization. Furthermore, it is also noted that increased Sr decreased the amount of beta precipitate at the grain boundaries and in the interdendritic regions whereby the grain boundaries became more permeable to dislocations. As a result, grain boundaries become less effective in blocking dislocations and recrystallization starts at higher strains.

At higher temperature (350^{o}C), due to the higher mobility of vacancies and activation of non basal slip systems, stable recrystallized nuclei form at lower strains (ε_c) and recrystallization starts sooner. However, interestingly at 350^{o}C, ε_c changes more significantly when the level of Sr is increased than it is at the lower temperature of 250^{o}C. Sr additions initially cause a drop in ε_c but further additions lead to a decrease. The main difference with respect to Sr in going from 250^{o}C to 350^{o}C is in the solubility of Sr. At 350^{o}C, the solid solubility of Sr in Mg is substantially higher than it is at 250^{o}C. At 350^{o}C, in addition to the effects of

twinning and of the beta precipitates, another micro mechanism related to the solid solubility of Sr becomes effective. Large Sr atoms pin the dislocations in α-Mg and delay the onset of recrystallization. At very low levels of Sr (0.01wt %), the effect of grain refinement is stronger than the effect of solute pinning and as a result ε_c becomes smaller than what has been measured for AZ31 with no Sr.

4.2.3.3. Texture

Fig. 4.2.9 shows the {0002} pole figures of the hot compressed samples. As expected, all the samples showed a concentration of poles in the center of the pole figure close to the compression axis. This texture is formed by twinning and has likely strengthened through the selective work hardening mechanism [22]. In grains having their c-axis aligned with the compression direction, dislocations were unable to move due to the very low resolved shear stress on the basal planes. While other grains with different orientations became work hardened and eventually recrystallized. This sequence is repeated in a cycle until all the non basal grains are consumed by DRX and only basal grains are left. It is observed that as the Sr level increased to 0.05wt%, the maximum intensity of the pole figures dropped at both hot compression temperatures. The maximum intensity values are shown in Fig.4.2.10a. Notably, the sample containing 0.01wt% Sr shows a maximum peak value. This trend, which has been previously noted for ε_c (Fig.4.2.8), was repeated here and demonstrates the close association between recrystallization and texture in these samples. The fraction of (0001) poles less than 20^o away from the compression axis is shown in Fig.4.2.10b. This value, which represents the distribution of basal poles, also showed the same trend seen in Fig.4.2.10a. The decrease in texture strength with increasing Sr can be explained by the effects of three micro-mechanisms; (1) grain refinement, (2) the effect of precipitates, and (3) the concentration change of solute atoms in α-Mg solid solution.

(1) When more Sr is present in the alloy the final grain size becomes smaller and as a result a more uniform deformation with lower amount of twinning and shear banding is expected. Twinning has a double effect on texture:

(i) the regions which undergo twinning have an orientation close to the basal texture and, (ii) The slip localizations due to a big orientation difference between two sides of twin boundary prepares perfect nucleation sites for newly recrystallized grains having the basal texture [23,24]. In the same way, shear bands are also regions of strain concentration and of recrystallization onset. As a result, when the grain size is refined and twinning and the formation of shear bands are reduced, the basal intensity will decrease.

(2) β precipitates can impede dislocation motion and cause dislocation pile-up near the β phases and inside the original grains, thus promoting the continuous DRX process [24]. Sr reduces the amount of beta precipitates and as a result it could decrease DRX followed by the basal texture.

(3) At elevated temperatures, by pinning the dislocations, Sr atoms in solid solution increase the critical resolved shear stress on the basal planes and the lattice resistance against dislocation movement and reduce work hardening. Moreover, Sr atoms are also able to limit the growth of newly recrystallized grains. Altogether, Sr in solid solution reduces the number of recrystallized grains by increasing the critical strain before recrystallization (ε_c). As described before, the smaller the number of grains consumed by DRX, the weaker the basal texture by the selective work hardening cycle [22].

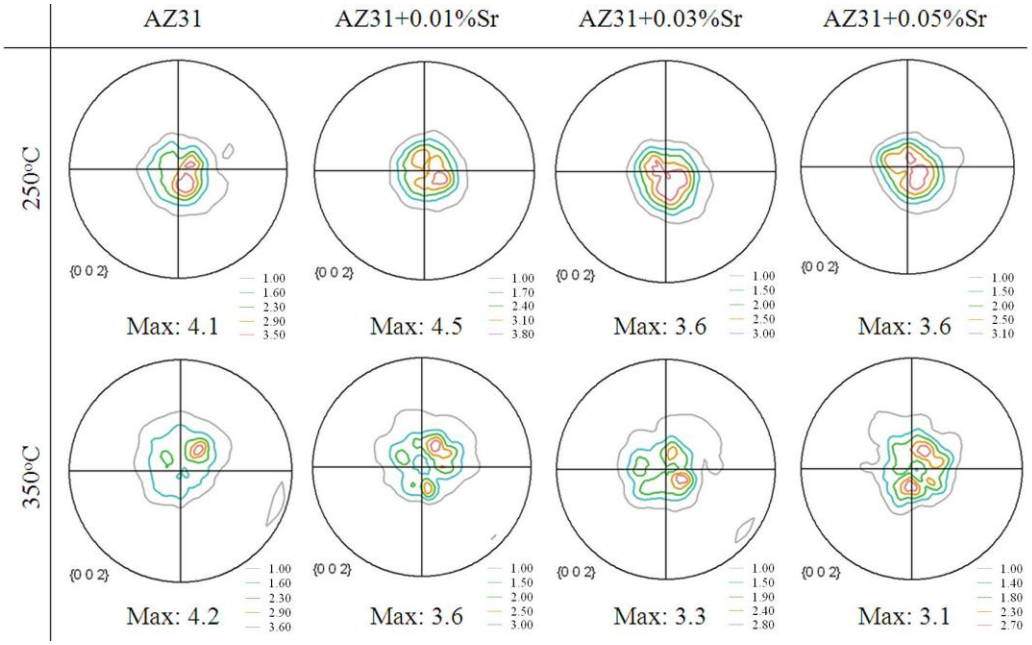

Figure.4.2 9.{0002} pole figures from the circular cross section of the hot compressed samples containing different levels of Sr at 250°C and 350°C.

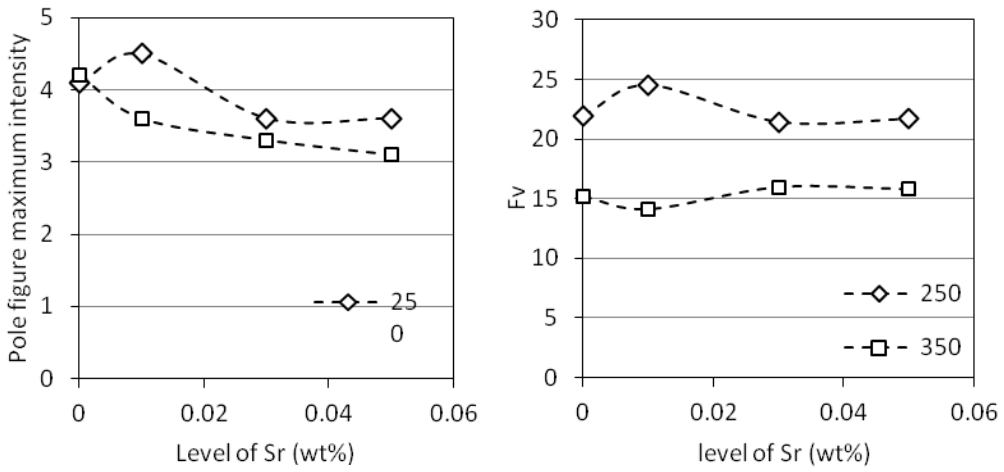

Figure.4.2. 10. (a) The maximum intensity of pole figures and (b) the volume fraction of basal normals <20° away from compression axis of hot compressed samples at 250°C and 350°C.

The initial increase of texture intensity by adding 0.01wt%Sr at 350°C could be related to the fact that the very low level of Sr is does not significantly effect β precipitation and is not enough to participate in dislocation pinning. Meanwhile, by slightly decreasing the Al content of the solid solution, Sr reduces

the lattice resistance against dislocation movement, promotes selective work hardening, and slightly increases the texture strength. While at 250^{o}C, there are less available slip systems and the solute atmosphere around the dislocations are less mobile and the pinning effect (the solute drag force) is higher which limits the work hardening process.

Extrusion trials also showed the same weakening effect on texture when 0.05wt% Sr was added to AZ31. X-ray pole figures measured from the rectangular cross-section of the extruded bars (cross section containing the extrusion direction) are shown in Fig. 4.2.11, which reveal that, in the sample containing a low level of Sr (Fig.4.2.11b), the contours spread out to a larger extent and the maximum intensity was lower. We have previously reported the effect of Sr additions on the extrusion texture of AZ31 [12-14]. It is known that according to the level of Sr and deformation temperature, different micro mechanisms are involved which effect the final texture.

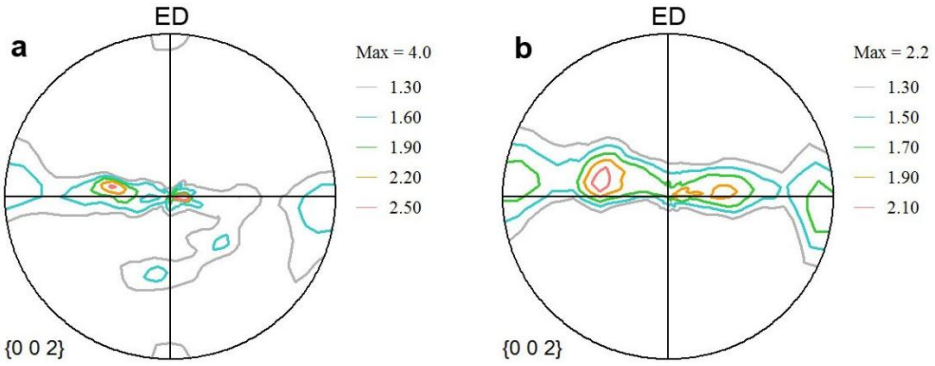

Figure.4.2.11. {0002} pole figures of extruded (a) AZ31 and (b) AZ31+0.05wt% Sr at 300^{o}C.

One of the important micro mechanisms is particle stimulated nucleation (PSN) where new grains are formed at the Al-Sr precipitates [12-14]. It is important to mention that, in the present research, the amount of the thermally stable precipitates is not high enough (0.2wt%Sr at 350^{o}C [14]) to support PSN. And the texture weakening effect in the samples containing low levels of Sr

(<0.05wt%) is a consequence of grain refinement and the other two micro mechanisms described above.

Note that the observed texture weakening effect in these alloys in extrusion at 300^{o}C cannot not be extrapolated to other temperatures and compositions. The extrusion behaviour of AZ31+Sr alloys is strongly dependent on temperature [12]. At temperatures below 300^{o}C, Al depletion increases the recrystallization rate and would increase the final texture strength [13]. While at temperatures above 300^{o}C, the density of vacancies is high enough to supply the activation energy of recrystallization even for smaller dislocation pileups (strains) and the effect of PSN then becomes more significant.

4.2.4. Conclusion

Microstructure, mechanical properties and deformation texture of AZ31 and AZ31 alloys containing low levels of Sr (0.01wt% to 0.05wt%) were compared and the following was concluded:

1- Microstructural observations supported by cooling curves and EPMA show grain and precipitate (β-$Mg_{17}Al_{12}$) refinement by growth poisoning and via nucleant formation, respectively with the addition of low levels of Sr to AZ31.

2- Low levels of Sr had a significant effect on the hot deformation behaviour of AZ31. The peak stress (σ_{max}) and critical strain before recrystallization (ε_c) first dropped with the addition of Sr and then increased. It is noted that σ_{max} first decreases due to the decrease of Al solubility in α-Mg and then increases when the amount of the Sr-containing precipitates becomes significant. Moreover, ε_c drops when the kinetics of DRX is accelerated by grain refinement. With the addition of Sr, ε_c increases when more Sr atoms pin dislocations and retard recrystallization.

3- Sr reduces the strength of the basal texture in hot compression and extrusion which can be attributed to the decrease in twinning and the change in the concentration of Al and Sr atoms in Mg solid solution.

4.2.5. References

1- J.E. Gruzleski and A. Aliravci, “Low Porosity, Fine-Grain Sized Strontium Treated Magnesium Alloy Castings,” US Patent US005143564A, (1992)

2- Liu S.F., Li B., Wang X.H., Su W., Han H., “Refinement Effect of Cerium, Calcium and Strontium in AZ91 Magnesium Alloy,” Journal of Materials Processing Technology, Vol 209, Issue 8, (2009)

3- S.F. Liu, B. Lia, X.H. Wanga, W. Sua, H. Han, “Refinement effect of cerium, calcium and strontium in AZ91 magnesium alloy,” Journal of Materials Processing Technology, Volume 209, Issue 8, 21 (2009) 3999-4004.

4- L. Koubichek, “Effect of Small Additions of Elements on Grain Size and the Refinement of the Mg4Al3 [Mg17Al12] Phase in ML5 Alloy,” Izv. Vyschikh. Outchebnykh Za Vedeny, Metallurgy of Non-Ferrous Metals, No 6, (1959)

5- X. Zeng, Y. Wang, W. Ding, A. A. Luo, A. K. Sachdev, “Effect of strontium on the microstructure, mechanical properties, and fracture behaviour of AZ31 magnesium alloy,” Metallurgical and Materials Transactions A, Vol 37, No 4 (2006) 1333-1341.

6- M. Pekguleryuz, E. Baril, P. Labelle, D. Argo, ”Creep resistant Mg-Al-Sr alloys,” Journal of Advanced Materials Vol 35, Issue: 3, (2003).

7- M. Pekguleryuz, A.A. Kaya, “Magnesium diecasting alloys for high temperature applications,” TMS Annual Meeting, Symposium on Magnesium Technology Charlotte, NC, (2004).

8- P. Zhao, Q. Wang, C. Zhai, Y. Zhu, “Effects of strontium and titanium on the microstructure, tensile properties and creep behaviour of AM50 alloys,” Materials Science and Engineering: A, Vol 444, Issues 1-2, (2007).

9- L'Espérance G., Plamondon P., Kunst M., Fischersworring-Bunk A., “Characterization of intermetallics in Mg–Al–Sr AJ62 alloys,” Intermetallics, Vol 18, Issue 1, (2010).

10- A. Janz, J. Gröbner, D. Mirković, M. Medraj, Jun Zhu, Y. A. Chang, R. Schmid-Fetzer: "Experimental study and thermodynamic calculation of Al-Mg-Sr phase equilibria," Intermetallics, 15, (2007) 506-519.

11- A. Sadeghi, M. Pekguleryuz, "Precipitation during the Solidification of Mg-3wt%Al-1wt%Zn-(0.001-1%) Sr Alloys," American Foundry Society annual congress, Orlando, USA, (2010).

12- A. Sadeghi, M. Pekguleryuz, "Recrystallization and Texture Evolution of Mg-3%Al-1%Zn-(0.4 -0.8) %Sr Alloys during Extrusion," Materials Science and Engineering A, (in press), 2010.

13- A. Sadeghi, M. Hoseini, M.O. Pekguleryuz, "Effect of Sr addition on Texture Evolution of Mg-3Al-1Zn (AZ31) Alloy during Extrusion," Materials Science and Engineering A 528 (2011) 1678–1685.

14- A. Sadeghi, M. Hoseini, M. Pekguleryuz, "Effect of Sr addition on texture evolution of Mg–3Al–1Zn (AZ31) alloy during Extrusion," Materials Science and Engineering A 528 (2011) 3096–3104

15- L. Pauling, in The Nature of the Chemical Bond, 2nd ed, Oxford University Press, Oxford, 1960.

16- E. Hehmann, E. Sommer, B. Predel, "Extension of Solid Solubility in Magnesium by Rapid Solidification," Materials Science and Engineering, A125 (1990) 249-265 249

17- A. Sadeghi, M. Pekguleryuz, "Precipitation of Mg-3%Al-1%Zn-(0.01-1)wt%Sr Alloys during solidification," Journal of Materials Research, Volume 26 / Issue 07 (2011) 896 – 903.

18- F.J. Humphreys, M. Hatherly, "Recrystallization and related annealing phenomena," Pergamon Press, Oxford (1996)

19- B. Tanga, S. Lib, X. Wanga, D. Zengc, R. Wuc, "Effect of Ca/Sr composite addition into AZ91D alloy on hot-crack mechanism," Scripta Materialia, Volume 53, Issue 9 (2005) 1076.1.1082

20- H.L. Zhao, S.K. Guan, F.Y. Zheng, "Effects of Sr and B addition on microstructure and mechanical properties of AZ91 magnesium alloy," J. Mater. Res., Vol. 22, No. 9 (2007) 2423-2428

21- S. Guan, S. Zhu, L. Wang, Q. Yang, W. Cao, "Microstructures and mechanical properties of double hot-extruded AZ80+xSr wrought alloys," Transactions of Nonferrous Metals Society of China,Volume 17, Issue 6, (2007) 1143-1151

22- Qinglin Jina, Sung-Yong Shima, Su-Gun Lim, "Correlation of microstructural evolution and formation of basal texture in a coarse grained Mg–Al alloy during hot rolling," Scripta Materialia, Vol 55, Issue 9 (2006) 843-846.

23- Maoyin Wang, Renlong Xin, Bingshu Wang, Qing Liu, "Effect of initial texture on dynamic recrystallization of AZ31 Mg alloy during hot rolling," Materials Science and Engineering A 528 (2011) 2941–2951.

24- S.W. Xu, S. Kamado, N. Matsumoto, T. Honma, Y. Kojim, "Recrystallization mechanism of as-cast AZ91 magnesium alloy during hot compressive deformation," Materials Science and Engineering A 527 (2009) 52–60

4.3. Effect of Sr addition on Texture Evolution of Mg-3Al-1Zn (AZ31) Alloy during extrusion

A. Sadeghi, M. Hoseini, M.O. Pekguleryuz

Materials Science and Engineering: A, Volume 528, Issues 6.1.8, 25 March 2011, Pages 3096-3104

4.3.1. Introduction

Because of their restricted workability and complex deformation behaviour, Mg wrought alloys have not reached their full potential where they could be widely used for weight-sensitive applications. These restrictions are due to the limited number of active slip systems in HCP (hexagonal close-packed) Mg, which necessitates the combination of different deformation modes to attain uniform deformation. In Mg alloys, the thermo-mechanical conditions play important roles in the activation of different deformation micro-mechanisms which influence the final texture [1-5]. Alloying elements can also affect the deformation modes and the final texture either by dissolving in the Mg matrix or by forming various precipitates [6-17]. It has been shown in a number of works [6-10] that the addition of rare earth elements and their dissolution in Mg matrix can improve ductility. The effect of alkali earth elements such as Calcium [10-12] and Strontium (Sr) [12,14] on the extrusion behaviour and mechanical properties of Mg alloys have also been previously studied.

Sr is known to be an effective element for improving the high temperature mechanical properties of Mg alloys via the formation of thermally stable precipitates [13-17]. The $Mg_{17}Sr_2$ intermetallic (melting point: 624^{o}C [18]) precipitates in Mg-Sr alloys that do not contain aluminum. In Mg-Al-Sr alloys, Sr binds with Al to form the Al_4Sr precipitate (melting point: 740^{o}C [18]) and minimizes or eliminates the β-$Mg_{17}Al_{12}$ observed in Mg-Al alloys [19]; Sr also decreases the solid solubility of Al in primary Mg [20]. Recently, the authors have studied the effect of Sr addition on the precipitation, microstructure and extrusion texture of AZ31 (Mg-3Al-1Zn) [14, 19, 20]. It was reported that 1 wt%Sr in AZ31 weakens the <10.0> extrusion texture at high temperatures (350^{o}C) as a result of

particle stimulated nucleation (PSN) of recrystallized grains at the Al_4Sr stringer boundaries. In contrast, at relatively lower temperatures (250^{o}C), Sr strengthens the texture by reducing the solute-drag effect due to the reduced Al solubility and by increasing dynamic recrystallization (DRX) via grain boundary bulging or twin induced mechanisms [20].

Even though Sr was seen to exert different effects depending on the Sr level and deformation temperature, it was noted that further experimental work across a range of temperatures and Sr levels would be necessary to elucidate the micro-mechanisms which affect the final texture under different thermo mechanical conditions. In the present paper, two-dimensional (2D) contours of recrystallization texture, peak stress of hot compression, and DRX critical strain have been plotted versus temperature and Sr concentration. The gradients and extrema between all three parameters have been compared and a comprehensive trend-view has been derived. Finally, by adding the boundaries of twinning, and surface cracking to the DRX contours, a general map for extruding AZ31 containing up to 1% Sr at 250^{o}C to 400^{o}C has been plotted.

4.3.2. Experimental procedure

Alloys were synthesized by adding different levels of Sr in to Mg-3wt%Al-1wt%Zn (AZ31) alloy. Four (4) alloys were selected for extrusion and ten (10) were hot compressed. The chemical compositions of the alloys with different Sr content were determined by inductively coupled plasma (ICP). The selected alloys for hot compression and hot extrusion deformation are listed in Table 3.1.1 and 4.1.1 respectively. All compositions are given in wt % unless otherwise specified. Molten alloys were cast into a preheated steel die under inert gas flow. Details of the casting method have been explained elsewhere [20].

Cylindrical bars were machined out of the castings to prepare the extrusion billets (30 mm in diameter, 50 mm in height) and hot compression samples (6 mm in diameter, 9 mm in height). Extrusion was performed at four temperatures (250, 300, 350, and 400^{o}C) for all four selected compositions (16 extrusion trials) to 1/9 cross section using a 100T hydraulic press, a steel die setup and a ceramic

insulated band heater to maintain the desired deformation temperature. Strain rate was kept constant through all the trials (0.3 sec^{-1}). A high temperature anti-seize paste (Molycote P-37) was used as a lubricant during hot extrusion. All extruded samples were air cooled after deformation.

Hot compression tests were conducted using a 510 MTS servohydraulic mechanical testing machine. Straining was carried out to true strains of 0.8 at a strain rate of 0.01 s−1. Samples were subjected to heat 15 minutes prior to deformation and were protected from oxidation at high temperatures using an argon shield. Mica plates and boron nitride powder were used to minimize friction and enhance uniform deformation in the compressed samples. The critical strain for the start of DRX (ε_c) and the maximum stress (σ_{max}) were obtained from the stress-strain curves which were plotted based on the hot compression data.

Microstructures were observed using optical microscopy (OM) and scanning electron microscopy (SEM) on samples etched with a picric acetic solution. In order to investigate the secondary phase morphologies and eliminate the effect of the Mg matrix during chemical analysis, precipitate extraction was performed using an acetic solution.. Surface characterization of the extruded samples was carried out using optical stereoscopic microscopy.

The crystallographic texture was measured by X-ray diffraction (XRD) using a Bruker D8 X-ray diffractometer. Pole figures and orientation distribution functions (ODF) were calculated using TexTools texture analysis software. The volume fraction of prismatic planes perpendicular to the extrusion direction (F_v) was used as a measure of <10.0> texture development during extrusion (Fig.4.3.1). F_v was calculated from ODF data using TextTools software. Details of experimental procedure have been described previously [20].

The F_v values of the sixteen (16) extrusion trials (four compositions at four temperatures), and the ε_c and σ_{max} data of the forty (40) hot-compression samples (ten compositions at four temperatures) were integrated in three numerical matrices. In order to find the general trend and gradients over the whole temperature and composition ranges, three-dimensional (3D) planes as a function

of second order temperature (T^2) and second order composition (C^2) were fitted through the data points using hyperbolic interpolation in MatLab software.

4.3.3. Results and Discussion

4.3.3.1. Method for Texture Comparison

During the hot extrusion of Mg alloys, prismatic planes align perpendicular to ED and form a strong <10.0> fiber texture [14, 22-24]. In the group of alloys investigated in the present study, this texture formed at all extrusion temperatures (Fig.4.3.1). However, the strength of the texture varied depending on the composition and temperature (Fig.4.3.1). The maximum intensity of the pole figures or the inverse pole figures (IPF) gives an indication as to how the texture changes in different extrusion conditions but it has its limitations. The magnitude of the maximum intensity of a pole figure does not include the orientation where the maximum is located. Hence, comparing the values originating from this parameter can be misleading.

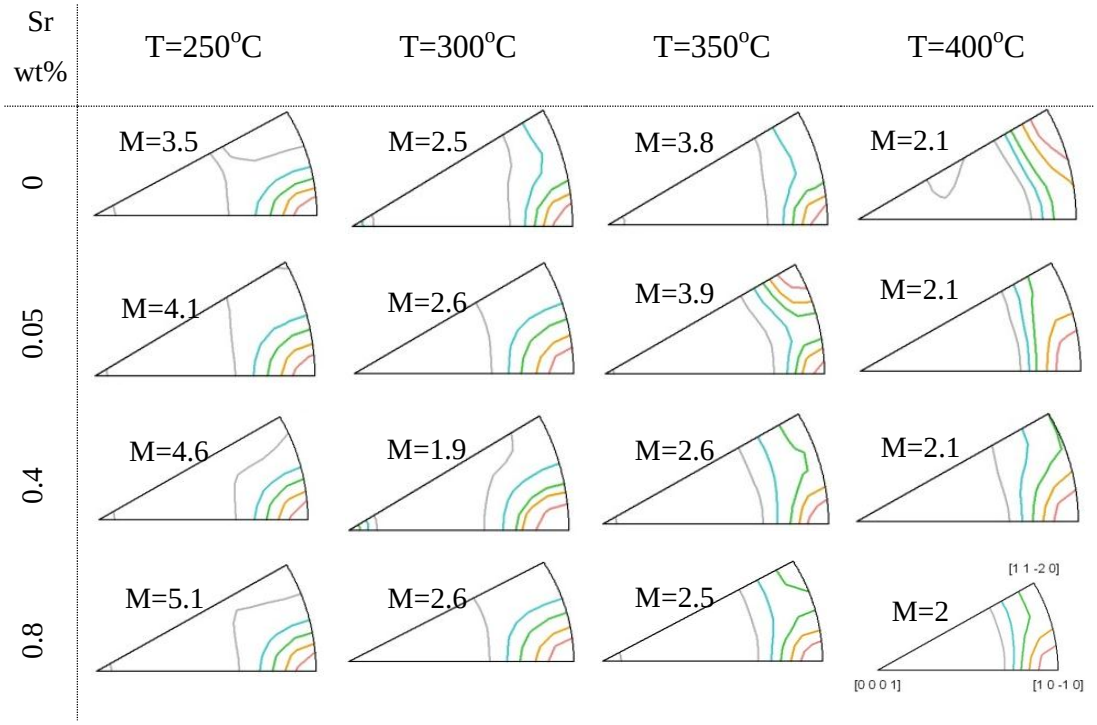

Figure.4.3.1. Inverse pole figures (IPF) at extrusion direction of the samples extruded at different temperatures and levels of Sr.

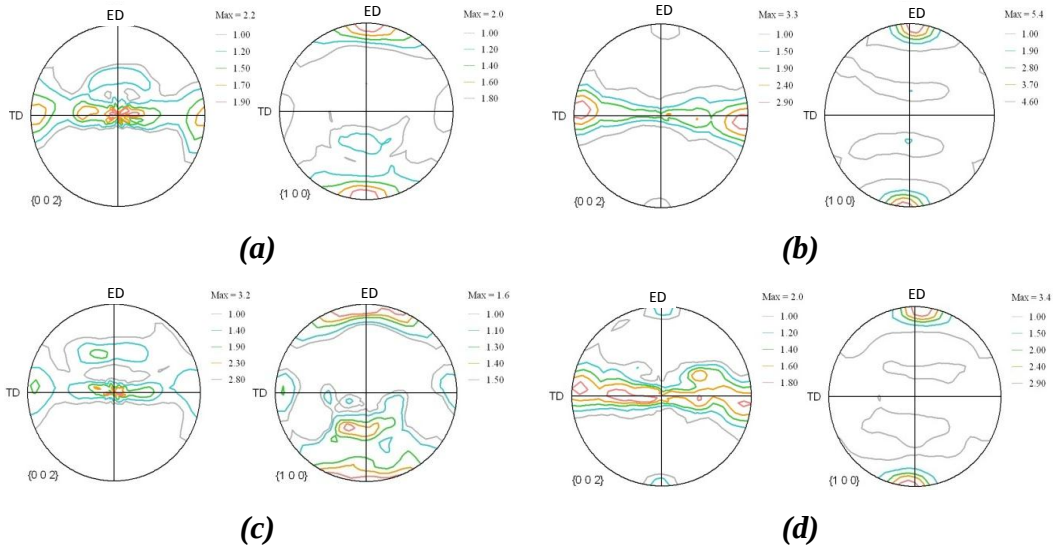

Figure.4.3.2. (0002) and (10-10) pole figures of AZ31+0.8%Sr following extrusion (a) at 400^{o}C, (b) at 250^{o}C and of AZ31 following extrusion (c) at 400^{o}C and (d) at 250^{o}C.

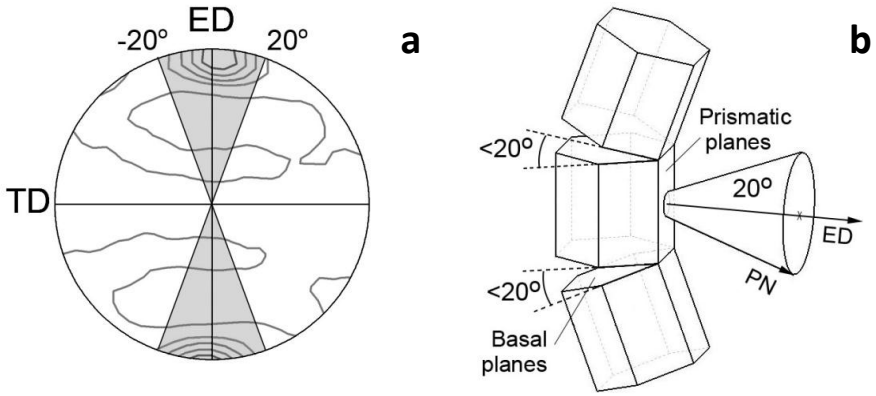

Figure.4.3.3. Selected orientations as prismatic normals (PN) less than 20^o away from the extrusion direction (ED). (a) the darker region in a {100} pole figure, (b)Schematic view of the hexagonal lattice.

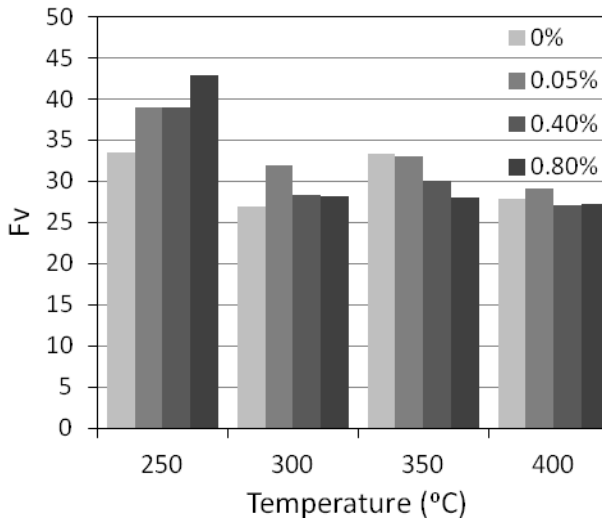

Figure.4.3.4. Volume fraction of prismatic planes having less than 20 degrees deviation from extrusion direction at different temperatures and Sr contents.

Fig.4.3.2 shows the {002} and {100} pole figures of extruded AZ31 and AZ31+0.8%Sr at 250 and 400^{o}C. It can be seen that the <10.0> texture developed in all conditions. More concentrated contours (stronger texture) could be distinguished for the samples extruded at 250^{o}C in the {100} pole figures. By comparing the pole figures of AZ31 and AZ31+0.8%Sr extruded at 400^{o}C, it was noticed that the maximum intensity of {002} pole figure for the alloy containing strontium was lower than AZ31 (2.2 compared to 3.2 for AZ31), in contrast the maximum intensity of the {100} pole figure was 2 for the alloy containing strontium compared to 1.6 for AZ31. This is because the value for maximum intensity is not dependent to the orientation of the poles, which confirms that judging the strength of the final fibre texture on the maximum intensity values alone may be misleading.

For a more accurate investigation, the orientation and volume fraction of the poles in relation to the specimen directions (ED, TD) can be combined into a single value. The dark section in Fig.4.3.3a shows the orientations in which the prismatic poles (normals) are less than 20^{o} away from to the extrusion direction. Fig.4.3.3b demonstrates the schematic of the range of orientations (as a cone) where the prismatic normals (PN) have less than 20^{o} misorientation from the

extrusion direction and the hexagonal lattice orientations that fit in the dark region shown in Fig.4.3.3a. The volume fractions of the planes with these specifications were used as a measure to quantify the <10.0> ring basal fiber texture in all the extruded samples. Fig.4.3.4 shows the effect of temperature and composition on the measured volume fraction of prismatic planes having normals < 20^o from the extrusion direction. It can be seen that the fiber texture looks stronger at lower temperatures. This can be explained by the different modes of DRX that become operative at different temperatures for different microstructures.

4.3.3.2. Microstructure

Depending on the Sr content, Mg-Al-Zn-Sr-(Mn) alloys have complex microstructures [20] which would significantly influence their deformation behaviour. In the Mg-3Al-Zn (AZ31) alloy, aluminum atoms could either form Al-Mg precipitates (β-$Mg_{17}Al_{12}$) or dissolve the in primary α-Mg grains. Moreover, in commercial Mg alloys containing Mn, aluminum binds with Mn as well and forms AlMn and Al_5Mn_8 precipitates [19]. The zinc atoms dissolve in the α-Mg grains and segregate at the grain boundaries [19,24]. Sr, added to this system, forms eutectic Al-Sr precipitates at the grain boundaries and in the interdendritic regions. These precipitates become continuous at the grain boundaries with increasing the level of Sr (at 1wt%Sr). For different Al/Sr ratios of the alloys, different stochiometries have been reported for the Al-Sr phase [13,15-16,25-27]. In the composition range studied in the present work, the equilibrium Al-Sr precipitate is Al_4Sr which has the ability to dissolve Mg and Zn in its lattice structure [19,28]. The stoichiometry of the Al-Sr precipitates, when subjected to heat, moves towards the more stable Al_4Sr by rejecting their excess solute atoms [28]. Thermodynamic calculations predict the formation of $SrZn_5$ and Al_2Sr at higher Sr concentrations (2.2 and 2.5wt%Sr respectively) [14].

The small amounts of Mn (<0.5wt%) which are present in commercial AZ31 alloys forms Al_8Mn_5 and AlMn precipitates. As Sr increases, a lower amount of Al remains available binding Mn in an intermetallic compound. Hence, Al-Mn precipitates having smaller Al/Mn ratio become stable [19]. In Fig.4.3.5,

the secondary electron (SE) image and energy dispersive spectroscopy (EDS) mapping of AZ31+0.8%Sr illustrates an Al_4Sr eutectic precipitate (A) and an Al-Mn dendrite (B) extracted out of the Mg matrix.

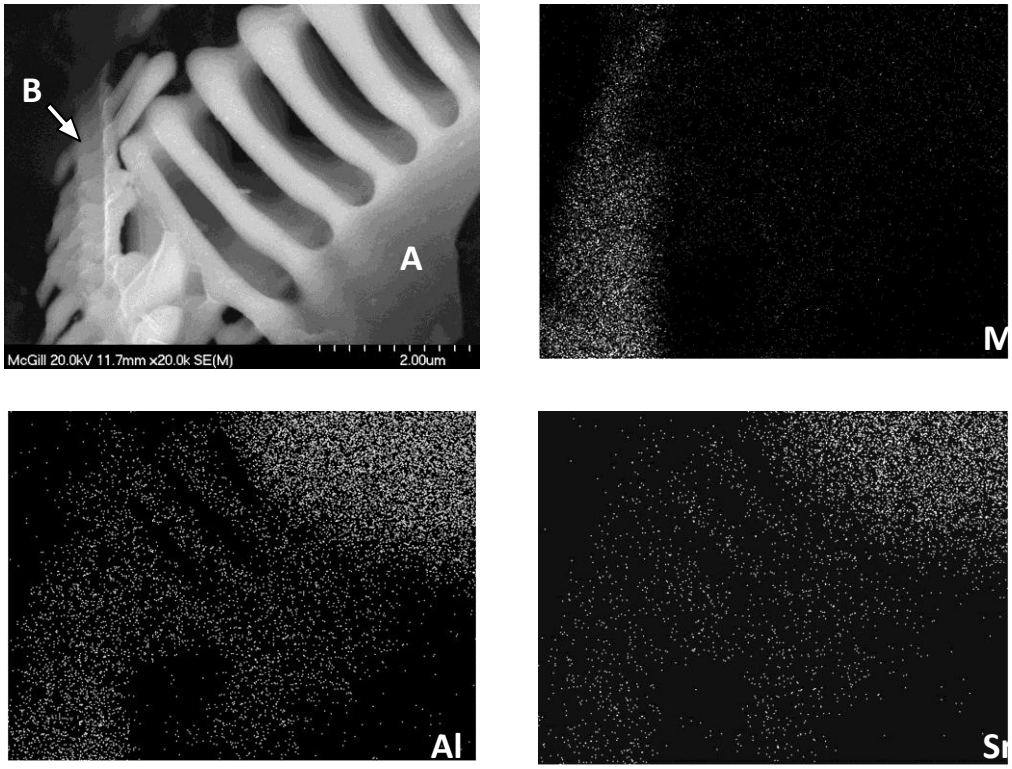

Figure.4.3.5. Scanning electron and EDS element maps for extracted Al-Sr (A) and Al-Mn (B) precipitates from as-cast AZ31+0.8%Sr

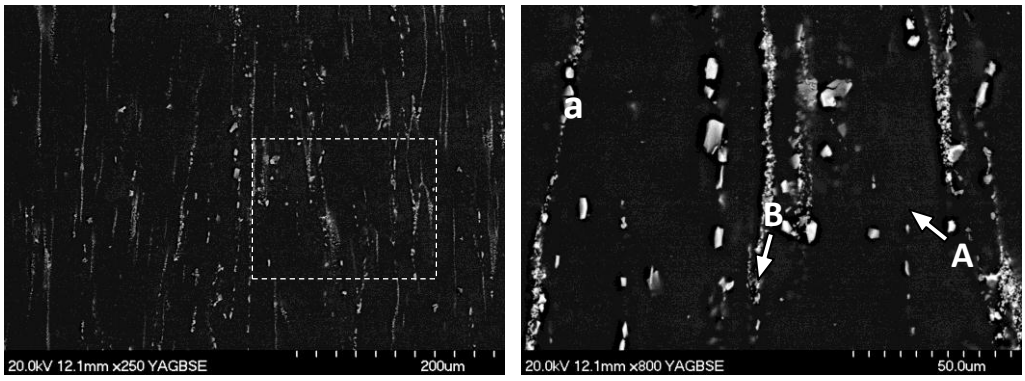

Figure.4.3.6. Back scattered electron image of (a) precipitates after extrusion of AZ31+0.8%Sr, (b) higher magnification of the dashed region (Al-Sr and Al-Mn precipitates are labled as A and B respectively).

The Al_4Sr precipitates were observed to be stable during hot deformation which results in the formation of stringer-shaped precipitates by breaking and relocating during extrusion (Fig.4.3.6a and b). It has previously been shown [20] that these precipitates are able to act as nucleation sites for DRX where the stored energy of accumulated dislocations provides the driving force for nucleation. Nonetheless, PSN is not the dominant micro mechanism for recrystallization at all temperature and composition ranges [20]. Under specific conditions where PSN is significant, a large number of new grains having different orientations from the fibre texture forms which results in texture weakening.

It should be noted that the Mg-Al-Zn-Sr (Mn) alloys exhibit varying microstructures and precipitate structures which can play significant roles in altering the deformation behaviour at elevated temperatures [14]. In order to determine the different micro-mechanisms that can be activated under different temperature-composition conditions, an analysis of the hot-compression response of the alloys was conducted and this was related to the alloy microstructures and the phases.

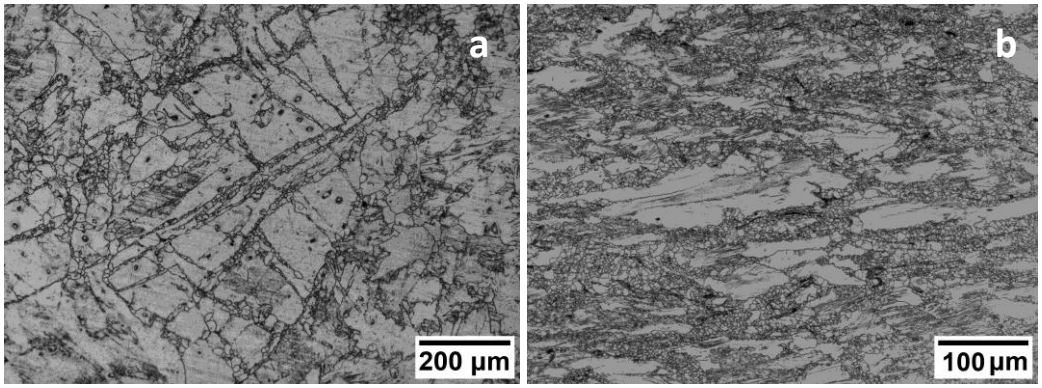

(a) ***(b)***

Figure.4.3.7. Optical micrographs of (a) AZ31 and (b) AZ31+0.8wt%Sr at the entrance of the extrusion die at 250^{o}C. The necklace structures of DRX grains around the large parent grains are visible.

The grain structures of samples extruded at 250^{o}C are shown in Fig.4.3.7; both AZ31 and AZ31+0.8%Sr exhibit necklaced recrystallization structures.

Microstructural investigations also reveal the activation of twinning at low temperatures and low levels of Sr (Fig.4.3.7a). The twins are distinguished from shear bands by their (i) straight boundaries and small inter-distance, (ii) the typical (of HCP) 60^o and 120^o angles between them and their formation at low strain (extrusion die entrance), Participation of twins in DRX has been reported previously [29].

4.3.3.3. Hot compression

The stress-strain curves for various temperatures and levels of Sr are shown in Fig.4.3.8. The maximum stress (σ_{max}) and the strain at maximum stress (critical strain for recrystallization, ε_c) are the two parameters which can be derived from a hot compression stress-strain curve [30]. The former is representative of the strength of the material at the onset of recrystallization. The latter is a measure of the amount of strain (stored energy of dislocation) needed to initiate recrystallization [30]. Although the state of stress in hot compression is different to extrusion, ε_c and σ_{max} are characteristics of the material which are comparable in either case and may be used to interpret extrusion results. Note that any mechanism that facilitates the nucleation of recrystallized grains would decrease ε_c and shift it to the left in the stress strain diagram and vice versa. An increase of 125^oC in the deformation temperature reduced the maximum peak by more than 50% (Fig.4.3.8a). In contrast, as Sr increased from 0 to 1wt% at the constant temperature of 350^oC, the maximum peak decreased only by 10% (Fig.4.3.8b). The limited number of active slip systems at low concentrations of Sr and the solute drag by Al in solid solution at low temperatures resulted in high strength.

In Fig.4.3.9, the ε_c and σ_{max} have been plotted as a function of deformation temperature (T) and the level of Sr(wt%Sr) for all forty hot-compressed samples. The strong dependence of σ_{max} on T is seen in Fig.4.3.9a. The ε_c decreases with increasing T and wt%Sr (Fig.4.3.9b).

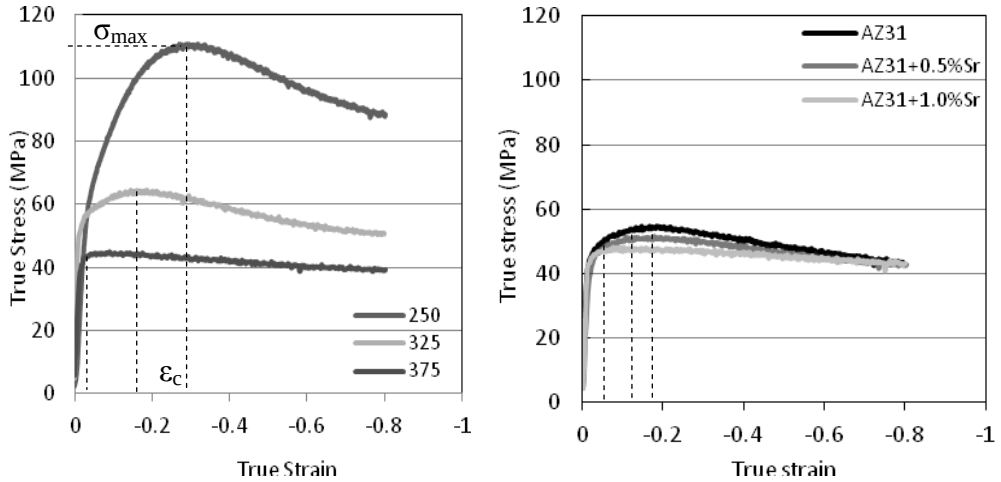

Figure.4.3.8. Stress-strain curves for (a) AZ31+0.5%Sr at different temperatures and (b) at 350^{o}C for different levels of Sr.

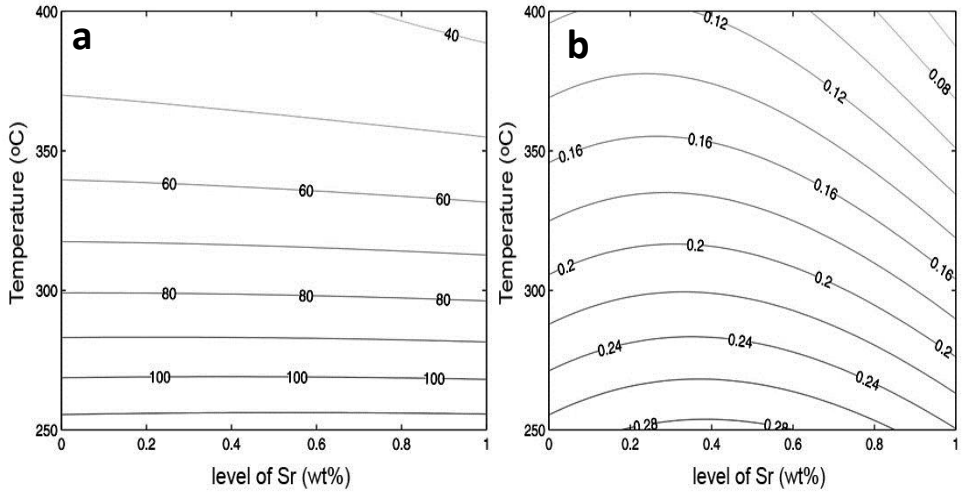

Figure.4.3.9. 2D projection of (a) peak stress and (b) critical strain against temperature and level of Sr.

The dependence of ε_c on T is attributed to the accelerated kinetics of recrystallization at high temperatures. Sr concentration also effects ε_c, however, as seen in Fig.4.3.9b; this effect has different trends at different temperatures. The explanations for these different trends, based on the activation of different micro-mechanisms at different temperatures and composition-dependant microstructure, are discussed further below.

4.3.3.4.Texture

Fig.4.3.10 presents the values of volume fraction of prismatic normals having less than 20 degrees deviation from the extrusion direction (F_V). Fig.4.3.10.a, shows a 3D surface of F_v as a function of second order temperature (T^2) and second order composition (C^2) fitted to data obtained from the sixteen extruded samples. The contour projection of the same surface is shown in Fig.4.3.10b, the ultimate maximum and minimum are labelled as A and C, respectively. Note that both of the extreme values and the highest dependence of Fv on temperature were at the maximum level of Sr (1wt%). At all levels of Sr, the texture was stronger at the lower extrusion temperatures. It is interesting that the dependency of Fv on the concentration of Sr changed its direction in lower temperatures from the one at higher temperatures. These trends are discussed below to explain the formation of different textures at high and low temperatures and at high and low Sr levels.

4.3.3.5. Texture at low temperatures:

DRX is activated in Mg alloys, even at quite low temperatures (150-200^{o}C). It is believed that the deformation-induced internal energy raises local temperatures sufficiently to activate DRX [23]. A fine recrystallized grain size is one of the distinguishing characteristics of low temperature DRX [30]. At lower temperatures the work hardening rate is high; therefore the growth of newly recrystallized grains is stopped by the increase of dislocation density inside them. During deformation, as the dislocation density difference between the parent grain and newly recrystallized grains decreases, the driving force for growth decreases, therefore growth stops and smaller grains are formed.

As shown in Fig.4.3.10, at lower temperatures the fiber texture becomes stronger with increasing Sr (moving from B to A in Fig.4.3.10a), which can be related to the solute drag effect. The addition of Sr to Mg-Al alloys not only forms Al-Sr precipitates but also decreases the solid solubility of Al in the primary α-Mg grains [14,19]. The effect of reduced Al in decreasing the solute drag and its influence on the DRX behaviour of Mg has been described previously [14].

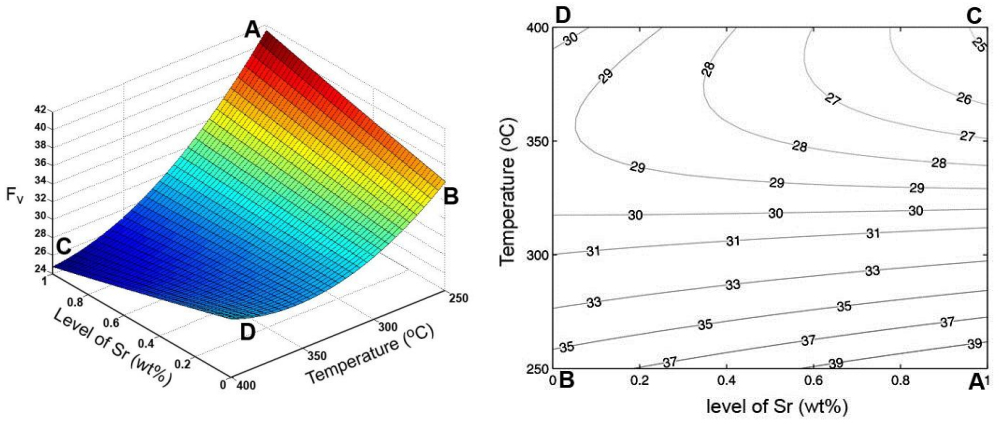

Figure.4.3.10. (a) Volume fraction of prismatic normals less than 20^o away from extrusion direction (F_v) of AZ31 vs. extrusion temperature and level of Sr. (b) Projection of the surface on to T-wt%Sr plane (with iso-F_v curves).

As seen in Fig.4.3.8a, despite the increase in the amount of precipitates with increasing Sr, σ_{max} is not changed; the strengthening effect of secondary phases is compensated with a decrease in Al solute drag with increasing Sr.

At low extrusion temperatures dislocations accumulate behind the boundaries and the dominant mechanism of DRX is the bulging of grain boundaries and the formation of a necklace structure (Fig.4.3.7). Even though there may be some degree of PSN, the newly formed grains would not have the chance to grow large. This is because the driving force of growth (dislocation density difference with the parent grain) quickly diminishes as a result of the increasing dislocation density inside the new grains. At low temperatures, nucleation at the grain boundaries is intense and this becomes the dominant mechanism with no significant contribution from other mechanisms. Consequently, by enhanced dislocation movement in the basal slip system, a stronger basal deformation texture is formed which is followed by the nucleation and growth of new grains with the same basal texture at a higher rate, leading to a stronger texture development during extrusion [30]. Studies of recrystallization texture show the deformation textures of HCP metals were retained after recrystallization, with some redistribution of intensity [30].

The reduction of ε_c with increasing Sr at low temperatures shows that the onset of DRX surmounts a smaller energy barrier (Fig.4.3.9b); i.e. lower strain is sufficient to initiate DRX. However, the magnitude of this decrease is less than the decrease at higher temperatures. At low temperatures the moving boundaries are held back by foreign atoms, and the speed of the boundary is controlled by the speed of the foreign atoms diffusing behind the boundary [31]. Since Al atoms would poison the growth of DRX grains and nuclei, this effect is reduced, therefore the dislocation density at a given stress level increases and a higher amount of dislocation accumulates behind obstacles in the microstructure. Hence, increasing Sr leads to reduced solute drag due to lower Al in solid solution; this facilitates nucleation and growth and decreases the critical strain for of the onset of recrystallization. This Al depletion effect would also exist at high temperatures, but at those temperatures the grain boundary growth cannot be held by the foreign atoms, the drag effect of solute atoms becomes negligible [32] and the boundary moves much faster [31].

4.3.3.6. Texture at high temperatures:

At higher temperatures, increasing Sr (moving from point D to C in Fig.4.3.10b) introduces a higher amount of Al-Sr precipitates, which activates recrystallization mechanisms that compete with grain boundary bulging. At these temperatures, grain boundaries become sinks for dislocations and precipitates can accumulate more dislocations compared to grain boundaries. Given the high density and mobility of vacancies at such high temperatures, polygonization of dislocations followed by nucleation of new grains occurs readily. Since potential sites available for PSN [14] increase with increasing Sr, a higher number of grains recrystallize to orientations different from the extrusion texture and the overall <10.0> fiber texture weakens.

In Fig.4.3.10b, it can be seen that at high temperatures, the critical strain for recrystallization onset drops significantly. This is due to the participation of Al-Sr precipitates (instead of grain boundaries) as nucleation sites for recrystallization of new grains. At high temperatures, Al-Sr precipitates block

dislocation movement more effectively and accelerate the kinetics of recrystallization (decrease ε_c). It should be noted that grain boundary bulging would still be operative to some extent at high temperatures. However, one of the distinguishing characteristics of high temperature recrystallization is a larger DRX grain size. Unlike the low temperature behaviour, high temperature recrystallized grains experience substantial growth. Since the number of recrystallized grains is lower at high temperatures, fewer new grains would have the <10.0> extrusion texture due to DRX via grain boundary bulging and hence the final texture would be weaker.

With increasing temperature (i) non basal slip systems activate, (ii) nucleation and growth kinetics are faster and the final grain size larger, and (iii), twinning and twinning induced DRX become less significant. In other words, extruding at higher temperatures activates non basal slip systems, resulting in deformation without twinning. Fig.4.3.9a and b show a considerable drop of ε_c and σ_{max} with increasing temperature which is a result of activation of non-basal slip systems and accelerated kinetics of DRX.

4.3.3.7. Texture at low levels of Sr

At low levels of Sr with an increase in temperature (moving from B to D in Fig.4.3.10b) the fiber texture is weakened, however the decrease in texture strength is not significant. At low levels of Sr, DRX initiates mainly at the grain boundaries and PSN is not significant; there is still a weakening of texture mainly due to the differences in the recrystallized grain size as described above.

4.3.3.8. Texture at high levels of Sr

At high levels of Sr, Sr stringers were always present; however the temperature caused different effects:

***At high temperatures*:**

(i) Dislocations are recovered and annihilated at the grain boundaries, but they can be effectively accumulated behind the precipitates. Therefore, when Al-Sr

precipitates are present in the microstructure, there would be a switch in dominant recrystallization micro-mechanism from bulging to PSN with increasing temperature, contributing to texture weakening. (ii) As shown (Fig.4.3.9b), ε_c dropped with increasing Sr at high temperatures, indicating that recrystallization started at lower strains with lower stored energy. As a result of more active slip systems, effective obstacles against dislocation movement and high recovery rates, work softening overcomes work hardening. Conversely, the ε_c decreased with increasing temperature (Fig.4.3.9a).

At low temperatures:

(i) In parallel with the PSN mechanism which produces a texture weakening effect, the grain boundary bulging mechanism is also operative because grain boundaries are also effective obstacles where dislocation accumulation occurs leading to texture strengthening.

(ii) Furthermore, a fine recrystallized grain size is obtained since there is a high work hardening rate; the growth of newly recrystallized grains is stopped. The effective competition of the grain boundary bulging mechanism and the fine recrystallized grain size leads to net texture strengthening at low temperatures.

4.3.4. Micro Mechanism Map

A general temperature-composition deformation map was derived based on an analysis of the deformation behaviour (during extrusion) of a number of alloys at low and high temperatures (Fig.4.3.11). The map could be used as a guide to select an alloy composition for extrusion. The F_v data derived from extruded samples and the microstructures of the extruded samples make two main regions distinguishable: (i) the region in which the dominant micro-mechanism of DRX is grain boundary bulging and necklacing and (ii) the region where PSN plays a dominant role. Also there is an intermediate region where both mechanisms are active and a mixed behaviour can be seen.

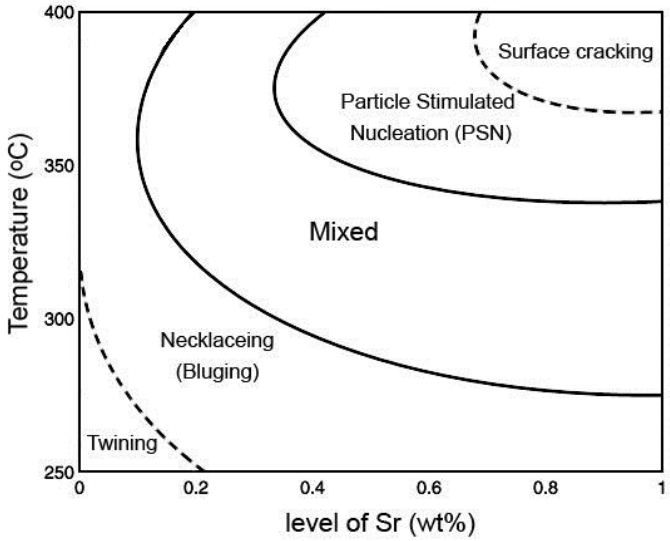

Figure.4.3.11. Micro-mechanism map during extrusion of AZ31 alloy containing up to 1% Sr at different temperatures.

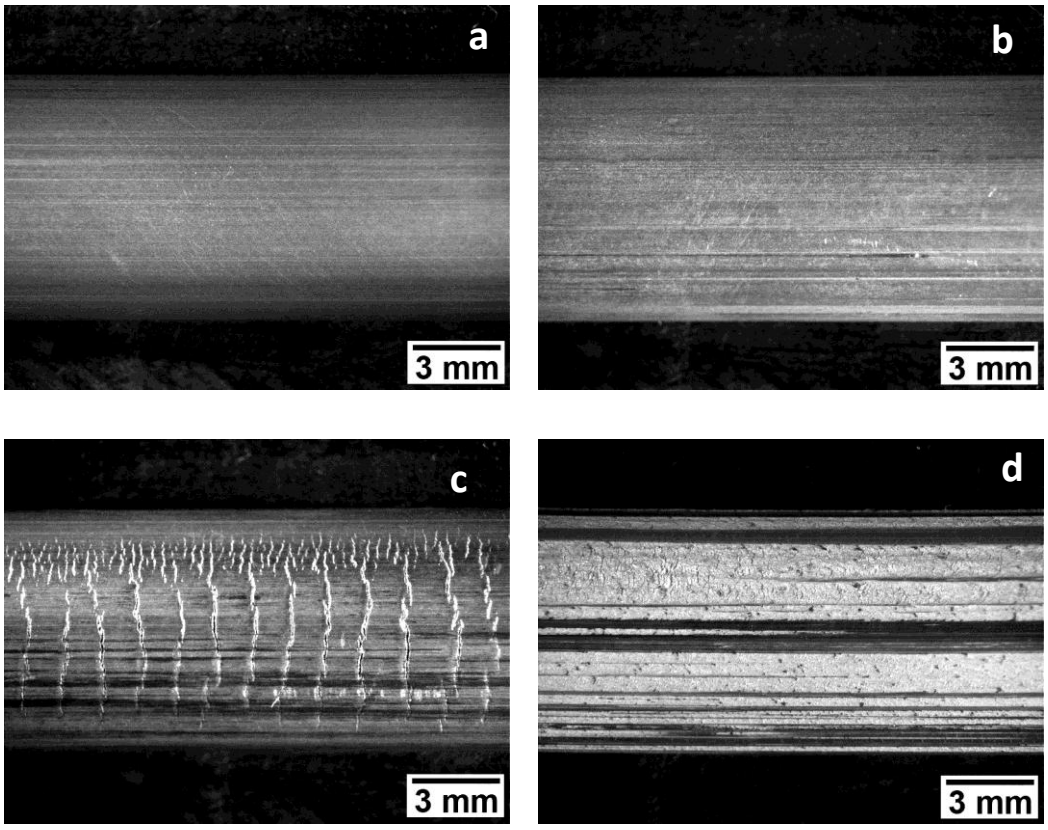

Figure.4.3. 12. Stereoscopic image of AZ31+0.8%Sr extruded product surface at (a) 250°C, (b) 300°C, (c) 350°C and (d) 400°C.

At high temperatures and high levels of Sr, PSN is active, however there is a limit where the onset of crack formation at the surface of extruded samples is observed. Increasing Sr, which introduces a large amount of Al-Sr precipitates at the contact surface between the die and the billet, can lead to possible surface-crack formation with increases in friction [33].

In Fig.4.3.12, the surfaces of the alloys containing 0, 0.05, 0.4 and 0.8wt% extruded at 400^{o}C are shown. Severe cracks are obvious in the alloys containing 0.4wt% Sr and above. The solidus temperature drops with increasing Sr [19,20] which could result in an increased probability of localized melting caused by the heat of deformation. Localized melting could result in severe cracking at the surface of the billet [34]. In Fig.4.3.12d, a layer of metal has been scratched away from the surface which is likely caused by melting of the surface at the die interface. The region of high potential for surface cracking has been delineated with a dashed line in the micro-mechanism map (Fig.4.3.11). There is another sub-region at low temperatures and low levels of Sr where twinning is activated prior to DRX and the twin boundaries provide potential sites for DRX nucleation (Fig.4.3.7a).

4.3.5. Conclusions

AZ31 alloy containing 0, 0.05, 0.4 and 0.8wt% Sr has been extruded at different temperatures (250-400^{o}C). The formation of <10.0> fiber texture was evaluated in terms of volume fraction of prismatic planes (PN) having their normal less than 20^{o} away from extrusion direction (F_v). Hot compression experiments were performed on AZ31 alloys containing 10 different levels of Sr (0-1wt%Sr) at 4 different temperatures (250-400^{o}C). The maximum point of the stress-strain curve was compared for all the compressed samples by means of stress (σ_{max}) and strain (ε_c). Results are concluded as follows:

1. *At low temperatures or low levels of Sr*, the main micro-mechanism involved in DRX is grain boundary bulging and the formation of necklace structure until the entire matrix is recrystallized, the prismatic planes of the

recrystallized grains are aligned perpendicular to the extrusion direction resulting in a strong <10.0> fiber texture.

2. *At high temperatures and high concentrations of Sr*, the contribution of PSN is considerable and the overall texture is weakened by nucleation of new grains with random orientations at the precipitate boundaries.
3. *At low temperatures*, ε_c and F_v drop with increasing Sr. This is attributed to reduced Al solubility which decreases the solute drag effect and enhances recrystallization.
4. *At high levels of Sr*, ε_c and F_v decrease with increasing temperature. This may be explained that, at high temperatures, the accumulation of dislocations behind the boundaries decreases (compared to low temperatures) and the contribution of the particles in blocking dislocations becomes more significant. Consequently, the effect of PSN becomes considerable and the final texture is weakened.
5. *At very high temperatures and high concentrations of Sr*, cracks initiate at the extruded bar surface. *At low temperatures and low levels of Sr*, twinning is active and the twin boundaries act as nucleation sites for DRX.

4.3.6. References

1. J. Bohlen, S.B. Yi, J. Swiostek, D. Letzig, H.G. Brokmeier, K.U. Kainer, "Microstructure and texture development during hydrostatic extrusion of magnesium alloy AZ31," Scripta Materialia Vol 53, Issue 2, (2005) 259-264.
2. S.S. Park, B.S. You, D.J. Yoon, "Effect of the extrusion conditions on the texture and mechanical properties of indirect-extruded Mg–3Al–1Zn alloy," Journal of Materials Processing Technology, Vol 209, Issues 18-19 (2009) 5940-5943.
3. Y. Chen, Q. Wang, J. Peng, C. Zhai, W. Ding, "Effects of extrusion ratio on the microstructure and mechanical properties of AZ31 Mg alloy," Journal of Materials Processing Technology, Vol 182, Issues 1-3 (2007) 281-285.
4. M. Shahzad, L. Wagner, "Influence of extrusion parameters on microstructure and texture developments, and their effects on mechanical properties of the

magnesium alloy AZ80," Materials Science and Engineering: A, Vol 506, Issues 1-2 (2009) 141-147T.

5. H. J. Mcqueen, M. Pekguleryuz, "Hot Workability of Magnesium Alloys" Magnesium Alloys and their Applications, Apr, 1992 Garmisch Partenkirchen, Germany, (1992) 101-108.
6. N. Stanford, M.R. Barnett, "The origin of "rare earth" texture development in extruded Mg-based alloys and its effect on tensile ductility," Materials Science and Engineering A, Volume 496, Issues 1-2 (2008) 399-408.
7. N. Stanford, "Micro-alloying Mg with Y, Ce, Gd and La for texture modification—A comparative study," Materials Science and Engineering A, Vol 527, Issues 10-11 (2010) 2669-2677.
8. L.W.F. Mackenzie, B. Davis, F.J. Humphreys, G.W. Lorimer, "The deformation, recrystallization and texture of three Mg alloy extrusions," Materials Science and Technology, Vol 23, No 10 (2007) 1173-1180.
9. L.W.F. Mackenzie, M.O. Pekguleryuz, "The recrystallization and texture of magnesium-zinc-cerium alloys," Scripta Materialia, Vol 59, No 6 (2008) 665-668.
10. T. Laser, Ch. Hartig, M.R. Nürnberg, D. Letzig. R. Bormann, "The influence of calcium and cerium mischmetal on the microstructural evolution of Mg–3Al–1Zn during extrusion and resulting mechanical properties," Acta Materialia, Vol 56, Issue 12 (2008) 2791-2798.
11. T. Abuleil, N. Hort, W. Dietzel, C. Blawert, Y. Huang, K.U. Kainer, K.P. Rao, " Microstructure and corrosion behaviour of Mg-Sn-Ca alloys after extrusion," Transactions of Nonferrous Metals Society of China, Vol 19, Issue 1 (2009) 40-44.
12. B. Jing, S. Yangshan, X. Feng, X. Shan, Q. Jing T. Weijian, "Effect of extrusion on microstructures, and mechanical and creep properties of Mg–Al–Sr and Mg–Al–Sr–Ca alloys," Scripta Materialia, Vol 55, Issue 12 (2006) 1163-1166.
13. X. Zeng, Y. Wang, W. Ding, A. A. Luo, A. K. Sachdev, "Effect of strontium on the microstructure, mechanical properties, and fracture behaviour of AZ31

magnesium alloy," Metallurgical and Materials Transactions A, Vol 37, No 4 (2006) 1333-1341.

14. A. Sadeghi, M. Pekguleryuz, "Recrystallization and Texture Evolution of Mg-3%Al-1%Zn-(0.4 -0.8) %Sr Alloys during Extrusion," Materials Science and Engineering A, Submitted August 2010.
15. M. Pekguleryuz, E. Baril, P. Labelle, D. Argo, "Creep resistant Mg-Al-Sr alloys," Journal of Advanced Materials Vol 35, Issue: 3, (2003).
16. M. Pekguleryuz, A.A. Kaya, "Magnesium diecasting alloys for high temperature applications," TMS Annual Meeting, Symposium on Magnesium Technology Charlotte, NC, (2004).
17. P. Zhao, Q. Wang, C. Zhai, Y. Zhu, "Effects of strontium and titanium on the microstructure, tensile properties and creep behaviour of AM50 alloys," Materials Science and Engineering: A, Vol 444, Issues 1-2, (2007).
18. X.L. Liu, X.D. Peng, W.D. Xie, Q.Y. Wei, "Preparation Technologies and Applications of Strontium-Magnesium Master Alloys," Mater Sci Forum 488–499, 31 (2005).
19. A. Sadeghi, M. Pekguleryuz, "Precipitation during the Solidification of Mg-3wt%Al-1wt%Zn-(0.001-1%) Sr Alloys," American Foundry Society annual congress, Orlando, USA, (2010).
20. A. Sadeghi, M. Pekguleryuz, "Precipitation of Mg-3%Al-1%Zn-(0.01-1)wt%Sr Alloys during solidification," Journal of Materials Research, submitted July 2010.
21. S. Kleiner, P.J. Uggowitzer, "Mechanical anisotropy of extruded Mg–6% Al–1% Zn alloy," Materials Science and Engineering: A, Volume 379, Issues 1-2 (2004) 258-263.
22. S. B. Yi, H. G. Brokmeier, J. Bohlen, D. Letzig, K. U. Kainer, "Neutron diffraction study on the texture development during extrusion of magnesium alloy AZ31," Physica B: Condensed Matter, Vol 350, Issues 1-3, Supplement 1, 2004, E506.1.E509

23. M. Chandrasekaran, Y.M. Shyan John, " Effect of materials and temperature on the forward extrusion of magnesium alloys," Materials Science and Engineering A Vol 381, Issues 1-2 (2004) 308-319.
24. A. Becerra, M. Pekguleryuz, "Effects of Lithium, Indium and Zinc on the Grain Size of Magnesium," Journal of Materials Research, vol. 24, No. 5 (2009) 1722.
25. E. Baril, P. Labelle, M.O. Pekguleryuz, "Elevated Temperature Mg-Al-Sr: Creep Resistance, Mechanical Properties & Microstructure," Journal of Metals (JOM-US), TMS, Vol 55, No 11, 34 (2003).
26. B. Jing, S. Yangshan, X. Shan, X. Feng, Z. Tianbai, "Microstructure and tensile creep behaviour of Mg–4Al based magnesium alloys with alkaline-earth elements Sr and Ca additions," Materials Science and Engineering: A, Volume 419, Issues 1-2, (2006), 181-188.
27. M.S. Dargusch, S.M. Zhu, J.F. Nie, G.L. Dunlop, "Microstructural analysis of the improved creep resistance of a die-cast magnesium–aluminium–rare earth alloy by strontium additions," Scripta Materialia, Volume 60, Issue 2, (2009), 116-119.
28. G. L'Esperance, P. Plamondon, M. Kunst, A. Fischersworring-Bunk, "Characterization of intermetallics in Mg–Al–Sr AJ62 alloys," Intermetallics 18, 1 (2010).
29. D.L. Yin, K.F. Zhang, G.F. Wang, W.B. Han, "Warm deformation behaviour of hot-rolled AZ31 Mg alloy," Materials Science and Engineering A, Vol 392 (2005) 320–325.
30. F.J. Humphreys, M. Hatherly, "Recrystallization and related annealing phenomena," Pergamon Press, Oxford (1996)
31. K Lücke, K Detert, "A quantitative theory of grain-boundary motion and recrystallization in metals in the presence of impurities," Acta Metallurgica, Vol 5, Issue 11 (1957) 628-637.
32. R. Le Gall, J. J. Jonas, "Solute drag effects during the dynamic recrystallization of nickel," Acta Materialia, Vol 47, Issue 17, 26, (1999).

33. L. Miao-quan, W. Shi-chun, T. Cai-rong, "Analysis of surface crack on forward extruding bar during axisymmetric cup-bar combined extrusion process," Applied Mathematics and Mechanics, Vol 11, No 8, (1990) 733-741.

34. Z.Peng, T.Sheppard, "Study of surface cracking during extrusion of aluminum alloy AA 2014," Materials Science and Technology, Vol 20, No 9 (2004) 1179-1191.

Chapter 5

Yield Asymmetry and Fracture Behaviour

This chapter presents tensile and compression experiments carried out on Mg-3Al-1Zn alloys containing different levels of Sr (0.05, 0.4 and 0.8wt %) extruded at elevated temperatures of 250, 300, 350 and 400^{o}C compared to AZ31 alloy.

The addition of 0.05wt% Sr to the alloy produced the highest strength and the alloy containing 0.4wt%Sr had the highest elongation during tensile tests. High levels of Sr (0.8wt%) reduced the yield strength by decreasing the solid solubility of Al in α-Mg and thereby decreased the solute pining effect of dislocations under both compression and tension loading.

The ultimate tensile strength (UTS) was also reduced due to the cracking of Al-Sr precipitates perpendicular to the tension direction. Cracking was also seen in compressed samples; however, the cracks which initiated were parallel to the compression axis, which impeded crack opening and the formation of large voids. As a result, fracture in compression was less sensitive to high concentrations of Sr. It was found that increasing the extrusion temperature increases the yield asymmetry and the improvement in yield symmetry was less significant in alloys containing the high levels of Sr.

5.1. Yield Asymmetry and Fracture Behaviour of Mg-3%Al-1%Zn-(0-1)%Sr Alloys Extruded at Elevated Temperatures

Alireza Sadeghi, Scott Shook, Mihriban Pekguleryuz

Materials Science and Engineering: A, Volume 528, Issues 25-26, 25 September 2011, Pages 7529-7536

5.1.1. Introduction

Mechanical anisotropy is the major obstacle limiting the widespread industrial use of wrought Mg alloys. The hexagonal crystal structure limits easy glide in various crystallographic directions and concentrates most of the dislocation movement on the basal planes [1]. As a result, the grains with their basal planes perpendicular to the compression axis exhibit a low amount of basal dislocation motion and are less hardened, thus less dynamically recrystallized during deformation. Grains with other orientations recrystallize at their boundaries and, for the same reason, newly formed grains with their c-axes parallel to the compression axis remain stable and resist recrystallization. As deformation progresses, a large amount of grains with their c-axis parallel to the compression direction survive and consequently a strong basal texture is formed [2]. In industrial applications, the use of wrought alloys in their as-extruded or as-rolled state is limited. Such alloys usually need a complementary processing step before application. For example, drawing and stretching of a rolled sheet is necessary to shape a part and an extruded rod or tube needs to be bent and formed before it can be used in an automotive assembly. In Mg alloys, the reorientation of hexagonal grains in a preferential direction and the formation of a strong basal texture increases deformation inhomogeneity during complementary processing and prohibit many potential applications for wrought Mg alloys [3].

Many attempts have been made to decrease the strength of the deformation texture of Mg, either by controlling the process parameters [4-8] or by introducing different alloying elements [9-18]. We authors have previously reported the effect of Sr on the formation of precipitates during solidification [19,20] and the nucleation of grains with random orientations during dynamic recrystallization

(DRX) of AZ31 alloy [21,22]. The thermally stable Al-Sr precipitates which are formed with the addition of Sr into AZ31 are potential sites to pile up dislocations and nucleate new grains with different orientations than the parent grains. Consequently, the overall texture is weakened through the formation grains with non-basal orientations. In the previous research, the effect of Sr on the anisotropy of Mg has been determined via X-ray and electron back scattered diffraction (EBSD) analysis of the deformation texture. In the present study, the anisotropy is determined as a function of yield asymmetry under tensile and compressive loading. This approach simulates the actual complementary deformation conditions of extruded products. For this purpose, AZ31 and AZ31 with three different levels of Sr (0.05, 0.4 and 0.8wt%Sr) have been cast and then extruded. Tensile and compression experiments were conducted on extruded samples. Fracture surface and cross sections were observed and results compared across the Sr concentration and extrusion temperature ranges.

5.1.2. Experimental Procedure

AZ31 extruded bars provided by Applied Magnesium (previously known as Timminco, Denver, CO) were used as the base material in the experiments. Alloys were melted in graphite crucibles using a high frequency induction furnace. Sr was added to the molten AZ31 using a 90Sr-10Al master alloy (Timminco, Haley, ON) at 700^{o}C. The melt was kept at 700^{o}C for 15 minutes to allow complete dissolution of the master alloy. After stirring and skimming the surface, the temperature was raised to 720^{o}C and the melt was cast into preheated cylindrical steel dies. Four different compositions of AZ31, one with no Sr addition and three others containing 0.05, 0.4 and 0.8wt%Sr were cast. Compositions of the cast alloys were measured using inductively coupled plasma (ICP) and are summarized in Table 3.1.1. Cylindrical specimens (3 cm diameter) were machined from the castings which were then extruded using a 100T hydraulic press and a steel die. The extrusion temperature was fixed at 250^{o}C, 300^{o}C, 350^{o}C and 400^{o}C using a ceramic insulator band-heater. Extrusion trials were carried out using a die with a 90^{o} half angle, 3:1 extrusion ratio, and a 4 mm s^{-1} ram speed.

With the extrusion of four different cast alloys at four different temperatures, a group of 16 "composition-temperature" samples were produced. Room temperature compression and tensile tests were performed on each of the samples. Compression samples (D=6mm, h=9mm) were machined from the extruded bars and compressed using a MTS universal machine. Boron nitride powder and mica plates were used to minimize the effect of friction during deformation. Tensile samples (D=5mm, L=25mm) were also machined from extruded bars and were tested at room temperature. A strain rate of 0.01 s^{-1} was used for both compression and tensile experiments and the tests was repeated three times until sample fracture. The results of the group of 16 were bi-linearly interpolated into two dimensional contours in a "composition-temperature" system.

The fracture surfaces of the tensile samples were observed using a Hitachi S-4700 field emission gun scanning electron microscope (FEG-SEM) at 15 KV. In order to study the origins of failure and microstructures close to the fractured surfaces, samples were sectioned perpendicular to the circular cross section. The cross sections were polished with 1 μm diamond paste and then examined using a back scattered electron (BSE) detector in FEG-SEM to investigate the behaviour of the precipitates during deformation. Microstructures were studied on etched cross sections prepared using a picric-acetic solution after polishing and micrographs were taken using an optical microscope (Fig.5.1.1).

5.1.3. Results and Discussion

Stress strain curves of AZ31 and AZ31+0.8Sr under tensile and compression are shown in Fig.5.1.2a and b. The results show different effects of Sr on mechanical properties of the cast alloys regarding their extrusion temperature both in compression and tensile experiments. The addition of 0.8wt% Sr increased the tensile strength when the alloy was extruded at 250^{o}C (Fig.5.1.2a). Although this amount of Sr did not change the compressive yield strength, it increased the final strength of AZ31 when extruded at 250^{o}C (Fig.5.1.2b). In contrast, when the extrusion temperature was 400^{o}C, the tensile

strength dropped at 0.8Sr, hence, when this alloy was extruded at 400^{o}C, the compressive yield and final strength both increased.

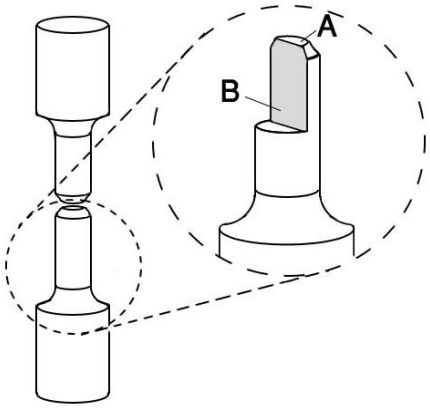

Figure.5.1.1. Schematic view showing the fractured tensile sample and the two studied sections, (A) fracture surface, (B) rectangular cross section parallel to extrusion direction.

5.1.3.1. Effect of Extrusion Temperature and Sr on Tensile Properties

(i) Extrusion temperature

Fig.5.1.3a to d shows the microstructure of cross sections close to the fractured surfaces of the samples. AZ31+0.8Sr extruded at 250^{o}C (Fig2.a) showed a finer grain size compared to the same alloy extruded at 400^{o}C (Fig2.b). In both of the micrographs, the Al-Sr precipitates are visible. The relatively higher tensile strength of the alloy extruded at 250^{o}C compared to the one extruded at 400^{o}C is attributed to the finer grain size formed during extrusion. The relationship between the hot extrusion temperature and grain size of AZ31 alloys containing different levels of Sr has been previously reported by the authors [22]. The same trend in grain size can be observed in the AZ31 samples in Fig.5.1.3c and d.

(ii) Sr addition

It can be seen in Fig.5.1.2a that samples extruded at 250^{o}C, addition of 0.8wt% Sr increased the tensile strength. For alloys extruded at 250^{o}C, the microstructures also reveal that the alloy containing 0.8wt% Sr had a finer grain size (Fig.5.1.3a and c). The grain refining effect of Sr on the Mg alloys has been previously

reported by the authors [19,20,23] and other researchers [24-27]. Furthermore, it is known that addition of Sr removes Al from α(Mg) solid solution and increases the kinetics of DRX by bulging of grain boundaries, resulting in a finer recrystallized grain size and a stronger basal texture [21,22].

In the strong-textured extruded bars, the c-axis of the grains were oriented in the radial direction. Therefore during tensile loading along the extrusion direction, the basal planes were in a favourable orientation for dislocation movement and work hardening occurred at a higher rate. It is deduced that this finer grain size and the stronger basal texture are responsible for the higher tensile strength of AZ31+0.8Sr compared to AZ31 when the alloys were extruded at 250^{o}C. When extruded at 400^{o}C, the addition of Sr had a reverse effect and reduces the tensile strength.

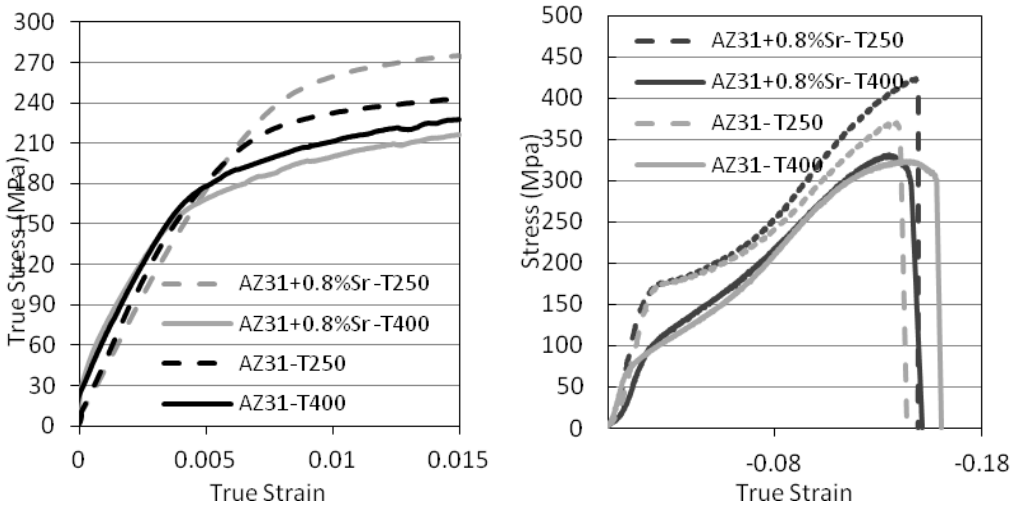

Figure.5.1.2. Stress-strain curves of AZ31 and AZ31+0.8%Sr extruded at 250^{o}C and 400^{o}C (a) under tension and (b) compression at room temperature.

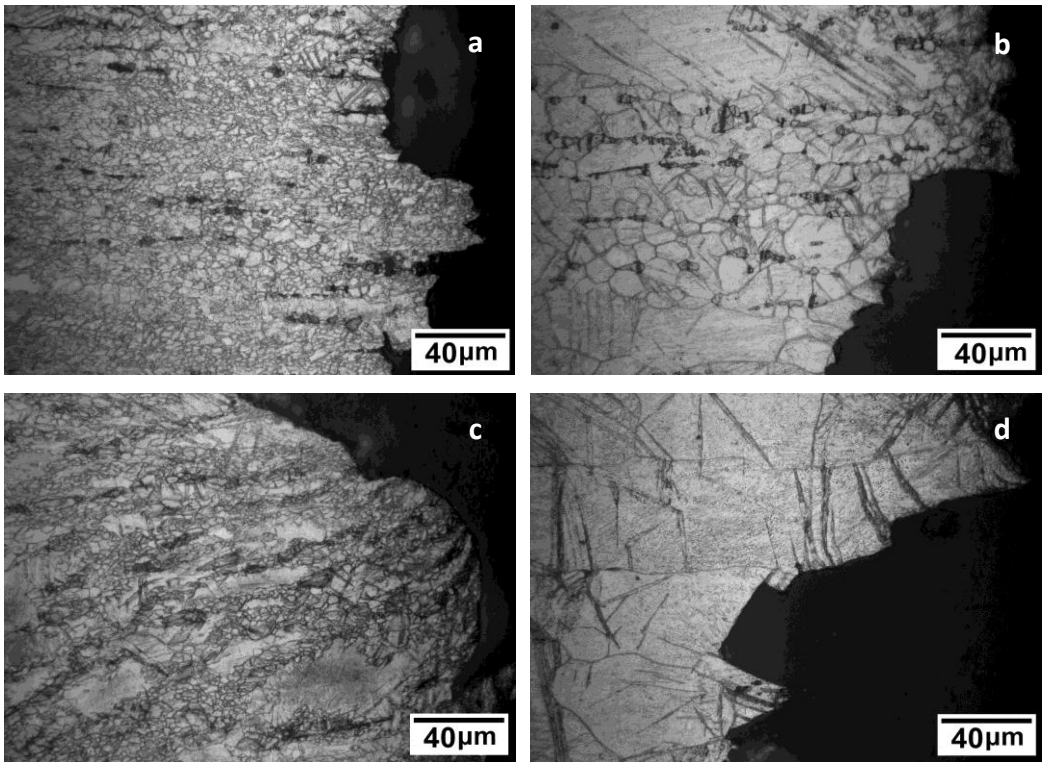

Figure.5.1.3. Optical micrograph from the tensile fracture cross section of AZ31+0.8%Sr (a) extruded at 250^{o}C and (b) extruded at 400^{o}C and of AZ31 (c) extruded at 250^{o}C and (d) extruded at 400^{o}C.

In AZ31 the large grains have activated twinning and fracture occurred in the twinned region, likely on the twin boundaries (Fig.5.1.2). The micrographs of the two alloys (Fig.5.1.3 b and d) show that Sr refined the large grains of AZ31 and twinning was minimized. Although the grain size was refined, a drop in tensile strength was also found. To determine the reason for this effect, fractography was carried out.

5.1.3.2. Fractography

Fig.5.1.4 presents the fracture surfaces of samples shown in Fig.5.1.3. In alloys containing 0.8wt%Sr (Fig.5.1.4a and b), small dimples and cleavage cracking can be seen in on the twinning surfaces of samples extruded at 400^{o}C (Fig.5.1.4b and d). Fig.5.1.5 is a higher magnification fractograph of the dimples and Fig.5.1.6b shows an Al-Sr precipitate with sharp cracked edges at the bottom of a dimple.

This observation supports the idea that Al-Sr precipitates are responsible for the decrease in strength when AZ31+Sr alloy is extruded at 400^{o}C.

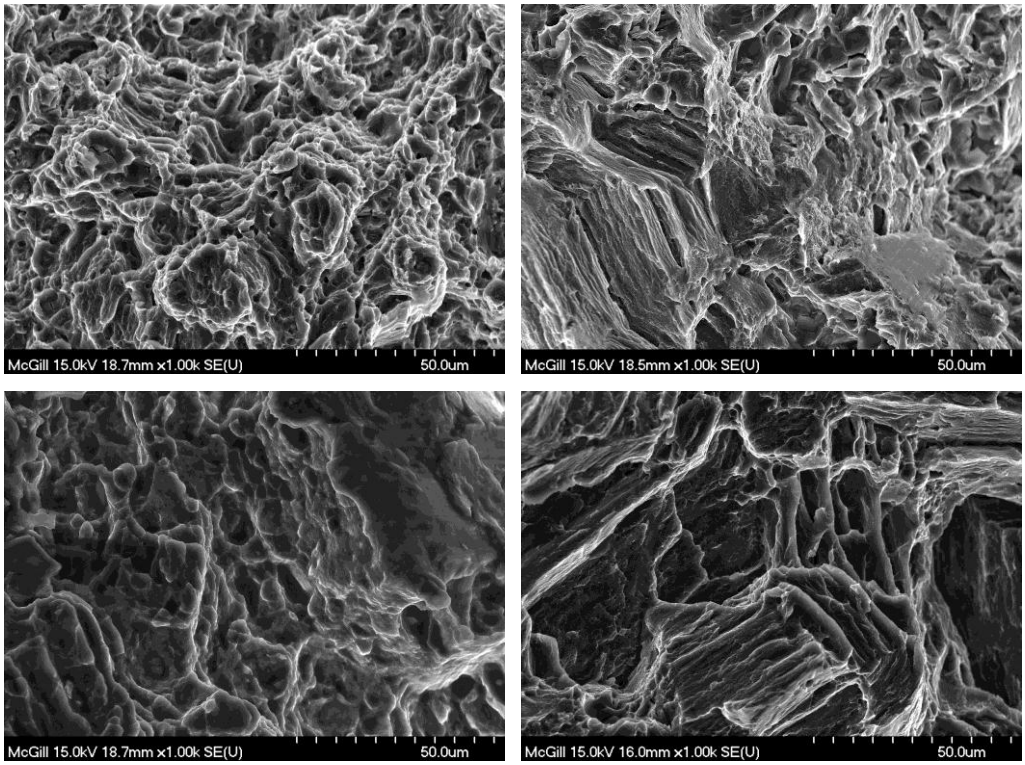

Figure .5.1.4. SEM fractographs of tensile fracture surfaces of AZ31+0.8%Sr (a) extruded at 250^{o}C, 1(b) Extruded at 400^{o}C and of AZ31(c) extruded at 250^{o}C, (d) Extruded at 400^{o}C.

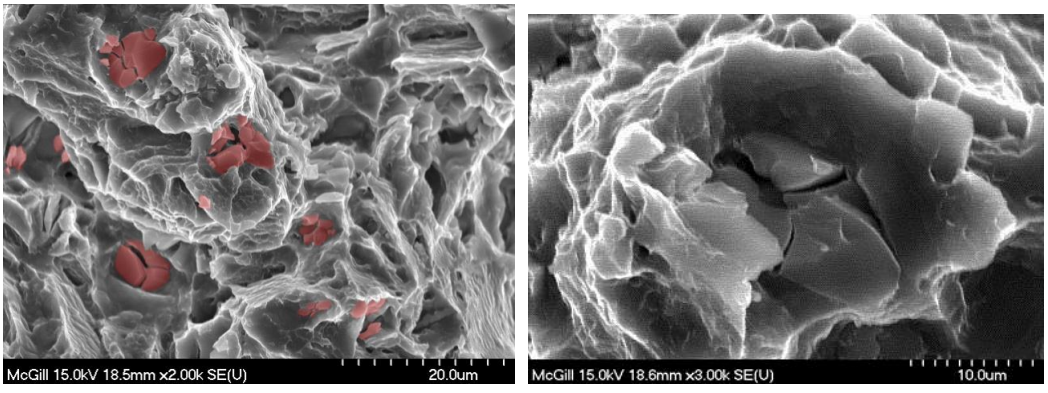

Figure.5.1.5. Void formation during tensile test by fracture of the Al-Mg-Sr precipitate in AZ31+0.8%Sr extruded at 400^{o}C.

BSE images on the cross sections of the fractured alloys are shown in Fig.5.1.6 BSE images provide a good contrast between the precipitates, the Mg matrix and the cracks that have formed as a result, therefore the origin of failure in each sample can be detected. It has been reported that the non-equilibrium Mg-Al-Sr precipitate can decompose to the eutectic Al_4Sr phase, [28] in these alloys both the equilibrium Al_4Sr and the non-equilibrium Mg-Al-Sr precipitates are seen in AZ31+0.8%Sr extruded at 400^{o}C(Fig.5.1.6a) together with cracks perpendicular to the extrusion direction. In Fig.5.1.6b, a series of cracks in a stringer of precipitates which has led to the formation of a void, ductile tearing and a dimple are shown in this alloy.

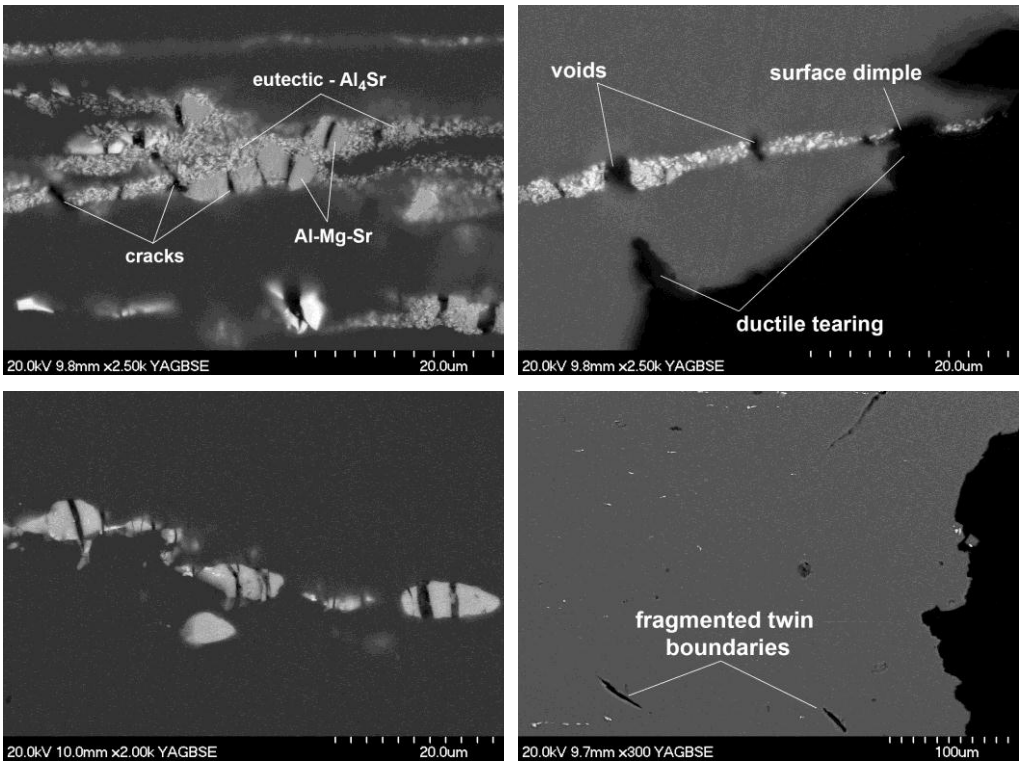

Figure.5.1.6. Back scattered electron image of the cross-section of the fractured samples (a) cracked Al_4Sr and Al-Mg-Sr stringers in AZ31+0.8%Sr extruded at 400^{o}C, (b) a series of cracks in an Al_4Sr stringer in the same sample reaching the surface and forming a dimple. (c) Cracked Al-Mg-Sr stringers in AZ31+0.8%Sr extruded at 250^{o}C, (d) formation of voids at the twin boundaries of AZ31 extruded at 400^{o}C.

A high magnification image of a partially decomposed Mg-Al-Sr precipitate which has cracked and opened is shown in Fig.5.1.7, which indicates that Al-Sr precipitates are effective in void formation and that micro cracks in the inner surface of the void are potential sites for initiating a ductile fracture.

Similar cracks can be observed at the precipitate stringer in the sample extruded at 250^{o}C (Fig.5.1.6c). However, there is a difference: in this sample, because of the low deformation temperature, the decomposition of the bulky Mg-Al-Sr precipitate to the eutectic Al_4Sr has not occurred. Results indicate that both the metastable Mg-Al-Sr and decomposed Al-Sr precipitates initiate fracture in the tensile samples. In Fig.5.1.6d, the fragment of twin boundaries and crack initiation in AZ31 extruded at 400^{o}C in the absence of Al-Sr precipitates were observed.

Room temperature tensile experiments were repeated for all four compositions (Table 4.1.1) which were extruded at 250^{o}C, 300^{o}C, 350^{o}C, and 400^{o}C. Yield and ultimate tensile strength of the sixteen samples were used in a mathematical interpolation method to plot two dimensional diagrams shown in Fig.5.1.8. (The measured values are sumerized in table 5.1.1 and the strain-stress curves are presented in appendix III) The same trends of Fig.5.1.2a could be seen in these diagrams. The strength decreases with increasing extrusion temperature and with the addition of Sr at low temperatures. The decrease of strength with increasing Sr at high extrusion temperatures can also be seen. Note that the highest strength among the composition range is related to the alloy containing 0.05wt% Sr. This effect has been previously been investigated by the authors [23]. It was found that addition of trace levels of Sr refines the grain structure by growth poisoning and refines the β-$Mg_{17}Al_{12}$ precipitates by providing nucleation sites [23].

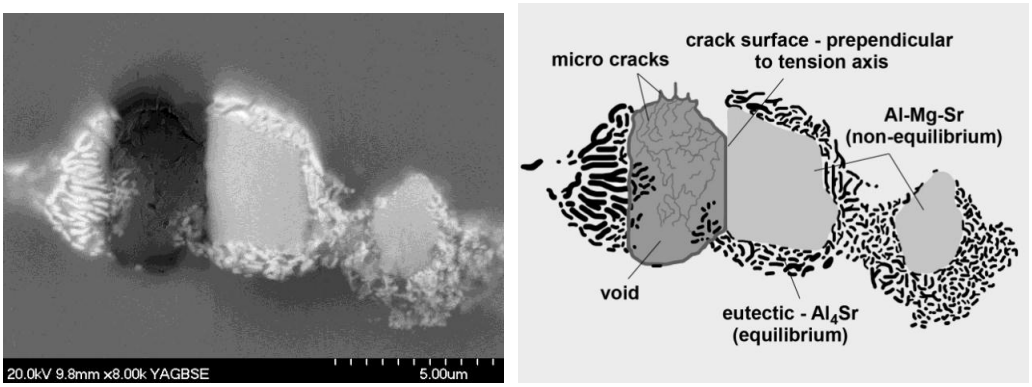

Figure.5.1.7.Cracking of Al-Mg-Sr precipitates by room temperature tension.

The effect of Al-Sr precipitates on the mechanical properties of the AZ31 alloy can also be studied by comparing the elongation of the tensile samples (Fig.5.1.9). Results indicate that Sr first increases the elongation of AZ31 up to 0.4wt%Sr and then, with a further increase in the amount of Al-Sr precipitates, void formation and crack initiation inside the Al-Sr precipitates become significant and the alloys fracture at smaller strains whereby the elongation of the extruded alloys decreases (Fig.5.1.9).

5.1.3.3. Effect of Sr on compressive properties

As described above, Sr precipitates have different effects on the compressive strength of Mg-Al-Zn alloy. Fig.5.1.2b shows that the compressive strength of the alloys extruded at 250^{o}C was higher. The finer grain size of alloys extruded at 250^{o}C can be seen in the micrographs presented in Fig.5.1.10a and c. while the alloys extruded at 400^{o}C (Fig.5.1.10b and d) have a larger grain size and extensive twinning.

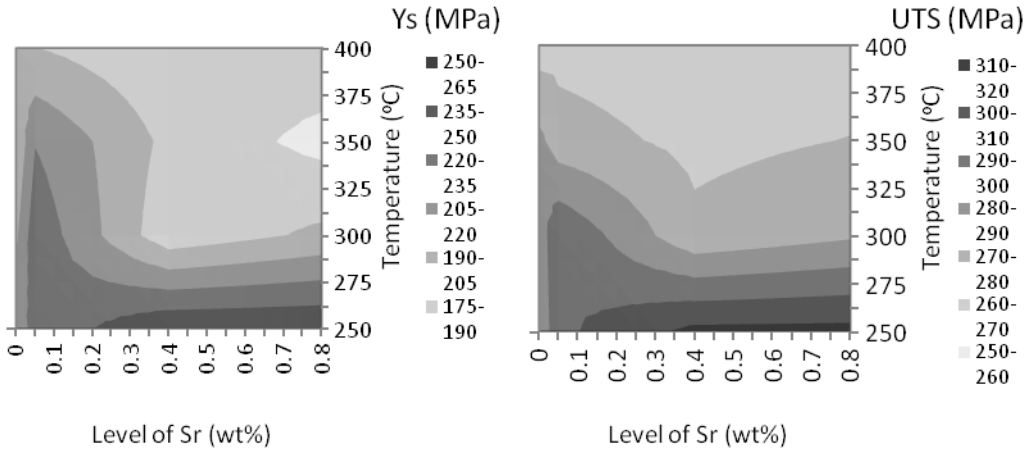

Figure.5.1.8. Two dimensional contours of (a) tensile yield strength (Y_s), (b) ultimate tensile stress (UTS) ofAZ31 alloy containing different levels of Sr extruded at different temperatures.

Table 5.1.1- Room temperature Yield strength and Ultimate tensile strength of extruded bars containing different levels of Sr extruded at elevated temperatures (MPa).

	250°C		300°C		350°C		400°C	
Sr (wt%)	YS	UTS	YS	UTS	YS	UTS	YS	UTS
0	213.0	369.3	202.0	364.7	190.9	341.4	194.0	323.3
0.05	224.2	381.8	230.2	393.1	219.2	333.6	190.2	314.6
0.4	248.5	401.8	179.2	345.6	186.1	350.8	177.4	338.0
0.8	248.9	423.1	193.0	348.4	170.3	347.6	185.2	331.8

By comparing the two AZ31 and AZ31+0.8Sr alloys extruded at 400°C, it is evident that the compressive yield strength of the alloy containing 0.8wt%Sr was lower even though the precipitate amount was higher. This is attributed to the decrease of solute strengthening via the reduction of Al solid solubility in Mg and the related decrease in dislocation pinning [20]. The alloy containing Al-Sr precipitates showed a slightly higher fracture strain (ε_f) when extruded at 250°C, while extrusion at 400°C slightly reduced the ε_f when 0.8wt%Sr was present in the alloy. Unlike the situation in tension, it seems that the precipitates are less effective in lowering the strain before fracture. BSE images of the cross section of a sample containing 0.8wt%Sr extruded at 250°C is shown in Fig.5.1.11.

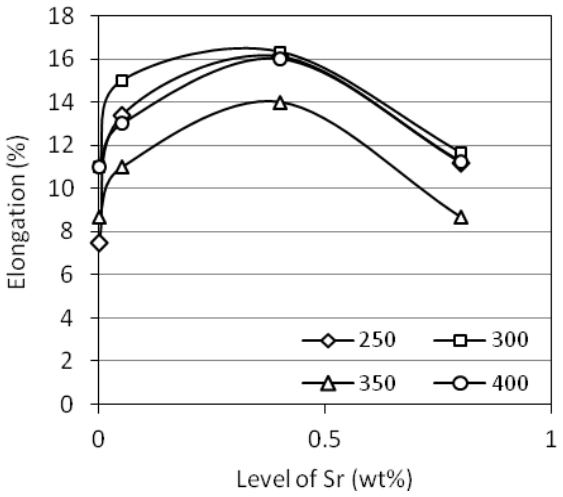

Figure.5.1.9. Effect of Sr content on elongation of extruded samples at different temperatures.

It is interesting to see that the cracks are parallel to the compression axis (extrusion direction) whereas in tension the cracks were perpendicular. During a tensile test, cracks are opened when force is increased but in compression the direction of force (material flow) is perpendicular to the void opening direction. Consequently cracking of precipitates will not play a role in the fracture of the compression samples.

The compressive yield and ultimate strength of the sixteen "composition-temperature" samples have been plotted in Fig.5.1.12a and b. A decrease in strength with increasing extrusion temperature can be observed in both diagrams. The high tensile strength of the alloy containing 0.05wt%Sr was also seen in compression. Note that this high strength was measured at lower extrusion temperatures (<300^{o}C) in compression than in tension.

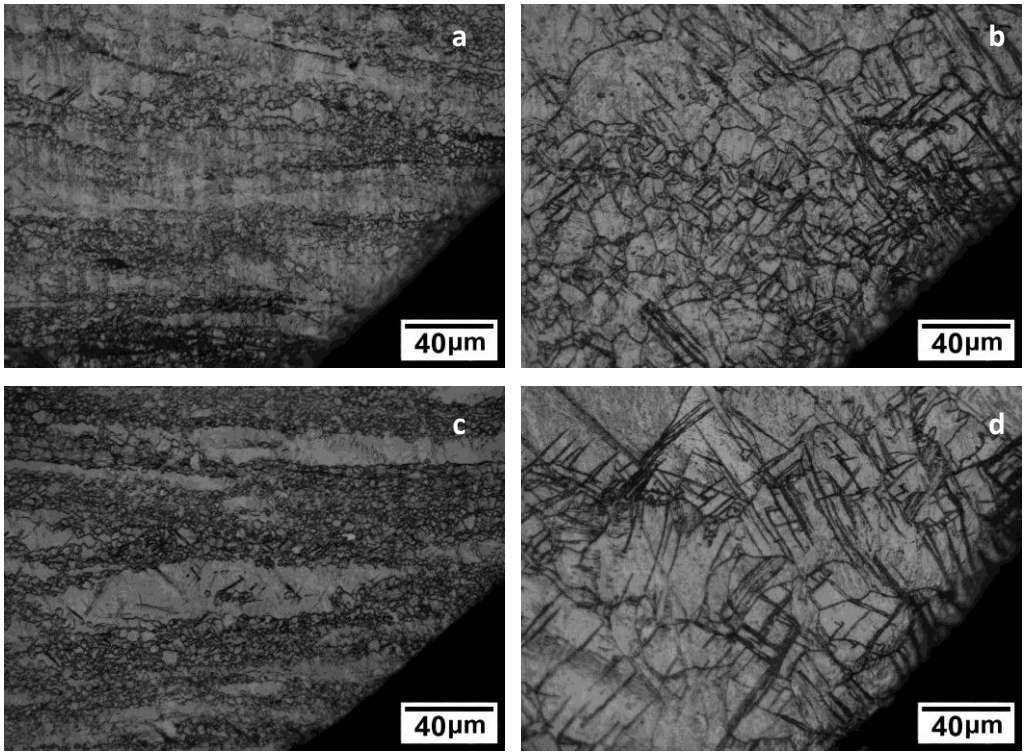

Figure.5.1.10. Optical micrograph from the compression fracture cross section of AZ31+0.8%Sr (a) extruded at 250^{o}C and (b) extruded at 400^{o}C and of AZ31 (c) extruded at 250^{o}C and (d) extruded at 400^{o}C.

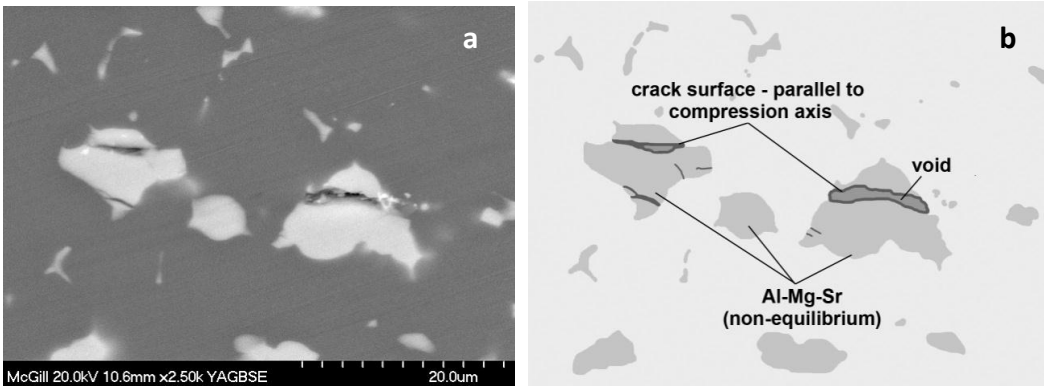

Figure.5.1.11. Cracking of Al-Mg-Sr precipitates by room temperature compression. The sample contains 0.8wt%Sr and is extruded at 250^{o}C.

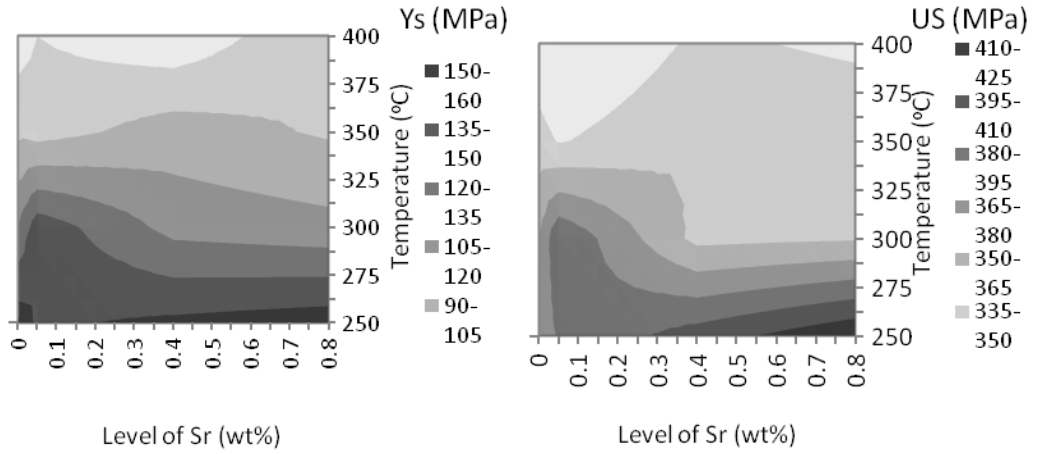

Figure.5.1.12. Two dimensional contours of (a) compressive yield strength (Y_s), (b) ultimate strength ofAZ31 alloy containing different levels of Sr extruded at different temperatures.

5.1.3.4. Yield Asymmetry

In Fig.5.1.13, the ratio of tensile yield strength to compressive yield strength been plotted as two dimensional contours in a composition – extrusion temperature map. As the ratio approaches unity, an increasingly more uniform deformation is expected. It is noted that the yield asymmetry increases with increasing extrusion temperature. As previously reported, at extrusion temperatures higher than 350^{o}C and Sr concentrations more that 0.4wt%, particle stimulated nucleation (PSN) is activated in AZ31+xSr [21]. As a result, at those conditions the basal texture is weakened by the nucleation of new grains with random texture. Since a randomized texture contributes to a more uniform deformation, a high tensile to compressive yield ratio close to one is expected under those conditions.

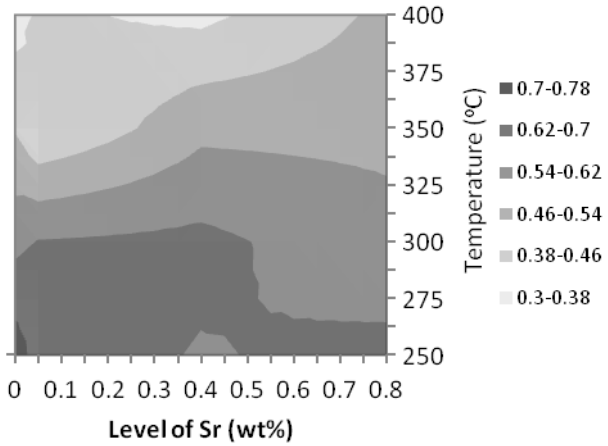

Figure .5.1.13. Two dimensional contours of tensile yield strength/compressive yield strength versus temperature and level of Sr.

The results show a milder slope of increasing yield asymmetry by an increase of extrusion temperature when Sr is present in the alloy. Here, there is a balance between (i) The effect of Al-Sr precipitates leading to crack initiation and to a decrease of tensile strength, which increases the yield asymmetry and (ii) Texture weakening by PSN which decreases yield asymmetry.

It has been previously reported that the high temperature extrusion of AZ31+xSr results in surface cracking and extensive grain growth [22]. In the present research, it was found that high extrusion temperatures also decreased the mechanical properties of the extruded alloys. Moreover, Al-Sr precipitates are able to initiate cracks in tension while the presence of low levels of Sr (0.05wt%) increases the strength and intermediate levels (0.4wt%Sr) increases the elongation. Regarding the derived anisotropy map and considering the micro-mechanism map previously introduced [22], specific Sr levels can be selected for different applications ranging from high formability to high strength.

5.1.4. Conclusions

Tensile and compression experiments were carried out on AZ31 alloys containing different levels of Sr (0, 0.05, 0.4 and 0.8wt%) extruded at elevated temperatures (250, 300, 350 and 400^{o}C). Fractured surface and cross sections were analyzed to investigate the origin of the failure. The following conclusions were drawn:

1- The tensile and compressive strength of extruded AZ31 alloys containing different levels of Sr depend more on the extrusion temperature than on the Sr concentration.
2- Low levels of Sr (0.05wt%) increases the tensile yield (Y_s) and ultimate tensile strength (UTS) of AZ31, while higher concentrations (0.8wt%) decrease the Y_s by lowering Al solid solubility and hence solute strengthening and decrease UTS by initiating cracks at the Al-Sr precipitates.
3- Fracture strain in compression is less sensitive to Sr additions than in tension. This is attributed to the direction of the crack inside the Al-Sr precipitates.
4- The yield asymmetry of the AZ31+xSr alloys increases with increasing extrusion temperature. However the amount of increase is smaller when Sr is present in the alloy.

5.1.5. References

1- Z. Keshavarz, M. R. Barnett, "EBSD analysis of deformation modes in Mg–3Al–1Zn," Scripta Materialia, Volume 55, Issue 10 (2006) 915-918.
2- Qinglin Jina, Sung-Yong Shima, Su-Gun Lim, "Correlation of microstructural evolution and formation of basal texture in a coarse grained Mg–Al alloy during hot rolling," Scripta Materialia, Vol 55, Issue 9 (2006) 843-846.
3- E.A. Balla, P.B. Prangnella, "Tensile-compressive yield asymmetries in high strength wrought magnesium alloys," Scripta Metallurgica et Materialia, Volume 31, Issue 2, 15 (1994) 111-116.
4- J. Bohlen, S.B. Yi, J. Swiostek, D. Letzig, H.G. Brokmeier, K.U. Kainer, "Microstructure and texture development during hydrostatic extrusion of magnesium alloy AZ31," Scripta Materialia Vol 53, Issue 2, (2005) 259-264.
5- S.S. Park, B.S. You, D.J. Yoon, "Effect of the extrusion conditions on the texture and mechanical properties of indirect-extruded Mg–3Al–1Zn alloy," Journal of Materials Processing Technology, Vol 209, Issues 18-19 (2009) 5940-5943.

6- Y. Chen, Q. Wang, J. Peng, C. Zhai, W. Ding, "Effects of extrusion ratio on the microstructure and mechanical properties of AZ31 Mg alloy," Journal of Materials Processing Technology, Vol 182, Issues 1-3 (2007) 281-285.

7- M. Shahzad, L. Wagner, "Influence of extrusion parameters on microstructure and texture developments, and their effects on mechanical properties of the magnesium alloy AZ80," Materials Science and Engineering: A, Vol 506, Issues 1-2 (2009) 141-147T.

8- H. J. Mcqueen, M. Pekguleryuz, "Hot Workability of Magnesium Alloys" Magnesium Alloys and their Applications, Apr, 1992 Garmisch Partenkirchen, Germany, (1992) 101- 108.

9- N. Stanford, M.R. Barnett, "The origin of rare earth texture development in extruded Mg based alloys and its effect on tensile ductility," Materials Science and Engineering A, Volume 496, Issues 1-2 (2008) 399-408.

10- N. Stanford, "Micro-alloying Mg with Y, Ce, Gd and La for texture modification A comparative study," Materials Science and Engineering A, Vol 527, Issues 10-11 (2010) 2669-2677.

11- L.W.F. Mackenzie, B. Davis, F.J. Humphreys, G.W. Lorimer, "The deformation, recrystallization and texture of three magnesium alloy extrusions," Materials Science and Technology, Vol 23, No 10 (2007) 1173-1180.

12- L.W.F. Mackenzie, M.O. Pekguleryuz, "The recrystallization and texture of magnesium zinc-cerium alloys," Scripta Materialia, Vol 59, No 6 (2008) 665-668.

13- T. Laser, Ch. Hartig, M.R. Nürnberg, D. Letzig. R. Bormann, "The influence of calcium and cerium mischmetal on the microstructural evolution of Mg–3Al–1Zn during extrusion and resulting mechanical properties," Acta Materialia, Vol 56, Issue 12 (2008) 2791-2798.

14- B. Jing, S. Yangshan, X. Feng, X. Shan, Q. Jing T. Weijian, "Effect of extrusion on microstructures, and mechanical and creep properties of Mg–

Al–Sr and Mg–Al–Sr– Ca alloys," Scripta Materialia, Vol 55, Issue 12 (2006) 1163-1166.

15- X. Zeng, Y. Wang, W. Ding, A. A. Luo, A. K. Sachdev, "Effect of strontium on the microstructure, mechanical properties, and fracture behaviour of AZ31 magnesium alloy, "Metallurgical and Materials Transactions A, Vol 37, No 4 (2006) 1333-1341.

16- M. Pekguleryuz, E. Baril, P. Labelle, D. Argo, "Creep resistant Mg-Al-Sr alloys," Journal of Advanced Materials Vol 35, Issue: 3, (2003).

17- M. Pekguleryuz, A.A. Kaya, "Magnesium diecasting alloys for high temperature applications," TMS Annual Meeting, Symposium on Magnesium Technology Charlotte, NC, (2004).

18- P. Zhao, Q. Wang, C. Zhai, Y. Zhu, "Effects of strontium and titanium on the microstructure, tensile properties and creep behaviour of AM50 alloys," Materials Science and Engineering: A, Vol 444, Issues 1-2, (2007).

19- A. Sadeghi, M. Pekguleryuz, "Precipitation during the Solidification of Mg-3wt%Al- 1wt%Zn-(0.001-1%) Sr Alloys," American Foundry Society annual congress, Orlando, USA, (2010).

20- A. Sadeghi, M. Pekguleryuz, "Precipitation of Mg-3%Al-1%Zn-(0.01-1)wt%Sr Alloys during solidification," Journal of Materials Research / Volume 26 / Issue07, pp 896 – 903.

21- A. Sadeghi, M. Pekguleryuz, "Recrystallization and Texture Evolution of Mg-3%Al- %Zn- (0.4 -0.8) %Sr Alloys during Extrusion," Materials Science and Engineering A 528 (2011) 1678–1685

22- A. Sadeghi, M. Pekguleryuz, "Effect of Sr addition on Texture Evolution of Mg-3Al-1Zn (AZ31) Alloy during Extrusion," Materials Science and Engineering A 528 (2011) 1678–1685.

23- A. Sadeghi, M. Pekguleryuz, "Effect of trace levels of Sr on microstructure and mechanical properties of AZ31 Mg alloy," Materials Science and Engineering A.

24- L. Koubichek, “Effect of Small Additions of Elements on Grain Size and the Refinement of the Mg4Al3 [Mg17Al12] Phase in ML5 Alloy,” Izv. Vyschikh. Outchebnykh Za Vedeny, Metallurgy of Non-Ferrous Metals, No 6, (1959).

25- H.W. King, “Solid solution and intermetallic phases containing strontium,” Int. Conf. Strontium Containing Compounds, NRC, Ottawa, Canada, (1973) 212-243.

26- C.A. Aliravci, J.E. Gruzleski, and F.C. Dimayuga, ” Effect of Strontium on the shrinkage microporosity in magnesium sand castings,” AFS Trans. 92, (1992).

27- M.O. Pekguleryuz, M.M. Avedesian, “Magnesium Alloying - Some Metallurgical Aspects” Magnesium Alloys & their Applications, B.L. Mordike, F. Hehman, Eds. DGM, Germany, (1992) 679-686.

28- G. L’Esperance, P. Plamondon, M. Kunst, A. Fischersworring-Bunk, “Characterization of intermetallics in Mg–Al–Sr AJ62 alloys,” Intermetallics 18, 1 (2010).

Chapter 6

Effect of Pre Extrusion Annealing

In this chapter the effect of pre-deformation annealing on the microstructure and texture of an AZ31 + 0.8wt% Sr alloy is reported. This section has been submitted as a journal paper to the *Journal of Materials Science*.

As-cast samples as well as three samples that were annealed at 400^{o}C for 10, 30 and 120 minutes were extruded at 300^{o}C. Results showed that annealing transformed the bulky non-equilibrium Al-Mg-Sr precipitates to stable Al_4Sr spheroids. As the extent of this transformation before extrusion increased, the amount of uniformly dispersed intermetallic stringers in the extruded material also increased.

Texture measurements showed the alignment of basal poles with the compression axis and the formation of a basal ring texture in all samples. However, an increase in the duration of the pre-deformation anneal switched the plane facing the extrusion direction from first order prismatic (10-10) to second order prismatic planes (11-20). Annealing decreased the Al solute concentration in Mg and lowered the lattice resistance against dislocation movement. Consequently, the more favorable (0002)[11-20] slip system was activated in grains that saw low basal resolved shear stress (τ). As a result, those grains work harden and are consumed by dynamic recrystallization (DRX). However, the (0002)[-1100] slip system with high τ still avoids basal dislocation movement. Hence, the grains with low $\tau_{(0002)[-1100]}$ which need to move dislocations in the (0002)[-1100] system to fulfill the strain compatibility conditions across the microstructure would be prevented from work hardening and DRX. This specific orientation has a (-1100) plane facing the extrusion direction.

6.1. Effect of Annealing on the Microstructure and Texture Evolution of Mg-3Al-1Zn-0.8Sr Alloy during Hot Extrusion

Alireza Sadeghi, Mihriban Pekguleryuz

McGill University, Department of Mining and Materials Science, Montreal, Quebec, Canada

Published in Journal of Materials Science Available online 10 April 2012, DOI: 10.1007/s10853-012-6416-0

6.1.1. Introduction

The design and development of high strength, formable and isotropic wrought Mg alloys has become the main focus of many researches in order to manufacture automotive body parts such as door panels or front-end components. The addition of rare earth (RE) elements can be one of the routes to attain improved mechanical properties of Mg alloys [1,2]. However, the high cost of the individual RE alloying additions limits the commercialization of those alloys [2], while using the more cost-effective mischmetall (combination of RE elements) can lead to microstructural instability. Strontium (Sr) has been added to Mg alloys to achieve effects similar to RE elements properties at a lower price [3]. Sr addition to a Mg alloy containing Al led to the development of the AJ series in 2002-2004 [4]. The alloy that was commercialized has considerable creep resistance which makes it an excellent choice for powertrain applications [5]. Sr has also been added to wrought Mg alloys and the hot deformation behaviour has been thoroughly studied [6-15]. The authors have previously reported that in AZ31+Sr alloys, at specific thermo-mechanical conditions, thermally stable Al-Sr precipitates are able to initiate particle stimulated nucleation (PSN) and form grains with orientations other than the dominant basal texture [13,14]. Nonetheless, there is an optimum level for Sr addition; excess levels of Sr will make the alloy brittle in deformation by inducing crack initiation at the Al-Sr precipitates [15].

When Sr is added to AZ31 (Mg-3Al-1Zn) alloy, the formation of β-$Mg_{17}Al_{12}$ precipitate is suppressed [6]. The equilibrium Al_4Sr precipitate formation is predicted [6,7]. However, it is seen that, instead of the binary Al-Sr, a

non-equilibrium ternary Al-Mg-Sr phase precipitates [7]. Janz *et al*. [16] have shown that the only ternary equilibrium precipitate in the Al-Mg-Sr system is τ-$Al_{38}Mg_{58}Sr_4$ which is seen in alloys containing high levels of Sr and all other ternary precipitates are non-equilibrium. It has been reported by L'Esperance *et al*. [17] that non-equilibrium Al-Mg-Sr precipitates reject excess Mg to the matrix and absorb Al from the surroundings and decompose to the equilibrium eutectic Al_4Sr. This decomposition has also been seen during the hot deformation of a cast alloy by the authors [15]. The unstable ternary precipitates can be partially or completely decomposed at different annealing times or temperatures. In the present research, four different Al-Mg-Sr/Al-Sr precipitate ratios have been prepared in AZ31+0.8Sr by controlling the annealing time and temperature. The as-cast and annealed samples were extruded at elevated temperatures and the final microstructure, precipitate distribution, hardness and texture was studied.

6.1.2. Experimental Procedure

AZ31 extruded bars (provided by Applied Magnesium, Denver, CO) and Sr-10Al master alloy (Timminco, Haley, ON) were melted in a graphite crucible using a high frequency induction furnace (NORAX) at 700^{o}C to prepare the AZ31+0.8wt%Sr alloy. The molten alloy was held at 700^{o}C for 15 minutes in order to completely dissolve the master alloy. After skimming the melt surface, the temperature was raised to 720^{o}C then cast into a preheated cylindrical steel die. The chemical composition of the cast sample was determined to be Mg-3.07Al-0.83Zn-0.55Mn-0.74Sr by inductively coupled plasma (ICP).

Four samples were machined to cylinders 3 cm in diameter and 6 cm height in order to fit the extrusion die chamber. Three samples were annealed at 400^{o}C for 10, 30 and 120 minutes using a Blue M Lindberg inert-gas mechanical convection-oven. Subsequently, the three annealed and the as-cast samples were extruded at 300^{o}C. Hot extrusion was performed using a steel die setup and a 100T hydraulic press down to a 1cm diameter bar. The ram speed was kept constant at 4 mm s^{-1} and a high temperature anti-seize paste (Molycote P-37) was used for die lubrication. In order to achieve special combinations of precipitates

two more samples were also prepared. One of the samples was annealed at 250^{o}C and the other at 350^{o}C, both for 30 minutes and then extruded at their corresponding annealing temperatures.

Extruded bars were sectioned along the extrusion direction. The surface was prepared for optical and scanning electron microscopy by grinding and polishing with 1 μm diamond paste. Optical microscopy results were used to measure the grain size and the distance between the precipitate stringers using the line intercept method. Polished samples were examined with a back scattered electron detector (BSE) in a Hitachi S-4700 field emission gun scanning electron microscope (FEG/SEM). Electron probe microanalysis (EPMA) and electron back scatter diffraction (EBSD) was also performed to identify the phase compositions and elemental distribution and to investigate the misorientations inside the grains across the microstructure. Electro-polishing in a 5 % natal solution at 0^{o}C was used to prepare the EBSD samples and the grain structure was revealed using a picric acetic solution in optical microscopy. Errors encountered with EBSD measurement are summerized in Appendix II.

Micro-Vickers hardness test was performed on the extruded bars to investigate the hardness variation across the rectangular cross section. Measurements were carried out using a 10 g force and in 0.5 mm intervals. Copper K_{α} X-rays were used in a D8 Bruker diffractometer to study the texture of the extruded samples. The beam was radiated on the center line of the rectangular cross sections with a 1mm oscillation. Orientation distribution functions (ODF), pole figures and volume fraction of different planes in the extrusion direction were calculated from the raw data using the TextTools texture analysis software.

6.1.3. Results and Discussion

6.1.3.1. Precipitates In As-Cast And Annealed Microstructures

EPMA results of an as-cast AZ31+0.8Sr sample are shown in Fig.6.1.1. The formation of the continuous precipitates at the grain boundaries and interdendritic regions can easily be distinguished in the back-scattered image and element maps.

Note that the interdendritic precipitate contains Mg and confirms the formation of a ternary Al-Mg-Sr phase.

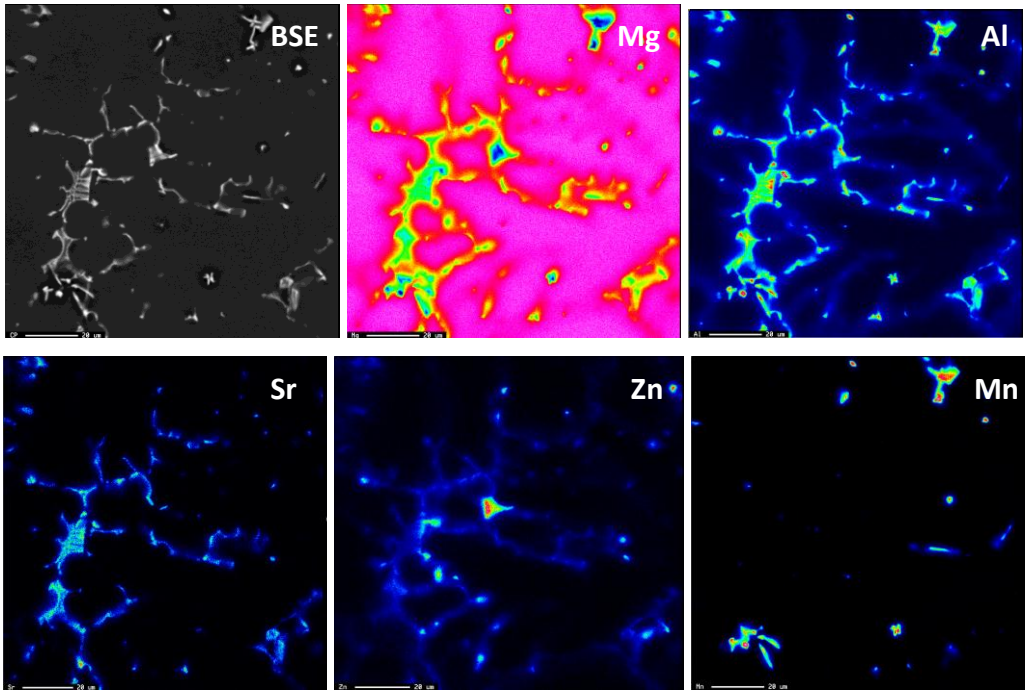

Figure.6.1.1. EPMA mapping of as-cast AZ31+0.8%Sr microstructure.

Moreover, the existence of Zn was also observed in this phase. Interestingly, pure Zn segregated to the interdendritic regions (the red color areas in the Zn map). This has been previously observed by the authors [7] and reported by other researchers [18]. The Mn map, reveals the presence of needle shaped Al-Mn phase as well which is known to be Al_8Mn_5 [7].

The BSE images of the as-cast and annealed precipitates are illustrated in Fig.6.1.2. It is seen that increasing the annealing time at 400^{o}C up to 120 minutes (Fig.6.1.2a to 2d) increased the fraction of the decomposed precipitate which was identified via its spheroidized morphology. In Fig.6.1.3, a partially decomposed Al-Mg-Sr precipitate is shown. As noted, upon thermal exposure, the non-equilibrium precipitate decomposed starting at its boundaries and by rejecting Mg and absorbing Al, the eutectic Al_4Sr precipitate was formed.

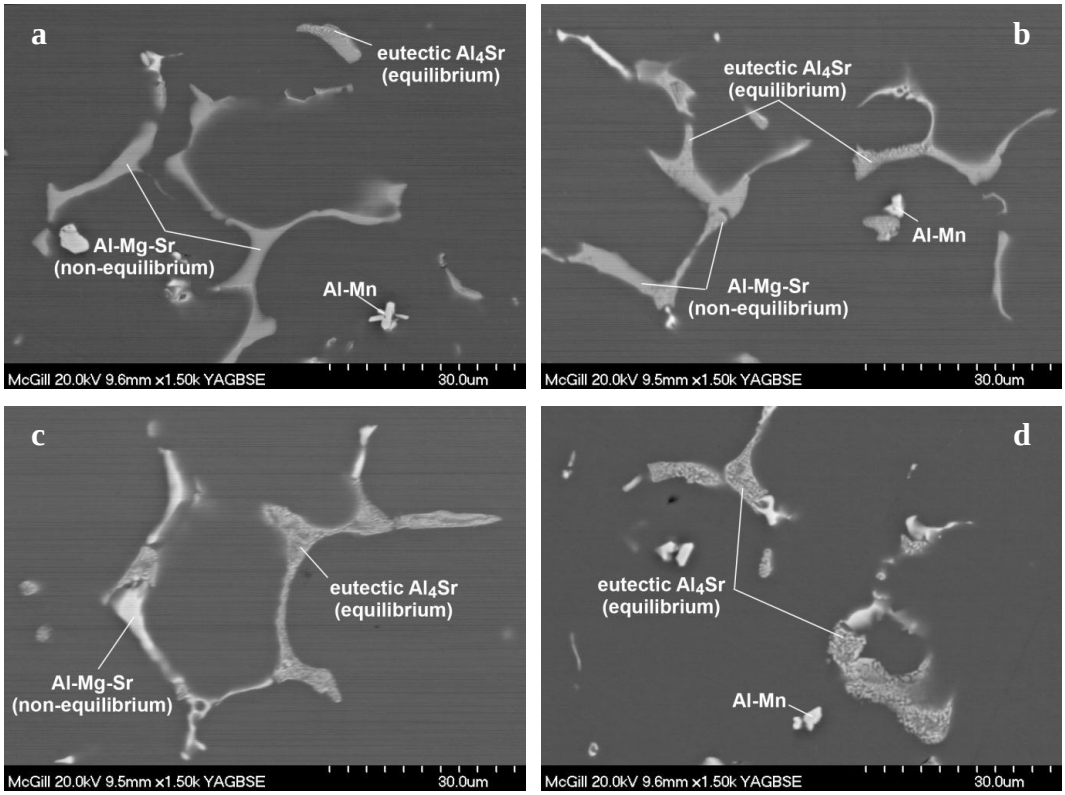

Figure .6.1.2. Decomposition sequence of Al-Mg-Sr precipitate in AZ31+0.8wt%Sr as a result of annealing at 400^{o}C, (a) as-cast, (b) 10 min, (c) 30 min, (d) 120 min.

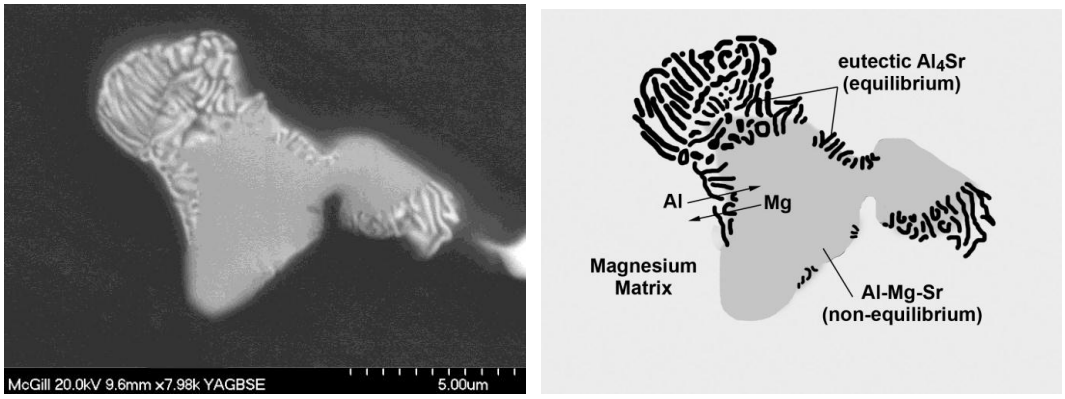

Figure .6.1.3. Partial decomposition of an Mg-Al-Sr precipitate in as-cast AZ31+0.7wt%Sr to laminar Al_4Sr precipitates.

As seen in the optical micrographs of the extruded samples (Fig.6.1.4), the non-annealed sample (Fig.6.1.4a) had the finest grain size and the final grain size of the alloy increased with increasing annealing time before extrusion. The grain size

values of the four extruded samples are shown graphically in Fig.6.1.5. The increase in grain size with increasing annealing time can be attributed to two mechanisms:

(i) The precipitate sizes at the stringers become smaller and less effective in blocking the movement of the grain boundaries and the growth of DRX grains.

(ii) Through the consumption of Al atoms in the Al-Mg-Sr→Al-Sr transformation, the level of Al in Mg solid solution decreases and the efficiency of Al atoms in blocking dislocations at grain boundaries is reduced [13,14].

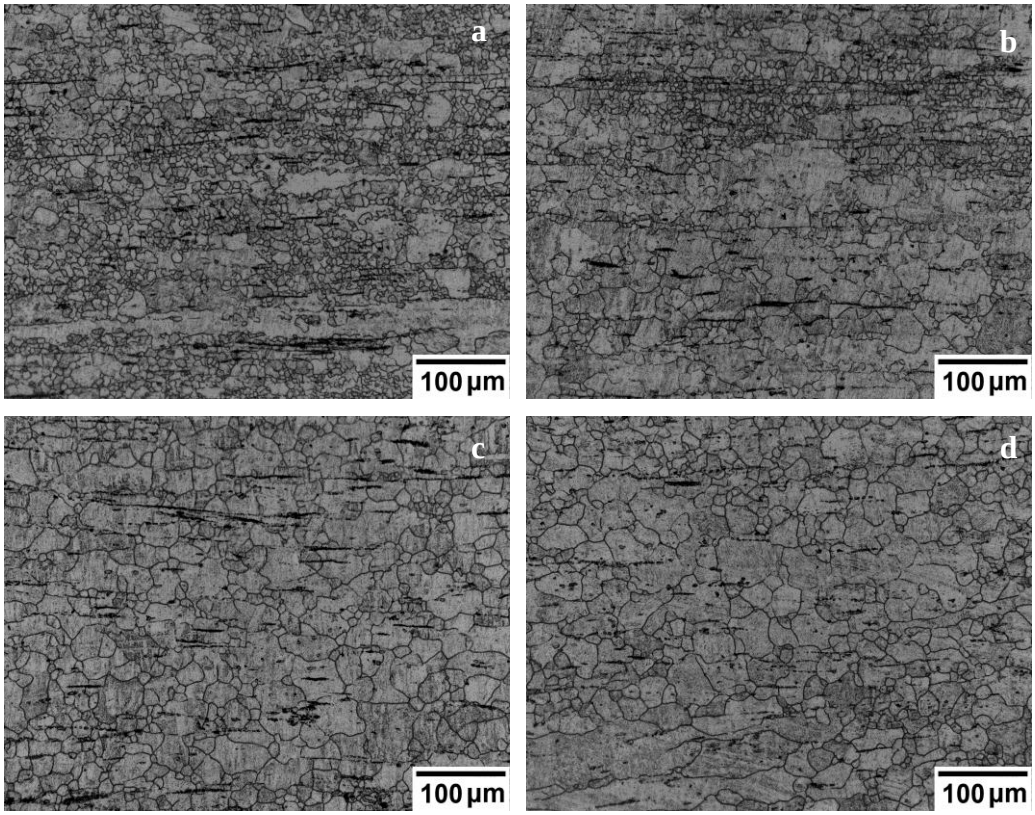

Figure .6.1.4. Optical microstructure of extruded AZ31+0.7wt%Sr. (a) no annealing before extrusion (as-cast), annealed for (b) 10 min, (c) 30 min, (d) 120 min before extrusion

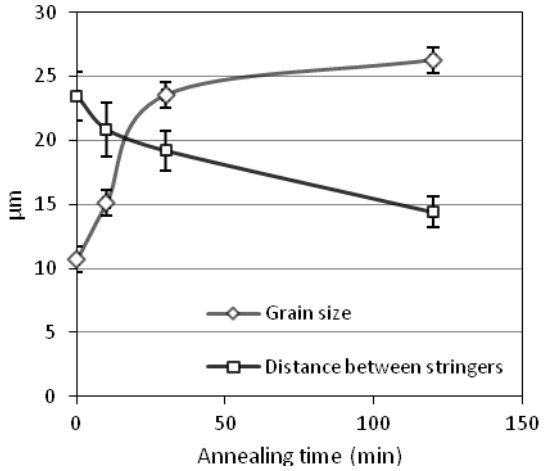

Figure.6.1.5. Grain size of extruded samples vs. annealing time before extrusion.

It can be predicted that when the Al-Mg-Sr precipitates are completely decomposed to small spheroids, they could be dispersed more easily in the Mg matrix during extrusion. In Fig.6.1.6a to 6d, the finer size of the precipitates and their more uniform distribution as a result of increasing annealing time are shown. Measurements show that the average distance between the stringer lines has decreased by 39 %, from 23 to 14 μm (Fig.6.1.5) when the as-cast material was annealed for 120 minutes. Fig.6.1.7 shows the precipitate stringers of the samples annealed for 10 and 120 minutes at a higher magnification. Note that the precipitates in the sample annealed for 10 minutes (Fig.6.1.7a) have also decomposed into spheroids, but the stringers are thicker compared to the sample annealed for 120 minutes (Fig.6.1.7b). This decomposition occurred during hot deformation and was not able to disperse the spheroids homogeneously. The partial decomposition of the Al-Mg-Sr precipitates has been witnessed even in as-cast samples [15].

To investigate the crack tendency of the different precipitates at different annealing conditions, two other samples were designed: (1) a sample with no decomposition of Al-Mg-Sr and (2) a partially decomposed sample with thick stringers. Fig.6.1.6 clearly shows how the precipitates of both samples were cracked. In Fig.6.1.8a and b, the dark crack lines are perpendicular to the tensile axis and are the starting points of crack propagation in the Mg matrix [15].

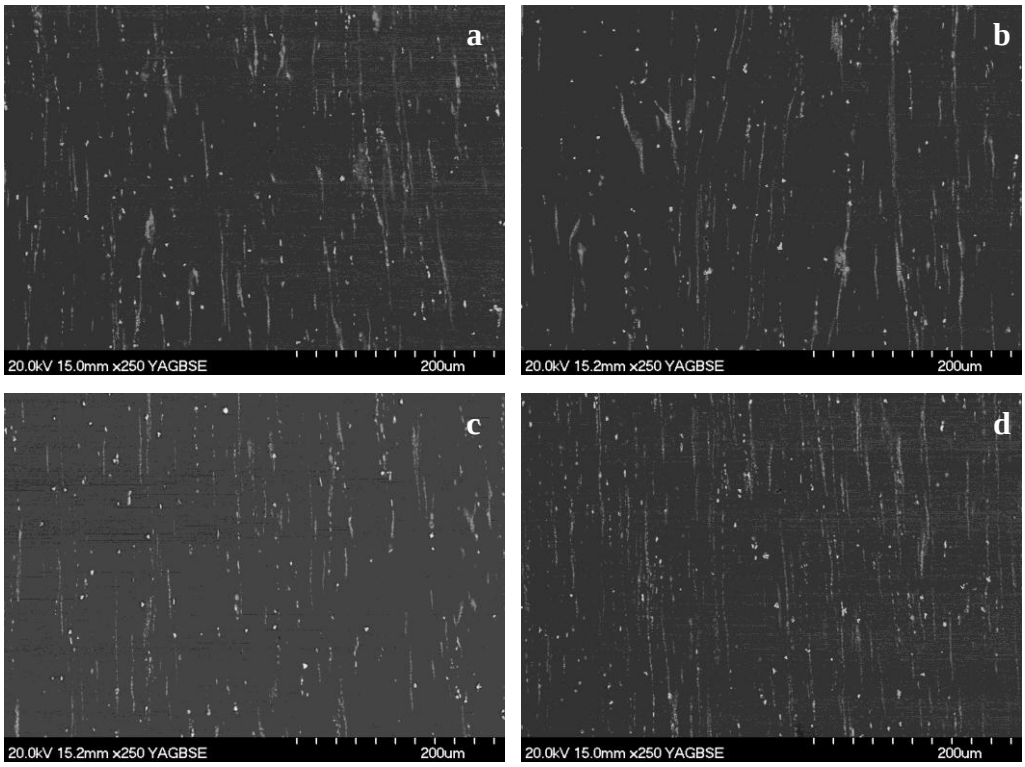

Figure .6.1.6. Back scattered electron images of AZ31+0.7wt%Sr. (a) no annealing before extrusion (as-cast), annealed for (b) 10 min, (c) 30 min, (d) 120 min before extrusion at 300^{o}C.

Results indicate that the cracking tendency depended more on stringer (precipitate) thickness (size) than on its composition or morphology. Both Fig.6.1.6.1.8a and 8b reveal that the large precipitates, regardless of their shape and composition, are cracked while the smaller precipitates have remained unaltered. It has p[reviously been reported [19] that the lattice rotation around a precipitate is proportional to the particle size. For non-deformable particles of diameter greater than ~2.5 μm, lattice rotations in the surrounding matrix are the only relaxation mechanism during deformation. However, for particles in the size range of 0.1 to 2.5 μm, plastic relaxation occurs both by the formation of dislocation loops around the particle and rotated deformation zones [19].

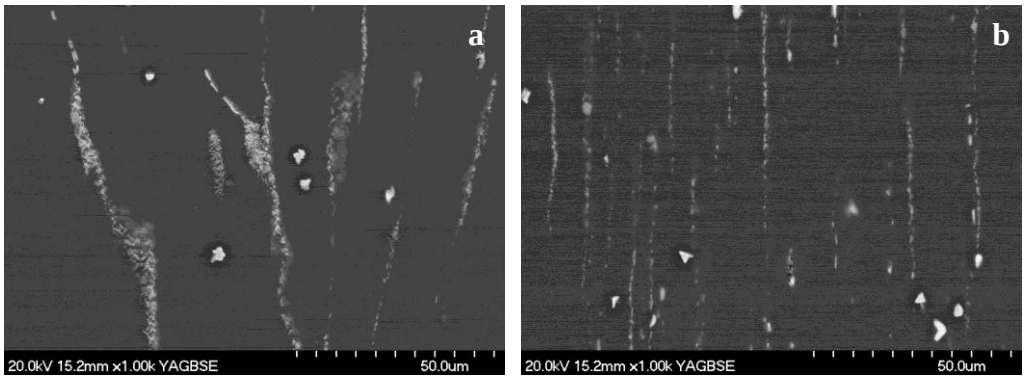

Figure .6.1.7. Back scattered electron images of AZ31+0.7wt%Sr. (a) annealed for 10 min, (b) 120 min before extrusion.

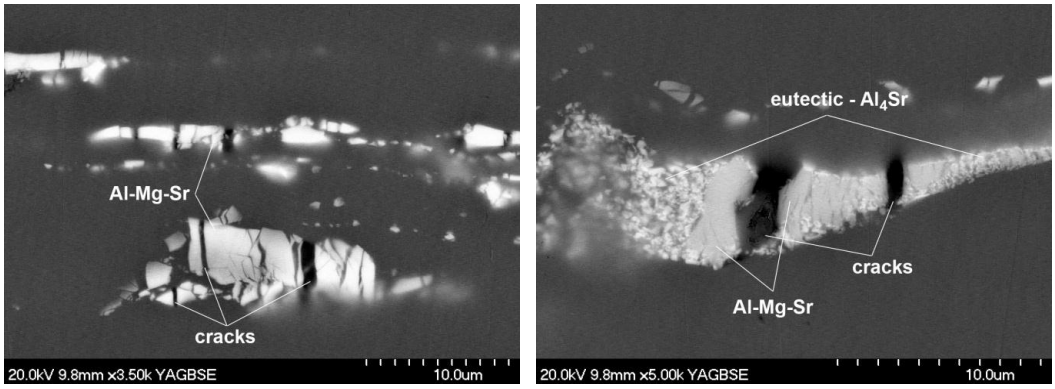

Figure .6.1.8. AZ31+0.7wt%Sr extrusion after tensile test (a) annealed at 250^{o}C for 30 min and extruded at the same temperature, and (b) annealed at 350^{o}C for 30 min and extruded at the same temperature.

In other words, smaller precipitates develop smaller deformation zones and the movement of dislocations around them eliminates a portion of the pressure caused by the rotation of the surrounding matrix. However, the large strain accumulation behind the large precipitates imposes a large stress on the particle and when the stress exceeds a certain level, the precipitate will eventually fracture.

6.1.3.2. Micro-hardness

Fig.6.1.9a shows the Vickers micro hardness distribution measured across the diameter of the extruded bars. As the annealing time prior to extrusion increases the hardness profile becomes smoother. The average hardness values and the

divergence from the average value are presented in Fig.6.1.9b, which indicates that the absolute value of the hardness of the extruded bars did not change with increasing annealing time, but the divergence was significantly reduced. This also confirms the previous microstructural observations which indicated increased homogeneity with increasing annealing time.

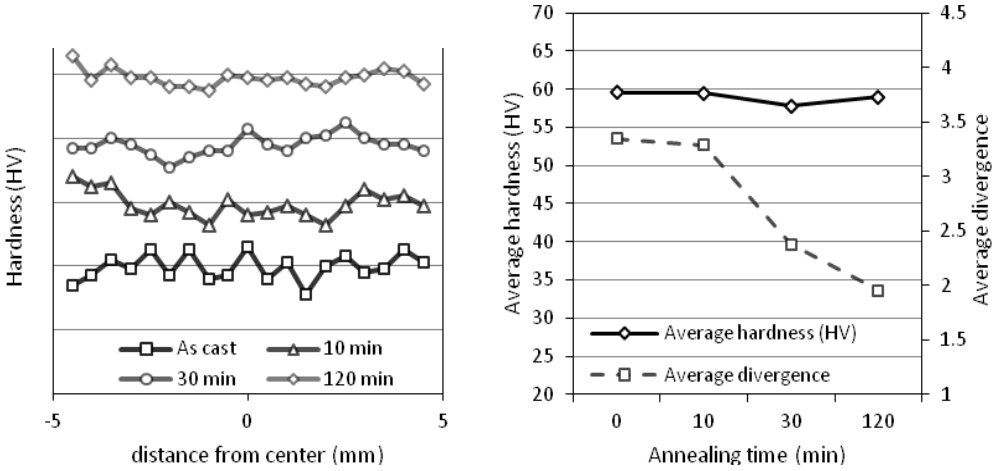

Figure .6.1.9. (a) Hardness distribution, (b) average hardness and average divergence vs. annealing time along the thickness of the extruded bars.

6.1.3.3. Texture

The {0002}, {10-10} and {11-20} pole figures of extruded samples with different annealing regimes prior to extrusion are listed in Fig.6.1.10. The basal pole figures (first row in Fig.6.1.10) indicate that the ring basal-texture formed in all samples, but there was no significant relationship between texture intensity/distribution and pre-extrusion annealing. However, the two other rows of pole figures in Fig.6.1.10, reveal notable relationships. The {10-10} pole figures (second row in Fig.6.1.10) show that the increase in annealing time has decreased the maximum intensity of the pole figures. Moreover, increasing annealing time weakened the concentration of contours around the ED pole. The third row of Fig.6.1.10 ({11-20} pole figures) shows that, when the annealing time was increased, the contours became more concentrated around the ED axis. The gradual change of texture can be more clearly distinguished in the inverse pole

figures presented in Fig.6.1.11. It is observed that increasing the annealing time spread out the contours from {10-10} toward the {11-20} corner.

6.1.3.4. Micro-Mechanisms in Texture Development

The texture measurements indicate that, although the basal texture has not altered, there is a change in the orientation of the crystal plane facing the extrusion direction.

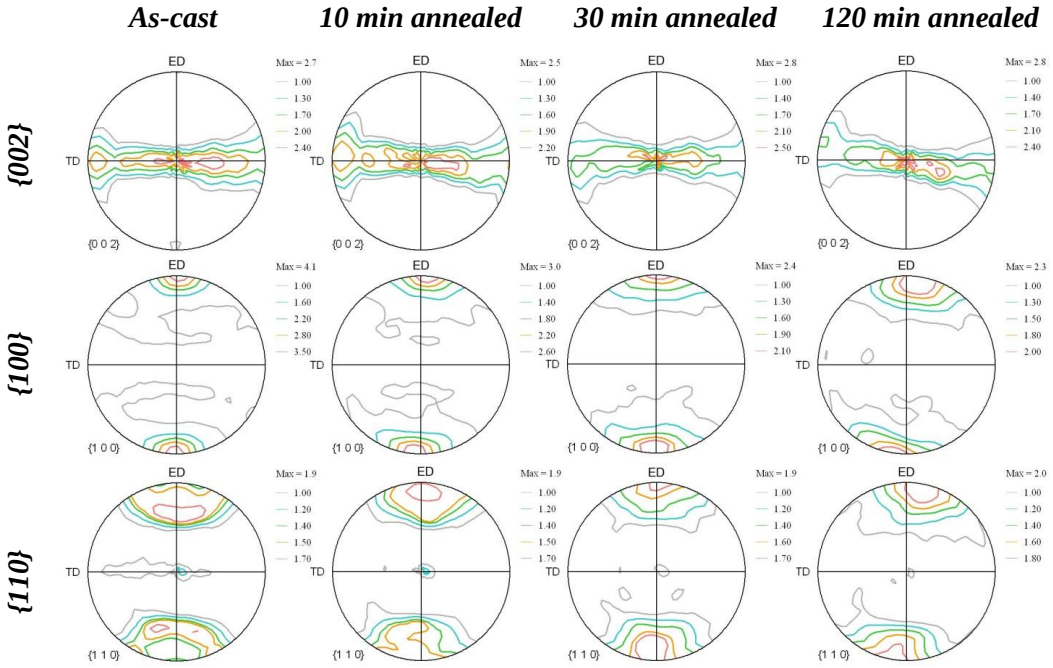

Figure .6.1.10. Pole figure representation of the hot extruded samples having different annealing times prior to extrusion.

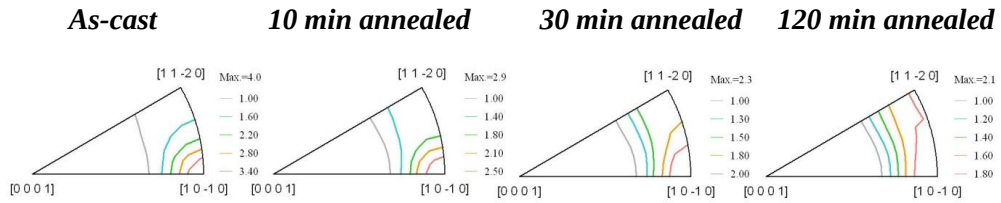

Figure .6.1.11. Inverse pole figures from the circular cross section of the extruded samples having different annealing times before extrusion

To understand which micro-mechanisms are affecting the change of plane orientations, it is necessary to carefully review two main concepts: (1) how DRX develops the basal texture during hot deformation and (2) which slip systems prepare the initial conditions of DRX.

Crystal Orientation

(1) As described above, during a deformation process, dislocations slip in differently oriented grains to fulfill the strain compatibility conditions in a polycrystalline microstructure. The slip process is considered in terms of the shear stress resolved on the slip plane in the slip direction (τ). In Mg, the (0002) basal plane and the three [11-20], [-12-10] and [2-1-10] directions prepare the favourable slip systems. As is well known, according to the orientation of the basal planes with respect to the compression axis, different grains would have different resolved shear stresses on the basal system, which could be calculated by the $\tau = \sigma \cos \Phi \cos \lambda$ equation, (where σ is the magnitude of the applied stress, Φ is the angle between the slip plane normal and the applied stress direction and λ is the angle between the slip and applied force directions). When the basal plane normal is close to the compression axis λ would be $\sim 90^{o}$ and τ approaches 0. Consequently there would be limited basal slip in such a grain and since the other slip systems in hcp have are not activated at moderate temperatures, work hardening would not be sufficient to initiate DRX. Conversely, grains with other orientations where the basal system sees a finite τ would be work hardened and then transformed, via DRX, to new grains with different orientations. Once again the grains with the basal plane facing the compression axis would stay stable and the others would be consumed via DRX. This cycle would be repeated until all of the structure becomes comprised of grains with the basal normals in the compression direction.

(2) Note that as before, there are three favourable slip directions in the basal plane, [11-20], [-12-10] and [2-1-10]. In Fig.6.1.12a the directions are shown in a hexagonal lattice. The [-1100] direction can be described entirely as a combination of slip in the two [11-20], [-12-10] directions. In Fig.6.1.12 b and c,

the slip directions and planes perpendicular to them are shown. If the movement of dislocations on the basal planes in the (11-20) directions becomes restricted, the first order prismatic planes ((10-10) planes) would face the extrusion direction (Fig.6.1.12b). However, if the movement of the (0002)[-1100] system is blocked, the second order prismatic planes ((11-20) planes) would become perpendicular to the extrusion direction (Fig.6.1.12c). The two final orientations resulting from basal slip blockage in different directions have 30^o deviation from one another (Fig.6.1.13a). The priority of activation of slip in the two different directions is based on a simple concept. To move a dislocation one step forward on the basal plane in the [11-20] direction only one atomic jump is enough. While one step movement in the [-1100] direction needs two jumps, one in the [11-20] direction and the other in [-12-10] (Fig.6.1.12a). Obviously, slip in the [-1100] direction becomes more energy consuming and would be less favourable.

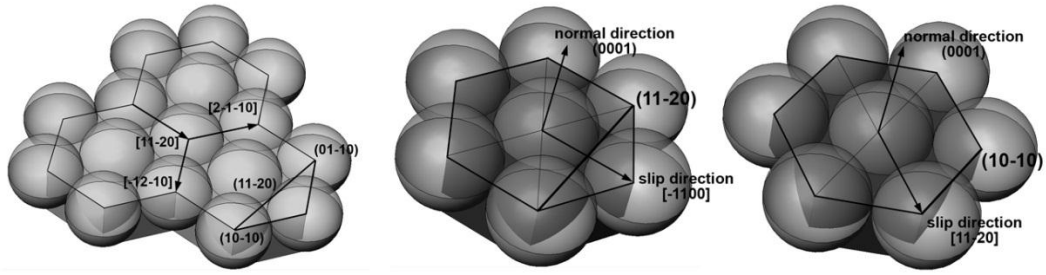

Figure .6.1.12. Favorable slip directions in the basal planes, (b) activation of the (0002)[-1100] slip system and (c) activation of the (0002)[11-20] system.

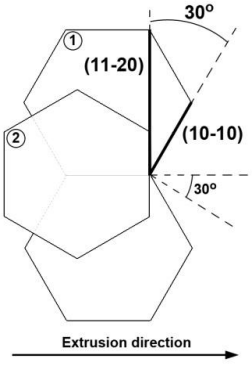

Figure .6.1.13. Schematic view showing the 30^o misorientation between the (10-10) and (11-20) planes in a hexagonal crystal.

6.1.3.5. Lattice Resistance:

Crystal orientation is not the only controlling parameter for the movement of dislocations. Lattice resistance against dislocation movement is another significant limiting factor. In the samples studied, the Al concentration in Mg solid solution (α-Mg) plays a key role in controlling the lattice resistance [13,14]. As described above, the initial precipitate which forms during solidification of the AZ31+0.8Sr alloy is a non-equilibrium Al-Mg-Sr phase. During annealing, this phase rejects excess Mg and absorbs Al from the surrounding matrix to reach a stable Al_4Sr stochiometry [7,15,17]. The diffusion of Al atoms to the precipitates lowers the concentration of dissolved Al in α-Mg [15,17] and directly effects lattice resistance against dislocation motion [13,14]. Consequently slip becomes easier and the dislocations are able to move in the active slip direction. In the non-annealed sample, when the c-axis of the grains is close to the compression axis, dislocation movement is restricted by the high lattice resistance even for the "single jump" [11-20] direction. As a result, there would be little or no work hardening in the grain; DRX would not occur and the grain would remain stable until the end of deformation. The longer the duration of annealing, the lower the lattice resistance and the easier the dislocation motion in the "single jump" directions. Therefore, work hardening followed by DRX occurs in grains which have the orientation of Fig11.b. However, dislocations are stopped in grains in which the [-1100] slip direction is needed to fulfill the strain compatibility criteria. This is why the IPF intensity decreases and the contours shift of toward the (11-20) corner in Fig.6.1.10 when the annealing time is increased.

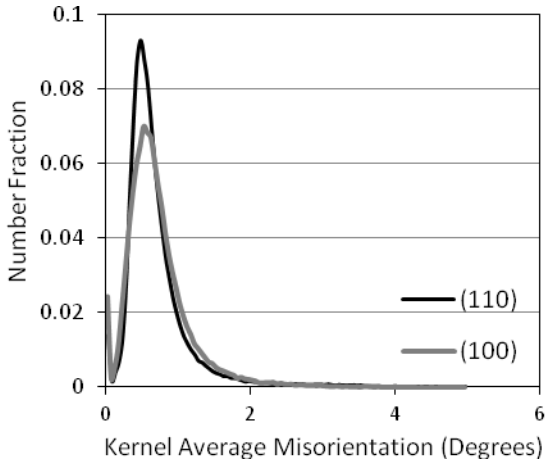

Figure .6.1.14. Kernel average misorientation distribution across the grains having their (11-20) (labelled as (100)) and (-1100) (labelled as 110) plane facing the extrusion direction.

The local misorientation in grains can be calculated by measuring the kernel average misorientation (KAM) using EBSD. For a given data point, KAM is the average misorientation between the data point and all of its neighbours (excluding misorientations greater than some prescribed value - 5 degrees in this case). In Fig.6.1.14, KAM distribution is plotted separately for grains having their (11-20) and (10-10) planes facing the extrusion direction (the basal poles are in the radial direction for both types of grains). It could be seen how the (11-20) grains illustrate a higher misorientation at very low angles ($<1^o$) which is a result of resistance against easy slip.

6.1.3.6. Quantitative Analysis of Texture Change

The texture change can be more quantitatively analyzed by measuring the volume fraction of the first and second order prismatic planes less than 15^o away from facing the extrusion direction (f_v) (shown in Fig.6.1.15). It is interesting to note that the volume fraction of (10-10) normals facing the extrusion direction decreased with increasing annealing time while the volume fraction of the (11-20) planes perpendicular to extrusion direction increased. The results show a 30% decrease in the f_v of the (10-10) and 20% increase in the (11-20) planes. The

competition between slip in the two [11-20] and [-1100] directions resulted in similar effects in other studies as well [20].

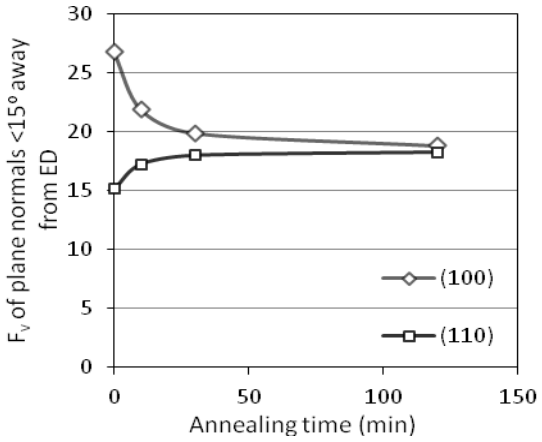

Figure .6.1.15. Volume fraction of the (10-10) and (11-20) normals less than 15^o away from extrusion direction vs. annealing time.

Yi *et al*. [20] previously reported a similar change of texture in AZ31 alloys as a result of annealing after extrusion, the texture component in the IPF moveed from the (10-10) to the (11-20) corner by increasing the annealing time after extrusion. Their EBSD results proved that the driving force for growth of (10-10) grains is diminished in early stages of annealing whereas, (11-20) grains grow extensively and affect the final texture [20]. The reason why there is a stronger driving force for (11-20) grains can be attributed to by the same factors described here. The lower amount of dislocation movement in the (0002)[-1100] slip system accumulates less work hardening in the grains facing the (11-20) plane toward the extrusion direction. Consequently, the new grains having this (11-20) orientation would have less dislocation density and a higher driving force to grow during annealing. Finally, the texture would be dominated by the orientation of grains with second prismatic planes facing the extrusion direction.

6.1.4. Conclusions

AZ31-0.74Sr alloy was cast and subsequently extruded at 300C. The samples were annealed at 400C for 10, 30, and 120 min before extrusion and were

compared with the sample without annealing. Microstructural analysis, mechanical characterization, and texture measurements have been employed to investigate the effect of annealing before extrusion on the Sr containing AZ31 alloy and the following conclusions are drawn:

1. Annealing at 400^{o}C results in the decomposition of the Mg-Al-Sr non-equilibrium phase to a stable Al_4Sr precipitate. Increasing annealing time increases the extent of the transformation.
2. Increasing annealing time causes stringers to disperse more homogeneously and leads to a more uniform hardness gradient across the diameter of the extruded bar.
3. When the annealing time prior to deformation is increased, smaller and more dispersed stringer particles form and the decrease of Al solute in α-Mg lessens the obstacles against grain growth after recrystallization; consequently a larger grain size is formed.
4. Although the basal texture was maintained during all annealing conditions studied, there was a slight gradual change in the plane facing the extrusion direction from first order to second order prism with increasing annealing time.
5. The change in basal orientation was described to be a result of change in the blockage of dislocations in different slip systems. In grains having a basal τ close to zero, the favourable (0002)[11-20] systems see less resistant to slip when Al is reduced in α-Mg during annealing. However, the higher energy consuming (0002)[-1100] system still avoids dislocation motion, work hardening and DRX. Consequently, the maximum intensity of IPF drops and the volume fraction of (11-20) planes facing the extrusion direction increases.

6.1.5. References

25- A. Luo, M.O. Pekguleryuz, “Cast Magnesium Alloys for Elevated Temperature Applications,” Journal of Materials Science, Vol 29, No 20, (1994) 5259-5271.

26- L.L. Rokhlin, "Magnesium Alloys Containing Rare Earth Metals: Structure and Properties," CRC Press, 1 edition (2003).

27- E. Baril, P. Labelle, M.O. Pekguleryuz, "Elevated Temperature Mg-Al-Sr: Creep Resistance, Mechanical Properties & Microstructure," Journal of Metals (JOM-US), TMS, Vol 55, No 11, (2003) 34-39.

28- E. Baril, P. Labelle, M.O. Pekguleryuz, "Elevated Temperature Mg-Al-Sr: Creep Resistance, Mechanical Properties & Microstructure," J. Metals (JOM-US), TMS, vol. 55, no. 11 2003, pp. 34-39.

29- M.O. Pekguleryuz, A.A. Kaya, "Creep Resistant Magnesium Alloys for Powertrain Applications," Magnesium Alloys and their Applications, Deutsche Gesellschaft für Materialkunde, Garmisch (DGM), Germany (2003) 74-93.

30- A. Sadeghi, M. Pekguleryuz, "Precipitation during the Solidification of Mg-3wt%Al-1wt%Zn-(0.001-1%) Sr Alloys," American Foundry Society annual congress, Orlando, USA, (2010).

31- A. Sadeghi, M. Pekguleryuz, "Precipitation of Mg-3%Al-1%Zn-(0.01-1)wt%Sr Alloys during solidification," Journal of Materials Research, (in press).

32- A. Sadeghi, M. Pekguleryuz, "Microstructure, mechanical properties and texture evolution of AZ31 alloy containing trace levels of strontium," (not yet published)

33- Zeng X., Wang Y., Ding W., Luo A A., Sachdev A.K., "Effect of strontium on the microstructure, mechanical properties, and fracture behaviour of AZ31 magnesium alloy," Metallurgical and Materials Transactions A, Vol 37, No 4, (2006)

34- Jing B., Yangshan S., Shan X., Feng X., Tianbai Z., "Microstructure and Tensile Creep Behaviour of Mg–4Al Based Magnesium Alloys with Alkaline-Earth Elements Sr and Ca Additions," Materials Science and Engineering A, Vol 419, Issues 1-2, (2006)

35- B. Jing, S. Yangshan, X. Feng, X. Shan, Q. Jing T. Weijian, "Effect of extrusion on microstructures, and mechanical and creep properties of

Mg–Al–Sr and Mg–Al–Sr–Ca alloys," Scripta Materialia, Vol 55, Issue 12 (2006) 1163-1166.

36- P. Zhao, Q. Wang, C. Zhai, Y. Zhu, "Effects of strontium and titanium on the microstructure, tensile properties and creep behaviour of AM50 alloys," Materials Science and Engineering: A, Vol 444, Issues 1-2, (2007).

37- A. Sadeghi, M. Pekguleryuz, "Recrystallization and texture evolution of Mg–3%Al–1%Zn–(0.4–0.8)%Sr alloys during extrusion," Materials Science and Engineering: A, Volume 528, Issue 3, (2011), 1678-1685.

38- A. Sadeghi, M. Hoseini, M. Pekguleryuz, "Effect of Sr addition on texture evolution of Mg–3Al–1Zn (AZ31) alloy during extrusion," Materials Science and Engineering: A, (In Press), Corrected Proof, Available online 4 January 2011.

39- A. Sadeghi, S. Shook, M. Pekguleryuz, "Yield Asymmetry and Fracture Behaviour of Mg-3%Al-1%Zn-(0-1)%Sr Alloys Extruded at Elevated Temperatures," (not yet published)

40- Janz, J. Gröbner, D. Mirković, M. Medraj, Jun Zhu, Y. A. Chang, R. Schmid-Fetzer: "Experimental study and thermodynamic calculation of Al-Mg-Sr phase equilibria," Intermetallics, 15, (2007) 506-519.

41- L'Espérance G., Plamondon P., Kunst M., Fischersworring-Bunk A., "Characterization of intermetallics in Mg–Al–Sr AJ62 alloys," Intermetallics, Vol 18, Issue 1, (2010).

42- A. Becerra, M. Pekguleryuz, "Effects of Lithium, Indium and Zinc on the Grain Size of Magnesium," Journal of Materials Research, vol. 24, No. 5 (2009) 1722.

43- F.J. Humphreys, M. Hatherly, "Recrystallization and related annealing phenomena," Pergamon Press, Oxford (1996)

44- S. Yia, H. Brokmeier, D. Letzig, "Microstructural evolution during the annealing of an extruded AZ31 magnesium alloy," Journal of Alloys and Compounds 506 (2010) 364–371.

Chapter 7

Seamed and Seamless Tube Extrusion

Three Mg alloys (AZ31, and AZ31+0.4 and 0.8wt%Sr) were hot extruded at 400^{o}C on a Lab Scale extrusion press at McGill through a porthole die into tubes (Section 7.1). Strontium (Sr) additions to AZ31 alloy reduced twinning and the DRX grain size. However, Sr also increased the surface cracking tendency during extrusion. It was noted that the complex deformation path in the porthole die distributes the Sr-rich precipitates homogeneously across the microstructure and stringer formation is effectively avoided.

The material flow in the die resembled that seen in multiple equal channel angular pressing (ECAP) routes, and similar and significant effects on the final texture are observed. The curvatures in the material flow rotate the basal poles 25^{o} from the radial direction and introduced a new texture component (δ) in the pole figures. The maximum intensity of the orientation distribution function (ODF) was reduced with increasing Sr. Notably, the maximum intensity in AZ31+0.8Sr occurred at the δ component while for AZ31 and AZ31+0.4Sr the maximum intensity was located at the basal components. The final texture presented a lower amount of basal planes perpendicular to the radial direction and the orientation of grains led to high Schmid factors on the basal system for further deformation. These results have been published in Journal of Materilas Science.

Section 7.2 presents work on seam-less tubes of AZ31, AZ31+0.4 and 0.8wt%Sr extruded at elevated temperatures. By compressing pure copper inserts inside the tubes, extruded tubes were expanded at room and elevated temperatures (100 and 200^{o}C). Microstructural examinations revealed the formation of twinning in the as-extruded and expanded tubes. The amount of twinning decreased with increasing Sr in the expanded microstructures as a result of grain refinement, and due to decreasing Al solubility, which facilitates dislocation motion. During expansion at room temperature, AZ31 showed higher elongation and lower strength than the alloys containing Sr. At 200^{o}C, the Sr containing alloys exhibited lower flow stress and no fracture in the strain range investigated.

The textures of the extruded alloys contained two main components named as RD (c-axis parallel to the radial direction) and HD (c-axis parallel to the radial hoop direction) based on their orientation with the sample coordinates. During expansion, extension twinning in the HD grains reorients the lattice to strengthen the RD and form a new ED (c-axis parallel to the radial extrusion direction) component. By increasing the temperature or level of Sr, the ED component was weakened due to the decrease in twinning. During expansion the RD grains undergo contraction and double twinning which reduced the overall texture strength. This section has been prepared as a manuscript to be submitted at Materials Transactions.

7.1. Tube Extrusion of AZ31 Alloy with Sr Additions

Alireza Sadeghi, Majid Hoseini, Mihriban Pekguleryuz

McGill University, Department of Mining and Materials Science, Montreal, Quebec, Canada

Materials Science and Engineering: A, Volume 544, 15 May 2012, Pages 70-79.

7.1.1. Introduction

If the issues related to the anisotropy and mechanical performance were resolved, magnesium alloys could be recognized as an excellent option for replacing steel and aluminum in manufacturing automotive components. Many alloying elements have been introduced to Mg alloys to improve the mechanical performance [1-7] and to control the strong basal texture [8-17] either by creating cubic solid solution (eg Mg-Li alloys) [8-10] or forming particular precipitates [11-17]. The AJ series of Mg alloys have been developed by the addition of Sr and Al into Mg in order to achieve a high temperature creep-resistant casting alloy [18]. This alloy has been successfully used in powertrain applications [19]. Recently, Sr has been added to wrought Mg alloys [7, 14-17, 20-24] and interesting results have been reported on texture evolution.

It is known that Sr modifies the microstructure and suppresses the formation of β-$Mg_{17}Al_{12}$ precipitates and, at certain compositions, forms a non-equilibrium Al-Mg-Sr phase [20,21]. However, the precipitate is transformed to stable Al_4Sr when exposed to heat, either by annealing [24] or hot deformation [23]. Adding Sr also eliminates the pinning effect of solute atoms by reducing the Al concentration in Mg solid solution [21,16, 17]. As a result, dislocation slip, grain boundary migration and recrystallization behaviour is directly effected [16,17,23,24]. Extrusion of AZ31+x%Sr alloys at elevated temperatures forms precipitate stringers [16,17,23,24]. Previous studies indicate that annealing prior to extrusion results in a more uniform dispersion of stringers across the Mg matrix [24]. It has been shown that the thermally stable Al-Sr precipitates are able to initiate particle stimulated nucleation (PSN) in special thermo-mechanical conditions during extrusion [16]. New grains at precipitate interfaces are

recrystallized with random orientation and are therefore able to weaken the dominant basal texture [16,17].

In previous investigations the authors have studied the thermo-mechanical behaviour of Sr containing AZ31 alloys during extrusion of cylindrical bars [16, 17, 23, and 24]. The geometrical symmetry in an extruding bar and the simple folds in material flow make bar extrusion an excellent option to study the basics of hot deformation in an alloy. However, in industrial applications hollow shapes with more complex geometries are more desirable. Seamed and seamless tubes are most widely used in manufacturing parts and assemblies. In the present paper, hot extrusion of an AZ31+0.7wt%Sr alloy in a porthole die has been studied.

7.1.2. Experimental Procedure

AZ31 extruded rods (Applied Magnesium, Denver, CO) and Sr-10Al master alloy (Timminco, Haley, ON) were used to prepare the alloy compositions. The melt was prepared at 700^{o}C in a graphite crucible using a high frequency induction furnace (NORAX Canada). At 720^{o}C the Melt was cast into a preheated (400^{o}C) cylindrical steel die. Extrusion billets were machined out of the cast bars to a 28 mm diameter and 50 mm height. Chemical composition of the cast alloys (table 7.1.1) were determined by inductively coupled plasma (ICP). Note that all compositions given hereafter are in wt%.

Table 7.1.1. Chemical Compositions of the Alloys

No.		1	2	3
	element	AZ31	AZ31+0.4Sr	AZ31+0.8Sr
Chemical comp. (*wt%*)	Al	3.08	3.19	3.07
	Zn	0.89	0.85	0.83
	Mn	0.38	0.38	0.35
	Sr	0	0.31	0.75

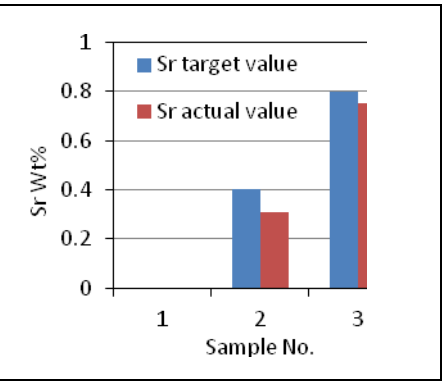

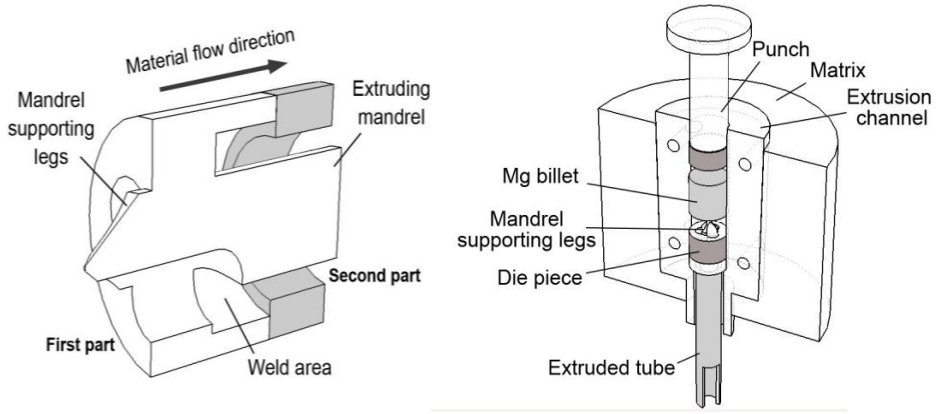

Figure.7.1.1. Schematic showing the cross section of the two part die assembly used for tube extrusion

A two piece porthole die was designed to extrude round tubes (Fig.7.1.1a). The first part of the die has three legs in its interior which support the mandrel. Here, the material is divided into three flows around the mandrel. The material is welded back together through the internal die passages and the hollow tube shape is formed by extruding through the orifice made by the second die piece and the mandrel (Fig.7.1.1a). The die pieces are fixed in a punch-and-matrix die assembly (Fig.7.1.1b). The cast and machined billet was squeezed through the die by the punch using a 100T hydraulic press. Extrusion temperature was fixed at 400^{o}C with a ceramic insulated band heater. All the contact surfaces were lubricated using an anti-seize paste (Molycote-37). The ram speed was kept constant at 4mm s^{-1}.

The extruded bars were sectioned both on the circular and rectangular cross sections. A 1 μm diamond paste was used to polish the sectioned samples and a picric acetic solution was used to reveal the microstructure for optical microscopy. The average grain size was measured using the line intercept method. Optical stereoscopy was used to observe the surface morphology of the extruded tubes. The surface cracks of the extruded tubes were studied in more detail using back scattered electron (BSE) microscopy in a Hitachi S-4700 scanning electron microscope.

A Bruker D8 X-ray diffractometer was used in order to evaluate the overall crystallographic texture with Co Kα radiation. Incomplete pole figures of $\{0001\}$, $\{10\bar{1}0\}$ and $\{10\bar{1}1\}$, were recorded, and the TextTools texture analysis software constructed the orientation distribution function (ODF) from the incomplete pole figures. Inverse pole figures (IPF) and complete pole figures were derived from the constructed ODFs.

7.1.3. Results and Discussion

7.1.3.1. Microstructure and Grain Structure of the Extruded Alloys

The microstructures of the three extruded alloys are presented in Fig.7.1.2. AZ31 (Fig.7.1.2a) had a bimodal grain structure consisting of large non-recrystallized and smaller recrystallized grains. Although the amount of twinning was not significant, the signs of twinning were apparent in the large grains. The addition of Sr (Fig.7.1.2c and d) led to a more homogeneous grain structure and refined the final grain size. The average grain size is of AZ31 is 18 μm but reduced to ~16 μm for AZ31+0.4Sr and to 14 μm for AZ31+0.8Sr.

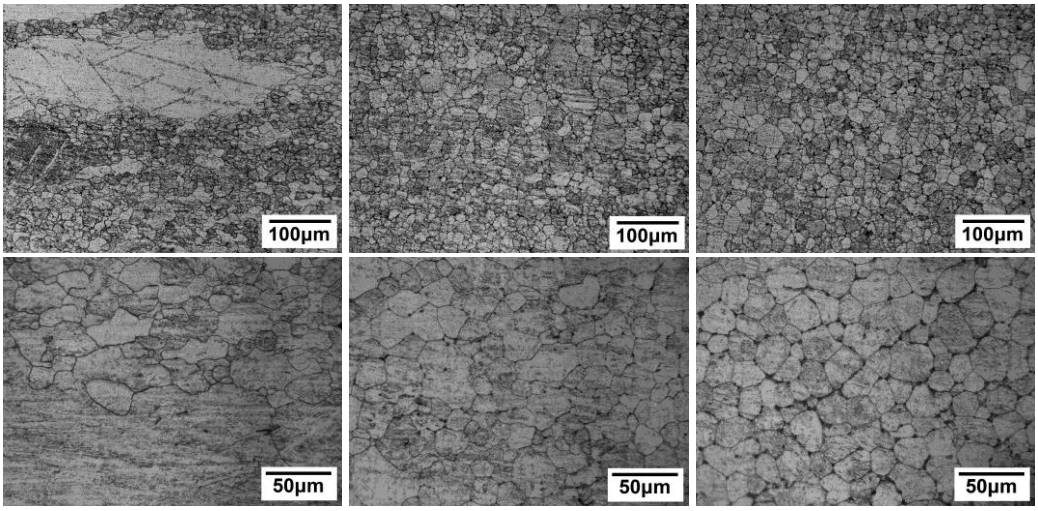

Figure .7.1.2. Microstructure of the rectangular cross sections of the extruded tubes at 400°C. (a,d) AZ31, (b,e) AZ31+0.4%Sr, (c,f) AZ31+0.7%Sr. the radial and extrusion directions are vertical and horizontal respectively.

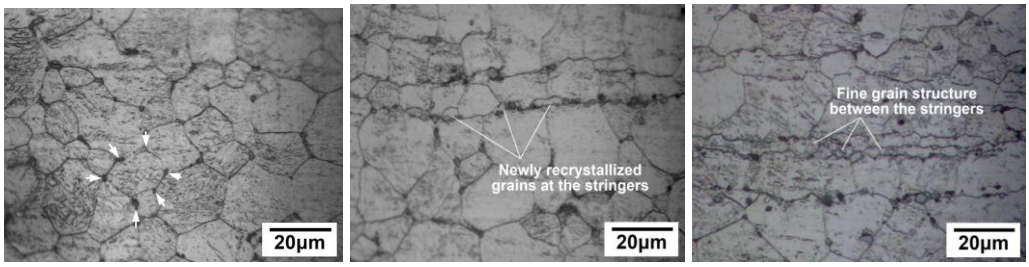

(a) **(b)** **(c)**

Figure.7.1.3. Microstructures of AZ31+0.8Sr tube extruded at 400^{o}C, (a) Al-Sr precipitates pining the grain boundaries preventing further growth, (b) recrystallization of new grains at the stringers, (c) formation of fine grain structure between parallel stringer lines.

Three characteristic microstrucutural features of the tube extruded alloys containing Sr can be summarised as follows:

(i) Unlike bar extrusion of AZ31+xSr alloys in which precipitates deform into stringers [16,17,23,24], the precipitates found following tube extrusion of AZ31+xSr alloys were dispersed more uniformly across the microstructure and stringers were rarely observed. The complex material flow in the porthole die was responsible for breaking down the stringers and making a more homogeneous distribution (Fig.7.1.2e,f).

(ii) The Al-Sr precipitates were located at the grain boundaries and pinned the boundaries of recrystallized grains stopping further growth (Fig.7.1.3a). This has been previously observed in the hot extrusion of AZ31+Sr alloys [16].

(iii) Evidence of nucleation of new grains at the precipitate interface (PSN) was been observed across the microstructure close to the elongated stringers. In these regions, the new grains were clearly distinguishable from those in the remaining equiaxed structure (Fig.7.1.3b). The newly recrystallized grains grew from both sides until they impinged on each other and formed a fine microstructure between the two stringers (Fig.7.1.3d).

7.1.3.2. Surface cracking

The complex deformation in the tube die used in this study involves bending, unbending, spreading and joining of the material flow. Each of the deformation stages produces different tensile and compressive stresses during deformation. The high surface stress along with the high localized heat of deformation [25] causes surface cracking during deformation. Fig.7.1.4a-c shows the stereographic images of the extruded tubes. It can be seen that as the level of Sr increased, the surface cracking became more severe. This has been previously reported by the authors for conventional bar extrusion [16].

Fig.7.1.5a presents a section of the circular cross section of the AZ31+0.8Sr extruded tube. The micrograph reveals the propagation of the cracks from the surface to the center. In Fig.7.1.5b, the BSE image of a crack in the circular cross section of the same sample is shown.

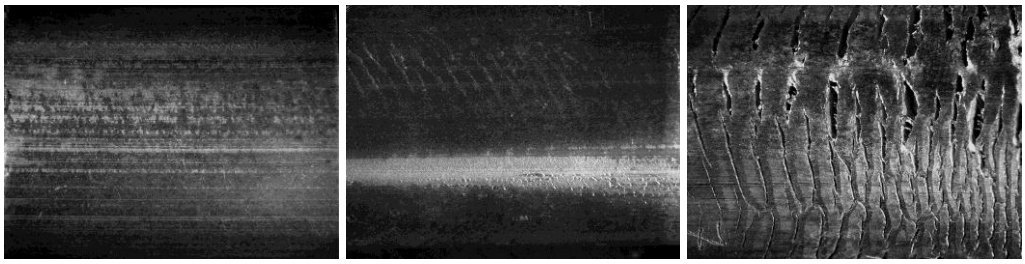

Figure .7.1.4. Surface cracks of the extruded tubes; optical Stereograph of (a) AZ31, (b) AZ31+0.4%Sr, (c) AZ31+0.7%Sr (the vertical axis represents the full diameter of the tube).

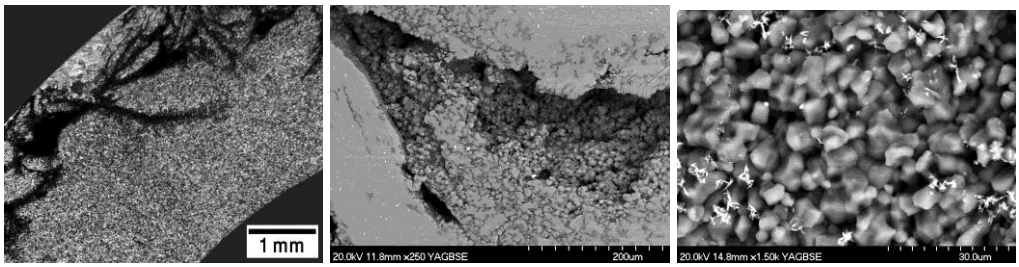

Figure .7.1.5. (a) The circular cross section of AZ31+0.7%Sr extruded tubes. (b,c) backscattered electron image of the crack surface in the circular cross section.

Crack propagation in the inter-granular region can be easily distinguished. The higher magnification image in Fig.7.1.5c interestingly shows a brittle fracture mode with rock candy appearance of the grain surfaces and the precipitates; this could be due to the fact that basal dislocation was prevented in these grains due to their orientation and instead the local stresses were relieved via crack nucleation and propagation. The cracks in the outer surface of the tube have threefold symmetry around the centerline of the tube. Another set of cracks are also visible with the same threefold rotational symmetry in the tube inner diameter. However, the latter has a 30^o lag from the former (Fig.7.1.6). The cracks in the outer diameter were formed when the material flow changed direction from an extrusion to circumferential direction to spread out and the fill the 120^o sector of the weld area. On the other hand, the cracks at the inner surface appeared in the region in which the three 120^o material sections reached and joined. In fact, the material flow direction in those regions suddenly changes from the circumferential to the extrusion direction. In both situations the tensile stresses associated with the change of direction resulted in crack initiation.

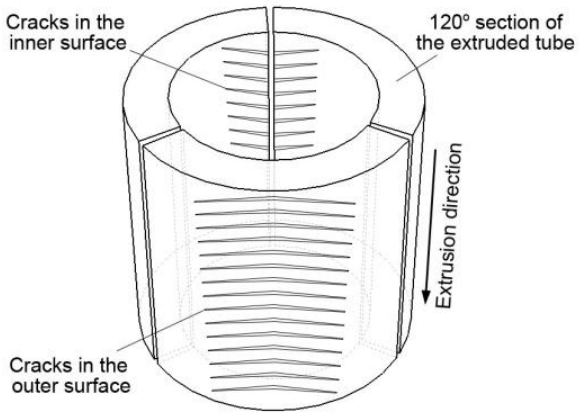

Figure.7.1.6. The possible locations of surface cracks in an extruded tube (the cracks have a rotational threefold symmetry around the tube axis).

7.1.3.3. Texture

There is a strong dependence between the compression direction and the final texture originating from DRX in hot deformation. Grains having their basal planes

perpendicular to the compression axis (radial direction) would have a resolved shear stress close to zero on the basal slip system; as a result work hardening and subsequent recrystallization do not occur [26]. However, in grains with other orientations, DRX results in recrystallization of new grains. Again, the grains with basal planes perpendicular to extrusion direction would remain stable. This cycle is repeated until all the structure is occupied by grains pointing their basal normals toward the compression direction [26]. Accordingly, a texture with radial symmetry is expected from a radial deformation process (e.g. extrusion of a round bar) [27]. However, the texture in an extruded tube (which has a radial symmetry) is more like the texture of a rolled sheet (or extruded slab) where the basal planes lie parallel to the tube surface. However, the complex material flow pattern in the porthole die used for tube extrusion in this study developed a more complex texture.

As shown in Fig.7.1.7a, the material went through a complex path in the tube extrusion die to eventually form the shape of a complete tube. In the first stage, the billet is separated into three smaller bars (main streams labelled as A in Fig.7.1.7). After passing the welding zone, each one of the initial bars forms a 120^{o} section of the final tube. The ring basal texture is formed in the "A" stage. After the first deformation, the material is passed through a progressive set of bends and curvatures to form the final tube shape. The second step would be a 90^{o} turn which diverts the material from the extrusion direction to the radial direction (labelled as B in Fig.7.1.7a). Next, there is another 90^{o} turn from the radial direction back to the extrusion direction (labelled as C in Fig.7.1.7a).

The deformation condition in passing the two first curvatures (B and C in Fig.7.1.7) is very similar to what happens in ECAP (equal channel angular pressing) when the material is extruded through a route C with an 180^{o} rotation between each pass [28]. After passing these two curvatures material is diverted again, this time toward the circumferential direction to fill the welding zone (labelled as D in Fig.7.1.7a). The angle of this final turn is not constant everywhere and it ranges from 0 (when it moves in a straight line) to 60^{o} (to fill half of the 120^{o} sector). The final stage of applied deformation occurs when the

material exits the die and the outer diameter of the tube is reduced (labelled as E in Fig.7.1.7).

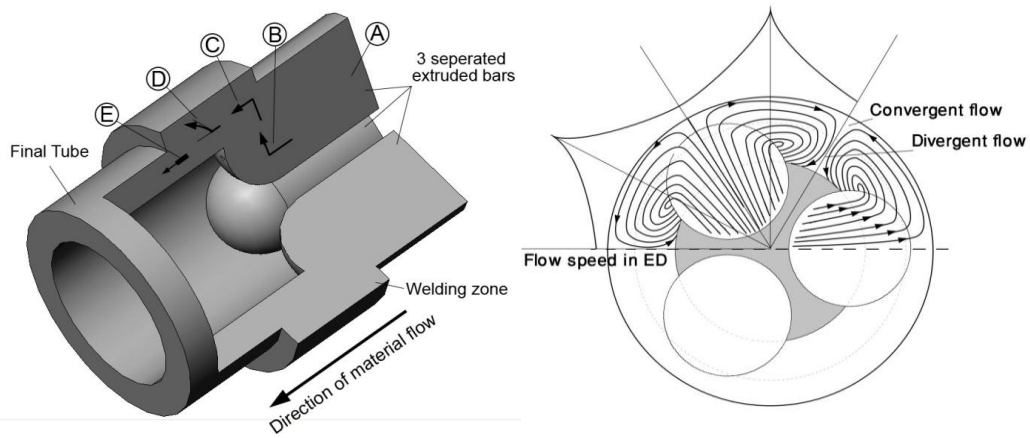

Figure.7.1.7. schematic showing a cross section of the material inside the porthole die (a) in the extrusion direction and (b) in the radial and circumferential directions.

In Fig.7.1.7b the flow of material in the cross section perpendicular to the extrusion direction has been plotted. It can be seen how the material in the main stream is spread out to its sides to fill the welding zone. When the material from two adjacent holes reach (converge), they change direction and return back toward the holes (diverge). As a result of complex flow geometry in the welding zone different points in the main stream travel different distances with different speeds inside the deformation zone before the final extrusion (point "E" in Fig.7.1.7a) and exiting the die. In Fig.7.1.7b the speed of deformation in the extrusion direction has been qualitatively plotted vs. distance from the main stream. As shown in the stereograph image in Fig.7.1.8a the first material coming out of the die forms an uneven but symmetrical geometry caused by the redundant work from the un-uniform movement of material in the welding zone.

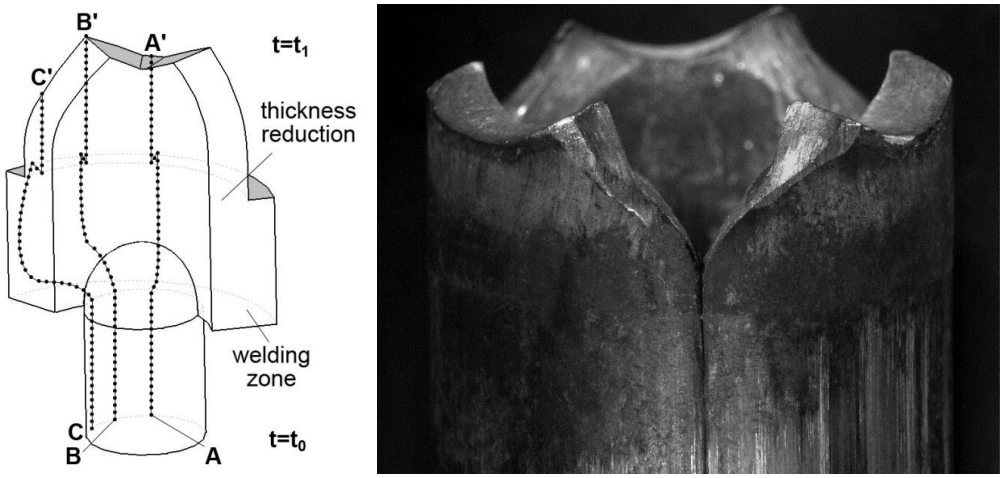

Figure .7.1.8. (a) Schematic showing the straight and curved flow of material inside the welding zone. (b) Stereographic image of the first material coming out of the tube extrusion die.

In Fig.7.1.8b, three different deformation routes are shown in a 120 degree sector of the extruded tube. Route AA' represents the path which doesn't go through any curvatures in the circumferential direction. Route BB' is the path with the maximum speed and route CC' ends at the seam. The more distance from the main stream the more curvature traveled by the material.

Based on the deformation speed of the AA' route, speed along different routes could be calculated by considering some basic boundary conditions. Deformation starts on all the routes at the same time (t_0) at the same level (x_0) and in all of them deformation ends at the same time (t_1) however each has gone through a different displacement with a different speed. Using the volume consistency rule at the inlet and out let of the die, the speed of deformation on the AA' route could be easily calculated ($V_A \approx 23$ mm s^{-1}).

By estimating the travel length in other routes (BB' and CC') deformation speed in each route could be obtained. To estimate the displacements, each 120 degree sector of the tube has been considered as a plate and the curved routes are simplified to straight lines. The deformation speed of individual points inside across the circumferential direction in the deformation zone is the result of three different speeds caused by different sources. (i) The first effecting speed is the

speed of the main stream. In the 120^o sector, points closer to the main stream have a higher speed in the extrusion direction. The spread of the material from the main stream to the sides reduces the speed in the extrusion direction and increases the speed in the circumferential direction. (ii) When the circumferential flow coming from two different holes join at the seam the flow direction is changed to the extrusion direction and the speed is increased. (iii) The friction between the two converging flows and the turbulence of flow at the seam is the third factor effecting the speed which reduces the speed in the extrusion direction. The diagram in Fig.7.1.9 shows the trend of the three speed sources and their combined effect. As shown in the diagram, by getting far from the main stream speed is initially increased then decreased to an absolute minimum by reaching the seam.

All of the mentioned deformation routes directly effect the final texture and change the ring basal texture formed in the first stage. Much research has been carried out to investigate and simulate the change of texture of an extruded bar passing different curvatures [26.1.31].

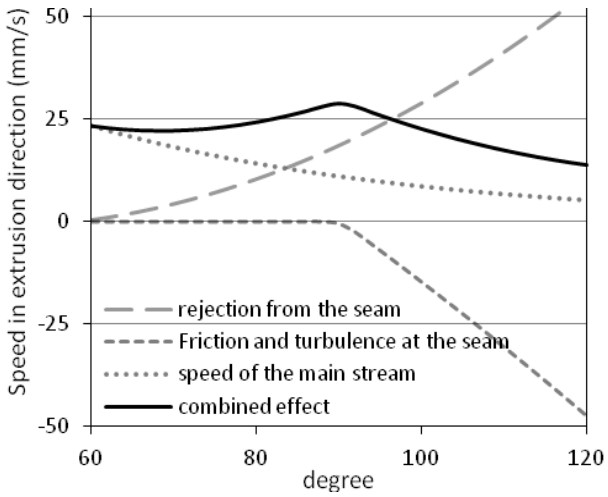

Figure.7.1.9. Speed of deformation in the extrusion direction vs. location as a function of speed of the main stream and rejection from the seam.

It has been reported that when extruded AZ31 is passed through a 90^o die, basal planes in the majority of grains will rearrange to become close to the

theoretical shearing plane [27], and ring basal texture becomes tilted [27,29-31]. This texture component places the basal planes nearly coincident with the predicted morphological texture (i.e. parallel to the most highly elongated direction of the sheared grains [32]. The reversal of strain on the second pass in route C (the "C" turn after the first "B" in Fig.7.1.7) does not eradicate the texture developed in the previous pass [29]. This demonstrates well that the evolution of deformation texture is path dependent [29].

In Fig.7.1.10 the (0002) pole figures of the extruded tube close to the main stream (Fig.7.1.10a), close to the seam (Fig.7.1.10c) and a point in the middle (Fig.7.1.10d) are shown. The material at the main stream had a titled basal texture, spread toward the extrusion direction. By getting close to the seam the tilted basal component started to split to form two extra components (δ_1,δ_2). In Fig.7.1.10c the two new components are completely separated and clearly visible. The circulation and spreading of material in the circumferential direction is responsible for formation of the extra texture component in the pole figures. The formation and strengthening of the strong extra component (δ_1) is associated with deformation in the circumferential direction. The formation of the weaker extra component (δ_1) is a result of rejection from the seam and movement of material in the circumferential direction from the seam toward the main stream.

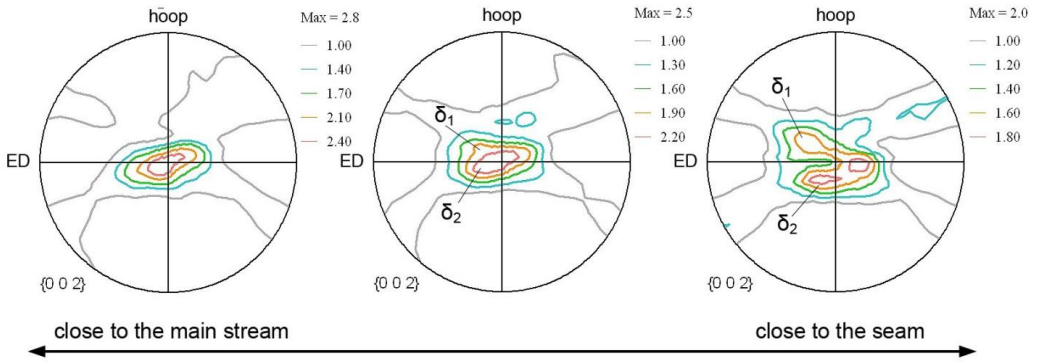

Figure .7.1.10. Basal pole figures showing the split of the basal texture to two extra components (δ_1 and δ_2) by moving from the main stream toward the seam region in the circumferential direction.

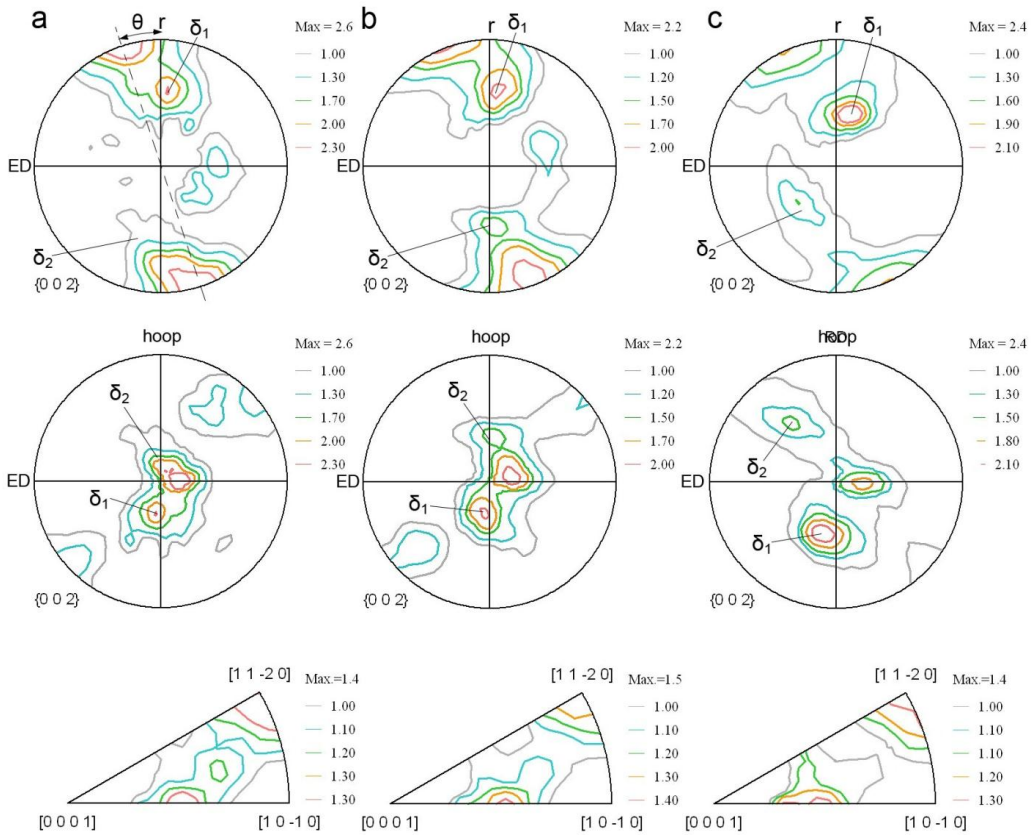

Figure.7.1.11. pole figures and inverse pole figures of (a) AZ31, (b) AZ31+0.4Sr, (c) AZ31+0.8Sr after extrusion.

The pole figures of the extruded tubes containing different levels of Sr in the radial and extrusion directions are shown in Fig.7.1.11. It can be seen that in all of the pole figures, the basal poles have been tilted (θ in Fig.7.1.11a) from the basal at the radial poles. Also extra texture components (δ_1,δ_2) are visible ~50^o away from the radial direction. As shown the intensity of the δ components increased over the rotated basal texture by addition of Sr. The concentration of poles close to the (012) axis was also observed in each corresponding inverse pole figure. In other words the (012) planes were lying almost parallel to the rectangular cross section of the tube.

Fig.7.1.12 presents the ODF sections at φ_2=0 and 30^o of the tube extruded AZ31 and AZ31+Sr alloys. The non symmetrical strain path during tube extrusion has nearly removed the texture symmetry along φ_2 ($0 < \varphi_2 < 360^o$). Moreover, the addition of Sr also reduced the level of symmetry across the φ_2 = 180° axis

(Fig.7.1.12). The maximum intensity of the ODF (texture strength) decreased from 4.4 to 3.1 and 2.8 by increasing the level of Sr from 0 to 0.4 and 0.8wt%. It can be seen that a new texture component (δ in Fig.7.1.11) emerged at $\varphi_2 = 0°$ for all the three compositions. It is interesting to note that the δ component had the maximum ODF intensity in AZ31+0.8% Sr while in the other two alloys the maximum occurred at the prismatic components (at $\varphi_2 = 30°$). The θ^o tilt of basal poles presented in Fig.7.1.11 can also be seen in the position of the two prismatic components ($(110) < \bar{1}12 >$ and $(110) < 1\bar{1}2 >$) shown in the ODFs ($\varphi_2 = 30°$ sections of Fig.7.1.12). In the $\varphi_2 = 30°$ section of the ODFs presented, the prismatic poles are located at the $\varphi_1 = 115°$ and 295^o instead of the 90^o and 270^o sections. This shows a 25^o tilt from where the prismatic poles are in conventional extrusion.

Intensity distributions across Φ at selected constant φ_1 orientations have been plotted in Fig.7.1.13. In order to compare the intensities of the δ components in the three samples, the intensity distributions across φ_2=0° and φ_1=90° are shown in Fig.7.1.13a.

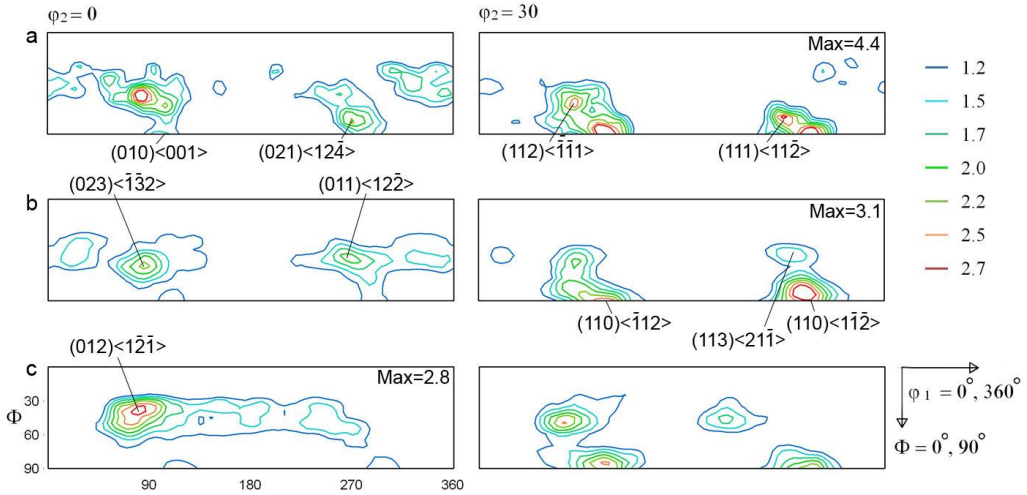

Figure.7.1.12. ODF sections at φ_2=0° and φ_2=30° of (a) AZ31, (b) AZ31+0.4%Sr and (c) AZ31+0.8%Sr extruded tubes. Orientations of interest are labelled. The maximum intensity for AZ31 and AZ31+0.4%Sr occurs at φ_2=0 while for AZ31+0.8%Sr is at φ_2=30.

It can be seen that the extra δ component was stronger in AZ31+0.8%Sr and occurred at a lower Φ compared to the other two alloys. By calculating the crystal orientations it can be said that the alloy containing 0.8% Sr has a (012) plane facing the rectangular cross section whereas the two other alloys have a (023) plane perpendicular to the circumferential direction. Although the two planes are parallel to the <a> direction of the hexagonal lattice, the (023) makes a larger angle with the basal plane, see Fig.7.1.13a. The crystal orientations of the tilted basal fiber and the two extra δ components are schematically shown in an extruded tube section in Fig.7.1.14. As shown, the orientations of the two δ components are very close to each other.

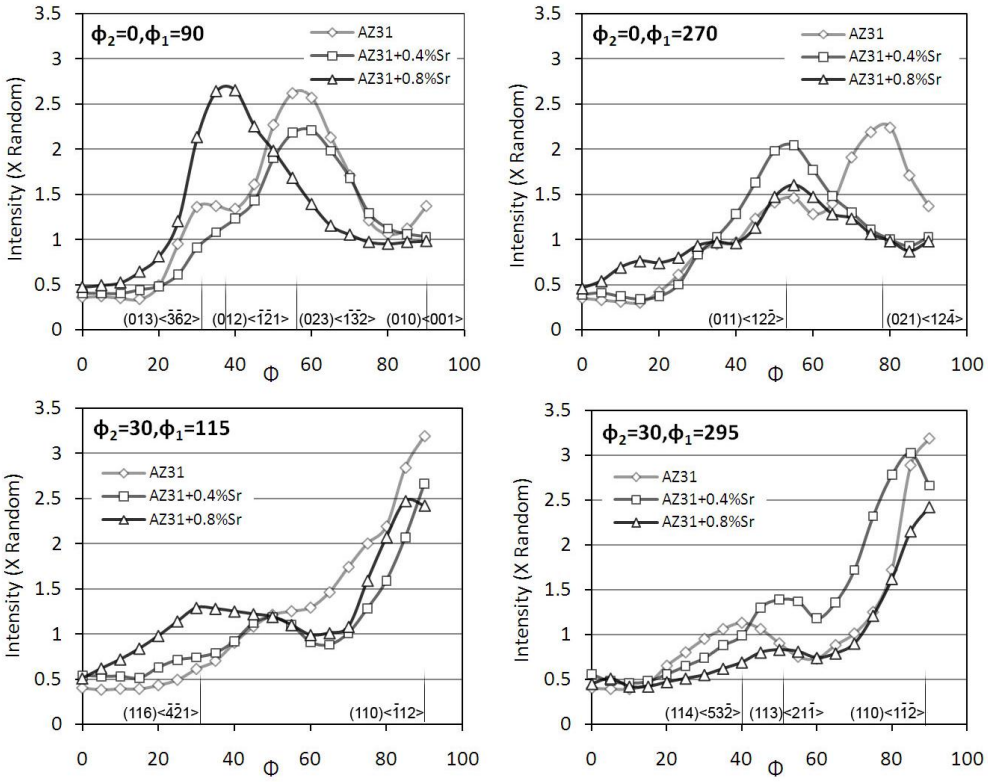

Figure.7.1.13. Intensity distribution across Φ at constant φ_1 orientations of AZ31, AZ31+0.4%Sr and AZ31+0.8%Sr extruded tubes. The maximum intensity for AZ31 and AZ31+0.4%Sr occurs at φ_2=0 while for AZ31+0.8%Sr is at φ_2=30.

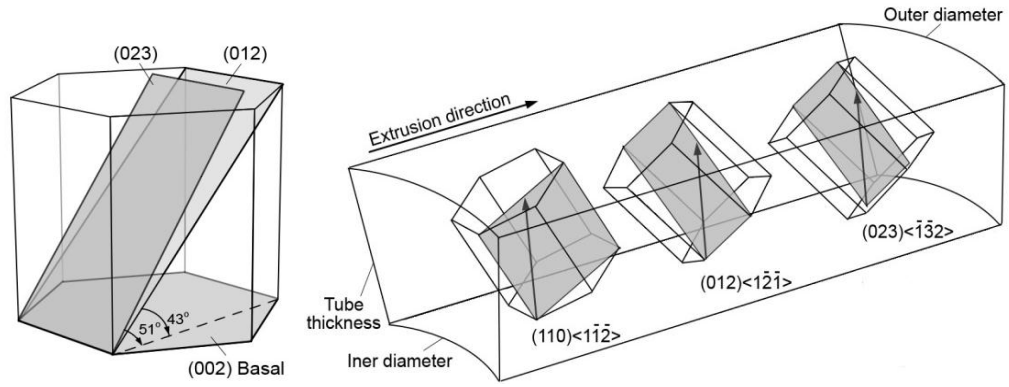

Figure.7.1.14. (a) orientation of the (0002), (01-12) and (02-23) planes in a hexagonal lattice, (b) Orientation of hexagonal crystals in an extruded tube section. The gray planes are parallel to the rectangular cross section and the directions are toward the radial direction of the tube.

In none of the three orientations did the basal plane make a right angle with the tube surface (Fig.7.1.14). Consequently, dislocations could move on basal planes during further processing. Previous studies have shown an increase in the Schmid orientation factor of basal planes from 0 for extruded material to 0.27 for the same material having a tilted basal texture after passing through a 90^o die [27]. The extra texture components have been previously seen in Mg alloys after extrusion through multiple passes in ECAP dies [26.1.33]. Figueiredo *et al*. [33] reported a split in the distribution of basal poles in the opposite direction of the bend after passing a 90^o ECAP die [33].

In the samples studied, the addition of Sr weakened the texture intensity. We have previously reported that thermally stable Al-Sr precipitates are able to activate PSN and reduce texture intensity during special thermo-mechanical conditions [16-17]. Going back to the micrographs of Fig.7.1.2, two facts should be taken into consideration;

(i) Twinning was observed in the AZ31 microstructure while there were no twins found in the alloy containing Sr. Addition of Sr depleted Al from Mg solid solution and dislocation movement became easier [17]. Moreover, adding Sr made the grain size more homogeneous and the large

un-recrystallized grains were removed from the microstructure. Consequently, twinning was not activated when Sr was present.

(ii) The microstructure of the alloy containing Sr was occupied with new recrystallized grains. Interestingly, they were all associated with the Al-Sr precipitates at their grain boundaries. The same microstructure has been previously observed in conventional extrusion of the same alloying system [16], where the grains are nucleated from the precipitate interface and grow until they reach another precipitate or impinge on another grain boundary coming from another precipitate [16].

Strengthening of the extra component over the tilted basal texture by addition of Sr could be attributed to the decrease of Al in Mg solid solution and decrease of the lattice resistance against dislocation movement [20-23]. As described before, the extra texture component is formed by spreading of material in the circumferential direction. Reduction of Al gives more freedom to grains to deform and workharden in the circumferential direction, consequently more DRX occurs in the grains and the selective workhardening-DRX cycle removes the grains perfectly oriented for dislocation movement. Therefore more grains having an unfavorable direction for slip (extra δ components) remain un-recrystallized.

7.1.4. Conclusions

AZ31 and AZ31+Sr alloys were cast and then hot extruded at 400^{o}C in a porthole die. The following conclusions are drawn:

1. Addition of Sr refines the grain size. Curvatures in the material flow during extrusion in the designed die breaks down precipitate stringers and uniformly distributes them throughout the microstructure.
2. High concentrations of Sr increase the amount of eutectic phase at grain boundaries and increase the surface cracking tendency.
3. The complex strain path inside the die can be divided in to several simple curvatures which occur during ECAP. The final textures of the extruded tubes also have many similarities with ECAP results.

4. The texture of the extruded tube consisted of a two texture components; a 25^{o} tilted basal pole and two extra δ components. The maximum intensity of ODF decreases with increasing Sr. In AZ31 and AZ31+0.4Sr the ODF maximum intensity occurs at the basal components while in AZ31+0.8Sr the ODF maximum is at the δ component.
5. The δ components are a result of circumferential flow in the welding zone. In AZ31 and AZ31+0.4Sr the δ_1 component is $(023) < \overline{1}32 >$ while the same component in AZ31+0.8Sr is 9^{o} more tilted and is $(012) < 1\overline{2}1 >$. The higher Sr in the alloy, the less Al in solid solution Mg and the less lattice resistance against dislocation slip. As a result grains can deform more easily in the circumferential directions and selective work hardening-DRX cycles leave more grains with an unfavorable slip orientation (δ components).

7.1.5. References

1. Yizhen Lu, Qudong Wang, Xiaoqin Zeng, Wenjiang Ding, Chunquan Zhai, Yanping Zh, "Effects of rare earths on the microstructure, properties and fracture behaviour of Mg–Al alloys," Materials Science and Engineering A278 (2000) 66–76.
2. P. Bakke, K. Pettersen, H. Westengen, "Investigation of Die Cast Mg-Al Alloys with Additions of Sn, Si and Sb, in Magnesium," Proceedings of the 6th International Conference Magnesium Alloys and Their Applications (ed K. U. Kainer), Wiley-VCH Verlag GmbH & Co. KGaA, Weinheim, FRG. (2005)
3. M. Pekguleryuz, E. Baril, "Development of Creep Resistant Magnesium-Aluminum-Strontium Alloys," 2001 Magnesium Technology, J. Hryn, Ed., TMS, New Orleans, (2001) 119-136.
4. Wenlong Xiao, Shusheng Jia, Lidong Wang, Yaoming Wu, Limin Wang, "The microstructures and mechanical properties of cast Mg–Zn–Al–RE alloys," Journal of Alloys and Compounds, Volume 480, Issue 2, (2009) L33-L36

5. A. Luo, M.O. Pekguleryuz, "Cast Magnesium Alloys for Elevated Temperature Applications," Journal of Materials Science, Vol 29, No 20, (1994) 5259-5271.
6. L.L. Rokhlin, "Magnesium Alloys Containing Rare Earth Metals: Structure and Properties," CRC Press, 1 edition (2003).
7. P. Zhao, Q. Wang, C. Zhai, Y. Zhu, "Effects of strontium and titanium on the microstructure, tensile properties and creep behaviour of AM50 alloys," Materials Science and Engineering: A, Vol 444, Issues 1-2, (2007).
8. N. Stanford, M.R. Barnett, "The origin of "rare earth" texture development in extruded Mg-based alloys and its effect on tensile ductility," Materials Science and Engineering A, Volume 496, Issues 1-2 (2008) 399-408.
9. N. Stanford, "Micro-alloying Mg with Y, Ce, Gd and La for texture modification—A comparative study," Materials Science and Engineering A, Vol 527, Issues 10-11 (2010) 2669-2677.
10. L.W.F. Mackenzie, B. Davis, F.J. Humphreys, G.W. Lorimer, "The deformation, recrystallization and texture of three magnesium alloy extrusions," Materials Science and Technology, Vol 23, No 10 (2007) 1173-1180.
11. L.W.F. Mackenzie, M.O. Pekguleryuz, "The recrystallization and texture of magnesium-zinc-cerium alloys," Scripta Materialia, Vol 59, No 6 (2008) 665-668.
12. T. Laser, Ch. Hartig, M.R. Nürnberg, D. Letzig. R. Bormann, "The influence of calcium and cerium mischmetal on the microstructural evolution of Mg–3Al–1Zn during extrusion and resulting mechanical properties," Acta Materialia, Vol 56, Issue 12 (2008) 2791-2798.
13. T. Abuleil, N. Hort, W. Dietzel, C. Blawert, Y. Huang, K.U. Kainer, K.P. Rao, " Microstructure and corrosion behaviour of Mg-Sn-Ca alloys after extrusion," Transactions of Nonferrous Metals Society of China, Vol 19, Issue 1 (2009) 40-44.

14. B. Jing, S. Yangshan, X. Feng, X. Shan, Q. Jing T. Weijian, "Effect of extrusion on microstructures, and mechanical and creep properties of Mg–Al–Sr and Mg–Al–Sr–Ca alloys," Scripta Materialia, Vol 55, Issue 12 (2006) 1163-1166.
15. X. Zeng, Y. Wang, W. Ding, A. A. Luo, A. K. Sachdev, "Effect of strontium on the microstructure, mechanical properties, and fracture behaviour of AZ31 magnesium alloy," Metallurgical and Materials Transactions A, Vol 37, No 4 (2006) 1333-1341.
16. A. Sadeghi, M. Pekguleryuz, "Recrystallization and Texture Evolution of Mg-3%Al-1%Zn-(0.4 -0.8) %Sr Alloys during Extrusion," Materials Science and Engineering A, Submitted August 2010.
17. A. Sadeghi, M. Hoseini, M. Pekguleryuz, "Effect of Sr addition on texture evolution of Mg–3Al–1Zn (AZ31) alloy during extrusion," Materials Science and Engineering: A, (In Press), Corrected Proof, Available online 4 January 2011.
18. M. Pekguleryuz, A.A. Kaya, "Magnesium diecasting alloys for high temperature applications," TMS Annual Meeting, Symposium on Magnesium Technology Charlotte, NC, (2004).
19. M.O. Pekguleryuz, A.A. Kaya, "Creep Resistant Magnesium Alloys for Powertrain Applications," Magnesium Alloys and their Applications, Deutsche Gesellschaft für Materialkunde, Garmisch (DGM), Germany (2003) 74-93.
20. A. Sadeghi, M. Pekguleryuz, "Precipitation during the Solidification of Mg-3wt%Al-1wt%Zn-(0.001-1%) Sr Alloys," American Foundry Society annual congress, Orlando, USA, (2010).
21. A. Sadeghi, M. Pekguleryuz, "Precipitation of Mg-3%Al-1%Zn-(0.01-1)wt%Sr Alloys during solidification," Journal of Materials Research, Journal of Materials Research, Available on CJO doi:10.1557/jmr.2010.75
22. A. Sadeghi, M. Pekguleryuz, "Microstructure, mechanical properties and texture evolution of AZ31 alloy containing trace levels of strontium," (Submitted to Materials Charachterization)

23. A. Sadeghi, S. Shook, M. Pekguleryuz, "Yield Asymmetry and Fracture Behaviour of Mg-3%Al-1%Zn-(0-1)%Sr Alloys Extruded at Elevated Temperatures," (submitted to Materials Science and Engineering A)
24. A. Sadeghi, M.Pekguleryuz, "Effect of annealing on microstructure and texture evolution of Mg-3Al-1Zn-0.8Sr alloy during hot extrusion," (not submitted yet)
25. L. Miao-quan, W. Shi-chun, T. Cai-rong, "Analysis of surface crack on forward extruding bar during axisymmetric cup-bar combined extrusion process," Applied Mathematics and Mechanics, Vol 11, No 8, (1990) 733-741.
26. Qinglin Jina, Sung-Yong Shima, Su-Gun Lim, "Correlation of microstructural evolution and formation of basal texture in a coarse grained Mg–Al alloy during hot rolling," Scripta Materialia, Vol 55, Issue 9 (2006) 843-846.
27. H.K. Lin, J.C. Huanga, T.G. Langdon, "Relationship between texture and low temperature superplasticity in an extruded AZ31 Mg alloy processed by ECAP," Materials Science and Engineering A, 402 (2005) 250–257.
28. S. Ferrasse, K. T. Hartwig, R. E. Goforth, V. M. Segal, "Microstructure and properties of copper and aluminum alloy 3003 heavily worked by equal channel angular extrusion," Metallurgical and Materials Transactions A, 28 4 (1997) 1046.1.1057.
29. S.R. Agnew, P. Mehrotra, T.M. Lillo, G.M. Stoica, P.K. Liawc, "Crystallographic texture evolution of three wrought magnesium alloys during equal channel angular extrusion," Materials Science and Engineering A, 408 (2005) 72–78.
30. S.R. Agnew, P. Mehrotra, T.M. Lillo, G.M. Stoica, P.K. Liaw, "Texture evolution of five wrought magnesium alloys during route A equal channel angular extrusion: Experiments and simulations," Acta Materialia 53 (2005) 3135–3146.

31. S.X. Ding, W.T. Lee, C.P. Chang, L.W. Chang and P.W. Kao, "Improvement of strength of magnesium alloy processed by equal channel angular extrusion," Scripta Materialia 59 (2008) 1006–1009.
32. R. D. Field, K. T. Hartwig, C. T. Necker, J. F. Bingert, S. R. Agnew, "Equal-channel angular extrusion of beryllium," Metallurgical and Materials Transactions A, 33 13 (2001) 965-972.
33. R. B. Figueiredo, I. J. Beyerlein, A. P. Zhilyaev, T. G. Langdon, "Evolution of texture in a magnesium alloy processed by ECAP through dies with different angles," Materials Science and Engineering A 527 (2010) 1709–1718.

7.2. Expansion of Hot Extruded AZ31+Sr Seamless tubes: Texture Evolution and Twinning

Alireza Sadeghi, Etienne Martin, Mihriban Pekguleryuz

Department of Mining and materials Engineering, McGill University, Montreal, Quebec, Canada

Submitted Metallurgical and Materials Transactions A

7.2.1. Introduction

During the deformation of Mg alloys, a preferred orientation of crystallographic planes and a strong basal texture form, resulting in a strong deformation texture. This heavily anisotropic alloy easily fails in its weaker direction which leads to reduced formability and workability. Investigating the ways to control and decrease the strength of this texture has been the main focus of much research in recent years [1-11]. One of the approaches in reducing the texture intensity is, among others, to add specific alloying elements to Mg to form solid solutions with altered lattice parameters, to either activate non basal slip systems [7,8] or precipitate certain particles to act as nucleation sites for newly recrystallized random texture grains [9, 11]. In the past few years, the authors have studied the addition of Sr in AZ31 (Mg-3wt%Al-1wt%Zn) alloy to form thermally stable Al-Sr precipitates that induced particle stimulated nucleation (PSN) and decreased the texture intensity [12-19]. Precipitation in the AZ31-Sr system was studied by thermodynamic calculations and cooling curves [12-14]. It was confirmed via extrusion that the texture intensity reduces in Sr containing AZ31 via PSN [15] and a micromechanism-temperature map was generated [16]. The brittleness of extruded samples caused by Al-Sr precipitates and the yield asymmetry in tension and compression have been analyzed [17], and the effect of pre-extrusion annealing on the precipitates and on the final texture of the extrudates [18] was investigated. Recently, the authors have extruded AZ31-Sr tubes using a porthole die [19] and have observed that a complicated material flow in the deformation zone spreads the Al-Sr stringers throughout the matrix and a tilted basal texture with two extra components forms [19]. It was noted that although the Sr additions

weakened and randomized the texture in the extruded tubes, the seams along the extrusion direction limited further deformation. In the present work, seam-less tubes have been produced by hot extrusion in order to investigate the tube expansion characteristics of AZ31 with different levels of Sr.

7.2.2. Experimental procedure

Starting Materials

AZ31 with 0, 0.4 and 0.8wt% Sr were synthesized and cast into preheated steel dies using graphite crucibles in a high-frequency induction furnace. The details of casting procedure have previously been described [14]. Hollow cylindrical samples were machined out of the as-cast rods to an outer and inner diameter of 28 and 14 millimetres respectively. A special punch with a H13 steel mandrel was fabricated to extrude the seam-less tubes. The mandrel fits inside the hollow billets and the fixed punch and billet sit inside the extrusion channel, as shown in Fig.7.2.1a. To minimize the friction between the moving parts, all the interfaces were covered by a high temperature anti-seize paste (Molycote P-37). A uniform 350^{o}C temperature across the die pieces was achieved using a ceramic insulated band heater kept at a constant temperature for 30 minutes. Pressure was applied to the punch using a 100T hydraulic press with a ram speed of 2 mm s^{-1}. Seamless tubes were extruded with an outer diameter of 14 mm and inner diameter of 12 mm (the mandrel diameter). After completion of extrusion, the die was cooled to room temperature using a water cooling coil to minimize the effect of static recrystallization.

Mechanical Testing

The mechanical properties of the tubes in the hoop direction were determined using an indirect approach. Compression tests were carried out on pure copper cylinders fitted inside the extruded tubes and the force-displacement data were compared to the data of pure copper with no surrounding tube.

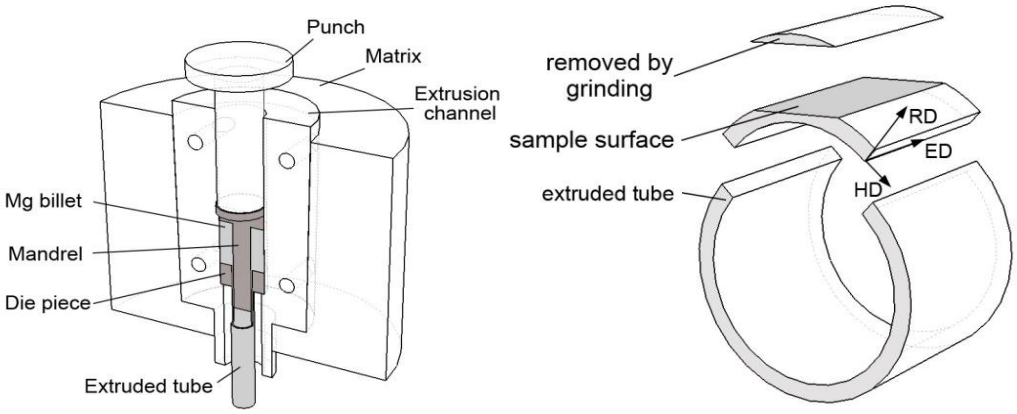

Figure.7.2.1. Schematic diagram showing the (a) extrusion die assembly, (b) the cross section used for characterization.

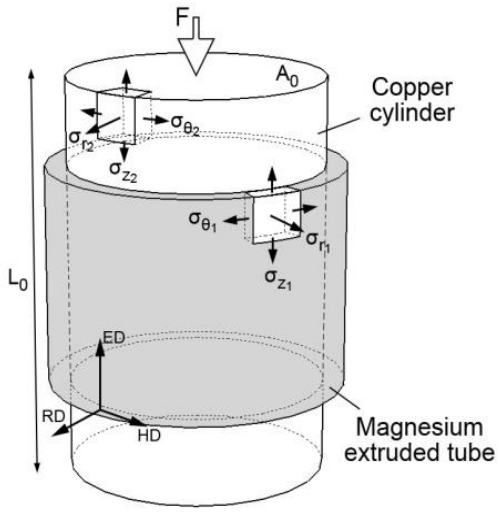

Figure.7.2.2. Schematic illustration of the magnesium extruded tube – copper cylinder insert.

By using a series of calculations and considering certain simplifying assumptions, the tensile stress-strain curves along the circumferential direction (HD) of the tubes was derived (see Appendix IV). When compression is applied, the surrounding cylinders expand and their diameter increases. The expanding cylinder applies pressure on the surrounding tube and will force the tube to deform and expand in its circumferential direction, which results in yield and failure of the extruded tube along the tube axis (perpendicular to the maximum stress). The test setup is shown schematically in Fig.7.2.2.

The strengthening effect of the extruded tubes on the total strength of the assembly was determined by comparing the results to the flow curves for pure copper cylinders with no surrounding tube. Room-temperature compression of the assemblies led to tube failure at low strains. When the tube fractured, the stress-strain curve suddenly dropped and reached the flow stress of pure copper. Note that the applied strain did not lead to tube failure at high temperatures. Measuring the flow stress of the copper insert and solving the plasticity equations by considering some simplifying assumptions, the force-displacement data of the machine was converted to stress-strain along the circumferential direction of the surrounding tube. To achieve this, the stress-strain in the circumferential direction of the tube ($\sigma_{\theta_2}, \varepsilon_{\theta_2}$) was solved in terms of force-displacement data ($F, \Delta l$) logged by the machine. The details of conversions and calculations are presented in Appendix VI.

In order to prepare the samples for compression tests, 18 mm high x 12 mm diameter pure copper cylinders were machined and inserted in 10 mm long extruded tubes (Fig.7.2.3a). To avoid distortion and residual stresses on the ends of the tubes, a low speed diamond blade cutter was used to cut the tubes. The deformed surfaces were further removed using grinding paper. The fixed copper inserts surrounded by the magnesium tubes (Fig.7.2.3a) were compressed at room and elevated temperatures by a 510 MTS servo-hydraulic mechanical testing machine.

Figure .7.2.3. (a) Copper insert and magnesium tube assembly before deformation, (b) magnesium tubes before and after deformation.

Compression tests were carried out using a strain rate of 0.01 s^{-1} at 25, 100 and 200^{o}C in an argon environment at elevated temperatures to avoid oxidation. Boron nitride powder and Mica plates were used to minimize the friction between the compressing anvils and the copper cylinders. Fig.7.2.3b shows an example AZ31+0.8Sr tube before and after compression of the tube-cylinder assembly at room temperature.

Texture and microstructure characterization

Microstructures and microtexture were examined using light and electron microscopy equipped with an EBSD detector. Sample cross-sections taken perpendicular to the RD were analyzed as shown in Fig.7.2.1b. Specimens were prepared using a series of grinding papers and polished with 1 µm diamond paste. Microstructures were etched using a picric acetic solution and electoropolished by 10% nital for optical and electron microscopy, respectively. Errors encountered with ebsd measurement are summerized in Appendix II.

The macrotexture was measured by X-ray diffraction (XRD). Incomplete $\{0001\}$, $\{10\bar{1}0\}$ and $\{10\bar{1}1\}$ pole figures were recorded using a Bruker D8 X-ray diffractometer equipped with cobalt Kα target. TexTools texture analysis software was used to construct the orientation distribution function (ODF). Recalculated pole figures and inverse pole figures were derived from the ODFs.

7.2.3. Results & Discussion

7.2.3.1. Mechanical Properties

Typical true stress–true strain curves determined under the present conditions are shown in Fig. 7.2.4. At room temperature, Fig.7.2.4a shows that the AZ31 tube exhibited a lower flow stress and tolerated more strain before failure compared to the alloys containing Sr. Although the two Sr-containing alloys showed similar strength, the tube containing more Sr fractured earlier. It is known that the Al-Sr intermetallics are responsible for the room temperature brittleness of AZ31-Sr alloys [17]. When the deformation temperature increased to 100^{o}C, no failure was

observed in the samples. Interestingly, the flow curves for all the samples were nearly the same (Fig.7.2.4b). At 200^{o}C, the flow curves of Sr-containing alloys were below the ones for AZ31 (Fig.7.2.4c). This softening effect of Sr is a result of the depletion of Al from the Mg-solid solution and the transformation of non-equilibrium Al-Mg-Sr precipitates to stable Al_4Sr intermetallics [15-17]. The isolated expansion curves of AZ31 and AZ31+Sr tubes at different temperatures are presented in Figs.7.2.4d-f. It can be seen that the stress to expand the tubes decreased with increasing temperature and the slope of the stress-strain curves decreased. This is due to the decrease of lattice resistance against dislocation motion and the activation of non basal slip systems at higher temperatures [16,17]. This decrease was more significant in Sr-containing alloys. This can be attributed to the enhanced ability of dislocations to bypass Al-Sr obstacles at elevated temperatures which increases the effect of temperature [15-17].

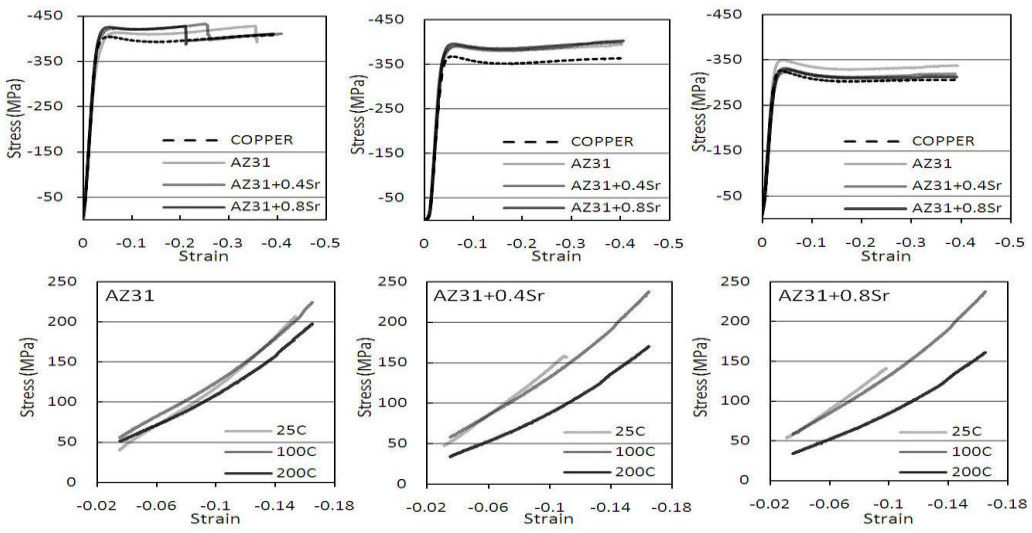

Figure .7.2.4. Stress-strain diagrams of compressed tube-copper assemblies at (a) room temperature, (b) 100^{o}C and (c) 200^{o}C. Isolated stress-strain curves of the tubes are presented at different temperatures for (d) AZ31, (e) AZ31+0.4Sr and (f) AZ31+0.8Sr.

7.2.3.2. Microstructure

Extrusion microstructure

During the extrusion of Mg alloys, coarse as-cast grains are gradually refined under the action of dynamic recrystallization (DRX) while Al-Sr precipitates formed during casting become elongated. The gradual change from the coarse grained as-cast (labelled as "1" in Fig.7.2.5a) to the fine microstructure of the extruded tube ("3" in Fig.7.2.5a) can be seen in the deformation zone of the AZ31+0.4wt%Sr (Fig.7.2.5a). The material was squeezed toward the die exit while recrystallizing ("2" in Fig.7.2.5a) and slid on the dead metal zone ("4" in Fig.7.2.5a). The microstructure of AZ31+0.4wt%Sr at early stages of extrusion is shown in Fig.7.2.5b. Dark Al-Sr precipitates with a globular shape are dispersed and new DRX grains have formed at the grain boundaries. With increasing deformation (Fig.7.2.5c), the volume fraction of DRX grains increased significantly while precipitates became elongated and formed stringers elongated towards the stress direction (HD). These precipitates are able to nucleate new grains (PSN) and pin the growing grain boundaries of newly recrystallized grains under specific hot deformation conditions [15,16].

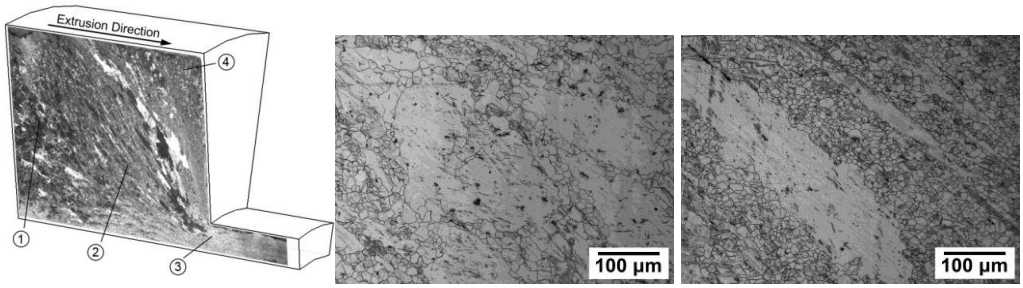

Figure .7.2.5. (a) The stereographic image of the deformation zone cross section of AZ31+0.4Sr tube extruded at 350^{o}C. (b) Early stages of recrystallization (region 2 in (a)) and (c) recrystallization in progress (region 3 in (a)).

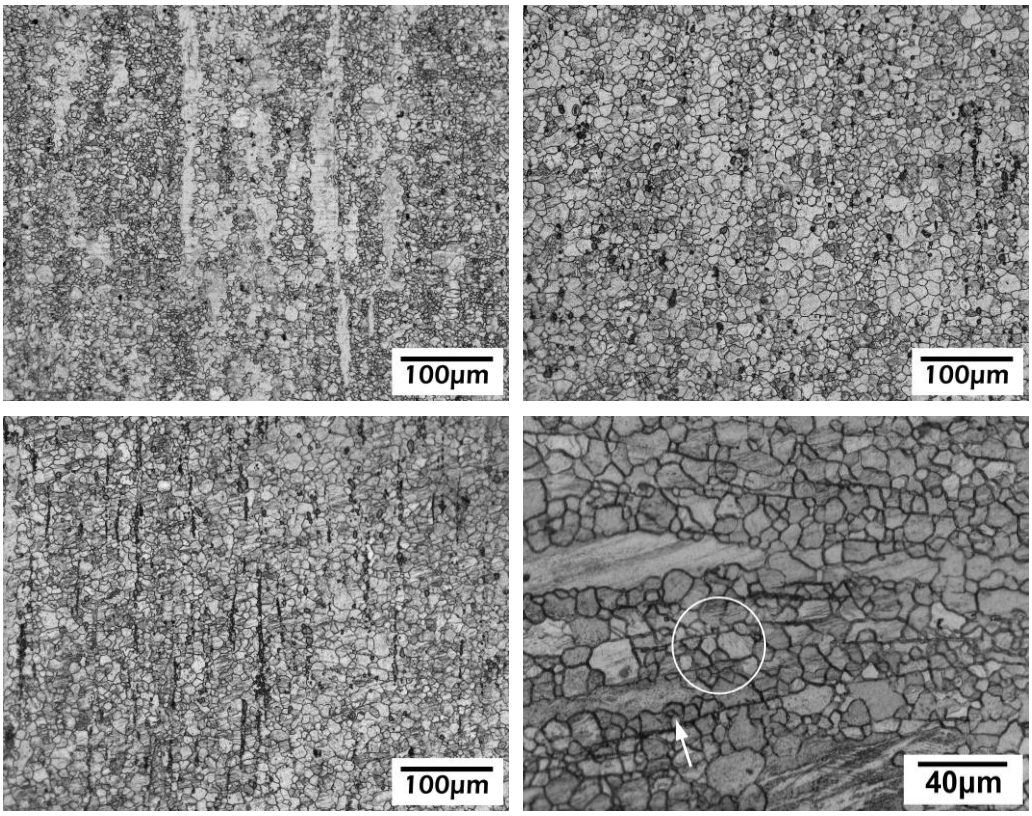

Figure 7.2.6. Microstructures of (a) AZ31, (b) AZ31+0.4Sr and (c,d) AZ31+0.8Sr tubes extruded at 350^{o}C. The extrusion direction is vertical.

At the end of extrusion, the AZ31 tube had a non uniform bimodal grain structure that consisted of very fine DRX and large elongated grains (Fig.7.2.6a) where twins can be observed. The AZ31+0.4Sr has a totally different microstructure with a more uniform grain size, fewer twins and some scattered Al-Sr stringers (Fig.7.2.6b).

The grain size was further reduced and more Al-Sr stringers were present in the microstructure when the Sr increased from 0.4wt% to 0.8wt% (Fig.7.2.6c). Interestingly, DRX nucleation at stringers can be observed in Mg+Sr alloys. In Fig.7.2.6d, new grains have nucleated at the stringer interface (marked with an arrow in Fig.7.2.6d) where growth was restricted either by other stringers or upon impingement on a grain boundary coming from another stringer (highlighted with a circle in Fig.7.2.6d). Fig.7.2.7a and b show the microstructure of the same region in the extruded AZ31+0.8Sr alloy. Fig.7.2.7b was taken with polarized

light which highlights the high angle boundaries. In the center of the image, many stringer lines spaced tightly together with a very fine grain structure between them can be seen.

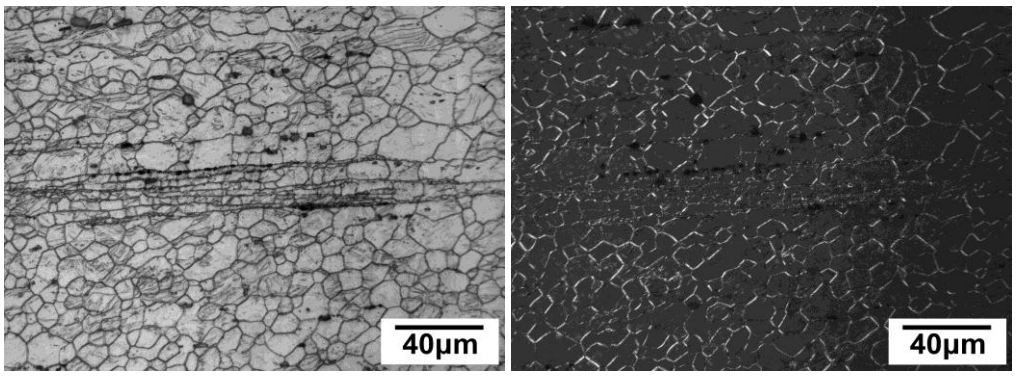

Figure .7.2.7. Microstructure of tube extruded AZ31+0.4Sr with (a) non polarized and (b) polarized light. The bright boundaries in the microstructure image taken by polarized light represent high angle boundaries

It is interesting to see that grain boundaries of the tiny grains were not apparent with sharp white lines in Fig.7.2.7b, revealing their low angle character. This mechanism is known as geometric dynamic recrystallization (GDRX) where the serrations of grain boundaries become comparable to the grain thickness and new equiaxed grains form by the interpenetration of the serrated boundaries [20]. Although, this mechanism is rarely seen throughout the microstructure, it is possible that it may be activated to a larger extent when the amount of precipitates increases.

Microstructure after expansion tests

As shown in Fig.7.2.8a tube expansion of AZ31 led to extensive twinning within large grains. Twinning volume fraction, determined using a systematic manual point count method (ASTM E 562 – 02), is shown in Fig. 7.2.9. At room temperature, ~23 of the AZ31 twinned, but increasing temperature (Fig.7.2.8b and c) significantly decreased the twinning activity to ~8% at 200^{o}C. Adding Sr to the AZ31 also contributed to a decrease in twinning during expansion tests

(Fig.7.2.8d-i). At room temperature, twinned volume fraction was decreased to ~ 19% and 17% in 0.4 and 0.8wt% Sr alloys, respectively. This difference in twinning was noted at all temperatures tested. It should be noted that the errors associated with this measurement ranged from 5-8% (higher for the lower values).

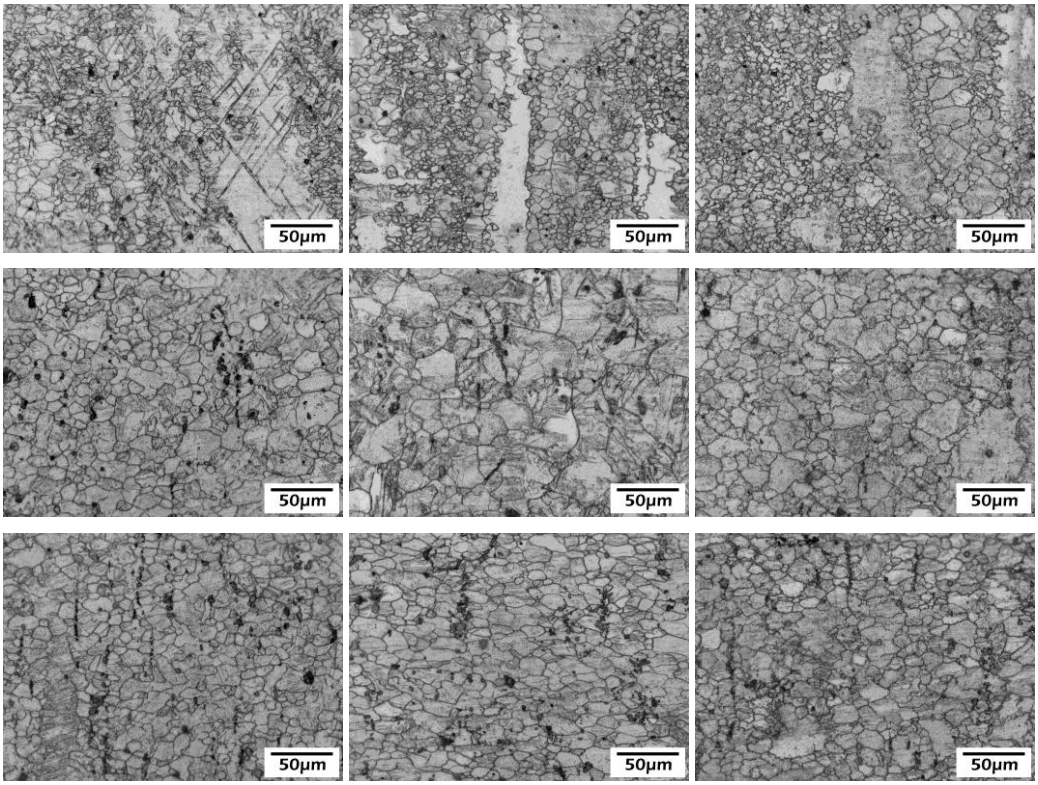

Figure.7.2.8. Microstructures of the expanded tubes. The first row represents the microstructures of AZ31, expanded at 25, 100 and 200^{o}C from left to right. The second and third rows show the microstructures of AZ31+0.4Sr and 0.8Sr respectively. The expansion temperatures are in the same order of AZ31. The extrusion direction is vertical and the hoop direction is horizontal.

This can be related to the finer microstructure and the decrease in lattice resistance to dislocation motion with the decrease of Al solubility in alloys containing Sr; since slip is facilitated, twinning is reduced [15, 16]. The evidence of grain boundary serration, shown in Fig.7.2.10, can be observed at 200 ^{o}C for all three alloys. This is a sign of early stages of DRX by grain boundary bulging [20, 28].

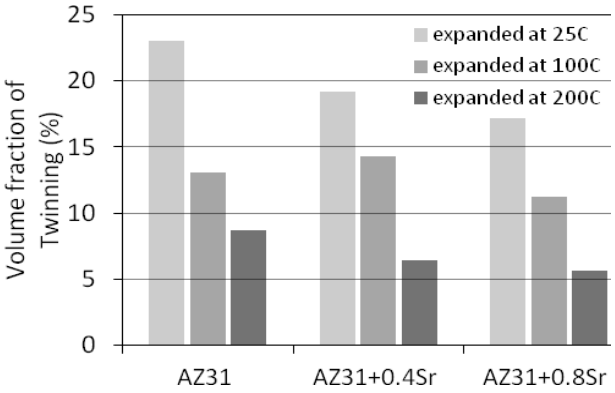

Figure.7.2.9. Volume fraction of twins in the expanded microstructures.

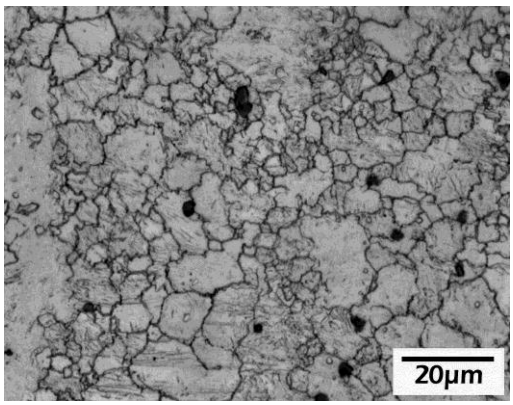

Figure.7.2.10. Serrations at the grain boundaries of the AZ31 tube after expansion at 200^{o}C.

7.2.3.3. Texture

Basal pole figures of the AZ31 and AZ31+Sr extruded and expanded tubes are shown in Fig.7.2.11. The extrusion texture of the three alloys was found to be similar, even though a slight change in intensity was found when Sr was added to AZ31 alloy. The texture consisted of two main components: one with the c-axis aligned with the radial direction (called the RD component) and the other approximately parallel to the hoop direction (called the HD component).

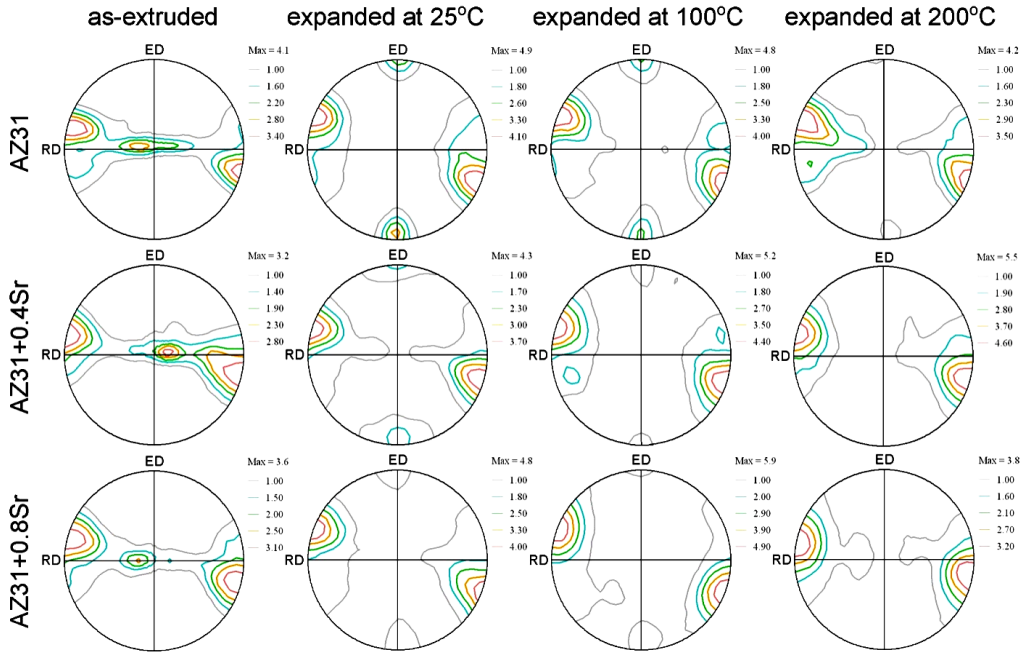

Figure.7.2.11. {002} pole figures representing the crystallographic texture of AZ31 and AZ31-Sr extruded and expanded tubes. The lowest and highest intensity contours are equal to 1 time random and maximum intensity respectively. Other five contours in between have an equal intensity difference from each other.

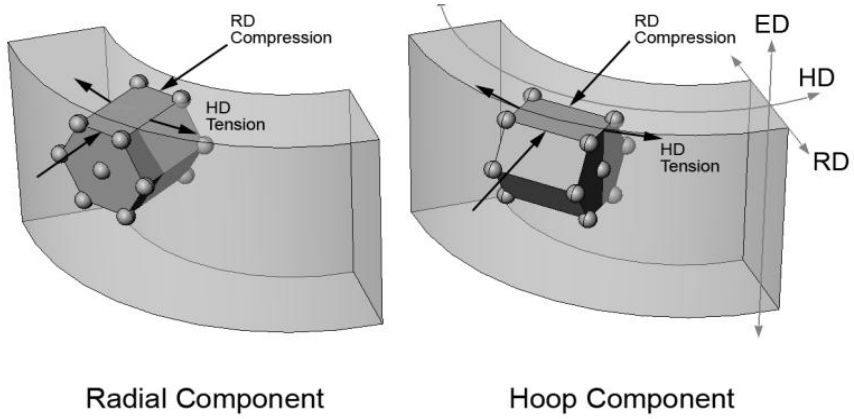

Figure.7.2.12. Schematic showing the position of the hexagonal lattice regarding the two basal components seen in the as extruded pole figures.

A schematic representation of the two texture components is presented in Fig. 7.2.12. The HD and RD components were formed by the circumferential and radial reduction of the forming tube during extrusion, respectively. It can be seen

in all the pole figures that the RD basal component deviatiated slightly from the RD axis. This deviation has previously been seen in the extrusion of seamed tubes [19] and in equal angle angular pressing (ECAP) where the flow of material folds and unfolds by passing through the hollow die [21-24]. A similar bending and unbending of material flow on the dead metal zone occurred here during the seam-less extrusion which rotated the basal poles from theoretically predicted positions. Note that the basal tilt was not seen in the bar extrusion of these alloys [16,18] since the symmetry of deformation prevents the incline of basal poles in a single direction.

The textures of the three alloys exhibited significant changes during tube expansion at room temperature. The RD component intensity was increased, while a new texture component appeared at the ED (i.e. grains with their c-axis aligned with the extrusion direction). Both changes coincided with the disappearance of the HD texture component in the as-extruded material. Such texture changes are due to crystallographic re-orientation occurring during twinning. Indeed, the expanded microstructures were characterized by numerous twins in all three alloys.

With increasing deformation temperature, the ED component lost strength and c-axes became aligned with the RD. At 200^{o}C, the HD component was not divided into RD and ED components, but was slowly rotated towards the RD. This corresponds to a stable end texture associated with basal glide. It is well known that with increasing temperature, decreased twinning and deformation becomes accommodated by dislocation glide and especially basal slip. A similar texture change was observed here for all three alloys when the deformation temperature was increased, as shown in Fig. 7.2.11. However it is interesting to note that the change in deformation mechanism from twinning at room temperature to dislocation glide at 200^{o}C led to an increase in deformation texture intensity in AZ31 and AZ31+0.4Sr, texture intensity in AZ31+0.8Sr was significantly decreased. This important finding will be discussed in the following sections.

7.2.3.4. Twinning

During expansion, straining HD and RD grains aligned their c-axes parallel and perpendicular to the tensile stress axis (HD) respectively. Consequently, the HD grains being pulled towards their c-axis underwent extension twinning, while RD grains, being pulled perpendicularly to their c-axes, evolved contraction and double twinning. Various crystal configurations associated with twinning are summarized in Fig.7.2.13. The $\{10\bar{1}2\}$ extension and $\{10\bar{1}1\}$ and $\{10\bar{1}3\}$ contraction twins all have six variants that led to a crystallographic misorientation of 86.17°, 56.26° and 63.89°, respectively.

In the case of double twinning associated with $\{10\bar{1}1\}$ contraction twins, [25-27] it was shown that 36 different double twin (DT) orientations may form within a grain that can be divided into four groups of variants, whose misorientations are 37.5°, 30.1°, 66.5° and 69.9°.

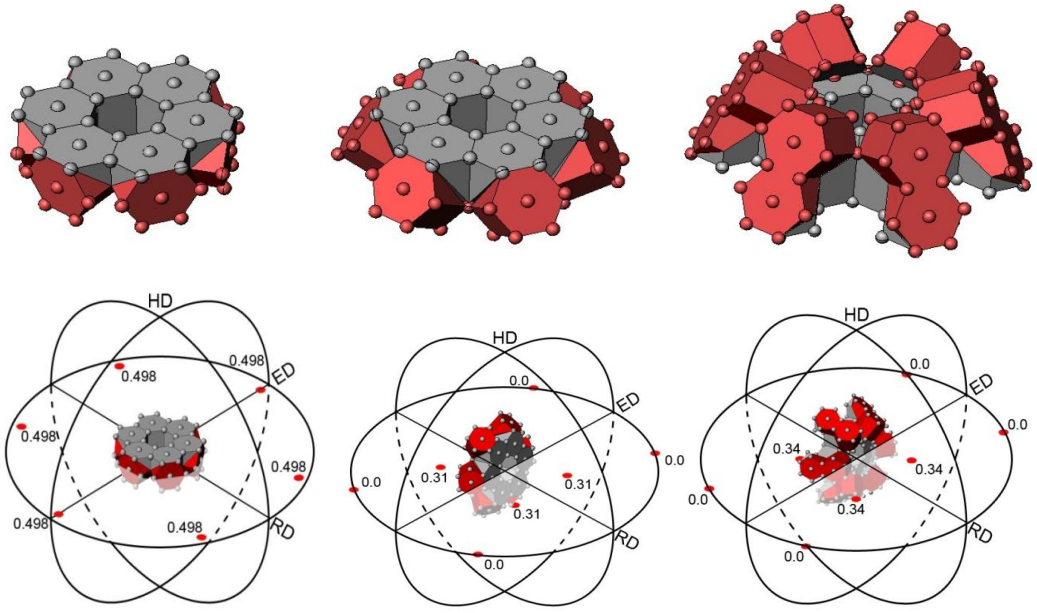

Figure.7.2.13. Spatial presentation of possible twinning variants for the hoop and radial texture components. (a) (10-12) extension of the hoop component (HD) (b) (10-11) and (c) (10-13) contraction variants of the radial component (RD). (d-f) Schmidt factors of different twins with the shear on the hoop direction.

Similarly, 36 possible DT orientations may form out of the six $\{10\bar{1}3\}$ contraction twin variants that can also be reclassified into four different groups of geometrically equivalent variants, whose misorientations now become 29.9°, 22.2°, 65.3° and 61.5°. The 36 DT variants associated with $\{10\bar{1}1\}$ and $\{10\bar{1}3\}$ contraction twins are shown in the form of basal pole figures as well as the four geometric configurations in Fig.7.2.14.

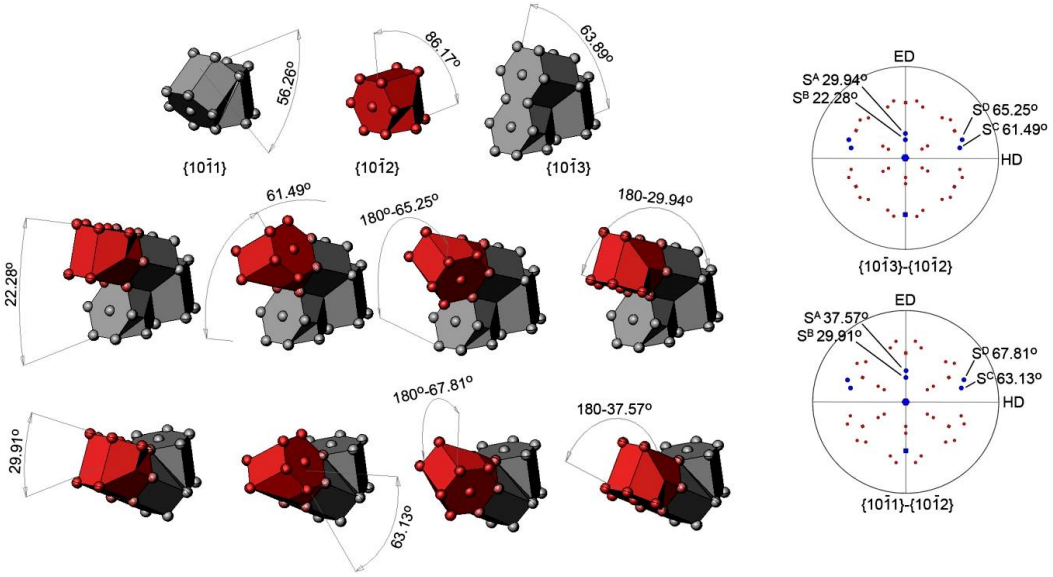

Figure.7.2.14. Schematic showing the configuration of the hexagonal lattice in single and double twinning. (b) Pole figure showing the {10-13} and {10-11} primary contraction twins and their 36 secondary twins.

It is known that twinning behaviour is dependent on the axial ratio of hcp metals [29]. Alloying elements forming solid solutions change the c/a ratio in the Mg lattice. Different alloying elements can either expand or contract the lattice parameters according to the atomic size and/or valence differences with the solid solution atoms [30]. Temperature alone and in combination with alloying can also influence the axial ratio. Temperature causes the <c> spacing to expand more than the <a> spacing, resulting in an increase in c/a [30].

Sr has very limited solubility in α-Mg, consequently the effect of Sr on c/a is negligible. For Al in α-Mg, it has been shown that both <a> and <c> lattice parameters decrease by increasing level of Al [31]. However, the slope of

decrease is higher for the <a> parameter. In other words, by increasing the Al content, the c/a increases. This has also been measured by other researchers [32]. Zn also reduces the <c> and <a>, but both parameters are reduced at the same rate and the c/a remains constant [30, 32]. Yoo *et al*. [33] have plotted the dependence of twinning shear versus c/a ratio for different twinning modes. The results indicate that when the c/a ratio is increased, twinning shear is decreased for $\{10\bar{1}2\}$ extension twins. Whereas for $\{10\bar{1}1\}$ and $\{10\bar{1}3\}$ contraction twins the twinning shear increases by increasing c/a [29]. Pekguleryuz *et al*. [34] studied the effect of c/a ratio on twinning and edge cracking in hot rolling. They reported that even a small change of c/a between pure Mg and AZ31 (0.04% increase) led to a difficulty in atomic reshuffling during double twinning, leaving a higher propensity of tension twins which are potent sites for crack nucleation. In the samples studied, with increasing Sr, the Al concentration in α-Mg and the c/a ratio decrease, which means that the shearing stress is increased for extension twinning and decreased for contraction twinning. The higher the c/a ratio, the lower the shear stress for extension twinning. The effect of decreasing c/a ratio and increasing temperature on twinning behaviour was also observed in the pole figures presented in Fig.7.2.11 where more Sr and higher expansion temperature resulted in a reduced extension twinning component at ED.

Twinning texture

Since different types of twins form within HD and RD grain orientations, their relative contribution to texture changes will be different and will thus be treated separately here. Extension twins that form within HD grains thicken and consume grains rapidly [29]. When extension twinning is activated, grains can be rotated towards six new orientations as shown in Fig.7.2.13a. In a perfect HD orientation, all twinning planes have a Schmid factor (SF) value close to 0.5, as shown in Fig. 7.2.13a, and thus experience a similar resolved shear stress. A small deviation of the c-axis from the perfect HD component will not significantly change the SF. Therefore, all six extension twins are likely to occur within the HD grains. Indeed, the contribution of the six extension twin variants was observed in all alloys

deformed at room temperature. In Fig. 7.2.13a, the two extension twin variants close to the ED led to the appearance of a new intensity peak at ED in deformation textures shown in Fig.7.2.11, while the four components close to the RD (Fig. 7.2.13a) contributed to the increase of the RD component (Fig. 7.2.11).

The contribution to twinning in HD grains to the RD component was also observed in the deformed microstructure (Fig.7.2.15). Three twins evolving two different variants (green and blue dots) formed within a HD grain (Fig. 7.2.15a). The twin orientation appeared to be close to the RD, as shown in the pole figure in Fig. 7.2.15 (b). The SF associated with both variants is also displayed on the pole figure in Fig.7.2.15c.

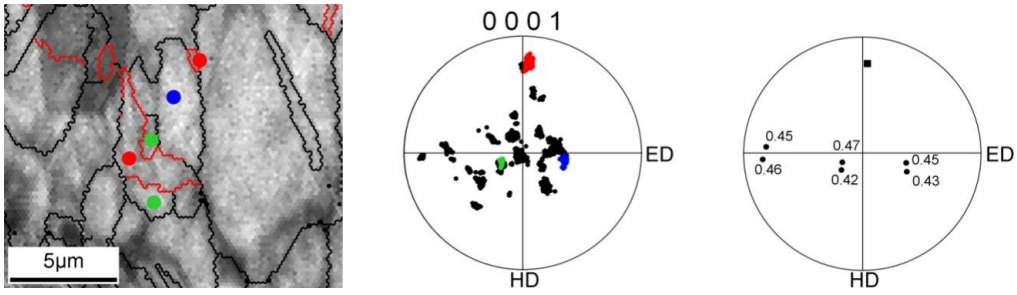

Figure.7.2.15. Initial grain (red dots) with two extensions twins (blue and green dots) that have rotated the c-axes toward the RD. The shmidt factor of extension twin orientations are also shown in the pole figure.

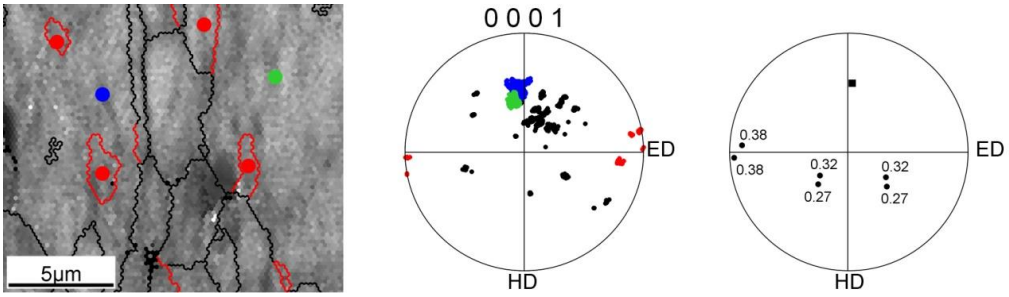

Figure.7.2.16. Initial grains (blue and green dots) with extensions twins (red dots) that have rotated the c-axes toward the ED. The shmidt factor of extension twin orientations are also shown in the pole figure.

An example of grains where twins have rotated the c-axis toward the ED is given in Fig.7.2.16. The pole figures clearly show that two extension twins variants with SF = 0.38 formed leading to the appearance of a new orientation with c-axis aligned with the ED.

On the other hand, contraction $\{10\bar{1}1\}$ and $\{10\bar{1}3\}$ form as primary twinning mode within initial (as-extruded) RD or as secondary twinning mode within HD grains that have been rotated towards the RD during extension twinning. In Fig.7.2.13b and c, the possible positions of the basal poles after $\{10\bar{1}1\}$ and $\{10\bar{1}3\}$ twinning are shown. The two components associated with both types of contraction twins have relatively lower Schmidt factors (SF) and are unlikely to be activated.

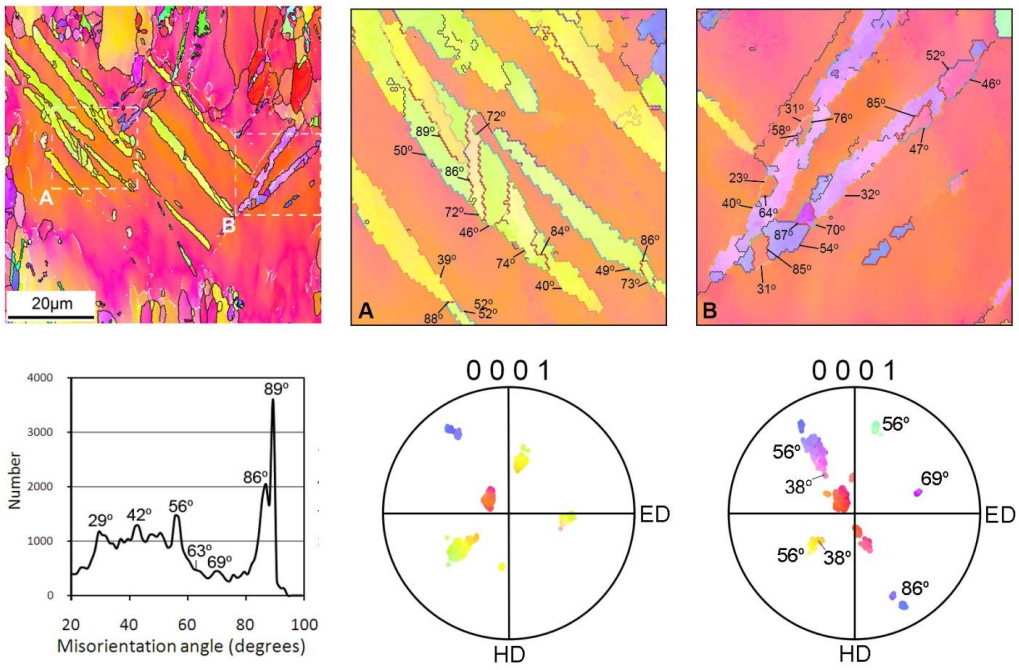

Figure.7.2.17. EBSD mapping of AZ31 extruded tube after expansion at room temperature. The grain boundary maps show the misorientation of grain boundaries at the twin regions in dicated by squares in the EBSD map. The labelled angles in the pole figure represent different twins.

Nevertheless, contraction twins will obviously lead to a spread of the RD texture component. Accordingly, the region delineating the RD component in Fig. 7.2.11 increased when the tube was deformed at room temperature and 100°C. Such behaviour is clearly illustrated in the A and B marked sections of EBSD map of Fig.7.2.17 (70-80% indexation). The pole figures of each section show how contraction twins rotate the c-axis around the RD texture component. The misorientation angles related to the twin orientations reveal that DT also contributes to the spread of the RD during expansion tests.

Since extension twins thicken, and in some cases consume the entire grain where they nucleate, their contribution to the textural changes during expansion at room temperature is more important than contraction twinning that remain thin. Therefore, the pole figure intensity increased rather than decrease as shown in Fig.7.2.11.

The effect of temperature

When the tube expansion temperature was increased, twinning was gradually replaced by dislocation glide as the dominant deformation mechanism. Accordingly, the intensity of the ED twinning component as shown in Fig.7.2.11 was found to decrease with increasing temperature for all three alloys. At 200 °C, the ED orientation was not apparent anymore. Similarly, the texture intensity decreased in AZ31 when the deformation essentially became dominated by dislocation glide. This is because the latter mechanism involves a smaller rotation than twinning and thus textural changes occur more slowly. Even though the RD orientation remained the stable end rotation with respect to basal slip, the changes became more progressive, as shown in Fig. 7.2.11, where c-axes that are aligned between the HD and RD component remained after the expansion of AZ31 at 200 °C.

Although twinning peaks were weakened in the AZ31+0.4Sr alloy by increasing the expansion temperature, the RD component became stronger. This shows that the increase of strength in the RD peaks at room temperature is not completely related to twinning. It has been previously reported [15,16] that Sr

reduces twinning in AZ31 alloys either by refining the grain size or promoting dislocation movement by depleting Mg solid solution from Al atoms. Additionaly, the depletion of Al could make atomic shuffling difficult for extension twinning to occur by reducing the c/a ratio [34]. In these alloys, the relocation of basal poles by dislocation glide is more significant than in AZ31 alloy which contains higher levels of Al solute available for pinning dislocations in α-Mg. Accordingly, the RD component also increased when room temperature deformation is compared to 100 °C in AZ31+0.8Sr alloy. However, at 200 °C texture intensity decreased significantly, even though there were no new texture components generated. Note that the RD texture component was the stable end texture of the present deformation condition only with respect to extension twinning and basal slips. The strong decrease in RD component intensity can therefore be due to an increasing amount of non basal slip systems that could be activated. Moreover, at high temperatures and high levels of Sr, recrystallization by means of PSN mechanism is increased at stringer boundaries and thus led to the formation of newly recrystallized grains with random orientations and therefore reducing overall texture intensity.

7.2.4. Conclusions

AZ31 and AZ31+Sr alloys were cast and hot extruded into seamless tubes. Expansion tests were performed by compressing pure copper cylinders inside the extruded tubes. The following conclusions were drawn based on interpretation of microstructural observations, mechanical tests and textural measurements:

1. Grain size becomes more uniform and average grain size is reduced with increasing Sr. Volume fraction of twins is decreased by an increasing level of Sr. In all the alloys studied, the volume fraction of twins after expansion decreased with increasing deformation temperature.
2. Due to the presence of Al-Sr stringers, Sr containing alloys showed higher strength at room temperature and their brittleness increased with increasing Sr. However, at 100°C the three alloys have almost the same

mechanical properties and at 200^{o}C Sr containing alloys become softer than AZ31. This is known to be a result of finer grain size and the lower amount of Al in Mg solid solution decreasing the lattice resistance against dislocation movement when Sr is present in the alloy.

3. The texture of the extruded alloys represents two components (HD and RD) which reoriented differently in expansion based on the orientation of the hcp lattice with respect to tension in the hoop direction. The HD component is likely to activate extension twins while contraction and double twinning appears in the RD grains.
4. During tube expansion, the weaker component (HD) is merged with the stronger component (RD) and the stronger component (RD) becomes more distributed. However, , the maximum intensity of the RD component dropped as a result of reduced twinning and enhanced dislocation motion when the expansion temperature was increased

7.2.5. References

1. Qinglin Jin, Sung-Yong Shim, Su-Gun Lim, "Correlation of microstructural evolution and formation of basal texture in a coarse grained Mg–Al alloy during hot rolling," Scripta Materialia 55 (2006) 843–846.
2. J. Bohlen, S.B. Yi, J. Swiostek, D. Letzig, H.G. Brokmeier, K.U. Kainer, "Microstructure and texture development during hydrostatic extrusion of magnesium alloy AZ31," Scripta Materialia Vol 53, Issue 2, (2005) 259-264.
3. S.S. Park, B.S. You, D.J. Yoon, "Effect of the extrusion conditions on the texture and mechanical properties of indirect-extruded Mg–3Al–1Zn alloy," Journal of Materials Processing Technology, Vol 209, Issues 18-19 (2009) 5940-5943.
4. Y. Chen, Q. Wang, J. Peng, C. Zhai, W. Ding, "Effects of extrusion ratio on the microstructure and mechanical properties of AZ31 Mg alloy," Journal of Materials Processing Technology, Vol 182, Issues 1-3 (2007) 281-285.
5. M. Shahzad, L. Wagner, "Influence of extrusion parameters on microstructure and texture developments, and their effects on mechanical properties of the

magnesium alloy AZ80," Materials Science and Engineering: A, Vol 506, Issues 1-2 (2009) 141-147T.

6. H. J. Mcqueen, M. Pekguleryuz, "Hot Workability of Magnesium Alloys" Magnesium Alloys and their Applications, Apr, 1992 Garmisch Partenkirchen, Germany, (1992) 101-108.
7. N. Stanford, M.R. Barnett, "The origin of "rare earth" texture development in extruded Mg-based alloys and its effect on tensile ductility," Materials Science and Engineering A, Volume 496, Issues 1-2 (2008) 399-408.
8. N. Stanford, "Micro-alloying Mg with Y, Ce, Gd and La for texture modification—A comparative study," Materials Science and Engineering A, Vol 527, Issues 10-11 (2010) 2669-2677.
9. L.W.F. Mackenzie, B. Davis, F.J. Humphreys, G.W. Lorimer, "The deformation, recrystallization and texture of three magnesium alloy extrusions," Materials Science and Technology, Vol 23, No 10 (2007) 1173-1180.
10. L.W.F. Mackenzie, M.O. Pekguleryuz, "The recrystallization and texture of magnesium-zinc-cerium alloys," Scripta Materialia, Vol 59, No 6 (2008) 665-668.
11. J.D. Robson, D.T. Henry, B. Davis, "Particle effects on recrystallization in magnesium–manganese alloys: Particle-stimulated nucleation," Acta Materialia, 57, (2009) 2739-2747.
12. A. Sadeghi, M. Pekguleryuz, "Precipitation during the Solidification of Mg-3wt%Al-1wt%Zn-(0.001-1%) Sr Alloys," American Foundry Society annual congress, Orlando, USA, (2010).
13. A. Sadeghi, M. Pekguleryuz, "Precipitation of Mg-3%Al-1%Zn-(0.01-1)wt%Sr Alloys during solidification," Journal of Materials Research, Journal of Materials Research, Volume 26, Issue 07 (2011) 896 – 903.
14. A. Sadeghi, M. Pekguleryuz, "Microstructure, mechanical properties and texture evolution of AZ31 alloy containing trace levels of strontium," Materials Characterization, Volume 62, Issue 8, (2011) 742-750.

15. A. Sadeghi, M. Pekguleryuz, "Recrystallization and Texture Evolution of Mg-3%Al-1%Zn-(0.4 -0.8) %Sr Alloys during Extrusion," Materials Science and Engineering A, Materials Science and Engineering: A, Volume 528, Issue 3 (2011) 1678-1685.
16. A. Sadeghi, M. Hoseini, M. Pekguleryuz, "Effect of Sr addition on texture evolution of Mg–3Al–1Zn (AZ31) alloy during extrusion," Materials Science and Engineering: A, Materials Science and Engineering: A, Volume 528, Issues 7-8 (2011) 3096-3104.
17. A. Sadeghi, S. Shook, M. Pekguleryuz, "Yield Asymmetry and Fracture Behaviour of Mg-3%Al-1%Zn-(0-1)%Sr Alloys Extruded at Elevated Temperatures," Materials Science and Engineering: A, In Press, Corrected Proof, Available online 28 June 2011.
18. A. Sadeghi, M.Pekguleryuz, "Effect of annealing on microstructure and texture evolution of Mg-3Al-1Zn-0.8Sr alloy during hot extrusion," (submitted to Journal of Materials Science)
19. A. Sadeghi, M. Pekguleryuz, "Tube Extrusion of AZ31 Alloy with Sr Additions," (submitted to Materials Science and Engineering A)
20. F.J. Humphreys, M. Hatherly, "Recrystallization and related annealing phenomena," Pergamon Press, Oxford (1996)
21. H.K. Lin, J.C. Huanga, T.G. Langdon, "Relationship between texture and low temperature superplasticity in an extruded AZ31 Mg alloy processed by ECAP," Materials Science and Engineering A, 402 (2005) 250–257.
22. S.R. Agnew, P. Mehrotra, T.M. Lillo, G.M. Stoica, P.K. Liawc, "Crystallographic texture evolution of three wrought magnesium alloys during equal channel angular extrusion," Materials Science and Engineering A, 408 (2005) 72–78.
23. S.R. Agnew, P. Mehrotra, T.M. Lillo, G.M. Stoica, P.K. Liaw, "Texture evolution of five wrought magnesium alloys during route A equal channel angular extrusion: Experiments and simulations," Acta Materialia 53 (2005) 3135–3146.

24. S.X. Ding, W.T. Lee, C.P. Chang, L.W. Chang and P.W. Kao, "Improvement of strength of magnesium alloy processed by equal channel angular extrusion," Scripta Materialia 59 (2008) 1006–1009.
25. E. Bertrand, P. Castany, I. Pe´ron, T. Gloriant, "Twinning system selection in a metastable β-titanium alloy by Schmid factor analysis," Scripta Materialia 64 (2011) 1110–1113.
26. E´. Martin, L. Capolungo, L. Jiang, J.J. Jonas, "Variant selection during secondary twinning in Mg–3%Al," Acta Materialia 58 (2010) 3970–3983.
27. M.R. Barnett, Z. Keshavarz, A.G. Beer and X. Ma: Non-Schmid Behaviour of Secondary Twinning in a Polycrystalline Magnesium Alloy, Acta Materialia, Vol. 56, No. 1, 2008, 5-15.
28. Etienne Martin, John J. Jonas, "Evolution of microstructure and microtexture during the hot deformation of Mg–3% Al,"Acta Materialia, 2010, 58
29. M. H. Yoo, "Slip, Twinning, and Fracture in Hexagonal Close-Packed Metals" Metallurgical Transactions A, Volume 12a, (1981)
30. A. Becerra, M. Pekguleryuz, "Effects of lithium, indium, and zinc on the lattice parameters of magnesium," J. Mater. Res., Vol. 23, No. 12, (2008)
31. G.V. Raynor: The Physical Metallurgy of Magnesium and Its Alloys (Pergamon Press, New York, 1959).
32. J.S. Park, Young Won Chang, "The Effect of Alloying Elements on the c/a Ratio of Magnesium Binary Alloys," Advanced Materials Research, 26-28, 95, (2007)
33. M. H. Yoo; J. K. Lee, "Deformation twinning in h.c.p. metals and alloys," Philosophical Magazine A, 63: 5, 987 — 1000 (1991)
34. M. Pekguleryuz, M. Celikin, M. Hoseini, A. Becerra, L. Mackenziec, "Study on edge cracking and texture evolution during 150 .C rolling of magnesium alloys: The effects of axial ratio and grain size," Journal of Alloys and Compounds, article in press.

Chapter 8

Conclusions

Detailed studies of precipitation, microstructural evolution, mechanical properties and textural formation in AZ31-Sr alloys were carried out in this thesis. Alloys containing various levels of Sr were cast, heat treated, hot extruded and experimental work and analyses were carried out by means of thermal analysis, optical microscopy, scanning electron microscopy (SEM), energy dispersive spectrometry (EDS), electron probe micro-analysis (EPMA), electron back scattered diffraction (EBSD) and X-ray diffraction (XRD) techniques.

General Conclusions

The following general conclusions drawn are as follows:

1- Addition of Sr in to AZ31 supresses the formation of the $Mg_{17}Al_{12}$ precipitates and forms thermally stable Al-Sr intermetallics.

2- Formation of Al-Sr precipitates in the microstructure reduces the concentration of Al in α-Mg. Depletion of Al reduces the lattice resistance and increases the axial ratio of the hexagonal which changes the recrystallization-twinning behaviour and reduces the strength of the alloy.

3- The strength decrease due to the depletion of Al is partially counterbalanced by the reinforcement provided by the Al-Sr precipitates. However, these precipitates are the source of cracking and reduced elongation.

4- Sr-rich precipitates contribute to PSN and texture weakening, however, the amount of PSN is much less than DRX at the grain boundaries, which promotes the basal texture. Adding more Al-Sr precipitates at the grain boundaries (more than 1 wt% Sr in the alloy) might be effective in increasing the portion of PSN. However, it simultaneously increases the brittleness of the alloy.

5- The mutual relationship between PSN and brittleness is a common effect which is predicted to occur with other alloying elements as well (e.g.

calcium). The best way to overcome this effect is to increase the precipitate active nucleating surface by distributing it more across the grain boundaries. In this respect, the addition of another trace element can be investigated in a future study.

More specific conclusions are given below.

Precipitation and solidification of AZ31-Sr Alloys

1. Low levels of Sr (0.01-0.035%Sr) lead to grain refinement in AZ31 as well as secondary phase refinement while higher amounts of Sr (0.05-1%Sr) form Al-Sr (Mg) precipitates. Microstructural observations supported by cooling curves and EPMA show grain and precipitate (β-$Mg_{17}Al_{12}$) refinement by growth poisoning and via nucleus formation respectively, with the addition of low levels of Sr to AZ31.
2. Thermodynamic calculations predict the substitution of β-$Mg_{17}Al_{12}$ with Al_4Sr with increasing Sr. The onset of this substitution occurs at lower concentrations of Sr in the presence of Mn, which was confirmed by microstructural examinations.
3. TEM/EDS analysis and thermodynamic calculations both show a depletion of Al and slight increase of Mn inside the grains with increasing Sr.

Recrystalization and Texture Evolution during Hot Bar Extrusion

4. Al-Sr eutectic precipitates were found to elongate and distribute uniformly during extrusion and pin the grain boundaries consequently prevent grain growth during recrystallization. The Mg matrix adjacent to the stringers underwent local lattice rotation which leads to a misorientation gradient (strain accumulation) close to the particles.
5. PSN occurs in the deformed regions around the precipitates in certain hot working conditions at 350^{o}C. Increasing the amount of Al-Sr stringers in AZ31 increases likely potential sites for PSN. PSN through Al-Sr stringers

results in the recrystallization of new grains with orientations different to the basal fiber texture, resulting in the reduction of fiber texture strength.

6. At low temperatures or low levels of Sr, the main micro-mechanism involved in DRX is grain boundary bulging and the formation of necklace structure until the entire matrix is recrystallized. The prismatic planes of recrystallized grains are aligned perpendicular to the extrusion direction resulting in a strong <10.0> fiber texture.
7. At high temperatures and high concentrations of Sr, the contribution of PSN is considerable and the overall texture is weakened by nucleation of new grains with random orientations at the precipitate boundaries.
8. At low temperatures, ε_c and F_v decrease with increasing Sr. This is attributed to reduced Al solubility which decreases the solute drag effect and enhances recrystallization.
9. At high levels of Sr, ε_c and F_v decrease with increasing temperature. This has been attributed to the observation that at high temperatures, the accumulation of dislocations behind the boundaries is decreased (compared to low temperatures) and the contribution of the particles in blocking dislocations becomes more significant. Consequently, the effect of PSN becomes considerable and the final texture is weakened.
10. At very high temperatures and high concentrations of Sr, cracks initiate at the extruded bar surface. At low temperatures and low levels of Sr, twinning is active and the twin boundaries act as nucleation sites for DRX.
11. Trace levels of Sr reduces the strength of the basal texture in hot compression and extrusion which can be attributed to the decrease in twinning and the change in the concentration of Al and Sr atoms in Mg.
12. The tensile and compressive strength of extruded AZ31 alloys containing different levels of Sr depend more on the extrusion temperature than on the Sr concentration.

Yield Asymmetry and Fracture Behaviour

13. Low levels of Sr (0.05wt%) increases the tensile yield (Y_s) and ultimate tensile strength (UTS) of AZ31, while higher concentrations (0.8wt%)

decrease the Y_s by lowering Al solid solubility and hence solute strengthening and decrease UTS by initiating cracks at the Al-Sr precipitates.

14. Fracture strain in compression is less sensitive to Sr additions than in tension. This is attributed to the direction of the crack inside the Al-Sr precipitates.
15. The yield asymmetry of the AZ31+xSr alloys increases with increasing extrusion temperature. However the increase is smaller when Sr is present in the alloy.

Effect of Pre-Extrusion Annealing

16. Annealing at 400^{o}C results in the decomposition of the Mg-Al-Sr non-equilibrium phase to a stable Al_4Sr precipitate. Increasing annealing time increases the extent of the transformation. Increasing annealing time causes the stringers to disperse more homogeneously and leads to a more uniform hardness gradient across the diameter of the extruded bar.
17. Although the basal texture was maintained in all annealing conditions studied, there was a slight gradual change in the plane facing the extrusion direction from first order to second order prism with increasing annealing time.
18. The change in basal orientation was described to be a result of change in the blockage of dislocations in different slip systems. In grains having a basal $\boldsymbol{\tau}$ close to zero, the favourable (002)[100] systems see less resistance to slip when Al is reduced in α-Mg during annealing. However, the higher energy consuming (002)[110] system still avoids dislocation motion, work hardening and DRX. Consequently, maximum intensity of IPF drops and the volume fraction of (110) planes facing the extrusion direction increases.

Seamed and Seamless Tube Extrusion

19. The addition of Sr in the seamed tube extrudates resulted in a uniform and refined grain size. The curvatures in the material flow during extrusion in the designed die breaks down the precipitate stringers and uniformly distribute them across the microstructure.
20. The texture of the extruded tube consisted of a two texture components; a 25^{o} tilted basal pole and two extra δ components. The maximum intensity of ODF decreased with increasing Sr. In AZ31 and AZ31+0.4Sr the ODF maximum intensity occurred at the basal components while in AZ31+0.8Sr the ODF maximum was at the δ component.
21. The δ components are a result of circumferential flow in the welding zone. In AZ31 and AZ31+0.4Sr the δ_1 component is (023) $<\overline{1}32>$ while the same component in AZ31+0.8Sr is 9^{o} more tilted and is (012 $<1\,\overline{2}1>$. The higher Sr in the alloy, the less Al in solid solution Mg and the less lattice resistance against dislocation slip. As a result grains could deform more easily in the circumferential directions and selective work hardening-DRX cycle leaves more grains with the unfavourable slip orientation (δ components).
22. Due to the presence of Al-Sr stringers, Sr containing alloys (seam-less tubes) show higher strength at room temperature and their brittleness increases with increasing Sr. However, at 100^{o}C the three alloys have almost the same mechanical properties and at 200^{o}C Sr containing alloys become softer than AZ31. This is known to be a result of finer grain size and the lower amount of Al in Mg solid solution decreasing the lattice resistance against dislocation movement when Sr is present in the alloy.
23. The texture of the extruded alloys represents two components (HD and RD) which reorient differently in expansion based on the orientation of the hcp lattice with respect to tension in the hoop direction. The HD component is likely to activate extension twins while contraction and double twinning appears in the RD grains.

24. During tube expansion, the weaker component (HD) merged with the stronger component (RD) and the stronger component (RD) became more distributed. However, the maximum intensity of the RD component drops as a result of reduced twinning and enhanced dislocation motion when the expansion temperature is increased.

FUTURE WORK

The following questions and points of investigation have been identified for future studies as a result of the findings and observations of this study

1- The addition of grain and precipitate refiners into the AZ31-Sr system to disperse precipitates as much as possible.

2- Investigate the strain distribution around the Al-Sr precipitates by in-situ deformation/EBSD.

3- Investigate the effect of Sr additions on the twinning behaviour of AZ31 by in-situ acoustic emission and TEM.

4- Investigate the mechanical properties, anisotropy and texture properties of AZ31-Sr rolled sheets.

5- Perform creep tests on the as-cast and extruded AZ31-Sr alloys.

6- Extrude large industrial scale AZ31-Sr tubes and perform hydroforming tests.

Chapter 9

Contributions to Original Knowledge

This thesis offers a broad, new perspective on the microstructure and texture development during hot-extrusion of magnesium alloys, which can be categorized as:

1- ***Understanding the phases in a new Mg alloy system:*** Multi component phase diagrams, precipitation and concentration of solid solutions have been calculated by thermodynamic modelling for the AZ31-Sr system. Including Mn in the system and analyzing the solid solubility effects, provide a good basis to determine the deformation and recrystallization mechanisms in AZ31 and AZ31 + Sr alloys.

2- ***Understanding the role of Sr in the grain refinement and microstructural refinement of AZ31 alloy***: An in-depth analysis provided a good insight into the role of Sr in microstructural and grain refinement of the AZ31 alloy. Thorough microstructural examinations by EPMA and cooling curve analyses showed that the grain and precipitate (β-$Mg_{17}Al_{12}$) refinement occurs by growth poisoning and via nucleus formation, respectively, with the addition of low levels of Sr to AZ31.

3- ***Discovering Particle Stimulated Nucleation of Recrystallization in Mg-Al-Zn Sr alloys:*** Using EBSD and TEM techniques, the occurrence of PSN adjacent to Al-Sr stringers and the effect of the newly recrystallized grains on weakening the texture have been proven for the first time.

4- ***Generation of Micro-mechanisms Maps***: A comprehensive study on hot deformation properties and textural evolution in extruded AZ31-Sr has led to the determination of a *micro-mechanism map* over a wide range of temperatures and Sr concentrations.

5- ***Understanding the Role of Sr in Yield Asymmetry of AZ31***: Through mechaninal testing, it has been found that the yield asymmetry of the AZ31+xSr alloys increases with increasing extrusion temperature. However, the amount of increase is smaller when Sr is present in the alloy.

6- ***Determining an Interesting Effect of Pre-Extrusion Annealing Time on the Final Texture of AZ31 and AZ31+Sr:*** In this study the final texture of extruded bars was dependent on annealing conditions before extrusion. Although the basal texture was maintained in all annealing conditions studied, there is a slight gradual change in the plane facing the extrusion direction from first order to second order prism with increasing annealing time.

7- For the first time, AZ31-Sr tubes were extruded in both seamed and seamless shapes. Microstructures, textures and mechanical properties were thoroughly analyzed.

8- ***Insight into Texture Evolution during Tube Extrusion of AZ31+SR Alloys*** It has been shown that the textures of the extruded tubes are affected by the circumferential flow of material inside the die and consequently the texture is comprised of different components.

9- By means of expansion tests, the deformation behaviour of different texture components were analyzed by x-ray diffraction and EBSD. It has been shown in the seamless tubes that during tube expansion, the weaker texture component (HD) is merged with the stronger component (RD) and the stronger component (RD) becomes more distributed

10- ***Insight into Alloy Design:*** For the purpose of improving Mg as an extrusion alloy, it has bean shown that Sr additions up to 1 wt% do not significantly change extrusion conditions. However, up to a specific concentration (0.4wt%), Sr increases the room temperature strength and the elevated temperature workability of the alloys

APPENDIX I

Errors Encountered in Measuring Stress-Strain Curves

Errors can be generated in stress-strain measurements from the following experimental parameters:

- ***Sample imperfection and inappropriate positioning:*** Improper positioning of the sample with respect to the axes of the mechanical testing machine, or insufficient lubrication of samples under compression can cause non-uniform deformation and buckling, which is a source of error. Poor or imprecise machining of the samples could provide an inhomegenous samples structure with weak areas which fail early. *In addition to proper lubrication with mica plates and boron nitride, a height to diameter ratio of 1.5 was used in preparing the compression samples to minimize buckling.*
- ***Inaccuracy in data logging:*** In compression measurements the crosshead displacement rate used to calculate the strain can lead to errors originating from deflection of the machine or imprecisely machined specimens [Kuhn 2000]. In tension, slipping of the sample in the jaws or extensiometer within the sample could cause significant errors in strain measurement.
- ***Calculation errors:*** There are different methods for calculating various parameters in a stress-strain curve (YS, UTS and etc.), each of these methods have their own limitations and could be a potential source of error. In materials which do not exhibit a sharp yield point (such as the material we studied), an offset yield point is arbitrarily defined at 0.2% strain. This approximation was used to measure the tensile yield stress of the samples studied in this thesis.

APPENDIX II

Errors Encountered in EBSD Texture Measurement

Different sources of errors which occur in an EBSD analysis can be defined as:

- ***Apparatus restrictions;*** spatial and angular resolution, beam diameter and step size are the main variable parameters of an EBSD measurement. If the step size is not adjusted with respect to beam size important data points may be missed. *A 0.25-0.3 μm step size was used for all the measurements in this thesis.*
- ***Indexation and Data collection efficiency;*** sample surface condition effects the Kikuchi pattern that forms. Pattern quality and appropriate background selection influences the level of indexation in an EBSD measurement. In some heavily deformed microstructures, the number of successful indexes is significantly reduced. Un-even precipitates in the microstructure can block the electron beam by casting an elongated shadow on the tilted sample surface resulting in reduced indexation in the shaded area. *To increase the data collection efficiency specimen preparation was performed with special care. For more precise measurements, ion milling was used for surface preparation to form a flat surface (compared to electro-polishing which has a different reaction of precipitates and matrix).*
- ***Analysis accuracy;*** inaccurate pattern recognition and crystal orientation measurements may lead to false results. Pseudo-symmetry could also occur where 2 orientations cannot easily be distinguished due to an apparent n-fold rotation axis. *Different measurement parameters for pattern recognition (number of projected lines, edge selection, binning, and Hough resolution) were selected based on the manufacturers recommendations for magnesium alloys. The possiblity of pseudo-symmetry was eliminated by automatic data clean-up procedures in the TSL texture analysis software.*
- ***Statistical errors:*** Statistical limitations caused by insufficient data points are a significant source of error in generating texture entities.

Wright *et al*. [Wright 2007] compared textures measured by EBSD and X-Ray diffraction and reported that 10,000 grains provide a texture characterization equivalent to that obtained by X-ray diffraction. *However, in this study, EBSD was not used to construct pole figures for texture representation.*

- ***Data clean-up;*** in most EBSD measurements the raw data undergoes different clean-up cycles to remove artefacts and false data points generated by the apparatus. Inappropriate data clean-up could result in incorrect and misleading results. *Data clean-up was used as little as possible in this thesis. Whenever noise reduction and data clean-up was used it, the decision was based on the recommendation of the software developer.*

A large number of parameters were considered to minimize errors in the EBSD analysis presented in this thesis from machine setup and area selection to numerical analysis and data clean-up.

APPENDIX III

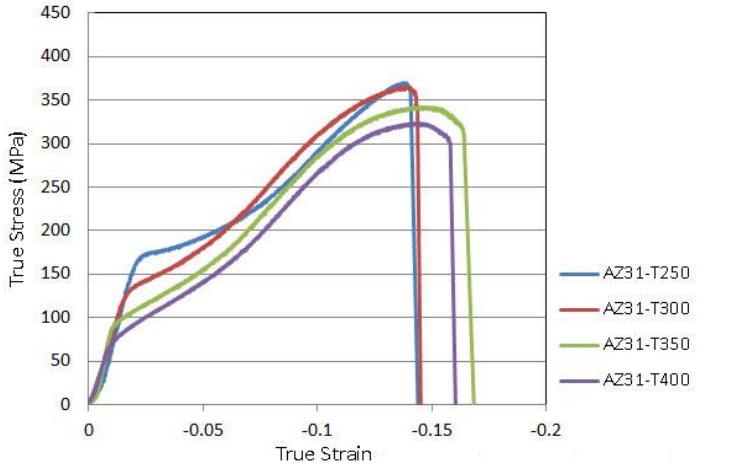

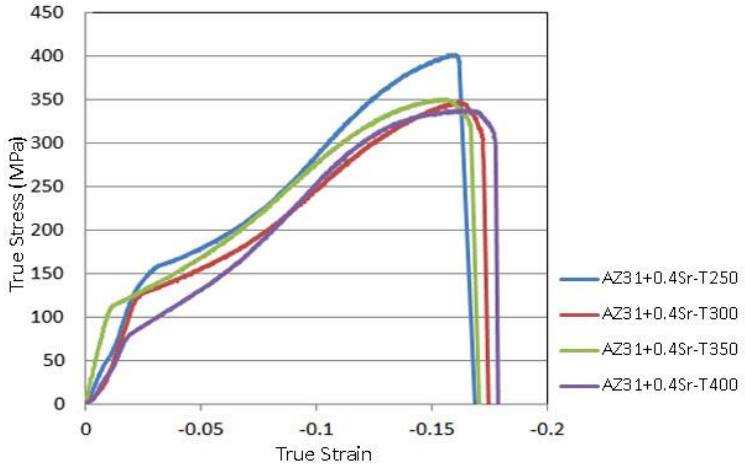

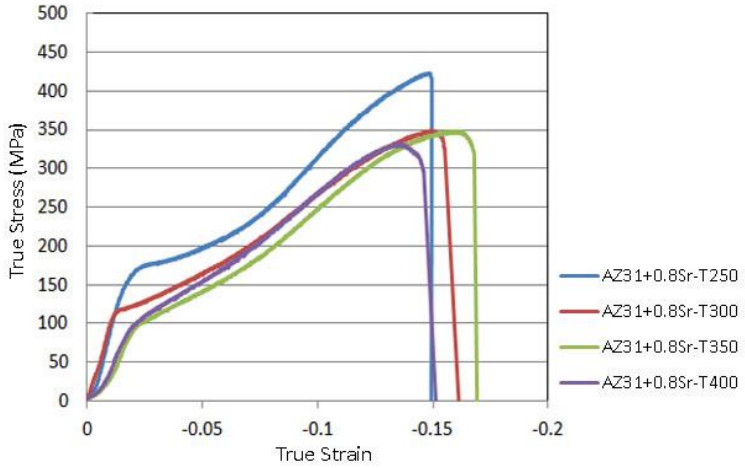

Room temperature true stress-true strain curves of AZ31-Sr bars extruded at four different temperatures.

APPENDIX IV

By considering the fundamental volume preservation assumption of plastic deformation and the fact that the circumferential and radial strains are equal in the compressed cylinder, ε_{θ_1} can be defined as

$$d\varepsilon_{\theta_1} = -\Delta l/2l_0 \qquad \text{(Eq.1)}$$

The contact surface between the cylinder and tube transfers circumferential strain into the tube through the deformation process and expends it. It is acceptable to consider the circumferential strain in the tube inner surface (which yield starts) and across its thickness equal to the same strain in the cylinder ($\varepsilon_{\theta_2} = \varepsilon_{\theta_1}$).

The circumferential stress in the tube can be defined by solving the work equilibrium equation (Eq. 2). The total work done by the machine is consumed by deformation (extruded tube and the copper cylinder) and friction (in the cylinder-jaws and the cylinder-tube interface). As a result, the total incremental work per volume (dW_t) can be described as:

$$dw_t = dw_{cylinder} + dw_{tube} + dw_{Friction} \qquad \text{(Eq.2)}$$

$$dw_t = {dW}/{V} = {F(\Delta l)}/{Al} = \bar{\sigma} d\bar{\varepsilon} \qquad \text{(Eq.3)}$$

Friction between the gliding surfaces was minimized by using proper lubrication and for simplicity in solving the equations the friction term was ignored. Therefore the incremental work per volume can be calculated separately for the tube and cylinder. By considering the plane strain condition in the tube ($\varepsilon_{z_1} = 0$) and the fact that the stress in the z direction is zero ($\sigma_{z_1} = 0$), the incremental work per unit volume for the tube can be simplified as

$$dw_{tube} = \sigma_{\theta_1} d\varepsilon_{\theta_1} + \sigma_{r_1} d\varepsilon_{r_1} + \sigma_{z_1} d\varepsilon_{z_1} = 2\sigma_{\theta_1} d\varepsilon_{\theta_1} \qquad \text{(Eq.4)}$$

By using the von Mises criterion and considering the equity of strain in the hoop and radial directions of the cylinder ($\varepsilon_{\theta_1} = \varepsilon_{r_1}$) and inserting it in the flow rules, equity of the magnitude of the tensile hoop and compressive radial stress can be derived. As a result $dw_{cylinder}$ can be defined as:

$$dw_{cylinder} = 2d\varepsilon_{\theta_2}\left(\sigma_{\theta_2} - \sigma_{z_2}\right) \qquad \text{(Eq.5)}$$

By substituting Eq.4 and Eq.5 in Eq.2 and considering the circumferential strains to be equal in both the cylinder and tube ($\varepsilon_{\downarrow}(\theta_{\downarrow}2) = \varepsilon_{\downarrow}(\theta_{\downarrow}1)$) Eq 2 becomes:

$$dw_t = 2d\varepsilon_{\theta_1}\left(\sigma_{\theta_1} - \sigma_{f_2}\right) \quad \text{(Eq.6)}$$

In which σ_{f_2} is the flow stress of the copper cylinder considering the von Mises flow criterion. Sustituting (Eq.1) and (Eq.6) in (Eq.3) gives:

$$\sigma_{\theta_1} = \sigma_{f_2} - {}^{F}/_{A_0} \quad \text{(Eq.6)}$$

Eq 6 defines the circumferential stress and strain in the tube $\left(\sigma_{\theta_2}, \varepsilon_{\theta_2}\right)$ as a function of force, displacement, and flow stress of the copper insert.